PROCESSING AND CHARACTERIZATION OF POROUS TITANIUM NICKEL
SHAPE MEMORY ALLOYS

A THESIS SUBMITTED TO
THE GRADUATE SCHOOL OF NATURAL AND APPLIED SCIENCES
OF
MIDDLE EAST TECHNICAL UNIVERSITY

BY

TARIK AYDOĞMUŞ

IN PARTIAL FULFILLMENT OF THE REQUIREMENTS
FOR
THE DEGREE OF DOCTOR OF PHILOSOPHY
IN
METALLURGICAL AND MATERIALS ENGINEERING

JULY 2010

Approval of the thesis:

PROCESSING AND CHARACTERIZATION OF POROUS TITANIUM NICKEL SHAPE MEMORY ALLOYS

submitted by **TARIK AYDOĞMUŞ** in partial fulfillment of the requirements for the degree of **Doctor of Philosophy in Metallurgical and Materials Engineering, Middle East Technical University** by,

Prof. Dr. Canan Özgen
Dean, Graduate School of **Natural and Applied Sciences**   _____

Prof. Dr. Tayfur Öztürk
Head of Department, **Metallurgical and Materials Engineering**   _____

Prof. Dr. Şakir Bor
Supervisor, **Metallurgical and Materials Engineering, METU**   _____

Prof. Dr. Bilgehan Ögel
Co-Supervisor, **Metallurgical and Materials Engineering, METU**   _____

Examining Committee Members

Prof. Dr. Çiğdem Erçelebi
Department of Physics, METU   _____

Prof. Dr. Şakir Bor
Metallurgical and Materials Engineering, METU   _____

Prof. Dr. Kadri Aydınol
Metallurgical and Materials Engineering, METU   _____

Assoc. Prof. Dr. Nuri Durlu
Mechanical Engineering, TOBB ETU   _____

Assoc. Prof. Dr. Arcan Dericioğlu
Metallurgical and Materials Engineering, METU   _____

Date : _____ 30.07.2010 _____

I hereby declare that all information in this document has been obtained and presented in accordance with academic rules and ethical conduct. I also declare that, as required by these rules and conduct, I have fully cited and referenced all material and results that are not original to this work.

Name, Last name: Tarık Aydoğmuş

Signature   :

ABSTRACT

PROCESSING AND CHARACTERIZATION OF
POROUS TITANIUM NICKEL SHAPE MEMORY ALLOYS

Aydoğmuş, Tarık

Ph.D., Department of Metallurgical and Materials Engineering

Supervisor: Prof. Dr. Şakir Bor

Co-supervisor: Prof. Dr. Bilgehan Ögel

July 2010, 184 pages

Porous TiNi alloys (Ti-50.4 at. %Ni and Ti-50.6 at. %Ni) with porosities in the range 21%-81% were prepared successfully applying a new powder metallurgy fabrication route in which magnesium was used as space holder resulting in either single austenite phase or a mixture of austenite and martensite phases dictated by the composition of the starting prealloyed powders but entirely free from secondary brittle intermetallics, oxides, nitrides and carbonitrides. Magnesium vapor do not only prevents secondary phase formation and contamination but also provides higher temperature sintering opportunity preventing liquid phase formation at the eutectic temperature, 1118 °C resulting from Ni enrichment due to oxidation. By two step sintering processing (holding the sample at 1100 °C for 30 minutes and subsequently sintering at temperatures higher than the eutectic temperature, 1118 °C) magnesium may allow sintering probably up to the melting point of TiNi.

The processed alloys exhibited interconnected (partially or completely depending on porosity content) open macro-pores spherical in shape and irregular micro-pores in the cell walls resulting from incomplete sintering. It has been found that porosity content of the foams have no influence on the phase transformation

temperatures while deformation and oxidation are severely influential. Porous TiNi alloys displayed excellent superelasticity and shape memory behavior. Space holder technique seems to be a promising method for production of porous TiNi alloys. Desired porosity level, pore shape and accordingly mechanical properties were found to be easily adjustable.

Keywords: Space Holder Technique, TiNi Foam, Martensitic Transformations, Superelasticity, Shape Memory Effect

ÖZ

GÖZENEKLİ TİTANYUM NİKEL ŞEKİL BELLEKLİ ALAŞIMLARIN ÜRETİMİ VE KARAKTERİZASYONU

Aydoğmuş, Tarık

Doktora, Metalurji ve Malzeme Mühendisliği Bölümü

Tez Yöneticisi: Prof. Dr. Şakir Bor

Ortak Tez Yöneticisi: Prof. Dr. Bilgehan Ögel

Temmuz 2010, 184 sayfa

Boşluk yapıcı olarak magnezyum tozunun kullanıldığı yeni bir toz metalurjisi yöntemi uygulanarak %21-81 arasında gözenek içeren TiNi köpükler (Ti-50.4 at. %Ni ve Ti-50.6 at. %Ni) başarıyla üretilmiştir. Çalışma sonucunda, başlangıç alaşım tozlarının içerdiği fazlara bağlı olarak, köpüklerin sadece östenit ya da östenit martensit karışımı fazlardan oluştuğu görülmüştür. Ayrıca, mikroyapı kırılgan ikincil intermetalik, oksit, nitrür ve karbonitrürleri içermemektedir. Magnezyum buharı ikincil fazların olusumunu ve kirlenmeyi önlemekle beraber, oksitlenme nedeniyle anafazın Ni miktarının artması sonucu 1118 °C ötektik reaksiyon ve buna bağlı sıvı faz oluşumundan kaçınmayı sağlayarak yüksek sıcaklıkta sinterleme olanağı sunmaktadır. İki aşamalı sinterleme prosesi ile (numuneyi 1100 °C'de 30 dakika tutma ve hemen akabinde 1118 °C'den daha yüksek sıcaklıklarda sinterleme) magnezyum TiNi'nin erime sıcaklığına kadar olan sıcaklıklarda sinterleme işlemine imkan verebilir.

Üretilen alaşımlar birbirleriyle bağlantılı (gözenek miktarına bağlı olarak kısmi ya da tam) açık küresel makro gözenekler ve kısmi sinterlemeden kaynaklanan ve hücre duvarlarında yer alan şekilsiz mikro gözenekler sergilemişlerdir. Gözenek

miktarı faz dönüşüm sıcaklıklarını etkilemezken deformasyon ve oksitlenmenin dramatik bir biçimde etkili olduğu bulunmuştur. Gözenekli TiNi alaşımları mükemmel süperelastisite ve şekil bellek davranışı göstermiştir. Boşluk yapıcı teknik gözenekli TiNi alaşımları üretimi için gelecek vaat eden bir metod olarak değerlendirilmiştir. Gözenek içeriği, şekli ve bunlara bağlı olarak mekanik özelliklerin kolaylıkla ayarlanabildiği görülmüştür.

Anahtar Kelimeler: Boşluk Yapıcı Yöntem, TiNi Köpük, Martensitik Dönüşümler, Süperelastisite, Şekil Bellek Etkisi

To Ahmet Çavuş and Nazmiye Aydoğmuş

ACKNOWLEDGMENTS

TABLE OF CONTENTS

CHAPTER 1

INTRODUCTION

Metallic foams, as other porous or cellular structures, exhibit extraordinary physical and mechanical features combining contradictory material characteristics, such as low density with a high stiffness or high gas permeability combined with high thermal conductivity. Therefore, they are new candidates for exceptional structural and functional applications.

Near equiatomic titanium-nickel based alloys are among the most promising functional materials due to their shape memory and superelasticity properties. Their additional distinctive characteristics such as, good ductility, high corrosion and fatigue resistance besides great damping capability and considerable strength and toughness led to various commercial applications such as couplings, actuators, sensors, retractable antenna for mobile phones, glasses frames and underwires for underwire bras in different industrial fields, among which the medical applications dominate. This results from not only the above mentioned unique and superior properties of TiNi alloys but also their proven biocompatibility, which is essential for biomedical applications.

TiNi foams retain their distinctive shape memory and superelasticity properties together with high strength and ductility while exhibiting considerable toughness and good corrosion resistance in porous form. Thus, TiNi foams have the potential to be used in different areas, such as energy absorbers, seperators or filters, light weight connectors and actuators. Recently, TiNi shape memory alloy foams have attracted an additional interest as armor materials in defense industry and as biomaterials for implantation and prosthesis in dentistry as well as in orthopaedics where its high cost is compansated. Shape memory and superelasticity properties

allow firm fixation and easier deployment of TiNi foam into the implantation site while the introduction of pores into the bulk material provides ingrowth of living tissues in addition to reducing the alloy density. Moreover, superelastic TiNi is the only alloy exhibiting a mechanical behaviour similar to those of living tissues which have a recoverable strain around 2%. This similarity in deformation behavior guarantees biomechanical compatibility.

One of the most critical issue frequently encountered in bone replacement applications is "stress shielding" originated from large mismatch of the Young's moduli between bone and the implant material and may results in loosening of implant. Commonly used metallic materials, such as titanium alloys, Co-based alloys, stainless steel and also Ca-based inherently brittle ceramics e.g., calcium aluminate ($CaO.Al_2O_3$), calcium hydroxyapatite ($Ca_{10}(PO_4)_6(OH)_2$) or tricalcium phosphate ($Ca_3(PO_4)_2$) in biomedical industry, have higher elastic moduli values ranging from 110 GPa to 210 GPa compared to elastic modulus of the bone which is smaller than 20 GPa. Equiatomic and near equiatomic TiNi alloys on the contrary have a stiffness around 28-80 GPa, still high, depending on the phases (austenitic or martensitic) of which they consist. In order to minimise "stress shielding" effect implant material must have a stiffness value which matches that of the bone. Reduction in Young's modulus of the implant material to a degree comparable to that of the bone cannot be achieved by compositional changes or heat treatments since it is an intrinsic material property but it could be reduced to the desired levels succesfully without considerable loss in strength by introducing pores into the bulk material.

High melting point (1310 °C) and extreme reactivity of TiNi with athmospheric gases and crucible materials make its foaming in liquid state substantially difficult, despite the expensive high vacuum and high temperature equipment required. Powder metallurgy techniques on the other hand, provide the flexibility of low temperature processing as well as close composition control and, mechanical and physical property modifications via adjustment of the processing parameters and characteristics of the powders used. Accordingly, various powder metallurgy methods, such as self propagating high temperature synthesis, hot isostatic pressing, conventional sintering, spark plasma sintering, metal injection molding and space

holder technique have been employed intensively to fabricate TiNi foams. However, incomplete diffusion when elemental powders were used and contamination during processing even when prealloyed powders were used by these methods led to formation of secondary intermetallics (Ti_2Ni, $TiNi_3$ and Ti_3Ni_4) and oxides (Ti_4Ni_2O) and/or carbonitrides, all of which deteriorate the shape memory and superelasticity characteristics. In fact, they, in addition to making the foam brittle, affect the phase transformation temperatures dramatically.

All these fabrication routes were observed to result in nonspherical pores, nonhomogeneous pore distribution in the structure and sharp pore edges that act as stress risers, and decrease both strength and ductility of the metallic foam. Also, adjustment of the desired porosity levels and pore size were difficult. None of these powder metallurgy techniques, which have been employed to produce TiNi foams for three decades, are satisfactory to fulfil the essential requirements (interconnected open pores with a size in the range 100-600 µm and a high porosity between 30-90% to facilitate bone ingrowth together with high strength) for biomedical applications.

Space holder technique seems to be best to fabricate TiNi foams with desired pore features and mechanical properties. However, in this technique generally two types of pores form: micro-pores resulting from incomplete sintering and macro-pores formed by removal of space holder material. Micro-pores although favour transportation of body fluids, they are not adequate in size to allow bone ingrowth and in fact, they are the origin of inferior mechanical properties. Elimination of micro-pores completely could be possible by combining space holder method with hot isostatic pressing. However, operational cost of hot isostatic pressing is quite high. Since sintering is a diffusion phenomenon elimination or minimisation of micro-pores can be attained by elevation of the sintering temperature or by using prolonged sintering time. Former is much more effective, because diffusion rate is affected from temperature exponentially. Eutectic reaction present in Ti-Ni binary system at 1118 °C prevents employment of higher sintering temperatures even when equiatomic prealloyed powders are used due to Ni enrichment of TiNi matrix as a result of oxidation. When the eutectic temperature is reached during heating, liquid phase formation occurs resulting in collapse of the compacted powder mixture.

The present study describes the solutions proposed to aforementioned problems in production of TiNi foams, using magnesium powder as a new space former and explaining the role of magnesium to hinder formation of secondary intermetallics and contamination. In addition, possiblity of employment of higher sintering temperatures than the euctectic by usage of magnesium is presented. Phase transformation temperatures, superelasticity, shape memory and mechanical behavior of porous TiNi alloys produced by this new approach are also presented describing the effects of composition, porosity, pre-straining, sintering temperature and aging treatment.

CHAPTER 2

THEORETICAL FRAMEWORK

2.1. Martensitic Transformations

Shape memory alloys are quite complicated systems and their behaviors are different from that of other common metal and alloys on the ground of solid state phase transformation occuring during thermomechanical loadings. Shape memory and superelasticity effects observed in these alloys are associated with the thermoelastic martensitic transformations. Hence, main features and mechanisms of martensitic transformations are given first prior to description of shape memory and superelasticity effects.

There are two basic types of composition invariant transformations. One is the massive transformation. In this type, a short-range diffusional transformation takes place without a definite orientation relationship. The interphase boundary (between parent and product phases) migrates to allow the new phase to grow. It is, however, a civilian transformation because the atoms move individually [1]. The other is the martensitic transformation. In this type, the change in phase involves a definite crystallographic relationship between the martensite and the parent phase, which allows a fast growth mechanism to operate, because the atoms have to move in a coordinated manner [2]. There is always a change in shape, which means that there is a strain associated with the transformation. The shape change appears to be a simple shear parallel to the habit plane (coherent invariant plane between the phases) and a uniaxial expansion (dilatation) or compression normal to the habit plane, Figure 2.1.
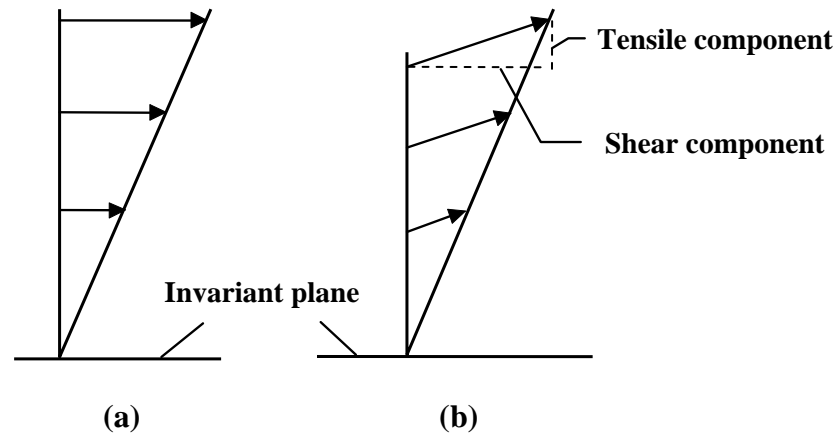
Figure 2.1 The shape strain in (a) simple shear and in (b) martensite [2].

Martensitic transformations are the most important type of military transformations that do not require diffusion for the change in crystal structure to occur. These transformations require larger driving forces than for diffusional transformations because of the large shape strains involved. These transformations that occur without long-range diffusion take place without a change in composition.

Martensitic transformations are usually first order solid state phase transformations occuring by a shear-like deformation in which atoms move cooperatively, i.e., each being displaced by only a small distance (less than interatomic spacing) relative to its neighbors [2-4]. Cooperative movement of atoms results in a macroscopic shape change, which is closely related to shape memory effect and superelasticity, despite the small relative atomic displacements. The transformation is driven by temperature change, mechanical deformation or magnetic field and the high temperature parent phase, (called austenite if FCC and beta if BCC), transforms to low temperature and lower symmetry phase (called martensite) upon cooling to some critical temperature, applying stress or magnetic field. This reaction is defined as forward transformation. Heating or removal of stress or magnetic field on the other hand, results in retransformation of martensite phase into austenite and this is the reverse transformation. It is quite common even in nonferrous martensites to refer to the high temperature phase as austenite and the

low temperature phase as martensite. In the present study, this terminology will also be used.

Kinetics and morphology of martensite are dictated by the strain energy arising from shear displacement. The displacement can be described as a combination of homogeneous lattice deformation, known also as Bain Distortion in steels [5], and shuffles. In a homogeneous lattice deformation, one Bravais lattice is converted to another by the coordinated shift of atoms. A shuffle is a coordinated shift of atoms within a unit cell, which may change the crystal lattice but does not produce homogeneous lattice distortive strain. Figure 2.2 displays the lattice change from B2 austenite to B19' martensite [6]. It is clear from the figure that B2 parent lattice is already a tetragonal cell which is delineated by bold lines (Figure 2.2 (a)). This tetragonal cell is the same with the one shown by dotted lines in Figure 2.2 (b).
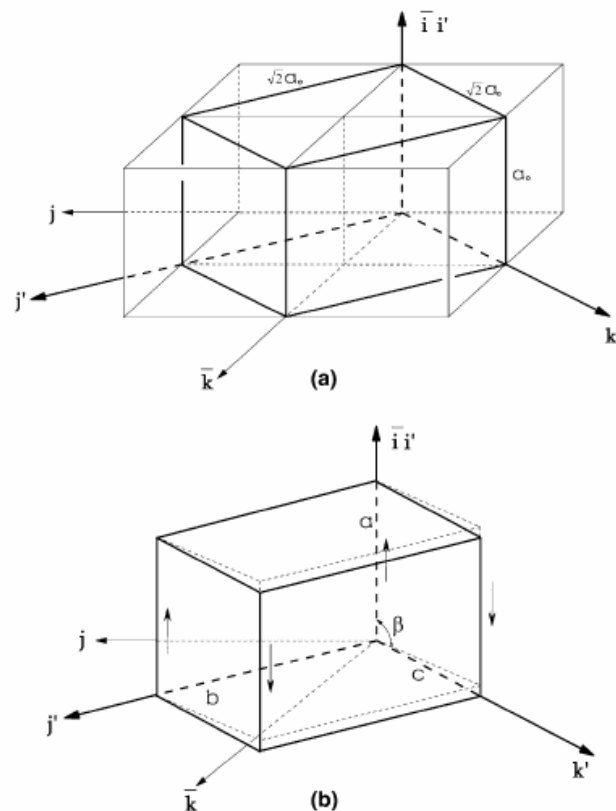
Figure 2.2 The lattice change from (a) B2 austenite to (b) B19' martensite. i, j, and k refer to parent lattice while i', j' and k' refer to the martensite lattice [6].

Upon transformation, B2 unit cell of the austenite phase contracts along $[\bar{1}00]_p$ and $[0\bar{1}\bar{1}]_p$ directions to form a and b axis of the martensite, respectively while expands along $[01\bar{1}]_p$ direction to form c axis of the martensite. During transformation $(011)_p$ $[100]_p$ shear is introduced and β angle changes from 90° to 96.8°. As a result monoclinic lattice is obtained as drawn in bold lines in Figure 2.2 (b). Actual and final B19' martensite structure [7] present in Figure 2.3 is created by further atomic shuffles. Lattice parameters for B19' martensite are: a = 0.2889 nm, b = 0.4120 nm, c = 0.4622 nm [8] and the space group was concluded to be $P2_1/m$ [9-11].
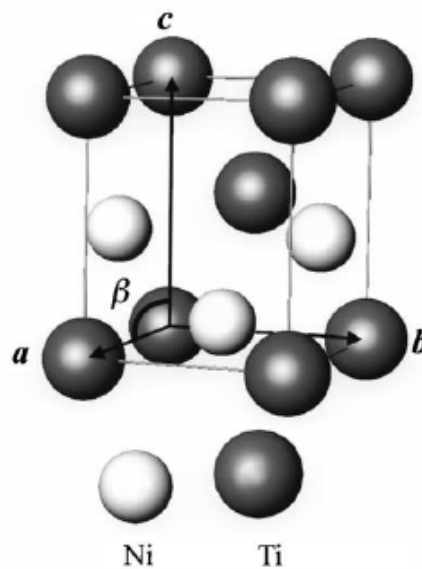
Figure 2.3 The structure of monoclinic B19' martensite [7].

2.1.1. Lattice Invariant Shear

The basis of crystallographic phenomenological theory of martensitic transformation [12, 13] is that in a martensitic transformation there should be an undistorted and unrotated interface between the martensite and the parent phase because of the invariant plain strain. Invariant plain strain is a homogeneous distortion in which the displacement is proportional to the distance from the

invariant plane (Figure 2.1), habit plane. Since always shape changes accompany martensitic transformations, a large strain arises around the martensite when it forms in the austenite phase. It is essential to reduce the strain for nucleation and growth processes of martensitic transformations. Strain energy is minimized if the shape deformation is an invariant plane deformation. Since the Bain strain that generates the martensite lattice is not an invariant plane strain it should be accompanied by other deformation processes that do not distort the martensite lattice but make the resultant of all the strains an invariant plane strain. This is attained by either slip or twinning [14] as shown in Figure 2.4. These are called the lattice invariant shear because neither process changes the structure of the martensite. Although an undistorted plane now exist, it has rotated from initial position. The bain distortion constitutes homogeneous lattice deformation, while the lattice invariant shear and rigid body rotation act to diminish the strain energy generated by lattice deformation.

parent phase   martensite
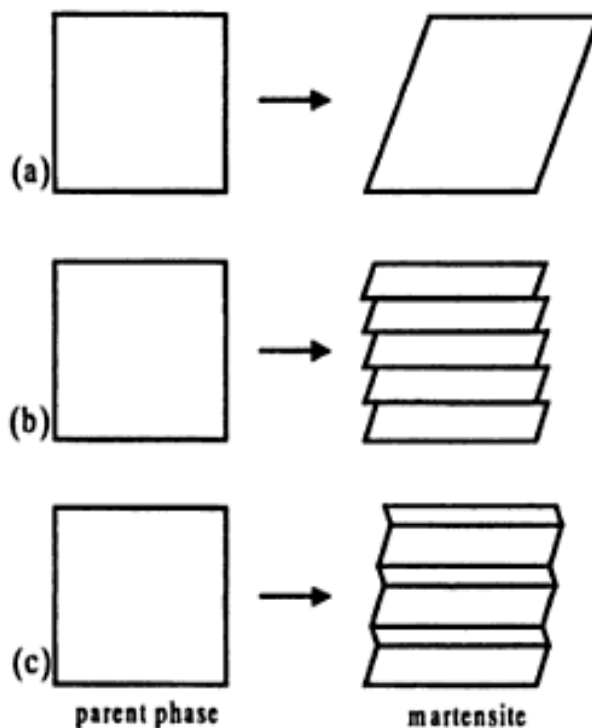
Figure 2.4 (a) Schematical shape change upon martensitic transformation and lattice invariant shears: (b) slip and (c) twinnning [14].

Since there are six types of $\{011\}_p$ planes and two $\langle 100 \rangle_p$ shearing directions in B2→B19' transformation occuring in solutionized and quenched TiNi shape memory alloys, totally 12 crystallographically equilavent lattice correspondences exist. These are listed in Table 2.1 [15]. In the table, the correspondence variants (c.v.'s) with and without prime for the same number refer to the ones with opposite shears. Since there are 12 lattice correspondences and two lattice invariant shears ($[011]_m$ and $[01\bar{1}]_m$ Type II twinning [16]), there are 24 (+) habit plane variants (h.p.v.'s) and 24 (-) h.p.v.'s. Phenomenological theory calculations show that (+) and (-) solutions are not equivalent [17]. Type II (-) solutions do not fit with the experimental observations however, Type II (+) solution is consistent with observed orientation relationship and the shape strain as well [16].

Table 2.1 Lattice correspondences between parent and B19' martensite [15].

Variants	$[100]_m$	$[010]_m$	$[001]_m$
1	$[100]_p$	$[011]_p$	$[0\bar{1}1]_p$
1′	$[\bar{1}00]_p$	$[0\bar{1}\bar{1}]_p$	$[0\bar{1}1]_p$
2	$[100]_p$	$[0\bar{1}1]_p$	$[0\bar{1}\bar{1}]_p$
2′	$[\bar{1}00]_p$	$[01\bar{1}]_p$	$[0\bar{1}\bar{1}]_p$
3	$[010]_p$	$[101]_p$	$[10\bar{1}]_p$
3′	$[0\bar{1}0]_p$	$[\bar{1}0\bar{1}]_p$	$[10\bar{1}]_p$
4	$[010]_p$	$[10\bar{1}]_p$	$[\bar{1}0\bar{1}]_p$
4′	$[0\bar{1}0]_p$	$[\bar{1}01]_p$	$[\bar{1}0\bar{1}]_p$
5	$[001]_p$	$[110]_p$	$[\bar{1}10]_p$
5′	$[00\bar{1}]_p$	$[\bar{1}\bar{1}0]_p$	$[\bar{1}10]_p$
6	$[001]_p$	$[\bar{1}10]_p$	$[\bar{1}\bar{1}0]_p$
6′	$[00\bar{1}]_p$	$[1\bar{1}0]_p$	$[\bar{1}\bar{1}0]_p$

2.1.2. Self-Accommodation of Martensite

Although the lattice invariant shear is very effective in relieving elastic strains associated with the invariant plane strain of the martensitic transformations, it cannot eliminate the transformation strains completely. However, when two or four h.p.v.'s with opposite shears are formed side by side, the shear strains are eliminated macroscopically. The process such that elastic strain energy is further reduced by the

combination of multiple variants is called self-accommodation of martensite. The mechanism of self-accommodation in β-phase alloys, which transform from ordered BCC to long period stacking order structures, was analyzed successfully [18-20] and it is quite easy to understand. Figure 2.5 (a) shows a typical SEM micrograph of a Ni-Al alloy [18] in which four h.p.v.'s make a self-accommodating group such that the strains created by each variant upon transformation cancel each other. Existence of these h.p.v.'s were also confirmed by trace analysis, as shown in Figure 2.5 (b).
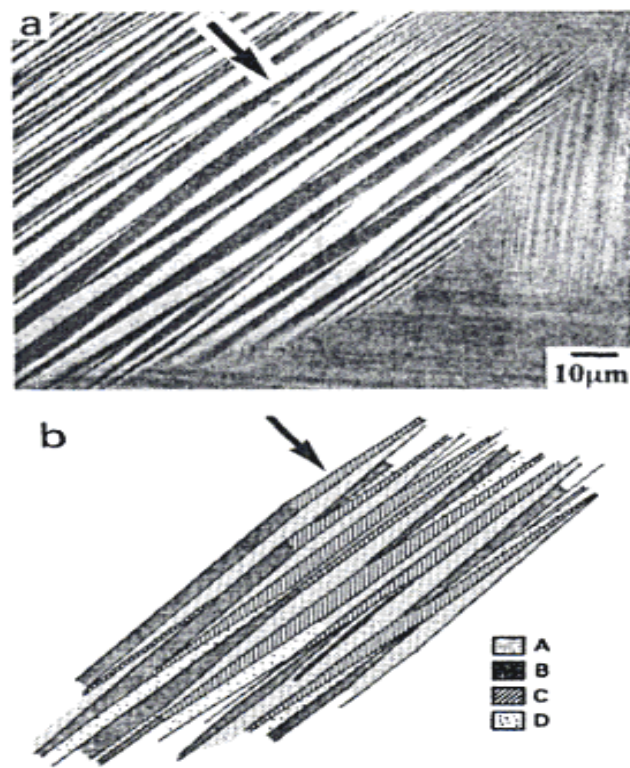
Figure 2.5 (a) SEM image of self-accommodation in 7R (14M) martensite formed in a Ni-37 at. %Al alloy, (b) four habit plane variants identified by trace analysis [18].

Four h.p.v.'s were designated as A,B,C and D in Figure 2.5 (b). It has been found that these h.p.v.'s are twin related to each other. A-C and B-D are Type I twin related while A-B and C-D are Type II twin related and A-D and B-C are compound twin related as they are displayed in Figure 2.6 (b). These twin boundaries are

11

mobile under stress and, thus, the twinning or detwinning work as deformation modes in the martensitic state, which is very important for shape memory effect. The introduction of compound twin does not accommodate strains, while both Type I twin and Type II twin accommodate strains effectively. The basic morphology of Figure 2.6 (b) applies not only for 7R (14M) martensite but also for other martensites such as 3R (2M) and 9R (6M) etc [18]. The diamond morphology (Figure 2.6 (a)) proposed for self-accommodation [19] is less consistent with the observations. Therefore, the parallelogram morphology has been found to be more suitable and also more reasonable in terms of theoretical aspect [21].
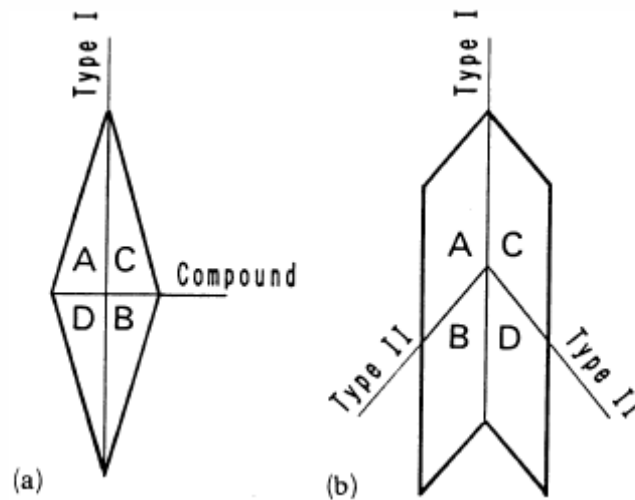
Figure 2.6 Scheme of the basic morphology of self-accommodation for (a) the diamond morphology and (b) the parallelogram morphology [18].

The self-accommodation in B19' martensite in Ti-Ni alloys is very complex due to the monoclinic structure and many available twinning modes in the martensitic state. The triangular morphology shown in Figure 2.7 is generally believed to be self-accommodation mechanism [6, 22].

Self-accommodation mechanism is very effective in reducing strains upon martensitic transformations. The resulting shape strain (that is the remaining strain composed of the Bain strain of which appreciable fraction is cancelled by lattice

invariant shear and self-accommodation mechanism) is mostly accommodated by elastic or plastic deformation of the parent phase.
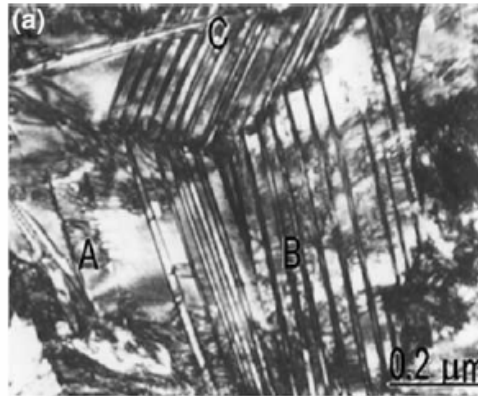
Figure 2.7 TEM image of typical triangular morphology of B19' martensite [22].

2.1.3. Thermoelastic Martensitic Transformations

Reversible martensitic transformations are generally classified into two categories, thermoelastic and non-thermoelastic. The non-thermoelastic transformations occur mainly in ferrous alloys. On the other hand, thermoelastic transformations appear in shape memory alloys. Figure 2.8 [23] shows the change in electrical resistivity with temperature for two types of transformations. Using electrical resistivity measurements as well as measuring some other physical properties as a function of temperature, critical phase transformation temperatures can be determined. Because many physical properties often dramatically change upon beginning or finishing of martensitic transformations. The transformation temperatures are defined as follows:

M_s: martensite or forward transformation start temperature,

M_f: martensite or forward transformation finish temperature. It is the temperature below which the austenite becomes completely unstable.

A_s: austenite or reverse transformation start temperature,

A$_f$: austenite or reverse transformation finish temperature. It is the temperature above which the martensite becomes completely unstable.

It is clear from Figure 2.8 that the transformation hysteresis (A$_s$-M$_s$) of Au-47.5 at. %Cd alloy is as small as 15 °C, while that of the Fe-30 at. %Ni alloy is extremely large, about 400 °C. The driving force for the transformation is smaller in the former due to its smaller temperature hysteresis, as it can also be seen from Figure 2.9, in which schematic representation of free energies of parent and martensitic phases as a function of temperature and their relation to martensitic transformations are shown [24]. G^p and G^m designate Gibbs free energies of parent and martensite phases, respectively, in the figure, while $\Delta G^{p \rightarrow m}$ and $\Delta G^{m \rightarrow p}$ represent Gibbs free energy changes or driving forces for forward and reverse transformations, respectively. ΔT_s is the supercooling required for the transformation, and T$_0$ is the thermodynamic equilibrium temperature between the two phases.
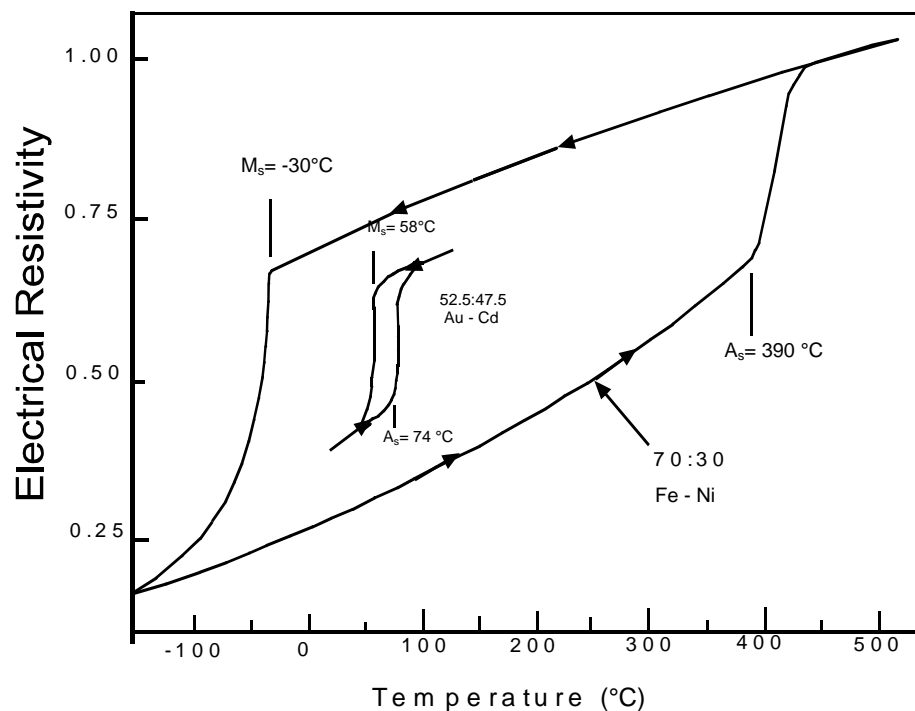
Figure 2.8 The temperature hysteresis in non-thermoelastic Fe-Ni and thermoelastic Au-Cd martensitic transformations [23].
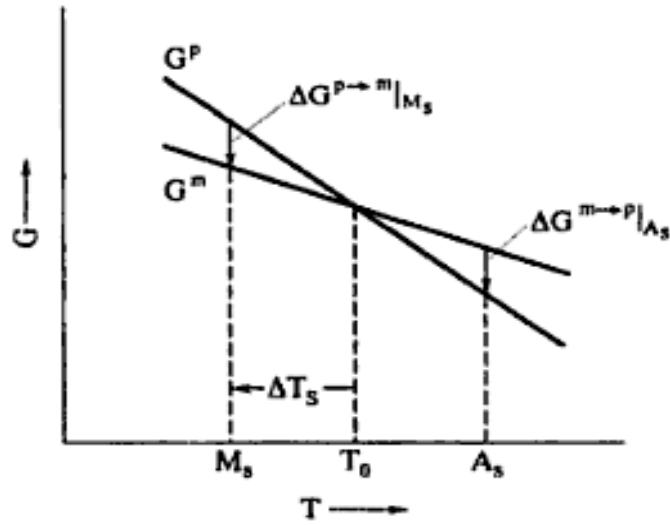
Figure 2.9 Schematic representation of free energies of parent and martensitic phases as a function of temperature and their relation to martensitic transformations [24].

Gibbs free energy (the total energy) change (ΔG) during martensitic transformations may be formulated as below [23]:

$$\Delta G = \Delta G_c + \Delta G_s + \Delta G_e = \Delta G_c + \Delta G_{nc} \qquad (2.1)$$

where ΔG_c is chemical free energy change, which is negative, ΔG_s surface energy change, ΔG_e is elastic (plus plastic in the non-thermoelastic case) energy change and ΔG_{nc} is total non-chemical energy change consisting of $\Delta G_s + \Delta G_e$, which are positive. To compensate ΔG_{nc} by ΔG_c supercooling is required for the nucleation of martensite and superheating is necessary for the reverse transformation. In the same manner, M_s is different from M_f because the elastic energy around the martensite increases more rapidly than the chemical free energy and resists the growth of the martensite unless the driving force is increased. The degree of supercooling in non-thermoelastic transformations can be as much as 200 °C but in thermoelastic transformations it is only about 5-30 °C.

In thermoelastic martensitic transformations interface energy is so small that it can be ignored. As a result, total energy change for thermoelastic transformations is stated with the Equation 2.2, in which only the thermal and elastic terms present:

$$\Delta G = \Delta G_c + \Delta G_e \qquad (2.2)$$

When parent phase is cooled below M_s martensite crystals nucleate and grow until the decrease in chemical energy term is not sufficient to compensate the increase in the elastic non-chemical term. When the equilibrium between thermal and elastic effects is achieved growth is arrested. Once the thermal equilibrium is disrupted by further cooling, stabilized martensite crystals will continue to grow at a velocity proportional to the cooling rate. Similarly, with heating they will shrink. External forces also disrupt the thermal equilibrium and cause growth or shrinkage of martensite crystals.

In non-thermoelastic transformations, the interface between martensite and parent phase is immobilezed and pinned by the defects (dislocations) produced in the austenite due to the large shape strain of the martensitic transformation. These transformations proceed by successive nucleation and growth. Individual martensites nucleate and grow rapidly with a velocity about 1/3 the speed of elastic waves in solids [4]. Due to re-nucleation of austenite during the reverse transformation [25], these transformations are crystallographically non-reversible. In other words, the martensite cannot revert to the parent phase in the original orientation [26]. The thermoelastic martensitic transformations, on the other hand, are associated with mobile interfaces between the parent and martensitic phases and, as mentioned before, transformation proceeds by growth of martensite crystals. Similarly, reverse transformation occurs by shrinkage of martensite plates instead of renucleation.

Shape memory effect and superelasticity behavior generally occur in the alloys which exhibit thermoelastic martensitic transformations [27]. These transformations require aforementioned small interface energy as well as small shape strain. This is attainable when the structural changes, and accordingly volume changes during

transformation is small. Furthermore, lattices of parent and martensite phases also should be in good coherency.

2.1.4. Shape Memory Effect

The shape memory effect (SME) is a feature exhibited by shape memory alloys undergoing thermoelastic martensitic transformations. It is the ability to remember initial shape upon heating subsequent to a deformation resulting in permanent strains, and is graphically depicted in Figure 2.10.
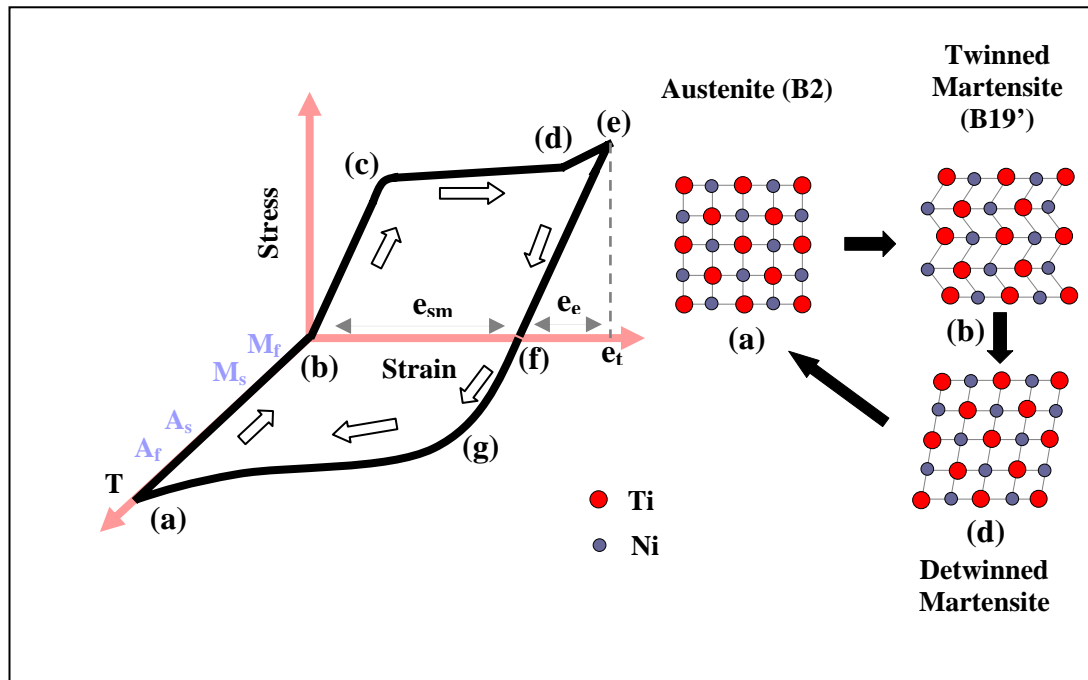
Figure 2.10 Typical representation of shape memory effect. e_t, e_e and e_{sm} represent total strain, elastic strain and shape memory strain respectively.

Above its A_f temperature a shape memory alloy is in the form of high-symmetry, usually cubic, austenitic phase which is designated as (a) in the figure. When it is cooled under M_f temperature, it transforms into a low-symmetry martensitic phase, twinned martensite (b), such as the monoclinic variants of B19' in TiNi alloys. In the absence of applied stresses, thermoelastic martensite variants arrange themselves

in a self-accommodating manner through twinning as mentioned before. Self-accommodation as well as lattice invariant plane strain prevent any observable macroscopic shape change by reducing the strains. In completely martensitic state, when the shape memory alloy is deformed by applying mechanical loading, firstly elastic deformation of twinned martensite occurs between (b) and (c). Starting from point (c) further deformation forces the martensitic variants to reorient or detwin into a single variant leading to large macroscopic inelastic strains. Deformation proceeds by detwinning mechanism, which is provided by mobile twin interfaces, instead of slip up to (d). If the load is further increased up to (e), detwinned martensite is elastically deformed. Upon unloading all the elastic strains are relieved, (f). Subsequently, heating above A_f temperature, detwinned martensite maintaining the same lattice of twinned martensite transforms back into the austenite between point (g) and (a) or between the temperatures A_s and A_f, and the inelastic strains are recovered while the initial, original shape is regained.

The mechanism or origin of the shape memory effect is associated with crystallographic reversibility. As it is previously shown that, there are a total of 12 equivalent lattice correspondences in the B2→B19' transformation. Each of the martensites with these lattice correspondences is called correspondence variants. When stress is applied to a specimen consisting of several groups of self-accommodating habit plane variants, a twinning deformation commences between the correspondence variants within each group. The deformation proceeds by the twin boundary motion, which is equivalent to the conversion of one martensite variant to the other. This process is called as coalescence of variants. Subsequently, similar conversions take place between the groups. The most favorable correspondence variant, which gives the largest strain under the given stress condition, grows at the expense of the others [19]. This process shown in Figure 2.11 proceed until the entire specimen becomes a single variant. Since all the correspondence variants have specific, crystallographically equilavent lattice correspondences with the parent phase lattice, upon heating to a temperature above A_f the martensite transforms back to the parent phase in the original orientation.
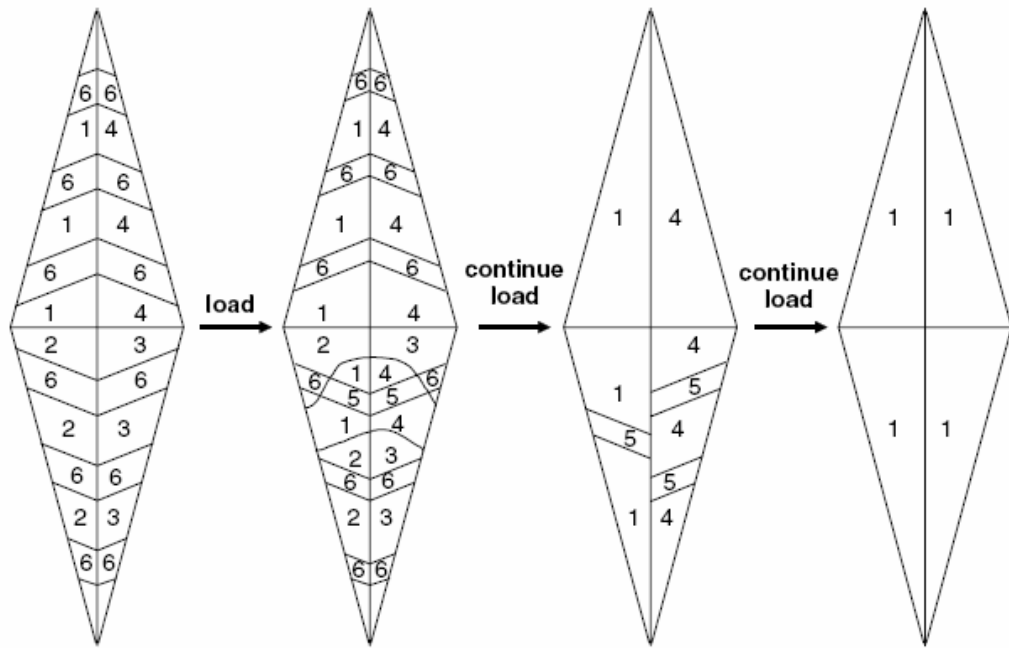
Figure 2.11 Schematical conversion process during loading of a thermally induced 2H (γ_1') martensite at low temperature [19].

2.1.5. Superelasticity

Superelasticity is also a characteristic behavior of shape memory alloys, and it is associated with stress-induced transformations. Since martensitic transformation is a by a shear-like mechanism, stress generally assists the martensitic transformations, and thus even above M_s temperature martensite formation is possible by application of stress. Martensite created in this way is called as stress-induced martensite (SIM). Then the superelasticity may be described as the ability of shape memory alloys to recover strains due to stress-induced martensite at temperatures above A_f upon unloading, and it is shown schematically in Figure 2.12. When a superelastic material is loaded while it is completely in austenitic state, initially elastic deformation occurs along the loading path (a) → (b). When the critical stress level (called as transformation stress) corresponding to stress at point (b) is reached, the material undergoes a stress-induced phase transformation ((b) → (c)) from austenite to martensite. At point (c) microstructure is completely stress-induced martensite. Upon unloading, firstly elastic strains of martensite are recovered up to point (d).

From (d) to (e) reverse transformation takes place, and finally remaining elastic strains are recovered during unloading between (e) and (a).

The stress-induced martensitic transformation was analyzed by Patel and Cohen [28]. The well known thermodynamic Clausius-Clapeyron relationship [29, 30] was also used for the same purpose, but the latter is simpler because it is summarized in the following mathematical form:

$$\frac{d\sigma}{dT} = -\frac{\Delta S}{\varepsilon} = -\frac{\Delta H^*}{\varepsilon T} \tag{2.3}$$

where σ is a uniaxial stress, ε is a transformation strain. ΔS and ΔH^* represent the entropy and the enthalpy of transformation per unit volume, respectively. T is the temperature at which parent and martensite phases are in equilibrium under σ.
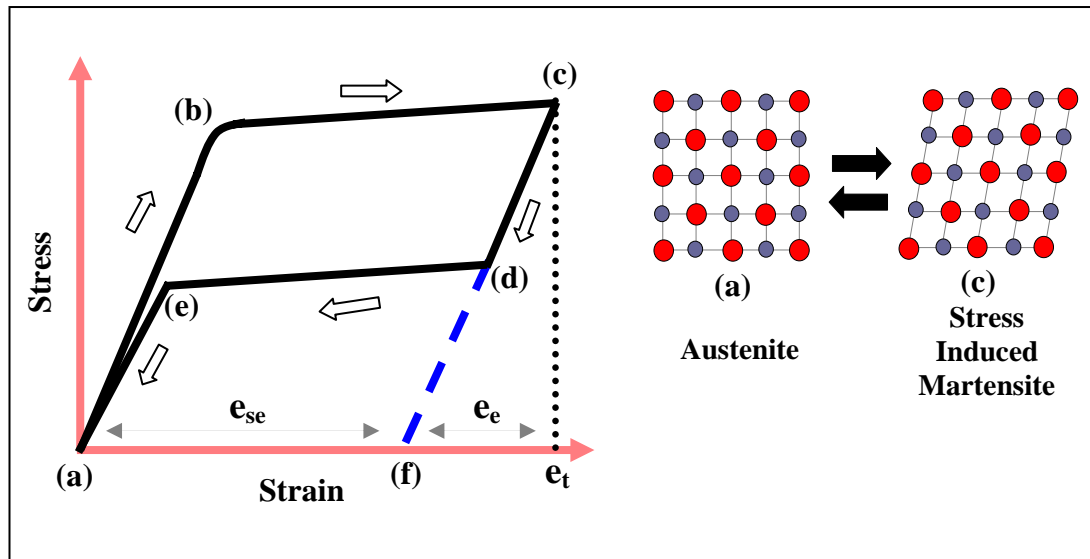
Figure 2.12 Typical representation of superelasticity. e_{se} designates the strain recovered by superelasticity mechanism.

Shape memory effect and superelasticity are two main phenomena occurring in shape memory alloys, and they are closely related to each other. Figure 2.13 shows this relation [31], and it is clear from the figure that, both behaviors are

observable for the same material, depending on the temperature. Below A_s only shape memory effect occurs, however, above A_f merely superelasticity is observed. Between A_s and A_f both mechanisms are active partially. Critical stress change to induce martensite and critical stress change for slip with temperature are schematically drawn in the figure. When the critical stress for slip is very low as in the case (B), a good or complete superelasticity is not possible since slip is easily introduced before the onset of the stress-induced transformation upon loading. For example, the critical stress for slip is so low in the single crystals of TiNi alloys (as low as less than 150 MPa for a solution treated Ti-50.3 at. %Ni single crystal [32]) in solutionized condition that superelasticity does not appear unless they are subjected to proper thermomechanical treatments [33]. In the same manner, polycrystal equiatomic alloy of TiNi also exhibit limited superelasticity and shape memory. Near equiatomic TiNi alloys with Ni content less than approximately 50.5 at. %Ni in solutionized condition displays only partial superelasticity. Critical stress for slip can be increased by increasing Ni content (solid solution hardening), precipitation hardening (aging), and work hardening.

Basic requirements for shape memory and superelasticity may be summarized as follows [34-38]:

1. Martensitic transformations must be thermoelastic in nature to provide mobile twin boundaries and low hysteresis.

2. Deformation mode must be twinning, because slip is an irreversible process.

3. Twinning or detwinning must be equivalent to the change of correspondence variant. Twins introduced as a lattice invariant shear must have this characteristic.

4. Ordering or unique lattice correspondence must exist. Ordering restricts the reverse path from martensite to the parent phase uniquely, and guarantees the reversibility of the thermoelastic transformation. Moreover, ordered structure requires the dislocations to be superdislocations, which have larger Burgers vectors leading to higher critical stress for slip, and thus better superelasticity and shape memory behavior.
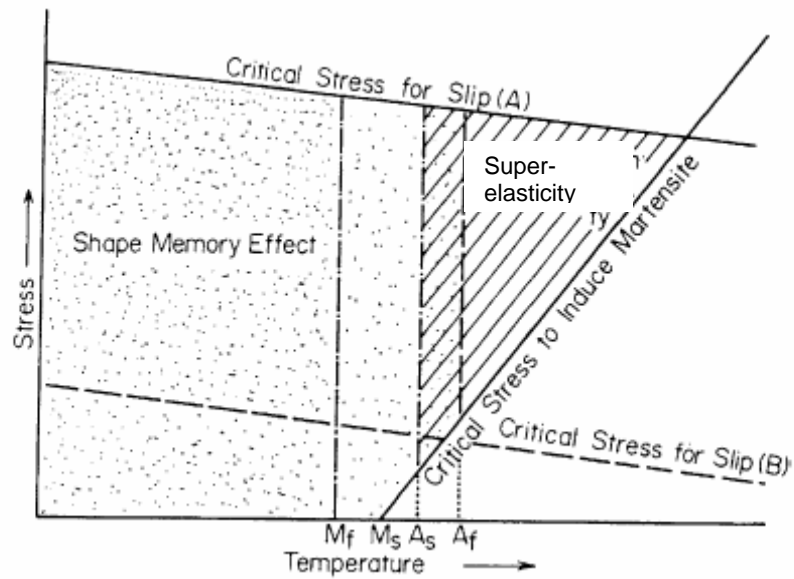
Figure 2.13 Schematic representation of the appearance of shape memory effect and superelasticity [31].

2.2. TiNi Shape Memory Alloys

2.2.1. General Characteristics and Applications

Near equiatomic titanium-nickel based alloys are among the most promising functional materials due to their shape memory and superelasticity properties. Their additional distinctive characteristics such as, good ductility, high corrosion and fatigue resistance besides great damping capability and considerable strength and toughness led to various commercial applications in different industrial fields, among which the medical applications dominate [6]. This results from not only the above mentioned unique and superior properties of TiNi alloys, but also their proven biocompatibility, which is essential for biomedical applications and revealed by systematic studies [39-46].

The first successful application of shape memory alloys was a coupling connecting titanium hydraulic tubing in a U.S. Navy F-14 fighter aircraft in 1970 [47] and the alloy used was NiTiFe [48]. Electrical connectors and fasteners were

22

the second and third, respectively used for military applications, where higher prices for superior performance were accepted. These early applications used only shape memory effect discovered in TiNi in 1963 by Buehler et al. [49]. In 1981 superelasticity in TiNi alloys was reported for the first time by Miyazaki et al. [50, 51], and new application areas for TiNi alloys were born such as, orthodontic wires for the correction of missalligned teeth, support wires for bras and glasses frames. Today, in addition to early applications, TiNi shape memory alloys are choice of the engineers in different industries to be used as retractable antenna for mobile phones, actuator/sensor in robotics, aerospace applications and control systems, air conditioner vent, safety valves, engine and automotive devices and also as toys [47, 48, 52-54].

Although consumption of TiNi shape memory alloys in industrial applications, which have reached large volume production, far exceeds the usage in the medical field, major applications for these alloys are in the field of medicine and orthodontics [47]. The combination of outstanding characteristics (shape memory and superelasticity) with good biocompatibility and magnetic resonance imaging (MRI) compatibility [55] coupled with high mechanical response (excellent kink resistance and higher fatigue resistance, etc.) has made TiNi alloys fabulous materials for dental and biomedical applications such as, stents, orthodontic arch wires, filters, orthopedic devices, clinical instruments, guide wires, maxillofacial and dental implants, cervical and lumbar vertebral replacements, bone plates and bone anchors and spine fracture fixation and repair [46, 54, 56-64].

The great interest to TiNi shape memory alloys are due to their unique shape memory and superelasticity properties, which ordinary materials do not have. Indeed there are more than ten alloy systems (AgCd, CuAlNi, CuSn, InTl, NiAl, FePt, MnCu etc.) which exhibit shape memory and superelasticity behavior. However, only TiNi-based and Cu-based, especially CuZnAl, alloys can be used in practical applications [54]. Other alloys have been found unsuitable in terms of either cost or inferior performance. Table 2.2 presents characteristics of TiNi and CuZnAl alloys. As can be seen performance of TiNi alloys surpass that of CuZnAl alloys. On the other hand, Cu-based shape memory alloys have the advantage of low cost. As a

result, applications requiring repeated operations and high reliability would prefer TiNi alloys.

Table 2.2 Comparison of TiNi and CuZnAl alloys in terms of selected features [54].

Property	TiNi Alloy	CuZnAl Alloy
Recovery Strain	max. 8%	max. 4%
Recovery Stress	max. 400 MPa	max. 200 MPa
Repetition Life	10^5 ($\varepsilon = 0.02$)	10^2 ($\varepsilon = 0.02$)
	10^7 ($\varepsilon = 0.005$)	10^5 ($\varepsilon = 0.005$)
Corrosion Resistance	good	problematic, especially stress corrosion cracking
Workability	poor	fair
Shape Memory Processing	comparatively easy	fairly difficult

2.2.2. Phase Diagram

So far, many investigations [65-74] have been carried out on the binary phase diagram of Ti-Ni system, and the central region bounded by Ti_2Ni and $TiNi_3$ phases given in Figure 2.14 had been still controversial until the end of 1980s. This ambiguity is related to the very high affinity of titanium to oxygen, nitrogen, carbon and hydrogen, and also to the existence of several metastable phases at intermediate temperatures. The equilibrium Ti-Ni phase diagram published by ASM International [75], formerly known as the American Society for Metals (ASM), is accepted as the most reliable phase diagram in the central portion of the Ti-Ni system [6]. Indeed, it is essentially the same as that shown in Figure 2.14, to which the metastable equilibrium between the TiNi and Ti_3Ni_4 phases, which will be discussed in heat treatment section, are added [76]. A possible eutectoid reaction, indicated by a dotted line at 630 °C, present in phase diagram published by ASM International is

24

deleted in Figure 2.14. Present study also proves the nonexistence of the mentioned eutectoid reaction, as it will be explained in Chapter 4. Figure 2.14 also includes an order-disorder transition from B2 to BCC at 1090 °C, which was proposed in 1979 [77] but has never been confirmed by independent works. However, a recent study [78] has clearly showed that there exists no order-disorder transition in the near equiatomic Ti-Ni alloys.
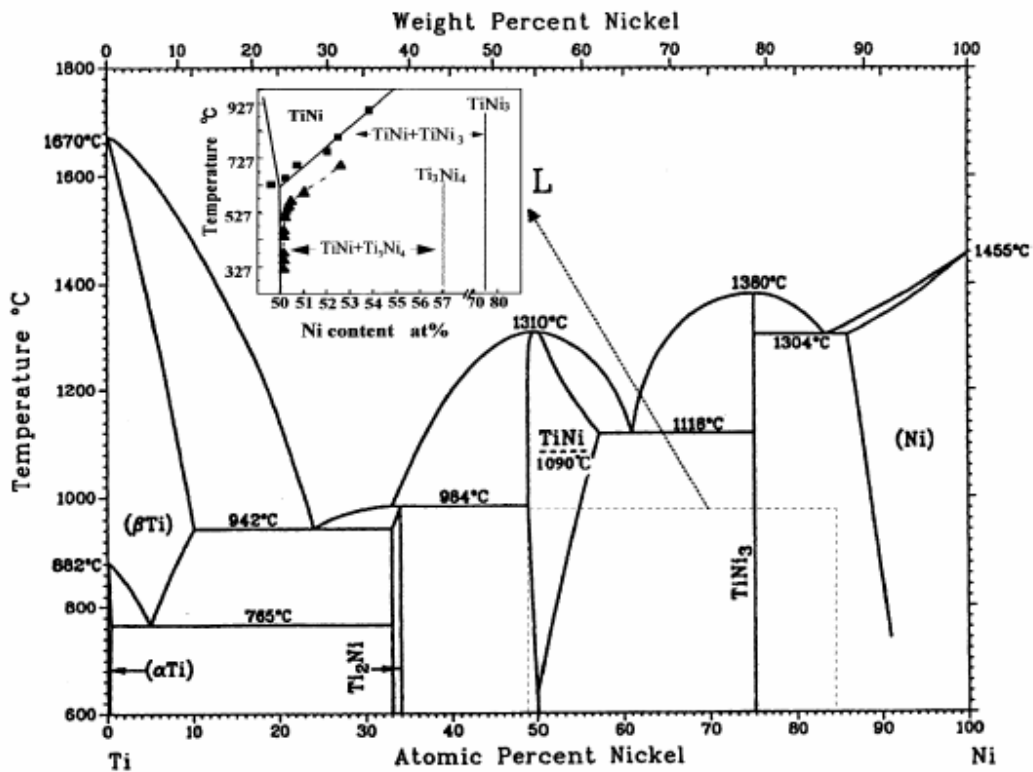
Figure 2.14 Equilibrium binary phase diagram for Ti-Ni system [75], to which the metastable equilibrium between the TiNi and Ti_3Ni_4 phases are added [76].

Although phase diagram present in Figure 2.14 do not show TiNi phase region below 600 °C, it is commonly accepted that TiNi region is very narrow below that temperature and presents only between 50 and 50.5 at. %Ni compositions. TiNi phase actually is an intermetallic compound with B2 (CsCl) order, Figure 2.15 [79], and with a lattice constant of 0.3015 nm at room temperature [80]. Nevertheless, it is

25

not a line-compound with a fixed composition. It cannot dissolve excess Ti atoms since Ti-rich side is almost vertical but Ni-rich side has some solubility at high temperatures decreasing with decreasing temperature greatly. Therefore, it may be more suitable to describe B2 TiNi phase as a solid solution.

In the CsCl type structure, if the identity of the two types of atoms is ignored, the structure is body centered cubic. The BCC lattice consists of two interpenetrating simple cubic lattices, one sublattice consisting of cube corners and the other sublattice consisting of cube centers.
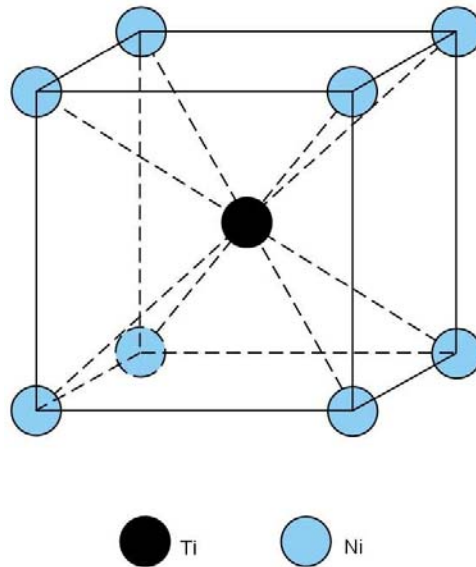
Figure 2.15 The structure of ordered B2 austenite TiNi [79].

The Ti_2Ni phase is cubic with space group Fd3m, and the lattice constant is 1.132 nm. Oxides appearing in Ti-Ni binary alloys are mostly the Ti_4Ni_2O phase, which has nearly the same structure with Ti_2Ni [81]. The $TiNi_3$ phase has the hexagonal DO_{24} type ordered structure. The lattice constants are a = 0.51010 nm, c = 0.83067 nm and c/a = 1.6284 [82].

Binary TiNi alloys with the composition range from approximately 48 to 52 at. %Ni (balance Ti) exhibit shape memory properties [45]. B2 phase is the only phase which can show shape memory or superelasticity behavior. Generally Ti-rich,

26

equiatomic or Ni-rich TiNi alloys with a Ni content up to 50.5 at.% are suitable for shape memory applications while other Ni-rich alloys are usually used in applications requiring superelasticity.

2.2.3. Phase Transformation Temperatures

Phase transformation temperatures, crucial in terms of practical applications, can be determined by measurement of some physical properties such as, electrical resistivity or heat flow as a function of temperature. Material composition, amount of impurities, deformation and heat treatment affect both superelasticity and shape memory behaviour by altering the corresponding transformation temperatures of the alloys.

Martensitic transformation temperature is strongly dependent on Ni content in Ti-Ni binary shape memory alloys, as shown in Figure 2.16. Different data symbols in the figure designate data obtained from different authors and the solid line is calculated using thermodynamic relations [83]. As it is easily can be seen from the figure, M_s is almost independent of Ni concentration up to 50 at.% (composition of equiatomic TiNi alloy) and around 60 °C. Considering phase diagram of Ti-Ni, it is not possible to get Ti-rich TiNi solid solution since the solubility limit of TiNi phase on Ti-rich side is almost vertical. As a result, Ti-rich TiNi alloys show a behavior same as the equiatomic TiNi alloy because Ni content of TiNi phase in Ti-rich TiNi alloys is constant, 50 at.%. On the other hand, Ni-rich TiNi alloys have different and lower M_s temperatures. Although experimental results show a large scattering, thermodynamic calculations give a linear relation between Ni content and transformation temperature. An increase of 1% in Ni content results in a drastic decrease, more than 100 °C, in transformation temperature.

Elastic constant c', which represents resistance for $\{110\} \langle 1\bar{1}0 \rangle$ shear in a cubic crystal, in martensitic alloys is strongly dependent on composition [84] because alloying alters lattice dynamic properties significantly. Prior to martensitic transformations, a softening occurs in elastic constant [85]. It has been experimentally shown that there exist a critical value of elastic constant at which

transformation takes place and this critical value seems to be insensitive to composition [86-89]. A small change in composition, which creates a large change in c', must be compensated by a large change in transformation temperature in order to keep elastic constant unchanged during transformation. That is why transformation temperature is strongly dependent on Ni content in Ni-rich TiNi alloys.

Alloying binary TiNi alloys with a third element often alters transformation temperatures greatly. Cr, Mn, Fe, V, Co, Al [90] and Nb [45] lower transformation temperatures while Pd, Pt, Au, Zr and Hf [91-94] increase. Addition of Cu as third element in Ti-Ni binary system do not affect transformation temperatures much, but decreases hysteresis [95-97]. Alloying elements also often lead to a change in the transformation route or final crystal structure of martensite.
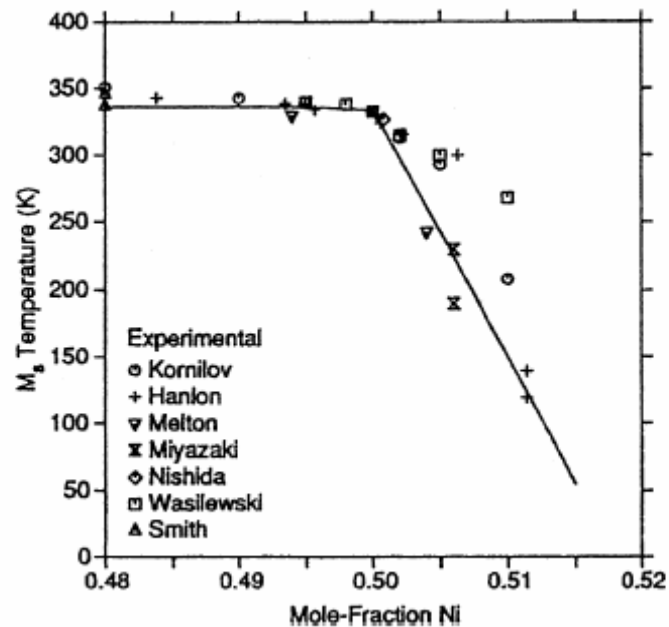
Figure 2.16 Dependence of M_s temperature on Ni content [83].

Phase transformation temperatures are severely affected by problematic impurity elements such as O, C, H and N which either form compounds and/or dissolves in the lattice. Like pure Ti and various Ti alloys TiNi alloys are prone to oxidation

severely. Figure 2.17 [98] exhibits the oxidation behavior of equiatomic TiNi alloy. In the temperature range 200-500 °C oxidation reaction proceeds linearly, however beyond 500 °C an exponential relation exists between temperature and the reaction. Oxidation of TiNi is actually a selective oxidation of Ti due to the large difference in the formation energy of the two oxides (TiO_2: 691.5 and 674 kJ/mol; NiO: 115.2 and 106.8 kJ/mol at 1100 and 1200 °C, respectively). Selective oxidation behavior results in formation of different Ti-oxide layers depending on O concentration as shown in Figure 2.18. Solid solubility of oxygen in TiNi alloys is extremely small and estimated to be around 0.045 at.% [99], and TiNi alloys with oxygen content exceeding this limit inevitably contains Ti_4Ni_2O phase. Since during its formation Ti atoms are consumed twice as much compared to Ni atoms in the matrix, in presence of oxygen $TiNi_3$ phase appears in the Ni enriched matrix. Ti_4Ni_2O phase formation occurs in the initial stage of reaction between TiNi and oxygen [100]. Therefore, in case of air atmosphere oxidation this stage would be very short and difficult to observe. On the other hand, if the partial pressure of O is reduced using vacuum or getters, metastable Ti_4Ni_2O phase, which does not present in pseudo binary equilibrium TiNi-O phase diagram, can be observed. O amount in commercial TiNi alloys is typically in the range 600-800 ppm (0.06-0.08 at.%) [90] and thus, Ti_4Ni_2O phase is observed frequently.
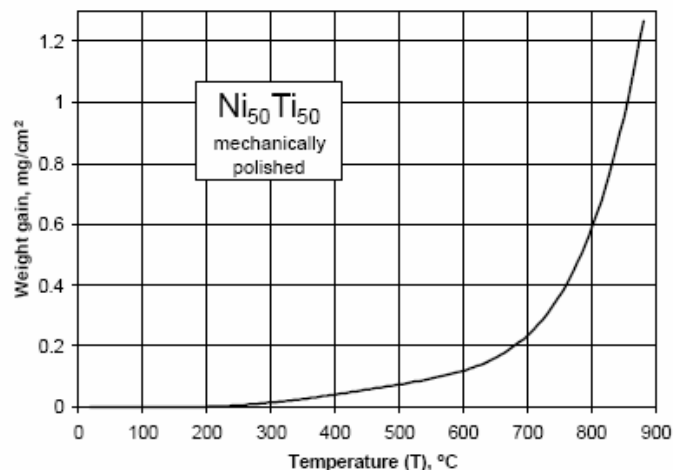
Figure 2.17 Oxidation behavior of equiatomic TiNi alloy on heating with the constant rate 1°C/min under air atmosphere [98].
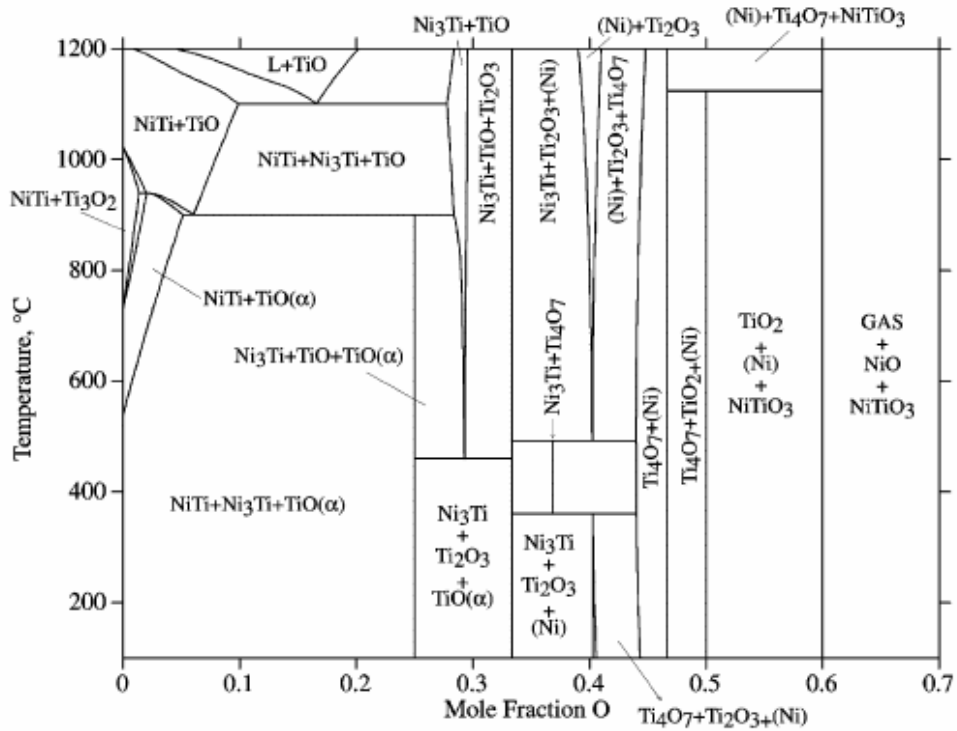
Figure 2.18 Calculated equilibrium pseudo-binary phase diagram of TiNi-O [98].

Figure 2.19 (a) shows the M_s temperature as a function of oxygen content (e.g. total O content: soluble and insoluble) in TiNi alloys prepared by specially adding O deliberately [101]. It is clear that M_s decreases linearly with increasing O content due to increase in Ni content of TiNi matrix resulting from Ti_4Ni_2O formation. When the oxygen solubility in TiNi phase is ignored and all the O atoms are assumed to exist in Ti_4Ni_2O, the Ni content in TiNi corrected for oxide (Y_{Ni}) can be calculated using equation 2.4.

$$Y_{Ni} = \{100(X_{Ni} - 2X_O)\}/\{100 - 7X_O\} \tag{2.4}$$

where X_{Ni} and X_O are total Ni content and total O content respectively in the alloy. All the units in this equation are at.%. Figure 2.19 (b) shows the M_s temperature versus Y_{Ni} (solid line) calculated using the above equation. Broken line represents the relation between M_s and Ni content measured from TiNi alloys with a very low

O content (0.009 at.%). It is obvious that two lines agree with each other well indicating that almost all the O atoms really exist in Ti_4Ni_2O, and therefore increasing the Ni content of TiNi phase. Accordingly, M_s temperatures decrease with increasing O content up to a critical O content at which $TiNi_3$ phase starts to form. Upon $TiNi_3$ formation, a new equilibrium will exist and final Ni content of TiNi will change.
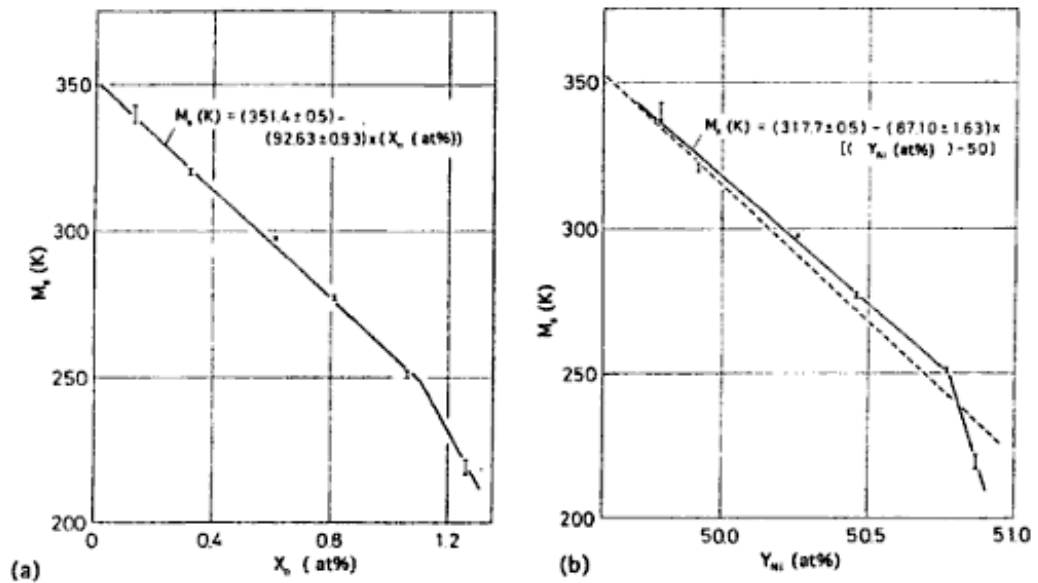
Figure 2.19 Dependence of M_s on (a) total O content, (b) Ni content in TiNi matrix corrected for Ti_4Ni_2O [101].

Carbon has a little solubility in TiNi phase and most of the C atoms present as TiC in TiNi alloys [102]. Corrected Ni content (Y_{Ni}) for the TiNi matrix, assuming all the C atoms are consumed to form TiC carbides, can be expressed as

$$Y_{Ni} = 100 X_{Ni} / \{100 - 2X_C\} \qquad (2.5)$$

in which all concentrations were given in at.% and X_{Ni}, X_C designate total Ni content and total C content respectively. It was found that M_s decreases linearly with

increasing C content forming TiC and thus increasing Ni content of the remaining TiNi phase [102, 103]. It was also determined that dissolved C in TiNi matrix lowers the M_s temperature by approximately 15 °C [90, 99, 102]. Dissolution of C atoms in the matrix imparts a lattice strain which makes martensitic transformation difficult to operate. This strain can be compensated by increasing driving force and as a result M_s temperature decreases.

Nitrogen has a high affinity to titanium and it forms TiN reacting with TiNi. Moreover it can also form, together with C, carbonitrides, $TiC_{1-x}N_x$, $0 \leq x \leq 1$ [104] and may dissolve with O in Ti_2Ni forming $Ti_4Ni_2(O,N)_x$ [45]. Since formation of these phases alter the Ni/Ti ratio of the TiNi matrix, phase transformation temperatures will inevitably be subject to change.

Similar to other Ti-based alloys, TiNi alloys are sensitive to hydrogen. Diffusivity of H in B2 ordered structures is quite high and H is absorbed to form an extended solid solution with a maximum concentration of $TiNiH_{1.4}$ (equal to 40 at.%H or 13000 ppm H) without hydride formation [105, 106] at temperatures 52-427 °C and at low pressures, 0.005-2 MPa. Higher H concentration leads to TiH_2 and $TiNi_3$ formation [107] with increasing pressure, 13 MPa, and temperature, 500 °C. Solubility of H decreases with increasing temperature. Increase of H content decreases both transformation temperatures and the relative enthalpy of the reactions severely [108]. Indeed, at a H content of 1809 ppm there exists no transformation anymore [108, 109].

TiNi alloys are over sensitive to deformation like other shape memory alloys and a stabilisation effect is observed after deformation. The critical temperatures for the reverse transformation (A_s and A_f) increase with increasing deformation amount as it is clearly seen in Figure 2.20 (a). However, this effect (martensite stabilization) is a one-time phenomenon and it vanishes once the deformed martensite is reverted back to austenite by second heating, Figure 2.20 (c). Unlike in the reverse transformation, the critical temperatures of forward transformation (M_s and M_f) slightly decrease with deformation as shown in Figure 2.20 (b). In subsequent heating and cooling cycles both forward and reverse transformation temperatures do not change, but relatively small decrease occurs due to thermal cycling [110-112]. Martensite stabilisation has always been observed in different deformation modes such as, in

tension [113-115], compression [115], shear [115, 116] and classical cold rolling [117, 118], and also in different deformation conditions, such as by martensite reorientation [113-118] or by stress-induced martensitic transformation [115, 119]. In thermoelastic martensitic alloys, during cooling (forward transformation) half of the chemical free energy change (Δg_{ch}) is stored as the elastic strain energy, expressed as the below equation [120]

$$\Delta g_{ch} + 2\Delta g_{el} = 0 \qquad (2.6)$$

where $\Delta g_{ch} = g_M - g_P$ represents the chemical free energy change between parent and martensite, and Δg_{el} designates the elastic strain energy stored around the martensite plate. This stored elastic energy assists the reverse transformation. When such elastic energy is relaxed by deformation A_s and A_f temperatures increase [113], and this is the mechanism of martensite stabilisation.
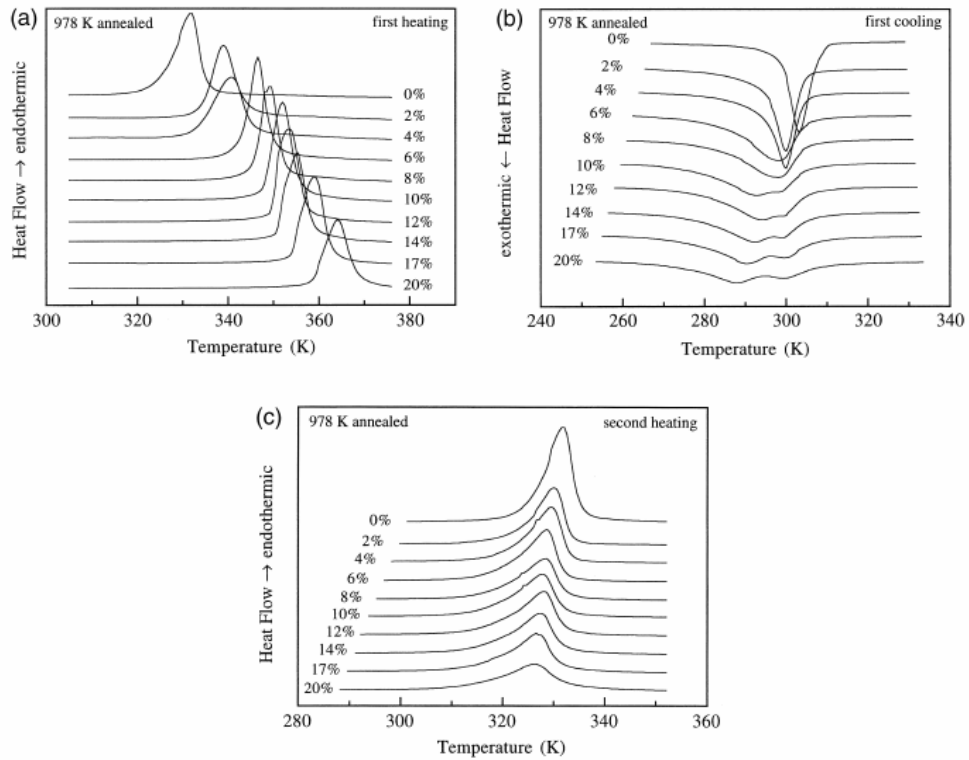
Figure 2.20 Effect of deformation on phase transformation temperatures [116].

33

2.2.4. Heat Treatment

Heat treatments used frequently for TiNi alloys involve the annealing after cold working to impart shape memory properties to the products and aging following solutionizing to modify and improve both phase transformation temperatures and mechanical properties. Annealing treatment after cold deformation is suitable for equiatomic and Ti-rich TiNi alloys whereas precipitation heat treatment (aging) is appropriate for Ni-rich (Ni content $\geq$ 50.5 at.%) TiNi alloys. In this section only aging treatment will be discussed.

Figure 2.21 shows the time-temperature-transformation (TTT) or more specifically the isothermal transformation (IT) diagram of Ti-52 at. %Ni alloy [121]. As shown on the diagram the precipitation sequence can be divided into three temperature ranges. Below ~680 °C for short aging times, metastable Ti_3Ni_4 (designated in the figure as $Ti_{11}Ni_{14}$) precipitates appear while at temperatures higher than ~750 °C and longer aging times equilibrium $TiNi_3$ phase forms. At intermediate temperatures, between 680 and 750 °C, metastable Ti_2Ni_3 phase precipitates. Intermediate phases are absorbed in the matrix with prolonged aging or with increase in aging temperature in the following order, and finally equilibrium $TiNi_3$ precipitates are obtained.

$$Ti_3Ni_4 \rightarrow Ti_2Ni_3 \rightarrow TiNi_3 \qquad (2.7)$$

Ti_3Ni_4 precipitate plays a very important role both in adjustment of transformation temperatures and mechanical features. Its crystal structure is rhombohedral with lattice parameters, a = 0.670 nm and α = 113.8° [122, 123] and its space group is R3 [123, 124]. Ti_3Ni_4 precipitates formed during aging change martensitic transformation path of TiNi alloys and trigger the formation of a different martensitic structure, called as R phase which has a trigonal structure. Martensitic transformations in properly aged TiNi alloys occur in two steps. Firstly, B2→R transformation takes place and subsequently R→B19' transformation is observed. Multistage martensitic transformation occurs in the sequence of increasing

transformation strain [86]. The reason for this multistage transformation is that fine precipitates have strong resistance to transformation with large transformation strain like B2→B19' but has much less resistance to transformation with small transformation strain like B2→R.
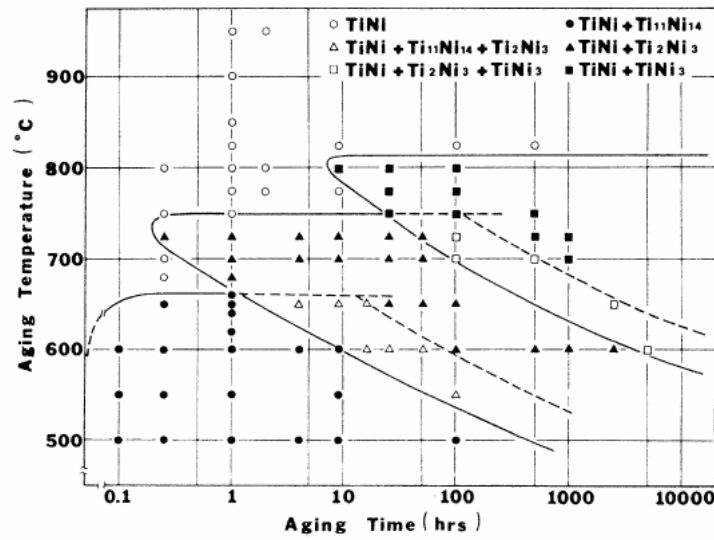
Figure 2.21 TTT diagram of Ti-52 at. %Ni alloy [121].

Figure 2.22 shows the phase diagram between TiNi and Ti_3Ni_4 phases [125]. It is obvious from the diagram that formation of Ti_3Ni_4 decreases Ni content of TiNi matrix. As previously stated, decrease in Ni content of TiNi phase results in increase of transformation temperatures. R_s is independent of aging time as can be seen from Figure 2.23 since B2→R transformation with a small transformation strain is insensitive to the density and size of the precipitates, and depends mainly on the composition of TiNi matrix [126]. On the other hand, M_s gradually increases with increasing aging time. Because Ti_3Ni_4 precipitates show a strong resistance to R→B19' transformation which generates large transformation strains. M_s temperature finally reaches a constant value which is independent of alloy composition, Figure 2.23. This originates from the equilibrium between the two phases. Aging at a different temperature for prolonged times of course yields another

35

constant M_s that corresponds to the equilibrium composition at that temperature [6, 126].
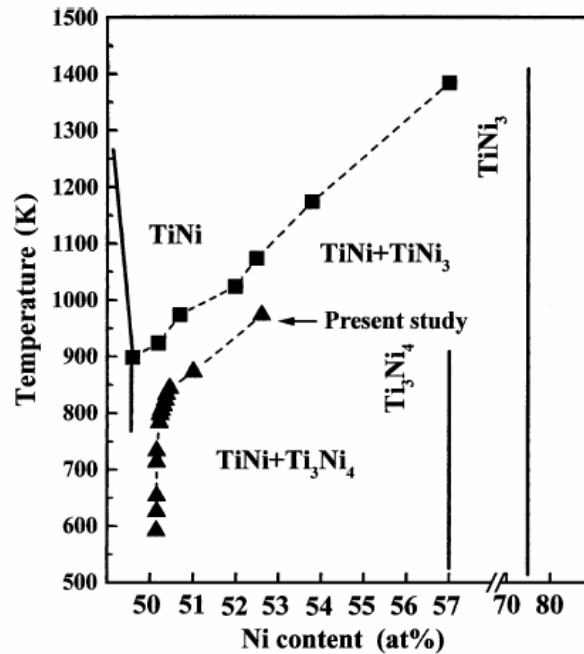
Figure 2.22 Phase diagram showing the equilibrium between TiNi and Ti$_3$Ni$_4$ phases and TiNi and TiNi$_3$ [125].
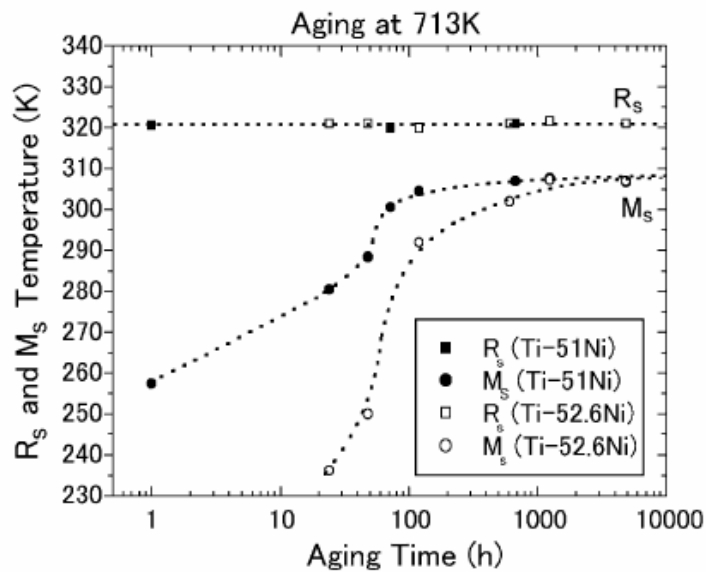
Figure 2.23 Effect of aging time on phase transformation temperatures [6].

36

2.2.5. Mechanical Behavior

Mechanical behavior of TiNi alloys is different from those of ordinary metallic materials. Because up to a critical strain level, generally 8% in tension, deformation mechanism of TiNi alloys is neither slip nor deformation twinning, both of which occur in common metallic materials. Instead, deformation takes place by detwinning or stress-induced martensitic transformation as previously pointed out in shape memory and superelasticity sections, and thus deformation behavior of TiNi shape memory alloys are severely dependent on temperature as shown in Figure 2.24 [50]. Stress-strain curves obtained at different test temperatures in the figure belong to Ti-50.6 at. %Ni alloy, which was solution-treated at 1000 °C for 1 h followed by quenching into water. At temperatures below M_f, Figure 2.24 (a)-(c), the deformation proceeds by the migration of twinning interfaces within the martensite phase. When the test temperature is increased to a value between M_s and M_f, Figure 2.24 (d) and (e), growth of new stress-induced martensite and stress-induced growth within the existing martensite phase accompany to coalescence of variants. At M_s-A_f temperature range, Figure 2.24 (f)-(i), deformation occurs by only stress-induced martensite transformation and martensite phase formed is stable upon removal of stress. When the test temperature exceeds A_f slightly complete superelasticity is observed, Figure 2.24 (j)-(l). Because the martensite phase only exists under stress at this temperature interval. Further increase of test temperature results in partial superelasticity behavior since plastic deformation also occurs together with stress-induced martensite nucleation and growth, Figure 2.24 (m)-(p).

Figure 2.25 shows the critical stress for inducing martensite and that for reverse transformation as a function of temperature, which were plotted from the data in Figure 2.24. At temperatures lower than M_s critical stress represents the detwinning stress of martensite. M_s determined by electrical resistivity measurement or differential scanning calorimetry roughly corresponds to the minimum of the critical stress curve upon loading. Therefore, the mechanical behavior at temperatures above the minimum point corresponds to the stress-induced martensitic transformation, while that below the minimum point to the deformation of martensite.
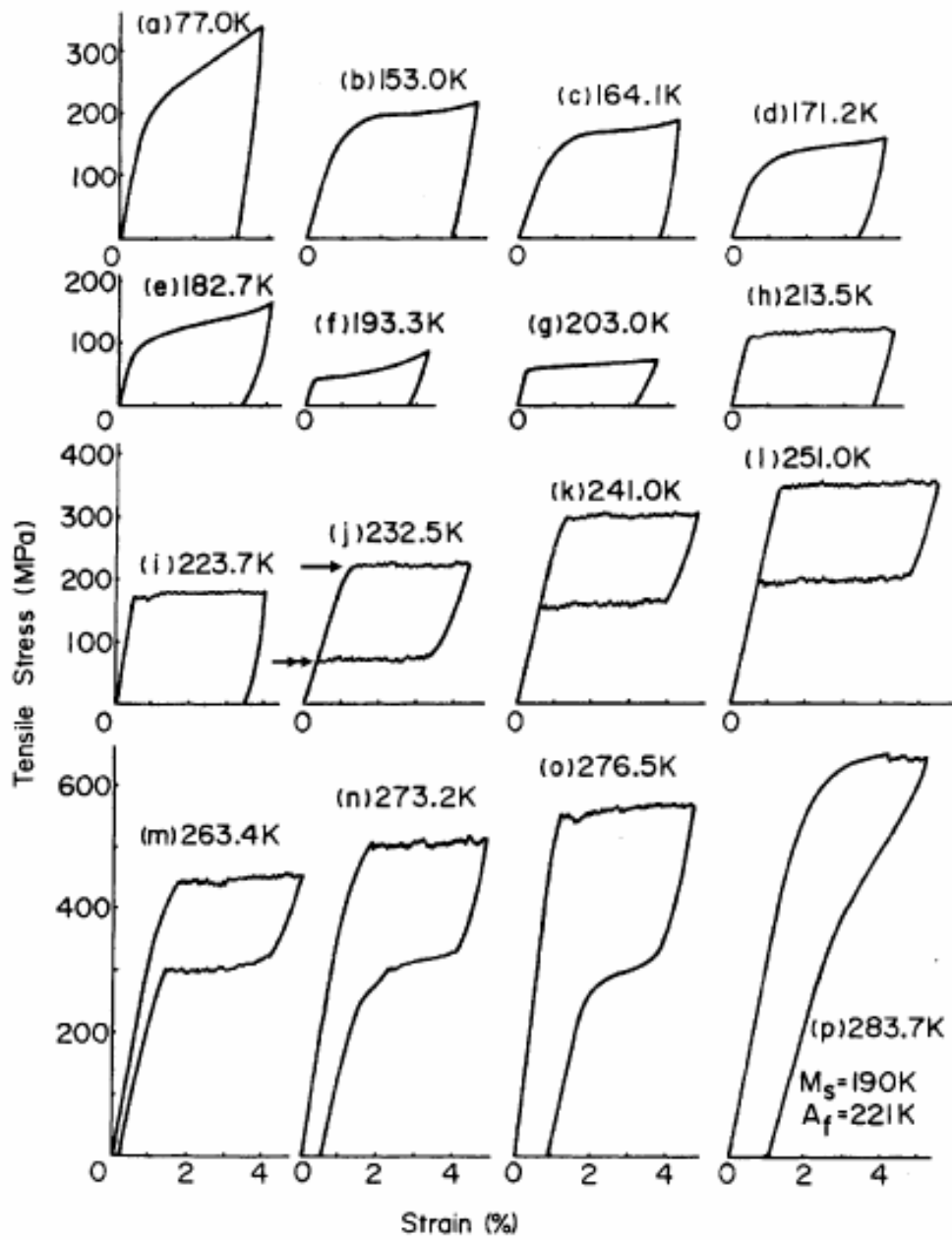
Figure 2.24 Stress-strain curves of Ti-50.6 at. %Ni alloy, which was solution-treated at 1273 K (1000 °C) for 1 h, at different test temperatures. The arrow and the double arrow in (j) indicate the critical stress for inducing martensite and that for reverse transformation respectively [50].
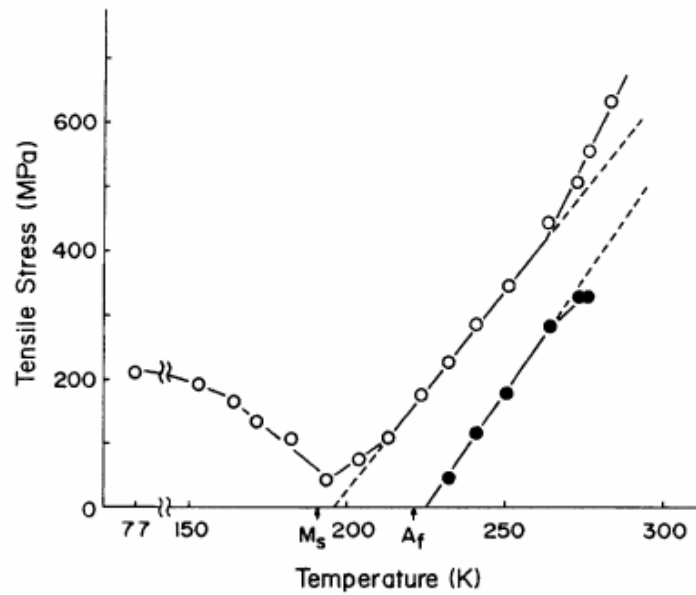
Figure 2.25 Critical stress as a function of temperature (open circles) and for reverse transformation (solid circles), which were plotted from the data in Figure 2.24 [50].

Deformation mechanisms operating in TiNi shape memory alloys change with temperature as well as with applied strain. Mainly they are analysed in two test temperature regimes: $T > A_f$ and $T < M_s$. Figure 2.26 (a) shows typical tensile stress-strain curves of solution-treated Ti-50.6 at. %Ni alloy, which was deformed at 243 K ($> A_f$) and Figure 2.26 (b) shows the superelastic strain (ε_s), residual strain (ε_r) and permanent strain (ε_p) as a function of total strain, which were obtained from Figure 2.26 (a). Stress-strain curves have been divided into three stages [50]. At stage I initially a linear deformation, which corresponds to elastic deformation of parent phase occurs. Afterwards, a plateau stage with serrations, which is due to stress-induced martensitic transformation is observed. At plateau stage deformation proceeds inhomogeneously since it is actually a Lüders type deformation [51, 127]. The required stress for nucleation is higher than that for growth in stress-induced martensitic transformations. As a result, stress concentration at the interface between deformed and undeformed regions causes the stress-induced transformation only at the neighboring region of the deformed one. The stage II is characterized by a rapid strain hardening. It is clear from Figure 2.26 (b) that superelastic strain is still

increasing in stage II meaning that stress-induced transformation is still occuring with increasing stress. Plastic strain by slip also occurs in this stage starting from 8% strain. In stage III only slip and twinning are the operating deformation mechanisms. Recovered strains decrease with increasing total strain while permanent plastic strains increase in this stage. The slip system in B19' martensite is estimated to be $[100](001)_m$, although it is not confirmed yet [11]. The twinning mode in stage III is probably $\{20\bar{1}\}\langle\bar{1}0\bar{2}\rangle_m$ with twining shear of 0.4250 [128]. This large twinning shear provide the twinning mode with large deformations. However, the strains produced by this twinning mode are irreversible since it is not the lattice invariant shear.

Figure 2.26 (a) Stress–strain curves for Ti-50.6 at. %Ni alloy, which was deformed at 243 K (>A_f). The alloy was solution-treated at 1273 K for 1 h followed by quenching into water. The recovered strain upon heating to 373 K is indicated by dashed lines. (b) Plots of different strains in (a) as a function of total strain [50].

Figure 2.27 (a) shows typical tensile stress-strain curves of solution-treated Ti-50.6 at. %Ni alloy, which was deformed at 173 K ($<M_s$). The alloy was solution-treated at 1273 K for 1 h followed by quenching into water. Stage II and stage III are similar to the previous case but stage I is different. At smooth plateau region there is no serrations and initial part is more gradually change as if elastic deformation is absent. Stage I is characterized by reorientation of martensites, while stage II is characterized by detwinning/twinning and slip, and stage III represents slip and twinning [50]. It is clear from the Figure 2.26 (a) and Figure 2.27 (a) nearequiatomic TiNi alloys are highly ductile both in martensitic and in austenitic phase. The fracture point represented by symbol (x) in both figures show that more than 50% deformation is possible without fracture.
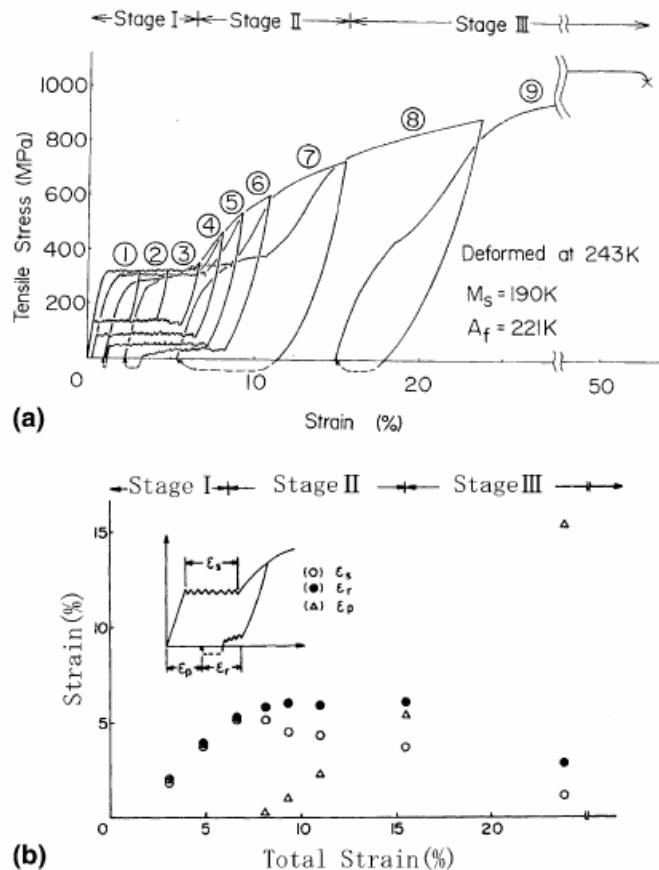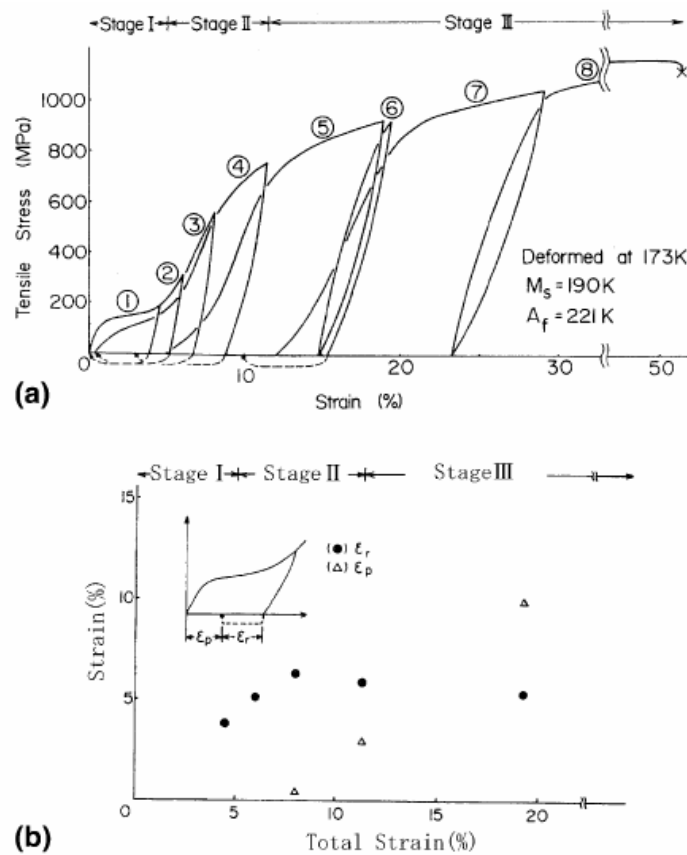

Figure 2.27 (a) Stress-strain curves for Ti-50.6 at. %Ni alloy, which was deformed at 173 K ($<M_s$). The alloy was solution-treated at 1273 K for 1 h followed by quenching into water. The recovered strain upon heating to 373 K is indicated by dashed lines. (b) Plots of various strains in (a) as a function of total strain [50].

41

Polycrystal equiatomic alloy of TiNi does not exhibit superelasticity and shape memory effect is also very poor as previously pointed out. Near equiatomic TiNi alloys with Ni content less than approximately 50.5 at.% Ni display only partial superelasticity [33, 50, 129] since critical stress to initiate slip is too low. It is essential to increase critical stress for slip for a good shape memory and superelasticity behavior. Critical stress for slip can be increased by increasing Ni content (solid solution hardening), precipitation hardening (aging), and cold working followed by annealing.

As Ni content exceeds 50.5 at.%, TiNi alloys show complete superelasticity behavior even in a solution-treated and water quenched condition as can be seen in Figure 2.24 (j)-(l), which belongs to Ti-50.6 at. %Ni alloy. However, complete superelasticity is observed in a narrow temperature regime. By applying aging heat treatment superelasticity properties can be further improved. Figure 2.28 [33] shows the effect of aging temperature on the critical stresses for inducing martensites and for reverse transformation in a Ti-50.6 at. %Ni alloy, which was aged at various temperatures for 1 h after solution treatment. It is clear that aging at 400 °C (673 K) for 1 hour gives the optimum shape memory and superelasticity characteristics. Because it gives the recoverable strain up to the highest stress level, which is recognized by the deviation from the linear stress-strain relationship (i.e. Clausius-Clapeyron relationship), and besides it exhibits superelasticity in a wide temperature range. 400 °C aging treatment results in formation of high density and small Ti_3Ni_4 precipitates. Thus, these precipitates are very effective for increasing critical stress for slip. Aging at 500 °C, on the other hand, gives low density and larger precipitates. When aging is carried out at 300 °C, the transformation is suppressed to lower temperature side, Figure 2.28, and the shape memory and superelastic characteristics is worse than those of 400 °C aging.

The annealing after cold working is a very efficient method to impart shape memory properties to Ti-rich TiNi alloys and slightly Ni-rich TiNi alloys with Ni content less than 50.5 at.% Ni [33]. Annealing at a proper temperature right after cold working retains TiNi alloy in recovered but un-recrystallized state. The alloy preserves its high strength due to presence of rearranged dislocations. As a result, similar to that in aging, critical stress for slip is increased and better shape memory

and superelasticity properties are observed. Recrystallization temperature of TiNi alloys depending on Ni content was reported to be around 500 [6]-600 °C [130]. Therefore annealing temperatures lower than recrystallization temperature (i.e 400 °C) gives superior shape memory features.

Work hardening and aging treatment can be combined to obtain better superelasticity. This method gives higher critical stress for slip and complete superelasticity is available at much higher stress levels, e.g., up to 700 MPa [131]. Stability of superelastic curves can also be increased using this combination [132]. Solutionizing treatment is omitted in this method and provides an extra advantage in terms of economy for practical productions.
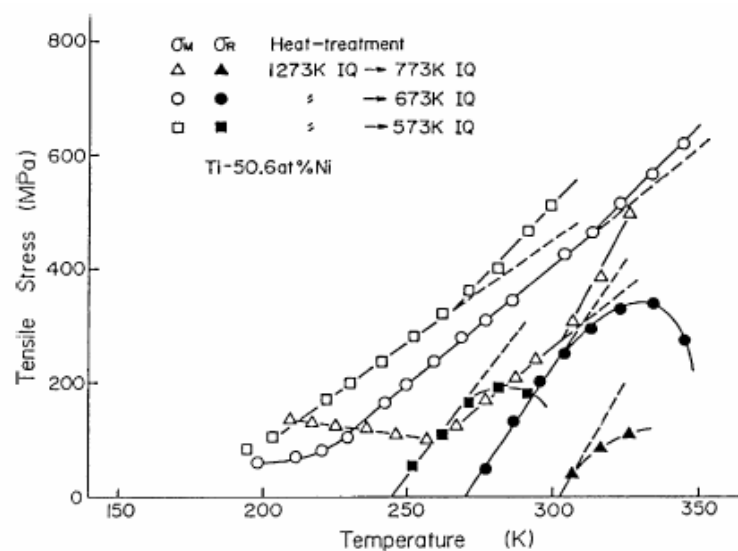
Figure 2.28 Effect of aging temperature on the critical stresses for inducing martensites and for reverse transformation in a Ti-50.6 at. %Ni alloy, which was aged at various temperatures for 1 h after solution treatment at 1273 K for 1 h [33].

2.3. TiNi Foams

Metallic foams, as other porous or cellular structures, exhibit extraordinary physical and mechanical features combining contradictory material characteristics such as, low density with a high stiffness or high gas permeability combined with

high thermal conductivity [133]. Therefore, they are new candidates for exceptional structural and functional applications.

Recently, TiNi shape memory alloys in porous form have attracted an additional interest as biomaterials for implantation and prosthesis [56] since TiNi alloys retain their unique properties when they are produced in metallic foam form while the introduction of pores into the bulk material provides ingrowth of living tissues and firm fixation in addition to reducing the alloy density. Moreover, Young's modulus of the material could be decreased easily to a degree, which matches that of the bone, ensuring biomechanical compatibility by adjusting the amount of porosity. Thus stress shielding effect, which arises from elastic modulus difference between the bone and the implant material, and may results in loosening of implant [134], is minimised.

The exploit of bulk TiNi shape memory alloy materials in biomedical sector is mainly due to their good biocompatibility, comparable to conventional stainless steel and titanium implant materials, and evaluated both in vivo and in vitro. Although nickel is in a tightly bound form in TiNi intermetallics, Ni release due to corrosion in the biological environment is unavoidable [135], and excessive Ni exposure can cause adverse symptoms such as asthma, allergic response, cellular hypersensitivity, cytotoxicity and genotoxicity, leading to serious health problems [136, 137]. Nickel release problem becomes more severe when TiNi foam implants are considered due to their large surface area and the amount of Ni release from porous TiNi may be two orders of magnitude greater than that from a solid implant [138, 139]. Stoichiometry of TiNi phase and also presence of secondary phases affect the amount of Ni release. Many systematic studies [140-149] have been done to evaluate biocompatibility, biological performance and corrosion resistance of porous TiNi alloys in the last decade, and they were found to be adequate or good. To reduce Ni release amount and to improve biocompatibility characteristics many surface treatments such as ion implantation [150-152], oxidation [153-156], and surface coating [157-160] have been applied to TiNi foams. It has been found that nickel ion release decreases relative to untreated samples in a broad range by factors of 2 and 14.

Biomedical applications, especially bone implants, stay one step ahead of other applications due to high cost of TiNi foam alloys. Shape memory and superelasticity properties can easily be used practically for insertion of implant ensuring better fixation with the host tissue. Superelastic porous TiNi alloys also display a mechanical behavior similar to that of the bones showing strain recovery around 2% [161]. Therefore, they exhibit a better mechanical compatibility compared to rival porous materials made up of stainless steel, tantalum, titanium, Ti6Al4V and ceramics such as hydroxiapatite. Porosity is of service to allow transportation of body fluids and bone ingrowth and also to decrease elastic modulus of the implant which is usually much higher than that of compact bone (12-17 GPa), and cancellous bone (< 3 GPa) [161]. Proposed applications of TiNi foams other than biomedical ones up to now include energy absorbers [162], separators [163] and lightweight actuators [164] as well as armor material in defense industry [165].

2.3.1. Processing and Characterization of TiNi Foams

There are many ways to manufacture cellular metallic materials summarized in Figure 2.29. Details of these techniques can be found in references [133, 166-169]. High melting point (1310 °C) and extreme reactivity of TiNi with atmospheric gases and crucible materials make its foaming in liquid state substantially difficult, despite the expensive high vacuum and high temperature equipment required. Powder metallurgy techniques, on the other hand, provide the flexibility of low temperature processing as well as close composition control and, mechanical and physical property modifications via adjustment of the processing parameters and characteristics of the powders used. Accordingly, up to now except for one study, using zone melting in a hydrogen atmosphere [170], only powder metallurgy methods, such as self propagating high temperature synthesis (SHS), hot isostatic pressing (HIP), metal injection molding (MIM), conventional sintering (CS), spark plasma sintering (SPS), and space holder technique (SHT) have been employed intensively to fabricate TiNi foams. In the following section, thus, only these powder metallurgy methods will be explained. Since characteristics of the foams such as, porosity, microstructure, martensitic transformations temperatures,

mechanical behavior, shape memory and superelasticity properties are directly related to the production techniques, they will also be included in the same section together with effect of various heat treatments applied.
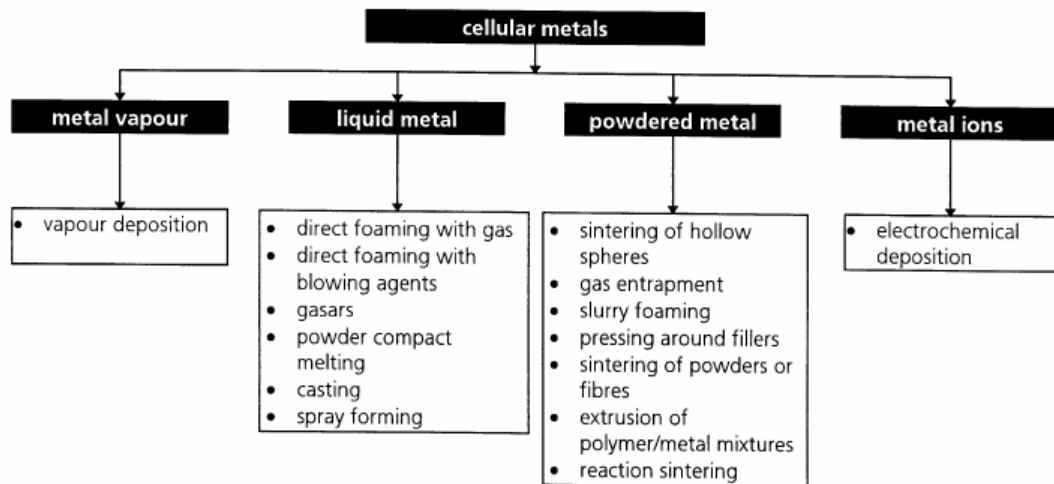
Figure 2.29 Classification of production methods for cellular metallic materials [133].

2.3.1.1. Self-Propogating High Temperature Synthesis

Most of the TiNi alloy foams have been manufactured using self-propagating high temperature synthesis, which is called also as combustion synthesis or reactive synthesis, up to now [171-180]. This rapid and energy saving method is a convenient way to produce such materials starting from elemental powders. After pressing the mixed Ni and Ti powders into desired shapes, ignition is accomplished usually by a heated tungsten coil at preheating temperature. Once initiated, the exothermic reaction starts and a combustion wave, which propagate through the reactant mixture, forms and reaction finishes just in seconds. The stages that are involved in SHS are schematically drawn in Figure 2.30. Preheating is necessary because the synthesis reaction between Ni and Ti powders is weakly exothermic. It is only 67 kJ/mol as can be seen below.

$$Ti + Ni = TiNi + 67 \, kJ/mol \qquad\qquad (2.8)$$

Depending on the preheating temperature, temperatures greater then the melting point of TiNi (1310 °C) may be reached [171]. During synthesis beside reaction (2.8) mainly following two reactions also occur.

$$Ti + Ni = Ti_2Ni + 83 \, kJ/mol \qquad\qquad (2.9)$$

$$Ti + Ni = TiNi_3 + 140 \, kJ/mol \qquad\qquad (2.10)$$

All of these three reactions are exothermic in nature and reactions (2.9) and (2.10) are more thermodynamically favored than reaction (2.8). As a result, formation of Ti_2Ni and $TiNi_3$ phases beside the desired dominant B2 (TiNi) or B19' (TiNi) are unavoidable, and they almost always exist in the microstructure. SHS process may also result in the formation of a fourth intermetallic, Ti_3Ni_4, and unreacted elemental Ni. Once formed, $TiNi_3$ and Ti_2Ni phases are difficult to remove completely just by changing the sintering conditions.

Figure 2.30 Schematic representation of the stages that are involved in SHS [169].

Incomplete diffusion and contamination during processing trigger the formation of secondary intermetallics (Ti_2Ni, $TiNi_3$ and Ti_3Ni_4) and oxides (Ti_4Ni_2O) and/or carbonitrides, all of which deteriorate the shape memory and superelasticity

47

characteristics. In fact, they in addition to making the foam brittle and less resistant to corrosion, affect the phase transformation temperatures dramatically. To overcome the aforem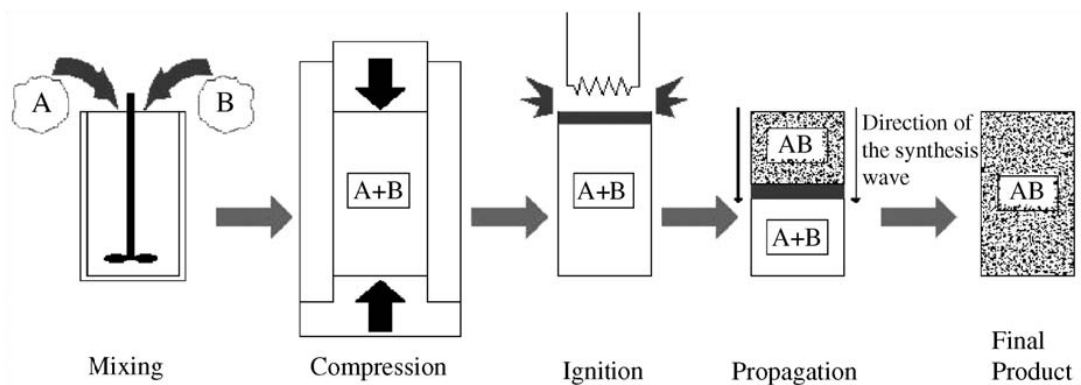entioned deficiencies various attempts have been made. Biswas [181] used a two step sintering procedure consisting of SHS and a post reaction heat treatment in which specimens synthesised were heated at a rate of 1 °C/min up to 1150 °C and soaked for one hour before cooling to room temperature at the same rate and a single phase TiNi foam was obtained for the first time. Bertheville [182] is the second who produced single phase porous TiNi conducting SHS process under calcium reducing vapor. Goh et al. [183] used a mixture of nanocrystalline Ni-Ti powder obtained from mechanical alloying and elemental Ni and Ti powders in SHS. Undesired Ti_2Ni phase amount was reduced significantly while unreacted Ni was completely eliminated using this method. Chu et al. [184] applied solution heat treatment at 1050 °C for 4 h to porous TiNi synthesised by SHS and they observed that amount of Ti_3Ni_4 sharply decreased but Ti_2Ni phase could not be removed by solution treatment. Kaya et al. [185] carried out the solution treatment at 1050 °C for 1 h under a stress of 6.41 MPa and completely eliminated Ti_2Ni and Ti_3Ni_4 phases.

Porosity of TiNi foams produced by SHS generally is in the range 40-70% [186-188]. It is difficult to adjust porosity amount, pore size and pore shape. Pore formation mechanisms proposed in SHS can be summarized as follows [171, 175]:

1. Existing pores in the pressed compacts.

2. Differences in diffusion rates between Ti and Ni. For example the diffusion rate of Ni atoms in Ti atoms is 4000 times higher than that of Ti atoms in Ni atoms at 900 °C [189].

3. Thermal migration due to the high thermal gradient along the self-propagating direction.

4. Gas evolution during combustion raection.

5. Differences in molar volume between reactants and products.

TiNi shape memory alloys prepared by SHS show large pore size (about 200-500 μm) [188]. It is important to select suitable powders and process parameters (pressure, preheating temperature, heating rate etc.) prior to SHS in order to prepare high quality products, as the microstructure and properties of the final products depend on the SHS reaction conditions. Generally anisotropy in pore morphology,

Figure 2.31, due to the liquid formation during processing is observed. Pores tend to be linear aligned along the propagating wave direction, Figure 2.31 (a) and most of the pores are interconnected to each other, Figure 2.31 (b).
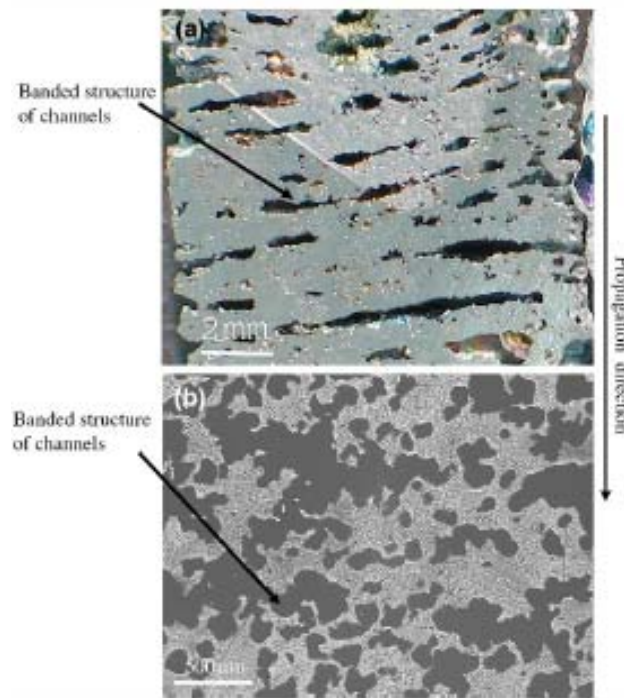
Figure 2.31 Morphology of pores in combustion synthesis (a) low magnification and (b) high magnification [183].

Porous TiNi alloys produced by SHS method usually show brittle behavior and low strength in terms of mechanical properties [171, 172, 177, 184, 187]. Chu et al. [173] recently developed porous TiNi with high strength and isotropic pore structure by an improved SHS method, in which ignition is started using an ignition reagent composed of Ti and C powders instead using tungsten coil. Although strength was improved (up to 500 MPa) due to isotropic pores, the final product was still brittle as can be seen in Figure 2.32. Undesirable phases need to be eliminated to improve mechanical properties and shape memory effect as well as superelasticity.

Phase transformation temperatures of porous TiNi shape memory alloys produced by SHS with different porosity are almost identical, and the latent heats of

transformation increase with increasing porosity [190]. Like in bulk TiNi alloys the type of phase transformation changes from one step (after solution treatment) to two step after subsequent aging treatment for 1 hour. With increasing aging temperatures, the transformation temperatures (R_s and A_s) decrease [191, 192], which is in good agreement with the results of aged bulk TiNi alloys.
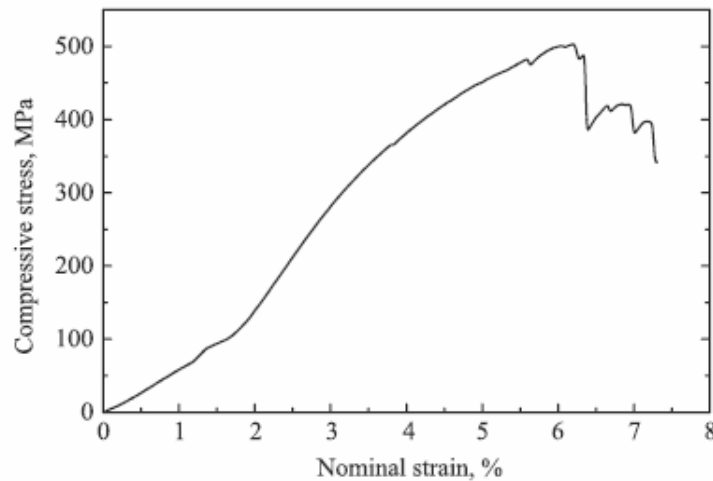
Figure 2.32 Compressive stress-strain curve of porous TiNi prepared by SHS method with the general porosity of 52.8 vol.% [173].

2.3.1.2. Hot Isostatic Pressing

HIP, which is also called as gas entrapment technique, is summarised in Figure 2.33 [193]. Mixed elemental or blended prealloyed powders are cold compacted into desired shape and during compaction gas is allowed to be entrapped in the material. Heating the precursor material in a second step (for 3-24 hours) then leads to metal expansion due to the internal pressure created by the entrapped gas. The expansion takes place in the solid state and it is, therefore, not an actual foaming but rather a solid state creep process. A porous body with partially interconnected porosity (20-50%) is obtained. Typical pore diameters range from 10 to 500 μm. [177, 193-195]. Theoretical considerations show that no more than 50% porosity can be expected for the gas entrapment technique.

Diffusion layers are easily formed when elemental powders are used, Figure 2.34. Actually, even when prealloyed powders were used in sintering, secondary intermetallic phases formation would be inevitable without providing the necessary oxygen partial pressure less than the critical value at the sintering temperature. Secondary undesired phases have been observed due to oxidation in the studies carried out to produce bulk TiNi alloys, although starting powders were prealloyed TiNi [196-199].
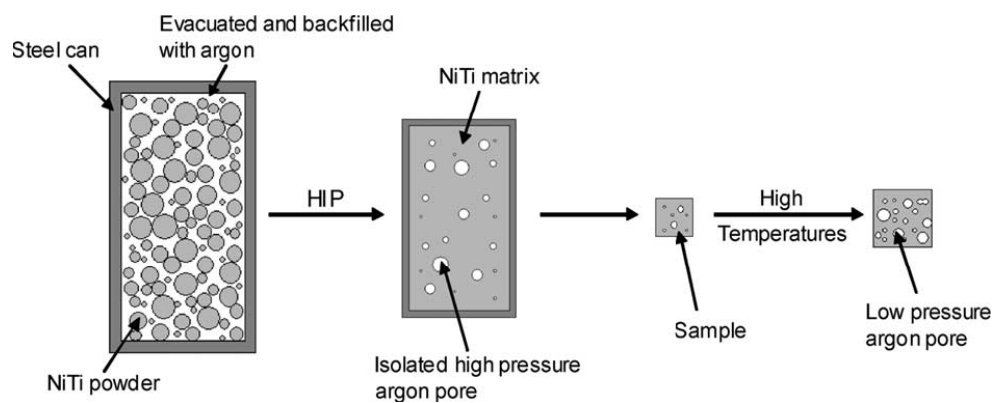
Figure 2.33 Schematic drawings indicating the stages involved in HIP [193].
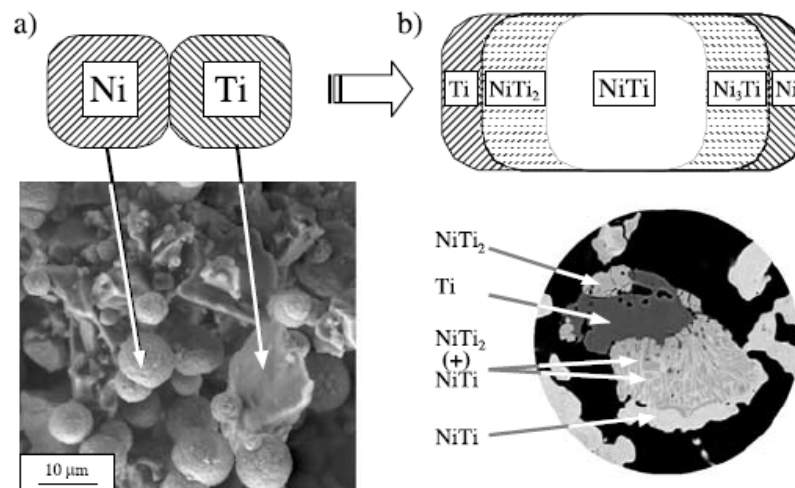
Figure 2.34 (a) Elemental Ni and Ti powders, (b) resulting phases due to incomplete diffusion [194].

Typical resulting pore morphology in HIP is given in Figure 2.35. Pores are smoother, more isotropic and more spherical compared to ones in SHS process. Pore distribution in the microstructure is also more homogeneous. As a result, porous TiNi alloys produced by HIP show superior mechanical properties, and superelasticity, up to 4-6% [177, 193-195, 200] in compression depending on the porosity content. However, operation cost of HIP is quite expensive.

The phase transformation behavior of aged porous TiNi SMA is similar to that of the dense TiNi alloy with the same composition and aged in the same condition; and transformation temperatures and latent heats of martensitic transformation were found to decrease with increasing porosity [201, 202].
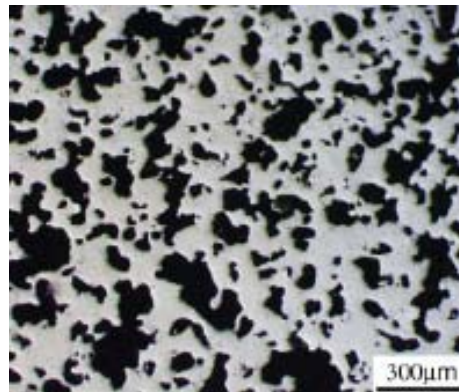
Figure 2.35 Micrograph of porous TiNi produced from elemental powders using HIP [194].

2.3.1.3. Metal Injection Moulding

Grummon et. al. [203] produced 100% open cell TiNi foams, Figure 2.36 with relative densities as low as 0.039 using a polymeric precursor coated with an equiatomic TiNi powder slurry, metal injection moulding (MIM), which was subsequently sintered. However, in all the foam samples contamination resulting from polymer decomposition during sintering was severe. These interstitial contaminants, namely oxygen, carbon, nitrogen and hydrogen considerably influence both SME and superelasticity behaviour of the TiNi foams, while reducing

their mechanical properties critically. Prealloyed powders were used in that study, but still the resultant foams were brittle.

Guoxin et al. [204] used elemental powders in MIM. The porosity of the TiNi foam was about 75 vol.% and the pores were almost three dimensionally interconnected, which forms an open porous structure. Microstructure was consisted of several intermetallic compounds such as TiNi and Ti_2Ni.

It is clear that MIM is an efficient method to produce metallic foams with higher porosities. However, resulting products seem to be not suitable for load-bearing applications.
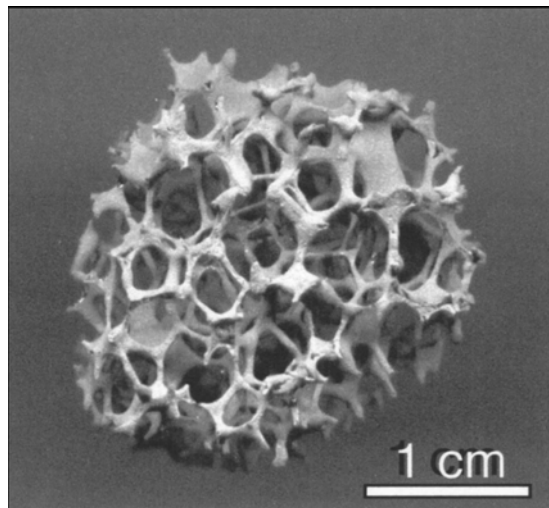
Figure 2.36 Optical photograph of open cell TiNi foam produced using MIM [203].

2.3.1.4. Conventional Sintering

In conventional sintering [177, 205-208] mixed elemental or prealloyed powders are compacted and subsequently sintered under vacuum or Ar gas atmosphere at elevated temperatures for times usually varying in the range of 2-72 hours. Both solid state and liquid phase sintering have been carried out and typical resulting irregular pore morphology in the product is shown in Figure 2.37. It is difficult to achieve high porosity, large pore size and smooth pore shape in CS method.
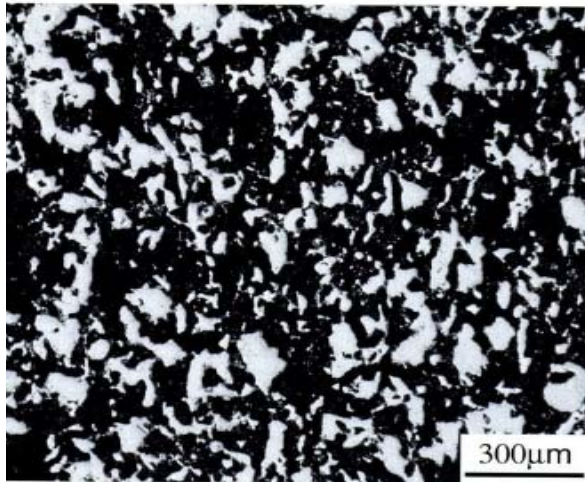
Figure 2.37 Pore morphology obtained from conventional sintering [177].

The strain recovery by superelasticity mechanism is complete when the applied strain is less than 2% for conventionally sintered TiNi alloys [205]. With the increase of applied strains, the permanent strains increase. Stress plateau observed in bulk TiNi alloys do not occur during compression test of porous TiNi alloys [209]. The transformation behavior of conventionally sintered porous TiNi alloys is different from that of cast TiNi alloys and two-peak phenomenon appears in both heating and cooling in the DSC curves. This is attributed to the microcompositional fluctuations [177, 180, 210].

2.3.1.5. Spark Plasma Sintering

Zhao et al. [211] introduced spark plasma sintering of prealloyed powders. Powders were loaded into a graphite die and pressed to the desired pressure (5-25 MPa) and then a huge on-off pulsed current was induced through the die and stacked powder particles (Figure 2.38). Under the condition of pulsed current heating, powder particles were activated to a high energy state and neck formation easily occured at low temperature (around 800 °C) in very short time, only 5 minutes. Moreover, the effect of spark discharge purified the surface of powder particles, which quarantees neck formation and high quality of sintered materials.

Typical material resulting from this process is shown in Figure 2.39. It is clear that porosity distribution is quite inhomogeneous. SPS results in inappropriate pore size (i.e. less than 100 μm) for bone replacement applications and irregular pore shapes acting as stress raisers. Moreover, adjustment of porosity ratio is also difficult and limited to powder characteristics. On the other hand, this technique produces porous TiNi alloys displaying good superelasticity behavior.
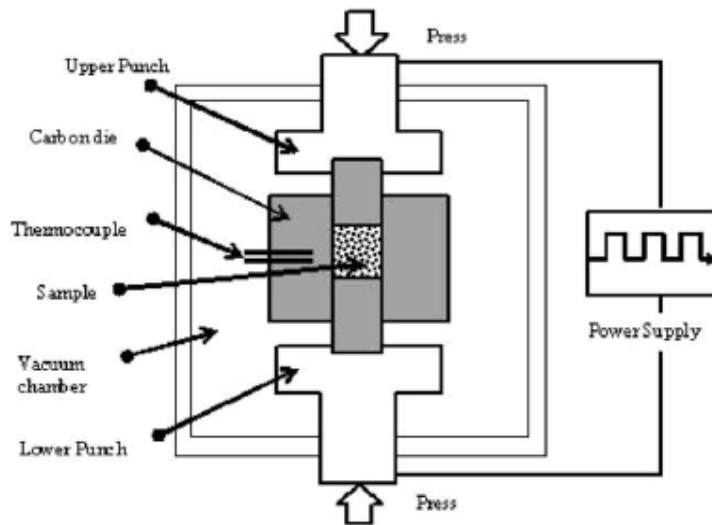
Figure 2.38 Schematic drawing of spark plasma sintering device [211].
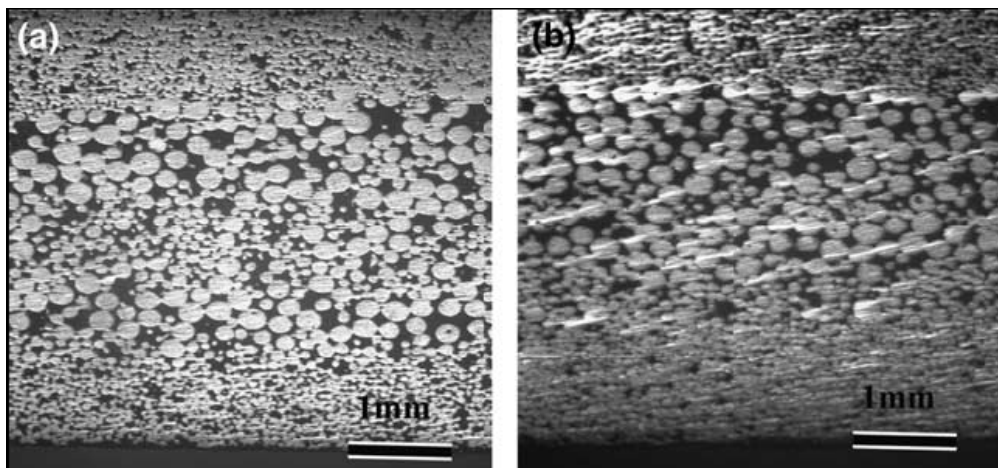
Figure 2.39 Microstructure of porous TiNi specimens fabricated by SPS: (a) 25% porosity; (b) 13% porosity [211].

2.3.1.6. Space Holder Technique

Space holder technique utilizes spacer particles (or space holders, pore formers, space fillers, pore forming reagents etc.) to create pores in the microstructure, and it seems to be a promising method for production of TiNi alloy foams. Desired porosity level, pore shape and pore size, and accordingly mechanical properties are easily adjustable in a broad range as long as a suitable space former is chosen in this method. Common space forming agents that have been used in metallic foam fabrication up to now involve sodium chloride [212] or carbamide [213, 214] for aluminum foams, polymers [215] or potassium carbonate [216] for copper foams, sodium carbonate for nickel foams [217], and ammonium bicarbonate [218] or magnesium [219] for titanium foams. Schematic representation of the process is given in Figure 2.40. SHT starts with powder densification in the presence of a space holder which is removed during or after the powder densification. Second step is sintering and it can be conducted in a HIP or under vacuum or flowing Ar gas.

Space holders used in TiNi foam production in the past consist of sodium floride (NaF) [220], sodium chloride (NaCl) [221], ammonium bicarbonate (NH_4HCO_3) [222-225], urea ($CO(NH_2)_2$) [226] and magnesium (Mg) [227]. Space holder material must be chemically unreactive with TiNi. For example Mg solubility in TiNi is expected to be negligible since magnesium is not soluble in any appreciable amount neither in Ti nor in Ni. Due to very limited solid solubility of magnesium in titanium (1% at RT), (Figure 2.41 (a)), and no solubility in nickel (Figure 2.41 (b)) it is possible to remove nearly all the magnesium present in compact by increasing the sintering temperature above the boiling point of Mg (1090 °C).

Space holder agents are removed from the compact either by heating to their decomposition temperatures (270 °C for NH_4HCO_3; 250 °C for $CO(NH_2)_2$) or dissolution in water, suitable for alkali metal salts. Incomplete removal of decomposition products mainly consisting of carbon, hydrogen, nitrogen or oxygen compounds will definitely react with TiNi due to extreme affinity of titanium to stated elements. In a similar manner, TiNi may also react with residual NaCl or NaF to form titanium chloride compounds that are thermodynamically much more favored. Possible selective reactions of titanium with the elements mentioned above

alters the Ni/Ti ratio of TiNi matrix. Shape memory and superelasticity properties as well as phase transformation temperatures are very sensitive to nickel content of TiNi matrix. Thus, they all will be effected seriously and most of the times negatively.
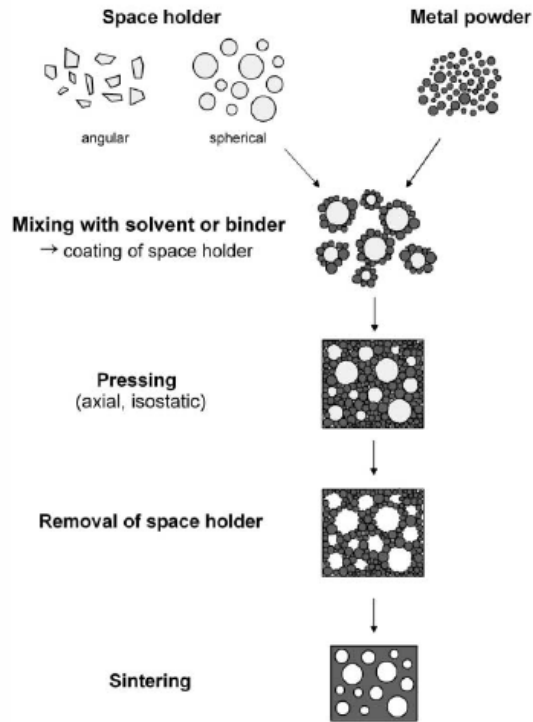
Figure 2.40 Schematic representation of space holder technique [133].

| (a) | (b) |
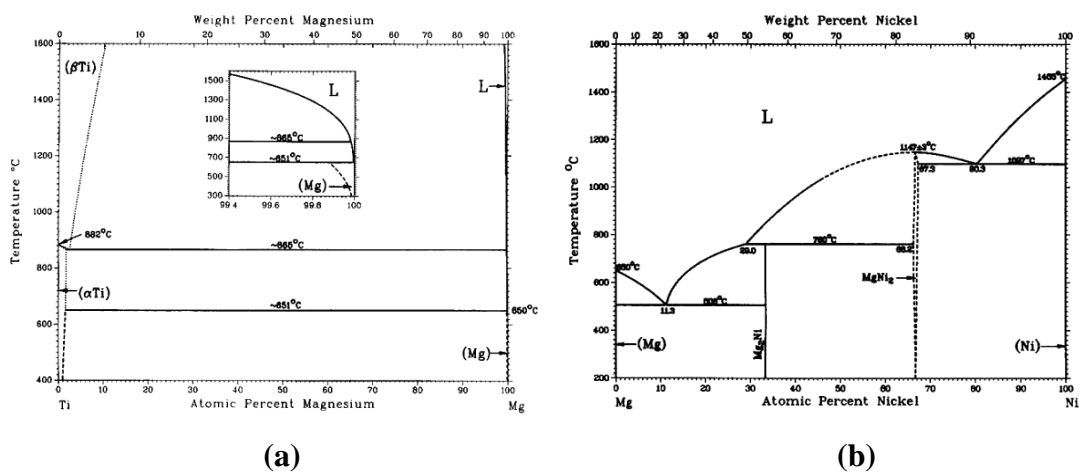
Figure 2.41 (a) Ti-Mg, (b) Mg-Ni equilibrium phase diagram [75].

SHT provides the best shape memory [220, 221] and superelasticity [224, 226] behavior as well as mechanical properties. Most of the studies in literature on characterization of transformation behaviour have dealt with the determination of martensitic phase transformation temperatures as a function of aging conditions without clearly specifying the important parameters, to which the phase transformation temperatures are very sensitive, such as composition, deformation and heat treatment details, and oxidation state. The outcome of such studies are mostly confusing because these parameters display opposing effects on phase transformation temperaures. For example, oxidation and Ti-rich precipitates lead to decrease in transformation temperatures while Ni-rich precipitates result in an increase in martensitic transformation temperatures. Since the processing techniques mentioned above usually end up with both formation of secondary phases and also a slight or severe oxidation, to distinguish the effect of porosity on transformation temperatures becomes almost impossible. These issues will be explained in detail in Chapter IV.

CHAPTER 3

EXPERIMENTAL PROCEDURE

3.1. Powders Used

In the present study, two different prealloyed spherical Ni-rich TiNi powders were used in foam production: Ti-50.6 at. %Ni (99.9% purity, supplied by Nanoval GmbH & Co. KG) which is suitable for precipitation heat treatment and Ti-50.4 at. %Ni (99.9 % purity, supplied by Special Metals Corp.). Spherical magnesium (Mg) powders (99.82% purity, supplied by Tangshan Weihao Magnesium Powder Co. LTD) were used as the space holder material. Prealloyed powder was preferred instead of elemental Ti and Ni powders to prevent the formation of secondary intermetallics. Both TiNi alloy powders used exhibited Gaussian (log-normal) particle size distribution with mean diameters of 21 μm and 40 μm for Ti-50.6 at. %Ni and Ti-50.4 at. %Ni powders, respectively, as it can be seen from Figure 3.1 (a) and 3.1 (b). Particle size of Mg powders was in the range 2 to 1124 μm, averaging at 400 μm, Figure 3.1 (c). D_{10} and D_{90} corresponding to the particle sizes at 10 and 90 percent points on the cumulative distribution curve of Mg powders were however 50 and 615 μm, respectively compatible with the desired range (100-600 μm).

Differential Thermal Analysis (DTA) of prealloyed TiNi powders showed that both of the powders melt partially at 1120 °C. DTA experiments were repeated using different atmospheres, namely, air and nitrogen. Nevertheless, DTA peak present around 1120 °C has always been observed. Inductively coupled plasma-mass spectrometer (ICP-MS) and X-ray mapping were employed to clarify the reason for the 1120 °C peak. Since the ICP-MS results confirmed the compositions of TiNi powders stated by the suppliers, and X-ray mapping did not point out a

compositional inhomogeneity, it was concluded that oxidation occuring during heating and cooling cycles of DTA was responsible from the partial melting as explained in detail in the following sections.

(a)

(b)

(c)
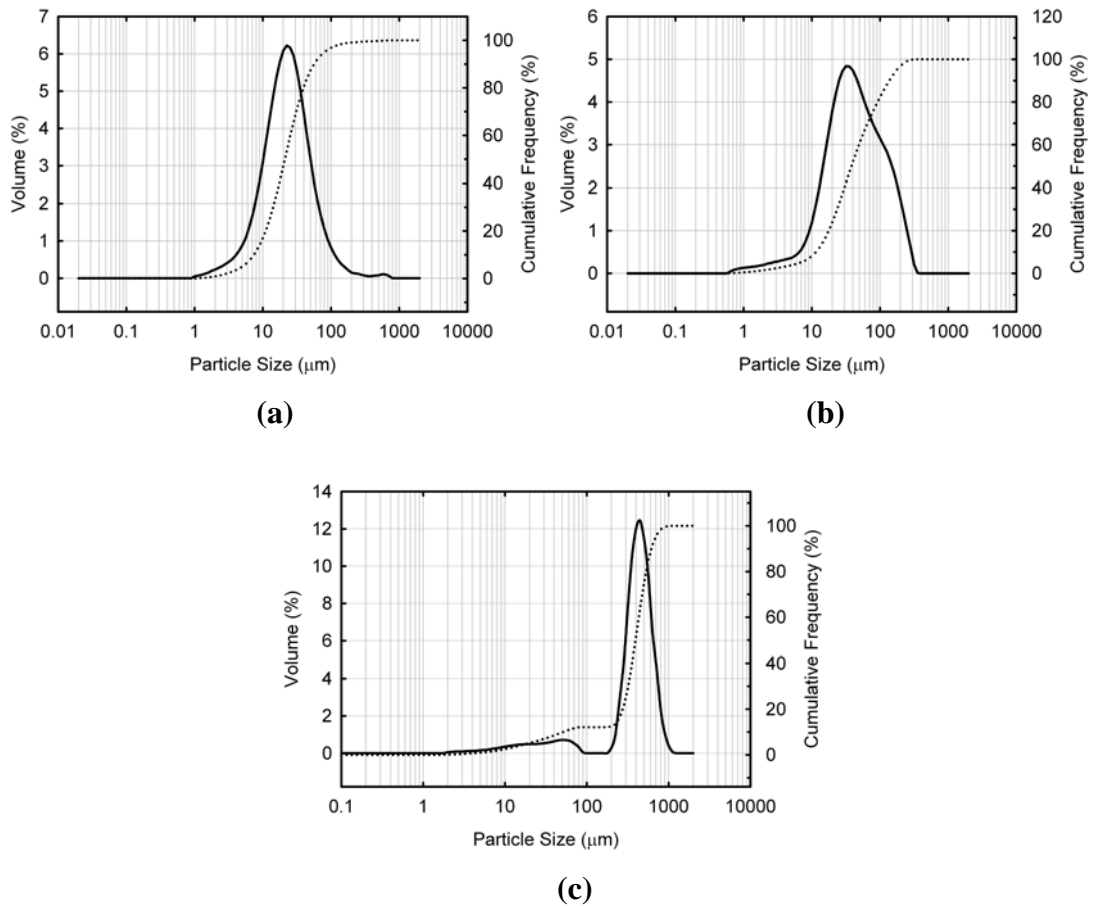
Figure 3.1 Partical size histograms of (a) prealloyed Ti-50.6 at. %Ni, (b) prealloyed Ti-50.4 at. %Ni, (c) magnesium powders. Solid lines show particle size distribution while dotted lines represent cumulative distribution.

Figure 3.2 shows the typical spherical morphology and dendritic microstructure of prealloyed TiNi and Mg powders all produced by inert gas atomization. Both TiNi powders exhibit agglomerates and satellites probably due to poor turbulence control and particle reentry into the atomization zone during processing.
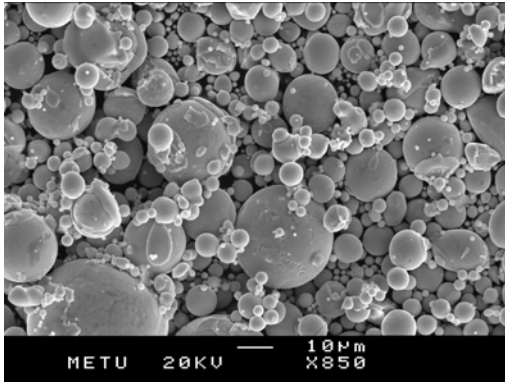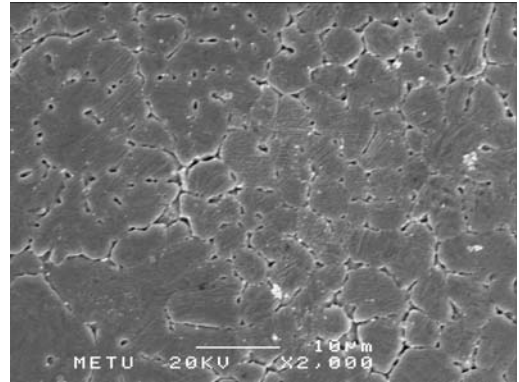
(a)   **(d)**
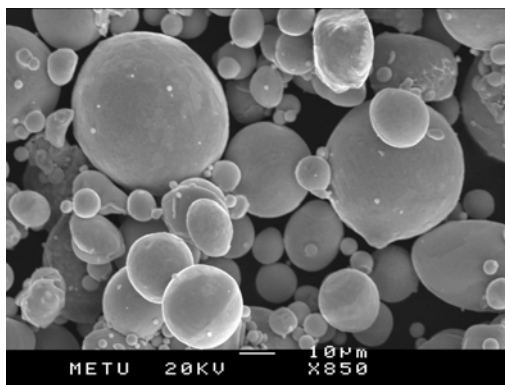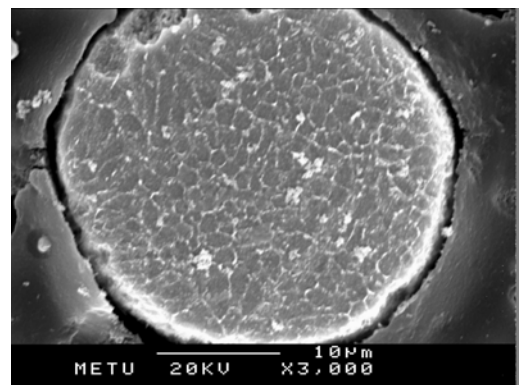
(b)   **(e)**
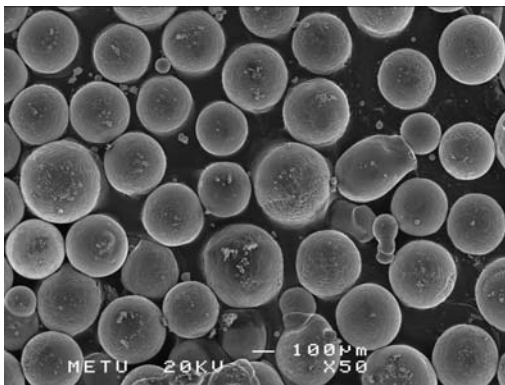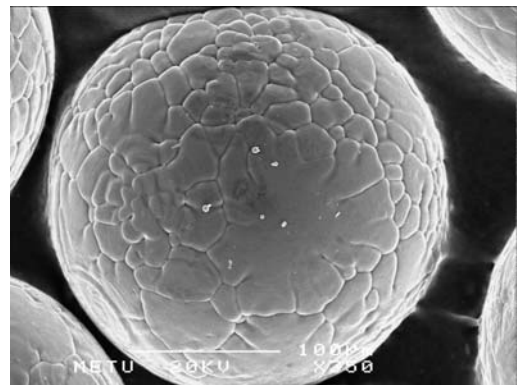
(c)   **(f)**

Figure 3.2 SEM micrographs showing morphology and dendritic microstructures formed as a result of atomization process of (a) and (d) Ti-50.6 at. %Ni, (b) and (e) Ti-50.4 at. %Ni, (c) and (f) magnesium powders.

Figure 3.3 shows XRD patterns of the as-received powders at room temperature. While the Ti-50.6 at. %Ni powder was observed to consist of only austenite phase, Ti-50.4 at. %Ni powder at room temperature was a mixture of austenite and martensite phases as confirmed also by SEM, Figure 3.4.

(a)   **(b)**
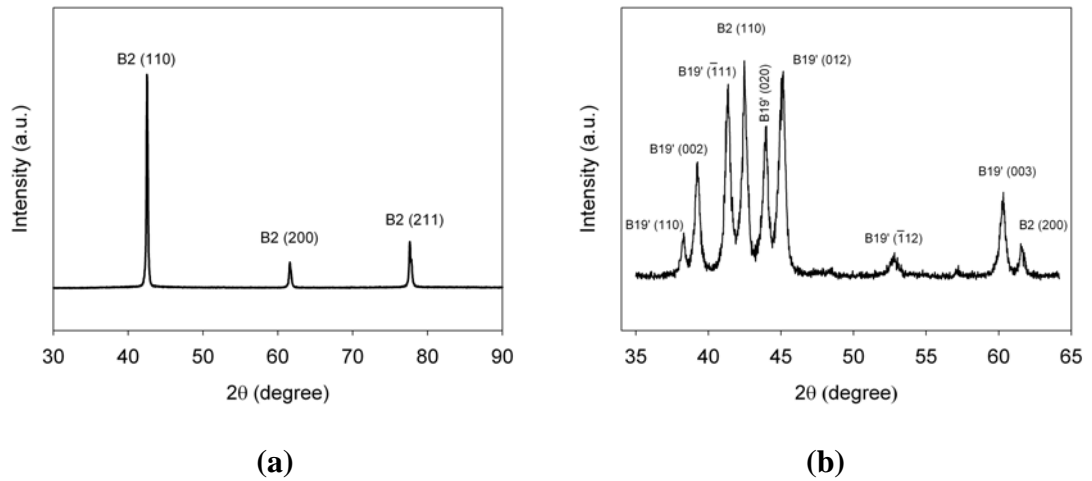
Figure 3.3 XRD patterns of the as-received Ni-rich prealloyed powders at room temperature, (a) Ti-50.6 at. %Ni, (b) Ti-50.4 at. %Ni.

(a)   **(b)**
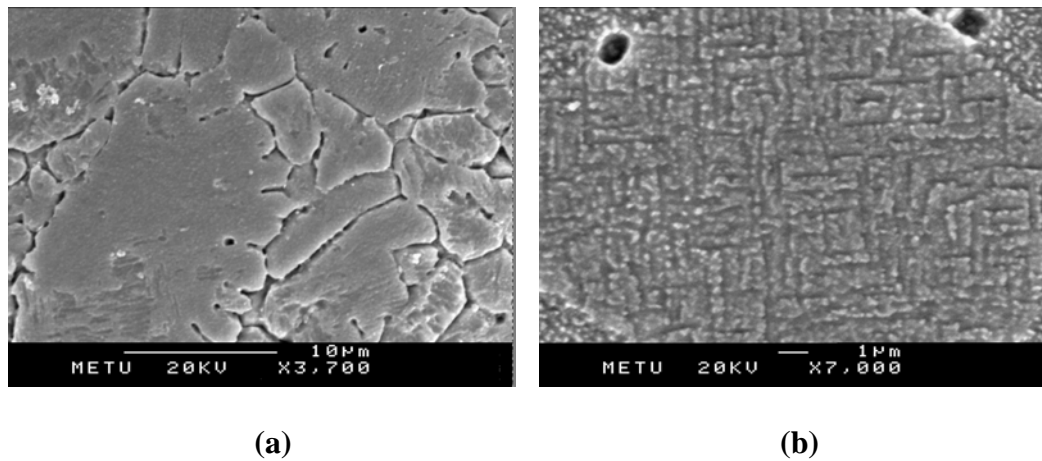
Figure 3.4 Room temperature SEM micrographs showing (a) austenite dendrites in Ti-50.6 at. %Ni, (b) martensite plates present in austenite matrix of Ti-50.4 at. %Ni powder.

Table 3.1 summarizes phase transformation temperatures of the raw powders, measured using DSC. XRD, SEM and DSC results are found to be in agreement.

Table 3.1 Phase transformation temperatures of raw TiNi powders in the as-received condition.

Powder composition	M_s (°C)	M_f (°C)	A_s (°C)	A_f (°C)
Ti-50.6 at. %Ni	10	-53	-11	30
Ti-50.4 at. %Ni	28	10	36	58

3.2. Experimental Method

In the scope of the present study, conventional sintering and space holder technique (SHT), two well known powder metallurgy processing methods, were used to produce TiNi foams. However, several problems occurring frequently in these techniques entailed modifications or improvements. For this reason a recent approach proposed by Esen and Bor [219] for the production of titanium and Ti6Al4V alloy foams is adapted and enhanced for the fabrication of single phase porous TiNi samples with suitable pore characteristics and mechanical properties. This basic, single step sintering method, also known as space holder technique, utilizes pure magnesium spacer particles for pore formation. Mg is found to be so suitable to maintain a protective atmosphere during sintering that it is also used in conventional sintering experiments.

Basically, three criteria were taken into account in choosing magnesium as space holder in TiNi alloy foam production. Firstly, Mg solubility in TiNi is expected to be negligible since magnesium is not soluble in any appreciable amount neither in Ti nor in Ni, so that superelasticity and shape memory properties would not be affected. Secondly, it dissolves in the body and compounds that form are non-toxic in small quantities, and can be removed by the body so that its incomplete removal from the foam does not constitute a drawback for biomedical applications. Finally, it provides a reducing atmosphere that prevents oxidation of TiNi during sintering.

3.2.1. Conventional Sintering

Studies on porous TiNi alloy production by conventional cold compaction and sintering method were conducted only on the Ti-50.6 at. %Ni alloy powder. Prealloyed TiNi powders were blended with 5 wt.% polyvinyl alcohol (PVA) solution (2.5 wt.% PVA ($[-CH_2CHOH]_n$) + distilled water) as the binder prior to compaction. Blended prealloyed TiNi powders were consolidated into compacts 10 mm in diameter and 10 mm in height in a double ended steel die using a hydraulic press at an optimum pressure of 770 MPa determined by preliminary experiments. Lower compaction pressures were found to be sufficient only for consolidation of disc shaped specimens 10 mm in diameter and 3 mm in height. Trials have shown that specimens 10 mm both in diameter and height necessary for compression testing could be produced with reasonable green strength only at pressures around 770 MPa. It has been observed that higher compaction pressures up to 1150 MPa experimented on compression testing samples although gave a better green density, ejection of the compacted samples from the die was much more difficult if not impossible. Various pressures in the range 190-1150 MPa were tested to investigate the effect of compaction pressure on porosity. To reduce the friction between the die wall and the powders and also to ease the ejection of the compacted samples from the die, zinc stearate, $Zn(C_{18}H_{35}O_2)_2$, was used as lubricant. Die wall lubrication instead of powder lubrication was preferred to avoid or minimise the contamination with the lubricant. Mg was added into the crucible as oxygen getter alongside the compacted specimen prior to sintering by an amount of 12 weight % of the TiNi compact. A few specimens were sintered not using Mg but only Ti sponge as getter and few others were sintered without using either Mg or Ti sponge to see the their role in preventing oxidation, secondary intermetallic formation and contamination. Sintering process was conducted at 1100 °C for 1 hour in purified argon atmosphere. However, a few samples were also sintered at 1100 °C for 2, 3 and 5 hours to determine the maximum sintering time during which Mg is still effective in preventing oxidation and to study the effect of sintering time on microstructure and transformation temperatures of TiNi foams produced. Heating and cooling rates

employed were same with the ones used in space holder method as presented in the following section.

3.2.2. Space Holder Method

Space holder technique employed to produce high porosity TiNi foams is shown schematically in Figure 3.5. Prealloyed TiNi powder and Mg powder in various ratios (20%, 30%, 40%, 50%, 60%, 70% and 80% Mg by volume, balance TiNi) were hand mixed using 5 wt.% PVA solution (2.5 wt.% PVA + H_2O) as the binder prior to compaction. PVA solution was necessary for the uniform coating of coarse Mg particles with fine TiNi powders. Mixing time was determined as 30 minutes to assure a homogeneous distribution.
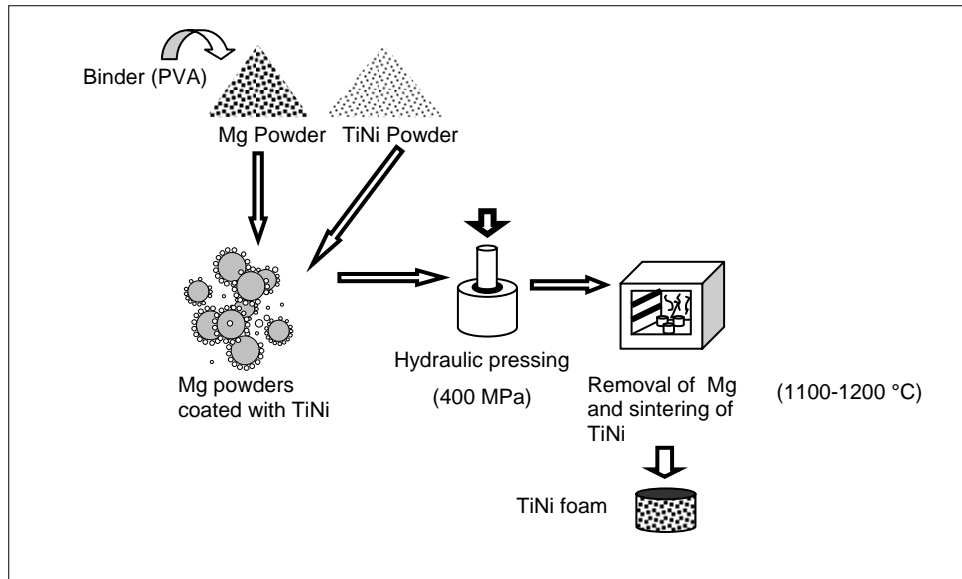
Figure 3.5 Schematic representation of space holder technique.

Then the mixtures were compacted in a double ended steel die, lubricated with a very thin zinc stearate layer, using a hydraulic press at 400 MPa at ambient temperature. Optimum compaction pressure was determined to be 400 MPa. At lower pressures consolidation of the powders was not enough for effective sintering

and fracture or cracks in the compacted specimens occurred frequently. Figure 3.6 shows an example of these cracks observed just after compaction process. At pressures higher than 400 MPa delamination cracks through the diameter of the consolidated samples, as shown in Figure 3.7, have been detected and SEM studies have shown that Mg powders were plastically deformed, especially in 70 and 80% Mg added specimens, as presented in Figure 3.8.

Figure 3.6 Cracks formed in the middle part of the compacted specimen due to inadequate compaction pressure, 260 MPa.

Figure 3.7 Delamination cracks due to excessive pressure applied, 770 MPa, during compaction.
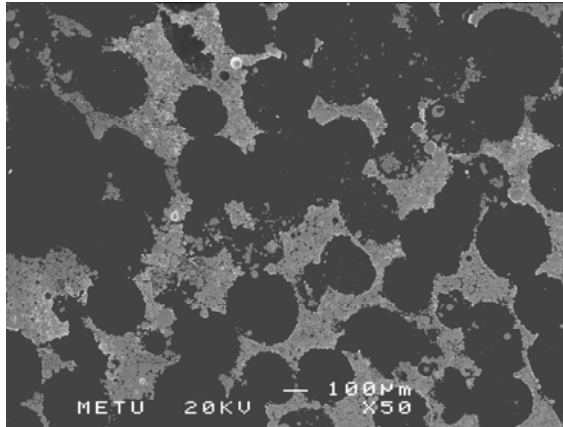
Figure 3.8 Elliptical pores resulting from yielding of Mg powders during compaction step. Compaction pressure: 510 MPa.

Subsequently, compacts 10 mm both in diameter and height were heated to 1100 °C in purified argon atmosphere at a rate of ~10 °C/min, which is low enough to allow debinding of PVA below 650 °C (melting temperature of Mg), and simultaneous Mg evaporation and sintering at higher temperatures. Sintering was carried out at 1100 °C, which is above the boiling point of magnesium, 1090 °C, for 1 and 2 hours and at 1200 °C for 2 hours. Extended sintering times resulted in oxidation of the specimens. Figure 3.9 shows two specimens with the same Mg content sintered at 1100 °C for 2 and 4 hours. Sintering temperatures greater than 1200 °C also led to oxidation of the foams, Figure 3.10.

Figure 3.9 TiNi samples produced from Ti-50.6 at. %Ni powder (40% Mg added) sintered at 1100 °C for 4 (left) and 2 hours (right).

Figure 3.10 TiNi foam sintered at 1100 °C for 0.5 h + 1250 °C for 1 h. Mg content: 60%. Used powder: Ti-50.6 at. %Ni.

1200 °C sintering experiments were carried out in two steps. Firstly, specimens were heated to 1100 °C and held at that temperature for 0.5 h. Then they were heated to 1200 °C and sintered for 2 h. Directly heating to the sintering temperature of 1200 °C could not be employed because of the eutectic reaction at 1118 °C on the Ni rich side of the Ti-Ni binary system. Although the compositions of the prealloyed powders used are not in the eutectic region, due to Ni enrichment of TiNi matrix as a result of oxidation, eutectic melting is observed upon exceeding the eutectic temperature, resulting in collapse of consolidated powder mixture. However, it has been found that holding the compact for 0.5 h at 1100 °C allows Mg to reduce the oxide layer on the TiNi powders and prevent liquid phase formation and collapse of the compacts. Single step sintering by direct heating of samples to 1200 °C can not prevent liquid phase formation due to insufficient time for reduction of surface oxide layers because of kinetical reasons.

In sintering the specimens with less than 50% Mg by volume as space holder, extra magnesium was added into the crucible as oxygen getter raising the total magnesium content of the crucible to 50%. But a few of such specimens were also sintered without extra magnesium addition to see the effect of oxidation on phase transformation temperatures. Figure 3.11 displays slightly oxidized porous TiNi with 30% Mg content sintered at 1100 °C for 1 h without addition of extra Mg. Argon flow rate was kept at a minimum adequate to provide a positive internal pressure inside the furnace to avoid possible leakage of air into the furnace. Pure

titanium sponges with diameter around 3 mm, Figure 3.12, were used as getter just above the specimen but not contacting with it, in order not to form a diffusion couple with TiNi powders which would melt at 984 °C according to Ti-Ni binary phase diagram.

Figure 3.11 Ti-50.6 at. %Ni foam with 30% Mg addition and sintered at 1100 °C for 1 h without addition of extra Mg.

Figure 3.12 Pure Ti sponge particles used as getter during sintering studies.

For the same reason TiNi compact must not be in direct contact also with the Ti or Ti6Al4V crucible, Figure 3.13, used in sintering experiments. Therefore, magnesia (MgO) pellets were placed onto the base of the crucible as a precaution.

Yttria (Y_2O_3) coated aluminum titanate ($Al_2O_3.TiO_2$ or Al_2TiO_5), or zirconia (ZrO_2) and yttria stabilized zirconia pellets may also be used instead of magnesia with the same purpose. It should be recalled that pure aluminum titanate is unstable at the temperatures above 750 °C where the solid solution decomposes into two separate phases, namely Al_2O_3 and TiO_2 that are potential candidates to react with TiNi alloys. Therefore, aluminum titanate doped with MgO and ZrO_2 in order to stabilize the solid solution structure should be preferred as refractory material rather than pure $Al_2O_3.TiO_2$.
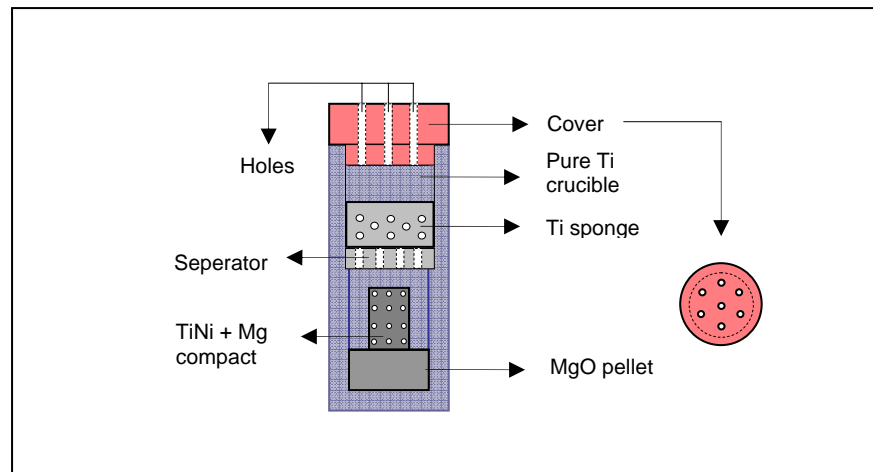
Figure 3.13 Schematic image of crucible used in sintering and aging processes.

Sintered porous specimens were cooled in the cold zone of the furnace at a rate (~60-75 °C/min) sufficient to prevent formation of intermetallics other than TiNi due to possible oxidation problem which may occur during furnace cooling. Some of the specimens were cooled in the hot zone of the vertical furnace (after sintering 2 hours) from 1100 °C to 150 °C lasting around 12 hours. In this case, (Figure 3.14) oxidation was desperate.

Heating, holding and cooling steps during sintering experiments is presented in Figure 3.15. Temperatures were measured using a K-type thermocouple in direct contact with the crucible but not with the sample in it.

(a)   (b)

Figure 3.14 TiNi foam samples cooled in the hot zone of the furnace after having
been sintered for 2 hours at 1100 °C. Samples were produced from (a) Ti-50.4 at.
%Ni, (b) Ti-50.6 at. %Ni powder with addition of 60% Mg.
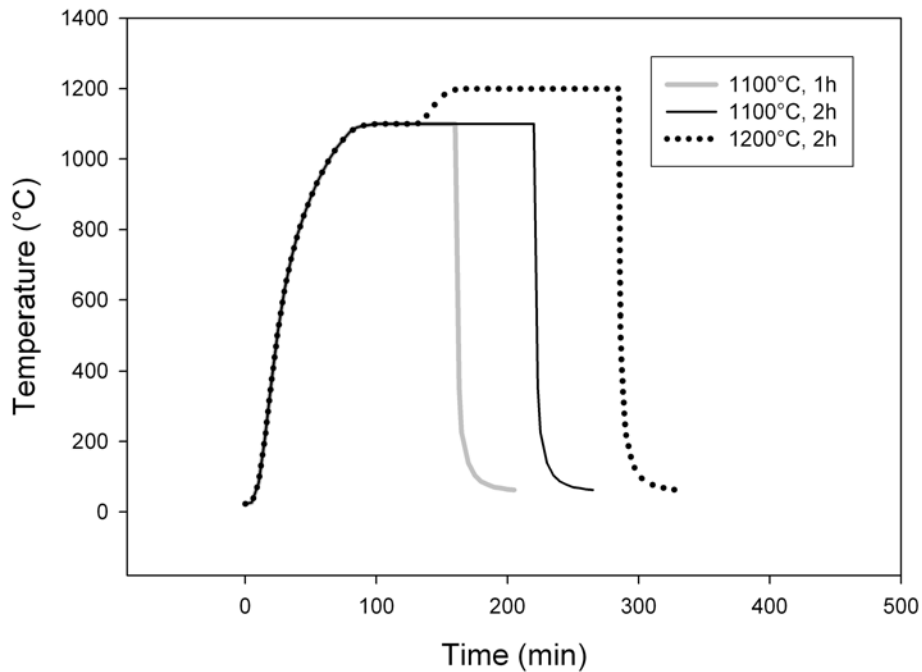
Figure 3.15 Three different sintering procedure used as fabrication method.

Based on the preliminary experiments, TiNi-Mg powder mixtures used, sintering
time and temperatures employed in space holder experiments are shown in Table
3.2.

71

Table 3.2 Composition of TiNi powders, magnesium content and sintering temperature and time used in space holder technique experiments.

Powder Type	Magnesium Content, Vol. (%)							Sintering temperature and time
	20	30	40	50	60	70	80	
Ti-50.6 at. %Ni	√	√	√	√	√	√	√	1100 °C, 1 h
Ti-50.6 at. %Ni	-	-	√	√	√	√	-	1100 °C, 2 h
Ti-50.6 at. %Ni	-	√	√	√	√	-	-	1200 °C, 2 h
Ti-50.4 at. %Ni	-	-	√	√	√	√	-	1100 °C, 2 h

3.3. Heat Treatment

A group of the Ti-50.6 at. %Ni foams produced were subjected to aging treatment at 400 °C for 1 hour under protective argon atmosphere subsequent to the sintering process. Solutionizing prior to aging was not required since preliminary experiments have shown that the sintered samples do not contain secondary phases to be dissolved. Aging temperature and time employed were chosen on the basis of optimizing the superelastic properties considering the literature survey results in bulk TiNi alloys with the same composition. Ti-50.4 at. %Ni foams were not subjected to aging treatment because TiNi alloys with a Ni content lower than 50.5% (atomic) are not suitable for precipitation heat treatment.

To minimise the oxidation during aging, TiNi foams were embedded in Mg powders before processing. TiNi foams held in the cold zone initially were placed into the hot zone of the furnace when it reached to the aging temperature. After aging for 1 h at 400 °C samples were moved again in the cold zone and cooled there for 3 minutes. Then they were removed from the furnace and cooled by spraying alcohol onto them immediately. Total cooling time was less than 4 minutes. Quenching was not performed since it resulted in considerable oxidation.

3.4. Experimental Set-Up

Experimental set-up consisting primarily of a vertical tube furnace used in fabrication of porous TiNi alloys by conventional sintering and space holder technique is displayed in Appendix A. High purity argon gas (99.999% purity, N_2: 8.0 vpm, O_2: 2.8 vpm, humidity: 1.5 vpm) was used to provide a protective atmosphere in the furnace during sintering and aging experiments. Although pure hydrogen gas (H_2) or a mixture of H_2 and Ar gases enables a lower oxygen partial pressure, it was not preferred due to excessive solubility of hydrogen in TiNi alloys.

Oxidation of TiNi is actually a selective oxidation of Ti, because of the large difference in the formation energies of the two oxides (TiO_2: 691.5 and 674 kJ/mol; NiO: 115.2 and 106.8 kJ/mol at 1100 and 1200 °C, respectively). Partial pressure of oxygen must be less than 5×10^{-25} atm at 1100 °C and 10^{-23} atm at 1200 °C to prevent TiO_2 formation at the surface of the TiNi samples according to the calculations based on the thermodynamic data for the oxidation reaction (3.1).
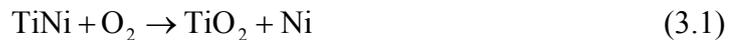
$$TiNi + O_2 \rightarrow TiO_2 + Ni \qquad\qquad (3.1)$$

High purity argon or vacuum which is usually employed as the TiNi sintering atmosphere can decrease the oxygen partial pressure only down to 10^{-8} atm which is still very high and results in severe oxidation.

As a precaution sintering furnace was equipped with a gas-cleaning unit which consists of silica gel or $CaCl_2$ to absorb water vapor in Ar and copper chips at 500 °C to remove the oxygen in the gas. At this temperature the corresponding $Cu-Cu_2O$ equilibrium oxygen pressure is 10^{-16} atm. Temperatures lower than 500 °C would thermodynamically yield lower oxygen potentials but kinetic restrictions prevent attainment of equilibrium at conventional flow rates, resulting in even higher oxygen partial pressures. Higher temperatures, on the other hand, would kinetically favor the oxygen removal but at the expense of a higher equilibrium oxygen partial pressure. Experimentally it was found that 500 °C is the optimum temperature offering a reasonable compromise to purify gaseous streams [228]. Mg, Ti or Si also can be

used instead of Cu with the same purpose but they are not preferred usually due to practical reasons. In fact, much lower oxygen potential is not expectable in a flowing gaseous atmosphere because of the unavoidable leaks in such a system. Cu chips are cheap and easily available and its oxides can be reduced by passing H_2 through it.

Figure 3.16 shows a sample sintered at 1100 °C for 2 hours in flowing argon atmosphere which was purified with the gas-cleaning unit. Severe oxidation at the surface and also at the interior regions is easily recognizable at first glance.

(a)   **(b)**

Figure 3.16 TiNi specimen sintered at 1100 °C for 2 hours in purified inert argon gas atmosphere without using Ti/Mg getters, (a) top view, (b) side view.

Pure Ti used as oxygen getter can theoretically create an extremely low oxygen partial pressure of 10^{-27} and 10^{-24} atm at 1100 and 1200 °C, respectively, and thus can prevent the sample from oxidizing, in despite of kinetical restrictions. On the other hand, at the same temperatures, 1100 and 1200 °C, critical oxygen partial pressure for formation of MgO is 10^{-34} and 10^{-32} atm, respectively. With regard to oxygen affinity, Mg is the second element just after calcium on the Ellingham diagram and it can reduce oxides of titanium effectively.

Oxygen sources during titanium alloy sintering are the gases used as protective atmosphere and surface oxide layers of the elemental or prealloyed powders used as raw material. In the present study, oxygen of the argon gas used as the sintering atmosphere is minimized by use of Ti getters in the form of small sized sponges

while keeping the gas flow rate at minimum. To reduce the surface oxygen of raw powders, on the other hand, it has been observed that Mg is very impressive. Ti alloys are also prone to carburization and nitriding but Ti and Mg, behaving as getters, have cleaned Ar gas from these impurities as well, and also, higher affinity of Mg to hydrogen prevented the possible hydrogenation of TiNi. In summary, sintering of TiNi alloys under protective Mg atmosphere ensures contamination free specimens.

All the processing and aging experiments were conducted in a home-made vertical tube furnace (Appendix A) with a maximum applicable temperature of 1300 °C. A K-type thermocouple placed just below the crucible in direct contact with it to measure the sample temperature. Titanium alloy crucibles were used to hold the compacts during experiments. Alternative crucibles not reacting with Mg and TiNi can also be used.

3.5. Sample Characterization

3.5.1. Particle Size Histograms

Particle size distribution of as-received prealloyed TiNi and sieved Mg powders were determined using Malvern Mastersizer 2000 particle size analyzer with a measurable size range of 0.02 to 2000 μm. The device is capable of low angle Fraunhofer light scattering (forward, side and back scattering) using monochromatic (laser) light and Mie scattering technique, as well as employment of wet and dry methods. Apparatus uses helium-neon laser as a source for red light in size determination of coarser particles up to 2000 μm and solid-state light source to produce blue light (Mie scattering) for finer particle size (below 3 μm) measurements. A short wavelength blue light source is used in conjunction with wide angle (90° with respect to incident light beam) forward and backscatter detection for enhanced sizing performance. Combination of both detectors (Fraunhofer and Mie) expands the dynamic ratio. In the present study, low angle Fraunhofer light scattering method was used for the determination of particle size distribution of Mg powders whereas Mie wide angle scattering was incorporated

into Fraunhofer technique to measure particle size of prealloyed TiNi powders. Wet method in which water used as dispersant was employed for all the measurements.

3.5.2. Density and Porosity Measurements

Green and bulk density, as well as porosity, of the samples produced were measured employing Archimedes' principle in a Sartorius precision balance (model CP2245-OCE) equipped with a density determination kit. Amounts of open and closed porosity were determined by impregnation of extra pure xylene ($C_6H_4(CH_3)_2$) into the samples. Firstly, specimens were weighted dry (W_{dry}) and then immersed in xylene. Immersion duration for complete impregnation of xylene into open pores was 2 hours under vacuum as determined from preliminary experiments. Afterwards xylene impregnated samples suspended in xylene solution were weighted (W_{susp}). Finally, samples were removed from the xylene bath, wiped immediately to remove the excess solution present over the surface and the last weight measurement was carried out in air (W_{sat}).

Bulk density of the samples was calculated as,

$$\rho_{bulk} = \frac{W_{dry} \cdot \rho_{xylene}}{W_{sat} - W_{susp}}$$
(3.2)

where,

ρ_{bulk} : bulk density of the sample,

W_{dry} : dry weight of the sample,

ρ_{xylene} : density of xylene, 0.861 g/cm^3,

W_{sat} : weight of the sample saturated with xylene,

W_{susp} : weight of the xylene impregnated sample suspended in xylene.

Total porosity of the specimens was calculated as,

$$P_{total} = 1 - \frac{\rho_{bulk}}{\rho_{TiNi}} \qquad (3.3)$$

where,

P_{total} : total porosity of the sample,

ρ_{TiNi} : theoretical density of binary TiNi alloy: 6.51 g/cm^3 for Ti-50.6 at. %Ni and 6.49 g/cm^3 for Ti-50.4 at. %Ni.

Open (P_{open}) and closed porosity (P_{closed}) of the specimens were calculated using the equations (3.4) and (3.5), respectively, where V_{sample} represents volume of the sample.

$$P_{open} = \frac{\text{Volume of xylene in pores}}{V_{sample}} = \frac{\dfrac{W_{sat} - W_{dry}}{\rho_{xyelene}}}{\dfrac{W_{sat} - W_{susp}}{\rho_{xylene}}} = \frac{W_{sat} - W_{dry}}{W_{sat} - W_{susp}} \qquad (3.4)$$

$$P_{closed} = P_{total} - P_{open} \qquad (3.5)$$

3.5.3. Pore Size and Porosity Distribution

Basically, two different characterization techniques were used to measure the pore sizes and porosity distribution. Mercury porosimetry was employed for determination of pore size and porosity distribution in green and sintered samples produced by conventional sintering. Poremaster 60 (Quantachrome Corporation) mercury porosimeter used for this purpose was equipped with high (0-60000 psi) and low (0-50 psi) pressure chambers and capable of performing pore size analysis in the range 200 μm to 0.0036 μm pore diameters. On the other hand, for samples produced by space holder method linear quantitative metallographic analysis was employed onto the scanning electron microscope images of metallographically

prepared sample cross sections by use of commercial image analyzer software Clemex Vision.

3.5.4. Microstructure

3.5.4.1. X-Ray Diffraction

Rigaku D/Max 2200/PC model X-Ray Diffractometer with CuKα radiation (λ=1.54178 Å) at 40kV, 40 mA was used within a range of diffraction angles 2θ from 20° to 90° at a scan speed of 2 degree/min to identify the phases present in the as-received and compacted powders and the sintered samples. Ambient temperature during X-ray diffraction (XRD) studies was 22 ± 2 °C.

3.5.4.2. Metallographic Investigations

Specimens chosen for metallographic examinations were infiltrated with epoxy resin to facilitate easy preparation and to reveal the pore shape more accurately. Metallographic preparation of porous TiNi alloys has found to be quiet problematic. Smearing of the removed particles to the surface during grinding step was observed frequently even though the samples were mounted. After polishing to 0.3 μm grit specimens were etched using two different etchants: 10 ml HF + 5 ml HNO_3 + 85 ml H_2O and 10 ml HF +10 ml HNO_3 +80 ml glycerin ($C_3H_5(OH)_3$). The former etchant was suitable for martensitic microstructures whereas the latter was employed to reveal austenite grain structure. These two acid solutions were decided to be best after trying ten different compositions of aqueous solutions of HF and HNO_3. Etching time applied was around 5 minutes.

Microscopic visualization was performed by a Jeol JSM 6400 scanning electron microscope (SEM) equipped with Noran System 6 (X-ray micro analyzer) to reveal the microstructure and pore characteristics.

3.5.5. Thermal Characterizations

To study the thermal behaviour of prealloyed TiNi powders a Setaram Setsys 1750 TG-DTA thermogravimetric differential thermal analysis system was used. Raw powders (25 mg) were heated up to 1200 °C with a rate of 10 °C/min under air and nitrogen (N_2) atmosphere. Phase transformation temperatures of the samples were determined employing differential scanning calorimetry.

3.5.5.1. Differential Scanning Calorimetry Studies

A diamond coated copper disk 100 mm in diameter and 0.2 mm in thickness was employed to cut the DSC samples from the TiNi foams produced. Two different cutting speeds were employed to investigate the effect of deformation during cutting on the transformation temperatures. Slow cutting corresponding to 80 ± 20 rpm was used for all the samples produced while fast cutting at 300 ± 50 rpm was applied to a few samples with different porosity contents to compare the effect of cutting speed.

The transformation temperatures of as-received TiNi alloy powders and the foams produced were measured under nitrogen atmosphere employing a Perkin Elmer Diamond Differential Scanning Calorimeter (DSC) with heating and cooling rates of 10 °C/min through the temperature range of -60 and +150 °C. Indium was used as the reference material. During heating and cooling, the specimens were kept for 2 and 5 minutes at the peak temperatures 150 and -60 °C, respectively, to attain thermal equilibrium. However, during cooling below -40 °C, since a deviation was observed from programmed sample temperatures, phase transformation temperatures measured below -40 °C are not reliable.

Phase transformation temperatures were determined from the second heating and cooling cycle curves applying the procedure described in the ASTM F2004-05 standard [229].

3.5.6. Mechanical Tests

Mechanical tests consisting of uniaxial compression, superelasticity and shape memory (both in compression) experiments were conducted using two screw driven universal tension-compression test machines: A 10 kN capacity Shimadzu ACS-J test system and a 30kN capacity Instron 3367 universal mechanical testing system equipped with a heating chamber.

Samples used in all the tests had a diameter and height of 10 mm. Both surfaces of the compression specimens were mechanically ground to render them parallel. Grease was used to reduce friction between the sample and compression plates and also to prevent or minimise barrelling during uniaxial compression testing.

3.5.6.1. Uniaxial Compression Tests

Uniaxial compression tests at ambient temperature (25 ± 5 °C) were conducted using Shimadzu ACS-J for higher porosity samples and Instron 3367 for lower porosity samples, at crosshead speeds of 0.5 (minimum crosshead speed applicable for Shimadzu) and 0.1 mm/min, respectively. Two different instruments were used for testing to optimize the accuracy of the tests and comparison experiments conducted have shown that the results obtained from these two instruments are consistent. To compensate the possible scattering of the results, at least four specimens were used in characterizing each sample group listed in Table 3.2. Elastic moduli were determined by applying least squares curve fitting to the linear portion of the stress-strain diagram, which has been corrected for mechanical compliance of the testing machine, while yield strengths (corresponding to the initiation of stress-induced martensitic transformations or detwinning of martensite plates) of the sintered samples were determined using the 0.2%-offset method. Elastic modulus results were corrected using the correlation determined by two different calibration samples (pure copper and pure aluminum), since using cross-head displacement for strain measurement was observed not to be accurate enough for Elastic moduli determination.

3.5.6.2. Superelasticity

Samples fabricated from Ti-50.6 at. %Ni powder and suitable for superelastic applications were subjected to superelasticity tests under uniaxial compression in as-processed and 1 hour age hardened at 400 °C conditions using Instron load frame. Superelasticity tests on the 10 mm diameter and 10 mm height cylindirical foam specimens produced, were conducted by cyclic loading in the stress range from 0 MPa upto a predetermined stress value, at room temperature (25 °C), body temperature (37 °C) and at a constant temperature approximately 10-20 °C above A_f of the specimens determined by differential scanning calorimetry measurements. Predetermined upper limit of the load cycle was increased with decreasing porosity of the sample up to a value of 400 MPa.

Strain measurements during superelasticity tests were done with the original extensometer of the apparatus.

3.5.6.3. Shape Memory Behaviour

Shape memory behaviour of TiNi foams produced from Ti-50.4 at. %Ni powder was determined in compression by loading the specimens to a predetermined strain, initially 2%, and then unloading at room temperature (where they are completely martensitic) followed by immersing in boiling water bath (~ 100 °C, which is above the A_f temperature) for 5 minutes for shape recovery. An Instron Testing Machine was used for this purpose and the loading strains applied were measured with the extensometer of the system. Free recovery by shape memory mechanism was quantified by measuring the height of the sample before and after the thermal recovery treatment by immersing into boiling water with a micrometer with an accuracy of 1μm. The sample was then dipped in liquid nitrogen to ensure it was cooled to a temperature lower than its martensite finish temperatures. And the above procedure was repeated subsequently for 4, 6 and 8% predetermined strains using the same specimen. Finally, the sample was subjected to mechanical compression loading until fracture.

CHAPTER 4

RESULTS AND DISCUSSION

4.1. Porous TiNi Produced by Conventional Sintering

SEM images in Figure 4.1 (a) to 4.1 (d) show microstructure of TiNi alloy compacted under 770 MPa and subsequently sintered at 1100 °C for 1 hour under protective argon atmosphere using only pure titanium sponge as getter but without addition of magnesium. Porous titanium or titanium nickel oxide layers covering the surface of the powders are easily distinguishable. Apart from this oxide layer denoted as "a", two other phases, labeled as "b" and "c" in Figure 4.1 (a) were detected. The compositions of these phases determined semi-quantitavely by energy-dispersive X-ray spectrometer (EDX) attached to SEM are listed in Table 4.1. From the surface of the powder to the interior regions, Ti_4Ni_2O, $TiNi_3$, and finally TiNi are the phases present, respectively. Actually, composition of the phase marked as "a" in Table 4.1 corresponds to Ti_2Ni as well as Ti_4Ni_2O, both with an ordered fcc structure of the Fe_3W_3C type and with lattice parameters $a_0 = 1.13193$ nm for the former and $a_0 = 1.13279$ nm for the later [74]. Because of the similarity of the compositions and crystal structures, it is very likely to confuse these two phases during both EDS analysis and X-ray or electron diffraction studies. In the present case, it is identified as Ti_4Ni_2O, because it is commonly observed in TiNi alloys in oxygeneous atmosphere since solid solubility of oxygen in TiNi alloys is extremely small, around 0.045 at.% [99], and TiNi alloys with oxygen content exceeding this limit inevitably contains Ti_4Ni_2O phase. It is clear from Figure 4.1 (a) that prealloyed TiNi powders, completely austenitic prior to sintering, are partly transformed during sintering. Powders with a diameter less than 10 μm have been

found to consist of completely Ti_4Ni_2O and $TiNi_3$ phases after the sintering operation and TiNi phase was observed to vanish fully.
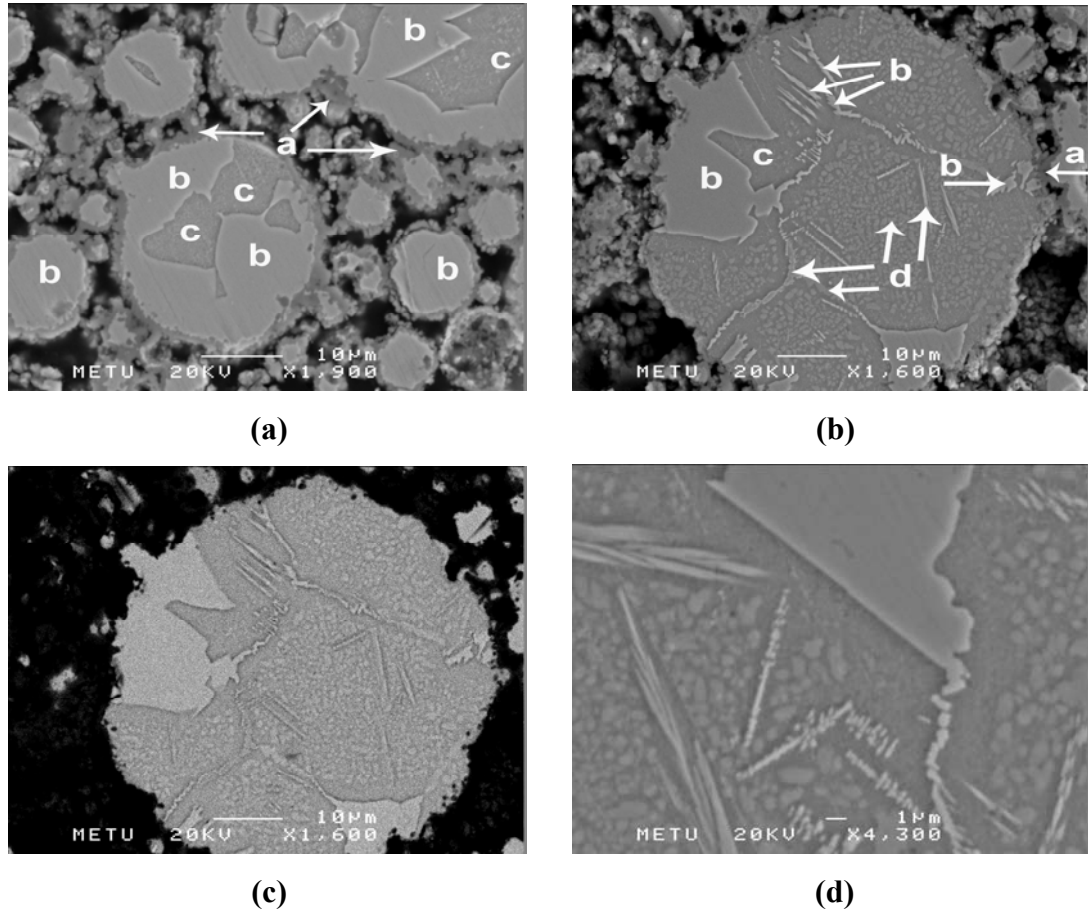
Figure 4.1 SEM micrographs showing microstructure development in porous TiNi compacted under 770 MPa and sintered at 1100 °C for 1 hour without using magnesium getters: (a) general view, (b) secondary electron and (c) backscattered electron images of an individual powder, and (d) morphology of the phases present at higher magnification.

Figure 4.1 (b) shows that TiNi phase, marked as "c" both in Figure 4.1 (a) and (b), actually embraces several phases with different morphologies in it and along its grain boundaries. EDS point analysis results obtained from the dispersed phases marked as "d" are also presented in Table 4.1. They were identified as $TiNi_3$ in XRD studies, despite their Ti and Ni contents appear to correspond to metastable Ti_3Ni_4. Since samples cooled at the cold zone of the furnace at a rate of ~70 °C/min after

sintering, which is similar to air cooling, precipitation of Ti_3Ni_4 phase is not expected as confirmed by XRD studies (Figure 4.2). It was concluded that deeper information depth and insufficient resolution (a few μm) of EDX analysis produced errors in determination of phase compositions.
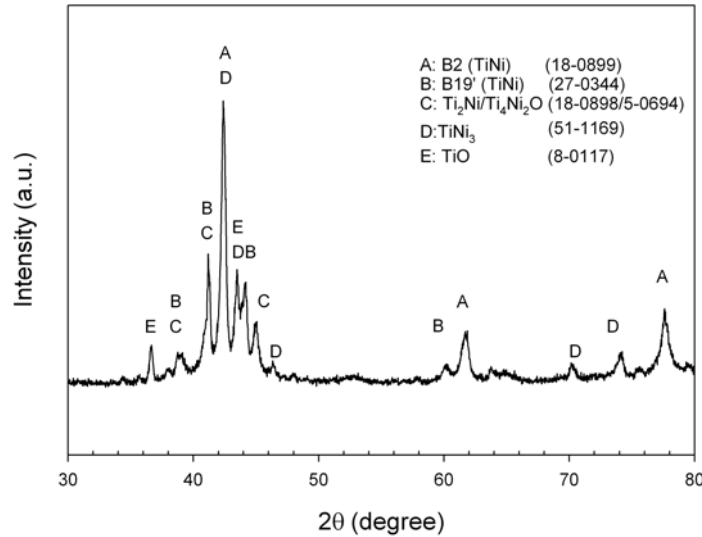
Figure 4.2. XRD pattern of porous TiNi compacted under 770 MPa and sintered at 1100 °C for 1 hour under argon gas atmosphere and using titanium getters. (Numbers in parentheses represent JCPDS card numbers.)

Table 4.1 Chemical compositions (at.%) and phase idendification at different locations in Figure 4.1.

	(a)	(b)	(c)	(d)
Ti	65.6 ± 3	27.9 ± 4	48.8 ± 1	42.5 ± 1
Ni	34.4 ± 3	72.1 ± 4	51.2 ± 1	57.5 ± 1
Phase identified	Ti_4Ni_2O	$TiNi_3$	TiNi	$TiNi_3$

Figure 4.3 (a) and (b) present microstructures developed in TiNi alloys sintered at 1100 °C under protective magnesium vapour atmosphere for 3 and 5 hours, respectively. Sintering process lasting 3 hours resulted in single B2 TiNi phase without any secondary intermetallics present in Ti-Ni binary phase diagram or

contamination products such as oxides, nitrides or carbonitrides. Grain size of TiNi was around 10 μm. Samples produced by sintering for 5 hours at the same temperature, on the other hand, showed secondary intermetallic formation both on the grain boundaries and interior of the grains.

(a)	**(b)**
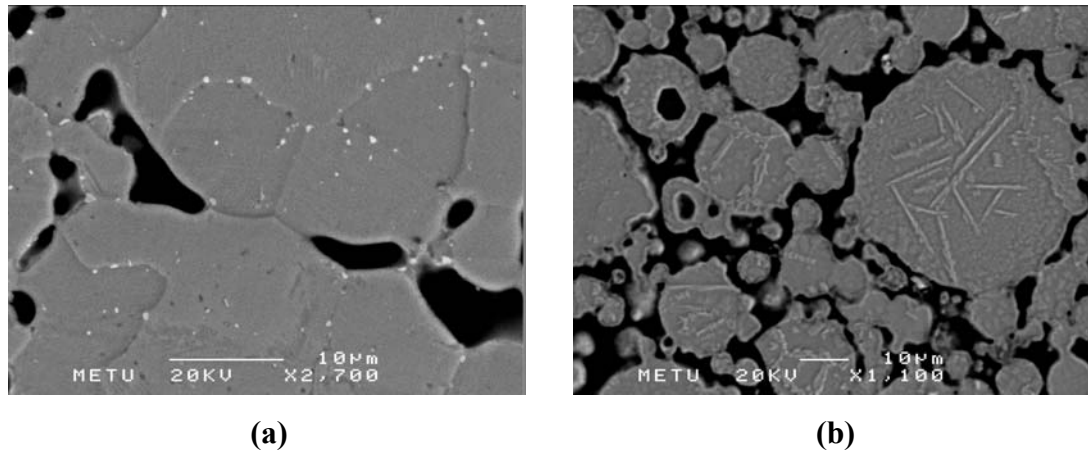
Figure 4.3 SEM micrographs of specimens sintered at 1100 °C for (a) 3 hours, (b) 5 hours under magnesium vapour atmosphere.

The phases labeled "a" and "c" in Figure 4.4 (a) correspond to TiO and TiNi matrix, respectively, as identified from EDX analysis. All the remaining phases (marked as "b") in TiNi matrix with different morphologies and on grain boundaries were determined to be $TiNi_3$ from the backscattered electron image shown in Figure 4.4 (b) and XRD analysis given in Figure 4.5. Contrary to EDX analysis from regions "b", XRD results did not show any Ti_2Ni_3 peak while corresponding peaks of $TiNi_3$ have been noted. Unexpectedly, XRD analysis also showed that there were elemental Ni in the microstructure whereas no Ti_4Ni_2O phase was observed.

Following the 900 °C isothermal section of Ti-Ni-O ternary phase diagram given in Figure 4.6, oxidation sequence in TiNi binary alloys at this temperature can be easily determined. It is clear from the figure that TiNi alloy can dissolve about 4 at.% oxygen and higher concentrations of oxygen results in formation of Ti_4Ni_2O phase. Oxygen amount in commercial TiNi alloys is typically in the range 600-800 ppm (0.06-0.08 at.%) [90] and Ti_4Ni_2O phase has almost always been observed in

their microstructures. Thus, in this study solid solubility of oxygen in TiNi alloys is accepted to be 0.045 at.% which is given in reference [99].

(a) **(b)**
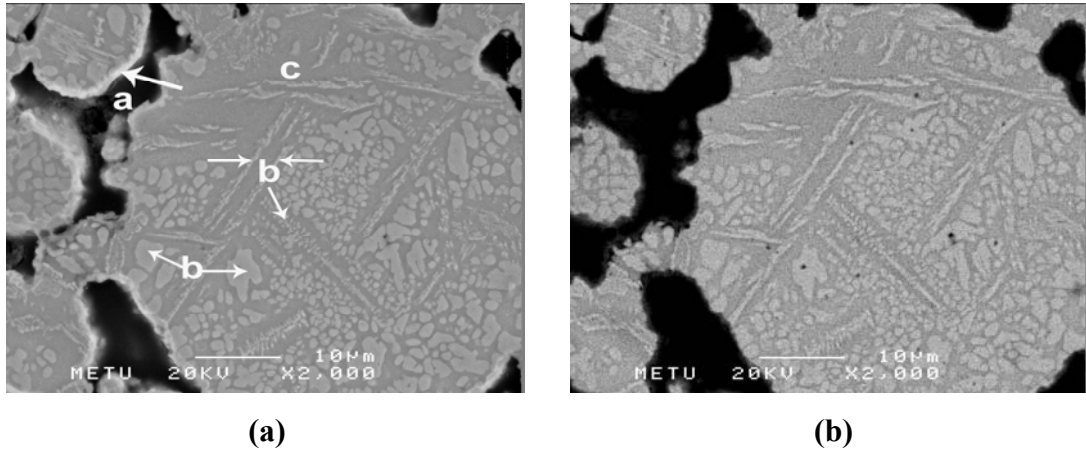
Figure 4.4 Microstructure of porous TiNi sintered at 1100 °C for 5 hours under magnesium vapour atmosphere, (a) secondary electron, (b) backscattered electron imaging.
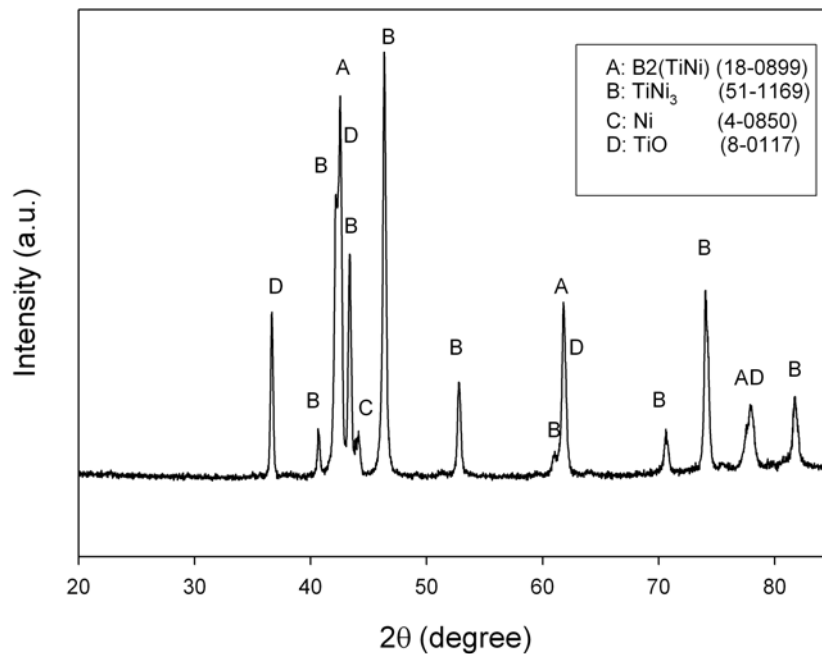
Figure 4.5 XRD pattern of the sample sintered at 1100 °C for 5 hours under magnesium vapour atmosphere. (Numbers in parentheses represent JCPDS card numbers.)

Indeed, Ti_4Ni_2O is not a distinct phase but the Ti_2Ni phase with dissolved oxygen in it. Therefore, it may be more suitable to designate this solid solution phase as $Ti_2Ni(O)_x$ ($0 \leq x \leq 0.5$). Since during its formation Ti atoms are consumed twice as much compared to Ni atoms in the matrix, in presence of oxygen $TiNi_3$ phase appears accompanying the $Ti_2Ni(O)_x$ phase in the Ni enriched matrix. Overall transformation may be given as:

$$TiNi + O_2 \Rightarrow Ti_2Ni(O)_x + TiNi_3 \qquad (4.1)$$
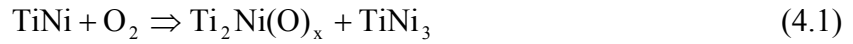
which imply coexistance of these three phases together up to about 8 at.% oxygen. Selective oxidation of $Ti_2Ni(O)_x$ to lower oxides take place by the solid state transformations (4.2) and (4.3)

$$Ti_2Ni(O)_x + O_2 \Rightarrow TiO + Ni \qquad (4.2)$$

$$Ti_2Ni(O)_x + O_2 \Rightarrow Ti_2O_3 + Ni \qquad (4.3)$$
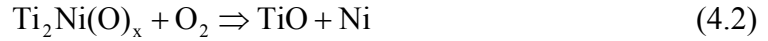
Subsequently, the lower oxides are oxidized to higher ones resulting in a scale formation consisting of TiO_2 and Ni. Further oxidation leads Ni to oxidize and formation of NiO. Finally TiO_2 reacts with NiO and produces $NiTiO_3$ [100]. The type of oxide that forms depends on oxygen potential, i.e., available oxygen amount and its partial pressure, present in the system or in other words severeness of oxidation as well as kinetic paramerters. For example, complete oxidation of TiNi powder in air atmosphere at high temperatures for a sufficient time would lead to formation of $NiTiO_3$, Ni(Ti) and $TiNi_3$ phases from the surface to the interior regions. However, oxidation at lower temperatures or short oxidation times would form TiO_2 or Ti_2O_3 or TiO phase beside $Ti_2Ni(O)_x$, $TiNi_3$ and TiNi. Relative

amounts of all these phases may change, even some of them may completely disappear, depending on the oxidation kinetics and thermodynamic constraints.
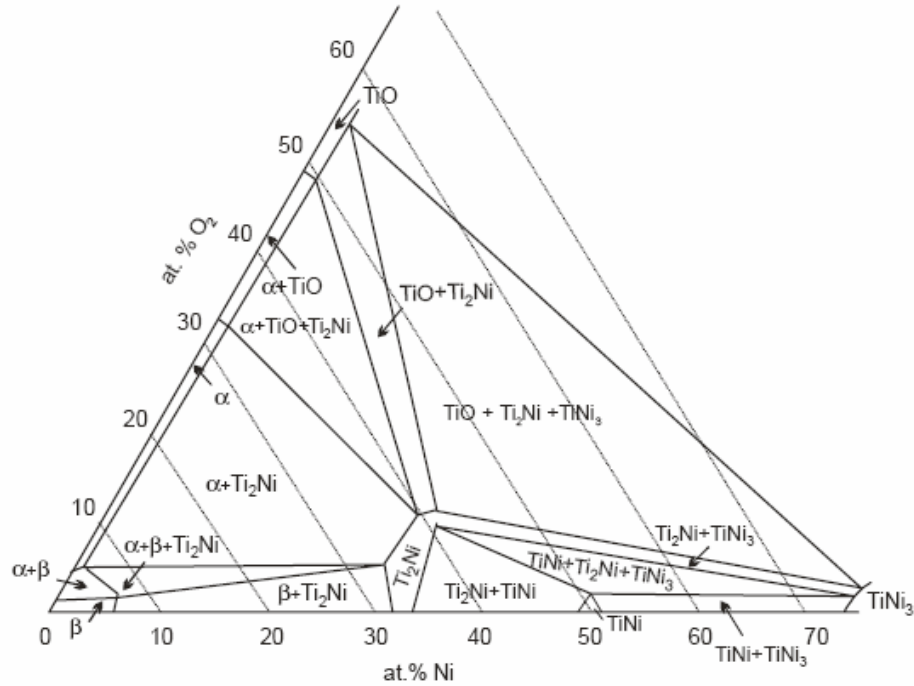
Figure 4.6 900 °C isotermal section for the Ti-Ni-O system [100].

As Chuprina and Shalya [100] stated, $Ti_2Ni(O)_x$ and $TiNi_3$ phase formation occur at the inital stages of reaction between TiNi and oxygen. In case of air atmosphere experiments this stage would be very short and difficult to observe for TiNi powders. Since argon atmosphere cleaned with titanium getters was used in the present study, oxygen potential was low enough to slow down the kinetics for the observation of simultaneous two phase formation, Figure 4.1. When magnesium was also used in addition to titanium getters, sintering up to 3 hours has not resulted in any secondary phase formation. However, sintering experiments for 5 hours resulted in both TiO and $TiNi_3$ secondary phases, Figures 4.3 and 4.5. Pure magnesium starts to melt at 650 °C and its vapour pressure increases with increasing temperature.

TiNi alloy oxidizes up to this temperature starting from 200 °C since solid magnesium is not sufficiently effective in preventing oxidation. Liquid or vapour magnesium, on the other hand, reacts with oxygen harshly through sintering process. When all the magnesium is used up in about 3 hours, oxygen partial pressure (due to the leaks and the oxygen in the argon) increases rapidly and results in oxidation of TiNi and formation of TiNi$_3$ phase.

It is noted from Figure 4.1 that during sintering not only oxygen atoms diffuse into powders but also excess nickel atoms formed as a result of Ti$_2$Ni(O)$_x$ formation diffuse from the surface to the interior regions, proven with marker experiments [230], using easy paths by dislocation and grain boundary diffusion mechanisms. There might be a difficulty in nucleation and subsequent growth of TiNi$_3$ confirmed by its faceted interface formed with TiNi matrix. Thus, it prefers to nucleate heterogeneously on favourable sites present in the matrix. Diffusion of titanium atoms from interiors to the surface, on the other hand, has not been found to be possible. Otherwise, there would be voids in TiNi grains.

Ti$_2$Ni phase can dissolve upto 14 at.% oxygen in it. Thus, after its formation on the surface of the powders, oxidation reaction proceeded by dissolution of free oxygen atoms in Ti$_2$Ni(O)$_x$ phase at the surface. Because of the wide range of solubility of oxygen in Ti$_2$Ni(O)$_x$ and as a result further diffusion of oxygen atoms from the surface towards the interior regions, Ti$_2$Ni(O)$_x$ layer at the surface of the powders was thickened. No Ti$_2$Ni(O)$_x$ was observed in grains or on grain boundaries, Figure 4.1, because all the oxygen that diffuses inwards are consumed at the inner interface of Ti$_2$Ni(O)$_x$ according to reaction 4.1 Further oxidation of TiNi$_3$ (equation 4.4) and Ti$_2$Ni(O)$_x$ phases (equation 4.2) on the other hand, resulted in formation of TiO and Ni as observed from Figure 4.5. Note that huge TiNi$_3$ grains seen in Figure 4.1 were not observed in Figure 4.4 due to more severe oxidation. A great majority of them were vanished producing Ti$_2$Ni(O)$_x$ according to:

$$TiNi_3 + O_2 \Rightarrow Ti_2Ni(O)_x + Ni \qquad (4.4)$$

This phase also disappeared with the progress of oxidation ending up with TiO and Ni formation.

Oxidation of TiNi is actually a selective oxidation of Ti, due to the large difference in the formation energy of the two oxides (TiO$_2$: 691.5 and 674 kJ/mol; NiO: 115.2 and 106.8 kJ/mol at 1100 and 1200 °C, respectively) as given in Table 4.3. Partial pressure of oxygen must be less than 5×10^{-25} atm at 1100 °C and 10^{-23} atm at 1200 °C to prevent TiO$_2$ formation at the surface of the TiNi samples according to the calculations based on the thermodynamics data [231] given in Table 4.2 for the oxidation reaction:

$$TiNi + O_2 \rightarrow TiO_2 + Ni \qquad\qquad (4.5)$$

High purity argon or vacuum which is usually employed as the TiNi sintering atmosphere can decrease the oxygen partial pressure only down to 10^{-6} - 10^{-8} atm, which is still very high and results in severe oxidation. Pure Ti used as getter can theoretically create an extremely low oxygen partial pressure of 10^{-27} and 10^{-24} atm at 1100 and 1200 °C, respectively and thus can prevent the sample from oxidizing. However, this cannot be achieved kinetically in a high vacuum, as it would take a very long time to achieve equilibrium. On the other hand, at the same temperatures, 1100 and 1200 °C, critical oxygen partial pressure for formation of MgO is 10^{-34} and 10^{-32} atm, respectively. With regard to oxygen affinity, Mg is the second element just after calcium on the Ellingham diagram and it can reduce oxides of titanium effectively.

Oxygen sources during titanium alloy sintering are the gases used as protective atmosphere and surface oxide layers of the elemental or prealloyed powders used as raw materials. In the present study, oxygen of the argon gas used as the sintering atmosphere is minimized by use of Ti getters in the form of small sponge particles, while keeping the gas flow rate at minimum. To reduce the surface oxygen of raw powders, on the other hand, it has been observed that Mg is very impressive. TiNi alloys are also prone to carburization and nitriding but Ti and Mg, behaving as getters, have cleaned Ar gas from these impurities as well, and also, higher affinities

of Mg and Ti to hydrogen prevented the possible hydrogenation of TiNi. As a result of these precautions, no secondary phase has been detected in the samples sintered for 3 hours. Thus, safe sintering time has been determined to be 3 hours. Since other foam production techniques such as SHS, HIP, argon sintering or MIM do not use getters, oxidation and/or secondary intermetallic formation are unavoidable. In addition, inhomogeneous blending of Ti and Ni powders in case of employing elemental powders leads to increase in diffusion distances and results in Ti or Ni rich regions. In summary, sintering TiNi alloy powders under protective Mg atmosphere ensures contamination free and chemically homogeneous specimens.

Table 4.2 Formation energies of selected Mg, Ti and Ni compounds at room temperature and sintering temperatures employed. Data were compiled from [231].

Compound	Formation energy, ΔG_f (kJ/mol)		
	1100 ° C	1200 ° C	25 ° C
$MgCO_3$ (Magnesium Carbonate)	-	-	-1012.186
MgH_2 (Magnesium Hydride)	-	-	-36.713
Mg_3N_2 (Trimagnesium Dinitride)	- 157.537	- 107.370	- 400.498
$Mg(NO_3)_2$ (Magnesium Nitrate)	-	-	- 589.182
$MgNi_2$ (Magnesium 2-Nickel)	-	-	- 54.119
MgO (Magnesium Oxide)	- 442.919	- 422.096	- 568.943
$MgOH$ (Magnesium Monohydroxide)	- 182.711	- 173.499	- 172.480
$Mg(OH)_2$ (Magnesium Hydroxide)	-	-	- 833.644
$NiCO_3$ (Nickel Carbonate)	-	-	- 617.876
$Ni(CO)_4$ (Nickel Tetracarbonyl)	- 545.260	- 541.551	- 587.249
NiO (Nickel Oxide)	- 115.193	- 106.753	- 211.539
$NiTiO_3$ (Nickel Titanium Trioxide)	- 816.664	- 789.789	- 1118.188
$TiNi$ (Titanium Nickel)	- 52.636	- 51.019	- 65.546
Ti_2Ni (2-Titanium Nickel)	-	-	- 78.034
$TiNi_3$ (Titanium 3-Nickel))	- 106.497	- 103.215	- 134.204
TiC (Titanium Monocarbide)	- 167.788	- 166.292	- 180.844
TiN (Titanium Mononitride)	- 205.779	- 196.429	- 309.155
TiO (Titanium Monoxide)	- 409.957	- 401.244	- 513.278
TiO_2 (Titanium Dioxide, Rutile)	- 691.634	- 673.947	- 889.406
Ti_2O_3 (Dititanium Trioxide)	- 1138.082	- 1112.637	- 1433.824
Ti_3O_5 (Trititanium Pentoxide)	- 1843.391	- 1801.840	- 2317.294
Ti_4O_7 (Tetratitanium Heptaoxide)	- 2539.272	- 2479.914	- 3213.016
TiH_2 (Titanium Dihydride)	50.036	64.148	- 105.073

4.1.1. Porosity and Pore Characteristics of Porous TiNi SMAs

Effect of compaction pressure on green density and porosity is shown in Figure 4.7. Tap density of initial prealloyed TiNi powders has been measured to be 4.195 g/cm^3 and corresponding porosity was 34.96%. Application of pressure resulted in increase in density while decrease in porosity as expected and maximum green density attained was 5.07 g/cm^3 corresponding to a porosity level of 22% after compaction at the maximum stress of 1150 MPa.
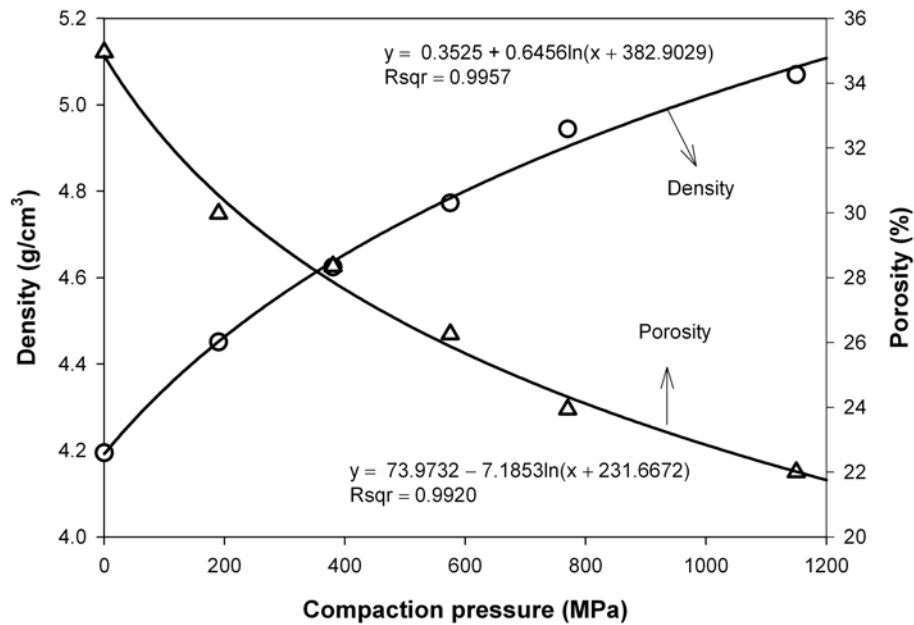
Figure 4.7 Density and porosity of compacts under different compaction pressures.

It is clear from Figure 4.7 that compaction behaviour of TiNi powders is similar to those of other prealloyed powders. Compaction operation starts with rearrangement of the powders. Interparticle friction between powders dominates at this step and is controlled by the surface area, surface chemistry and surface morphology or surface roughness of the powders. Since TiNi powders used in the present study were so fine (20μm in average) that their surface area was extremely large. Larger surface area means higher interparticle friction and lower packing and

also inadequate rearrangement. Subsequent to initial rearrangement of powders localized deformation occurs at powder contacts as pressure is applied. Increasing the pressure results in an increase in the relative volume of each particle undergoing plastic deformation. Further increase in pressure causes elimination of more pores and creation of new contacts, finally homogeneous deformation of whole compact. Work hardening inevitably comes along with plastic deformation and higher density levels require higher external energy. Compressibility of TiNi powders has been found to be lower than that of conventional powders, and getting a durable, crack free compact was also much more difficult due to the superelasticity during compaction. Austenitic TiNi powders subjected to consolidation process (where deformation is first by stress-induced martensite formation up to 7% strain and then by dislocations) regained their shape, at least partially, due to superelasticity as can be seen from Figure 4.8.

Figure 4.8 XRD pattern of green TiNi compacts obtained at different pressures. For clarity peak positions are relatively shifted 10° to the right.

At lower compaction pressures all martensites formed during compaction step transformed into austenite with release of load. On the contrary higher compaction

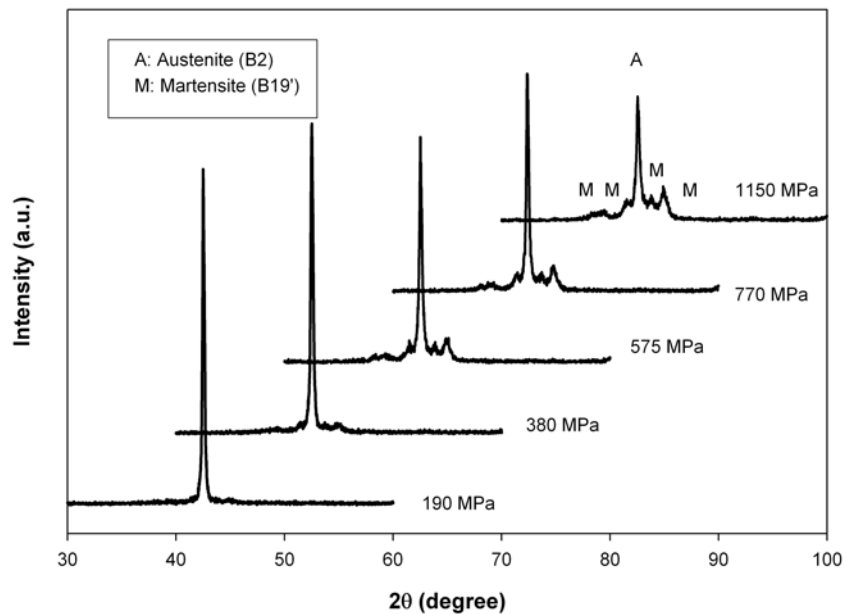pressures such as 575 MPa led to stabilisation of stress-induced martensites by introducing dislocations. Dislocations prevent movement of mobile austenite/martensite interfaces and as a result shape recovery deteriorates. This undesired phenomenon of martensite stabilization under normal circumstances turns into a required condition for compaction of superelastic TiNi alloy powders. Otherwise, sound green samples with lower porosity and sufficient green strength could not be produced. Thus, lower compaction pressures (< 575 MPa) would not be sufficient to produce crack-free compacts. Compaction pressure was observed not to be a critical parameter in the production of samples 10 mm in diameter and 3 mm in height. However, specimens 10 mm both in diameter and height for compression testing were producable only using a pressure around 770 MPa among the ones tried in this study. 1150 MPa although gave a better green density, ejection of compacted samples from the die was much more difficult, even when a lubricant such as zinc stearate was used. Both springback and superelasticity mechanisms obstruct easy ejection. Since the springback effect increases with approximately the square of the compaction pressure [232], it might be the dominating mechanism.

Powder shape, size and distribution effect the interparticle friction, packing density and pore size. Powders with a smaller particle size are more difficult to press. Log-normal particle size distribution leads to lower green densities. Instead, bimodal particle size distribution guarantees a better densification. Spherical powders are pressed more difficultly than irregular powders. Therefore, spherical, fine powders used in the present study also effect density negatively, but it was not of much concern since the aim of the present study was not to produce TiNi shape memory alloy with minimum porosity. However, durable compacts in a broad porosity range would be better. Nevertheless, adjustment of powder size, shape and distribution allows a limited control on final porosity and mechanical properties.

Figure 4.9 presents the effect of compaction pressure on final (sintered) density and porosity contents. Upon sintering a decrease in the range of 3.7-0.8% was observed in the porosity content of the compacts. Sintering shrinkage was lower than 2% in diameter for all the samples produced while up to 2% swelling was observed in height. Actually, the swelling observed in height results from strain recovery of TiNi compacts by shape memory mechanism during heating rather than

the conventional swelling that occurs frequently in elemental powder sintering of TiNi alloys.
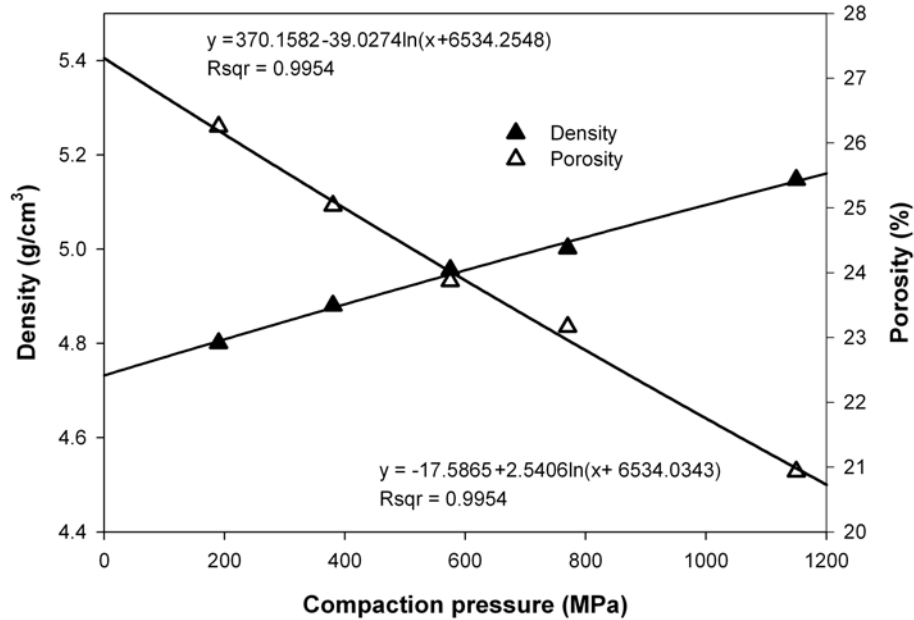
Figure 4.9 Density and porosity of porous TiNi alloys after sintering (1100 °C, 1 h) consolidated previously at different compaction pressures.

Porosity distribution of sintered TiNi alloys compacted at different pressures is presented in Figure 4.10. It can be seen that pore size decreases with increasing compaction pressure. Mean pore size corresponding to 50% cumulative was found to decrease from 65 μm for the lowest pressure applied, 190 MPa, to ~ 4 μm for the highest pressure of 1150 MPa. Largest pore size observed was around 200 μm. Biomedical applications require pore sizes in the range of 100-600 μm for bone tissue ingrowth [56]. Therefore, porosity content with pore size larger than 100 μm is an important parameter. Compaction pressure of 190 MPa provided 40% of the total porosity to be larger than 100 μm. This ratio decreased to 20% for 380 and 575 MPa while it was around only 5-6% for higher pressures applied. However, such large pore sizes (e.g. 100 μm and higher) has never been observed in SEM analysis, Figure 4.11, probably because these were interconnected pores which can not be sampled in polished specimens.
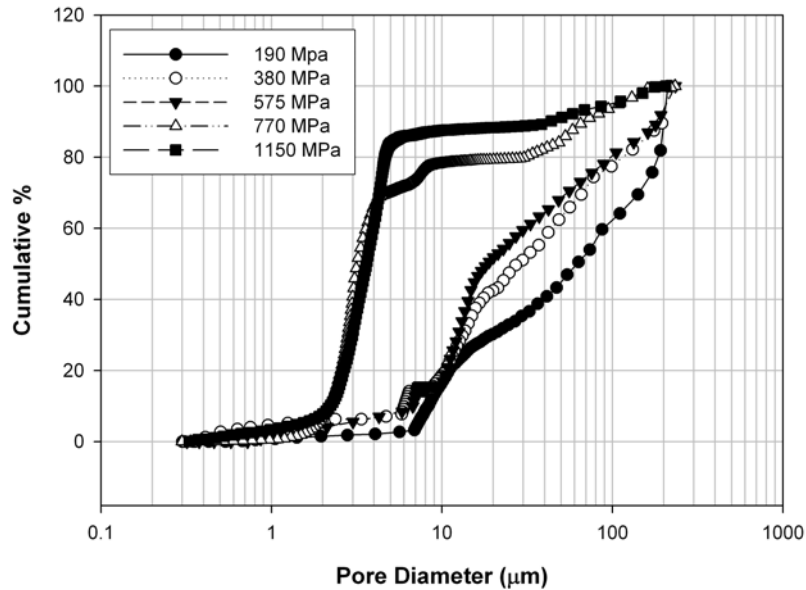
Figure 4.10 Porosity distribution in sintered (1100 °C, 1 h) porous TiNi alloys as a function of compaction pressure.

It is apparent from Figure 4.11 that pore shape in porous TiNi alloys produced by conventional sintering is irregular. In general, pores in a porous material or in a foam can be classified as open pores which are connected to the external surface of porous sample and closed pores (also defined as isolated pores) which are not connected to the external surface of the material. Almost all the pores resulting from incomplete sintering in conventionally sintered samples were interconnected and open type. Some isolated or closed pores have also been observed during SEM investigations as clearly seen in Figure 4.11. Majority of these pores were located at the interior regions of powders. It is highly probable that isolated pores in the powders were formed during atomization process. Incomplete densification of cell walls maybe also created some closed finer pores contributing to general closed porosity.

Open pore ratio, i.e., ratio of open porosity to total porosity in percentage, for conventionally cold compacted at different pressures and sintered porous TiNi samples was greater than 90%. Since the open pore ratio was quite high, it was difficult to distinguish the pore geometry and size metallographically using the

image analyzer. Moreover, to obtain a reasonable and accurate pore size distribution, image analysis method was found to be not appropriate due to irregular pore shapes and high connectivity.
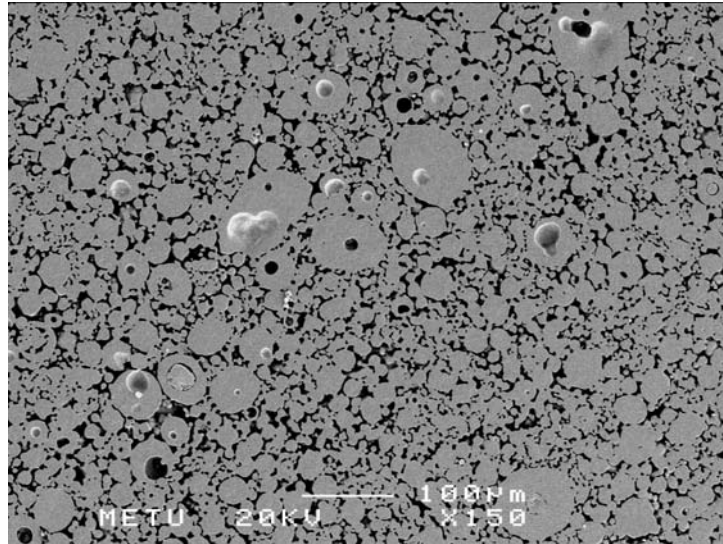
Figure 4.11 SEM micrograph of sintered (1100 °C, 1 h) 23% porous TiNi alloy. (compaction pressure: 770 MPa)

It should be noted that general porosity (i.e. total porosity), open pore ratio and pore size are very important factors for biomedical applications, especially for bone implantation. Because a sufficient porosity with a high open pore ratio allows natural bone regrowth to occur until complete intimate contact has been achieved between the bones and the porous implants. Pores should be interconnected giving a minimum open porosity of 30% for bone ingrowth and body fluid transportation while porosity should be in the range of 30-90% [135]. Pore size requirement, as mentioned before, is 100-600 μm. Porous TiNi alloys fabricated by classical cold compaction and sintering method, with porosities in the range 21 to 26% (which are lower than the required 30%) and average pore sizes are in the range of 4-65 μm are not suitable for artificial bone implants. On the other hand, they are appropriate for filtering applications due to their higly interconnected pore structures which provide excellent permeability.

4.1.2. Macro and Microstructure

SEM image given in Figure 4.12 displays the macro view of porous TiNi alloy in the as-sintered condition. It has been recognized that magnesium powders directly touching to the consolidated TiNi surface initially, got stuck there during sintering upon reacting with oxygen in the medium forming magnesium oxide particles a few μm (up to 5 μm) in size, Figure 4.13. In contrast, the surface regions not in direct contact with magnesium powder initially were found to be free of magnesium or magnesium oxide after sintering.
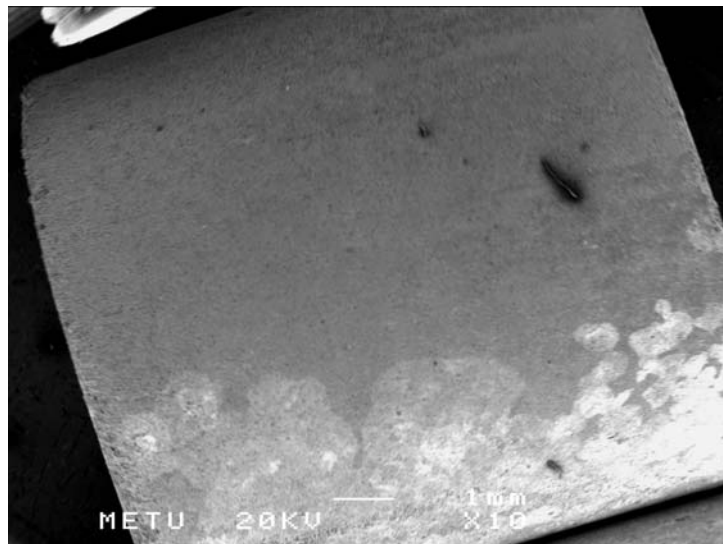
Figure 4.12 SEM picture showing residual MgO layer coated onto porous TiNi alloy during sintering (1100 °C, 1 h) operation.

Magnesium melts at 650 °C and its vapor pressure starts to increase drastically in liquid state with increasing temperature as pointed out previously. Temperature rise also accelerates the magnesium oxidation reaction. Liquid magnesium wets TiNi compact surface and reduces oxide of TiNi powders while reacting with residual oxygen of the furnace atmosphere in the crucible. As a result, magnesium oxide particles form on the surface of porous TiNi intensely but solely on the regions in direct contact with magnesium powders before sintering. It has also been

observed that liquid magnesium erodes TiNi compact surface in some degree which is clearly noticeable in Figure 4.13.
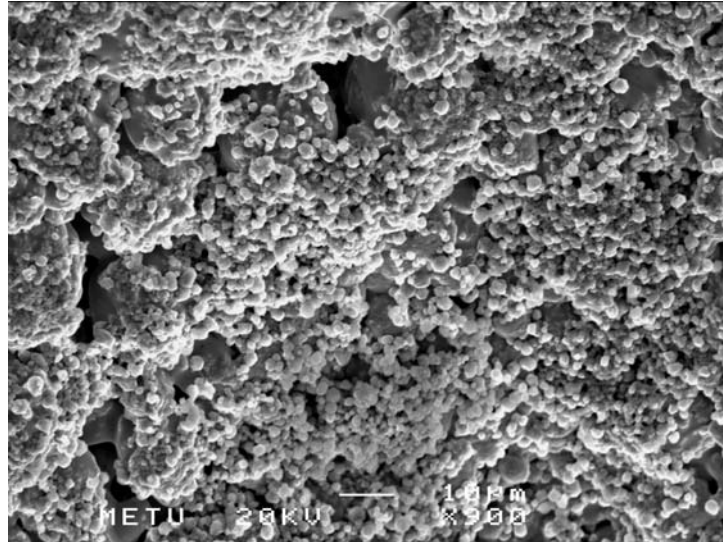
Figure 4.13 SEM micrograph indicating residual MgO particles on sintered (1100 °C, 1 h) TiNi powders.

Figure 4.14 shows the SEM micrograph taken at a higher magnification from the clean surface (not contacted by magnesium powders initially) of sintered porous TiNi. Areal EDX analysis in this region indicate only 2.3 weight % residual magnesium. Residual magnesium oxide particles, shown with black arrows in Figure 4.14, present on the powders or sintering necks were smaller than 2.5 μm. Also, any sign of erosion is not observed because these surface regions were subjected to merely vaporized magnesium. Interior regions of the porous TiNi alloys produced were completely free of magnesium and magnesium oxide particles.

In order to prevent erosion of TiNi compact by liquid magnesium and minimise residual MgO particles over the surface, magnesium powders were placed into the space formed between MgO pellets with a longer height and the crucible before sintering. Hereby, it was guaranteed that any part of the compact was not in contact with magnesium powders. This design allowed the production of porous TiNi alloys with minimised residual magnesium oxide particles. Figure 4.15 presents the sample

processed using improved design. There were not any MgO particles visible with naked eye or stereo microscope all over the sample surface.
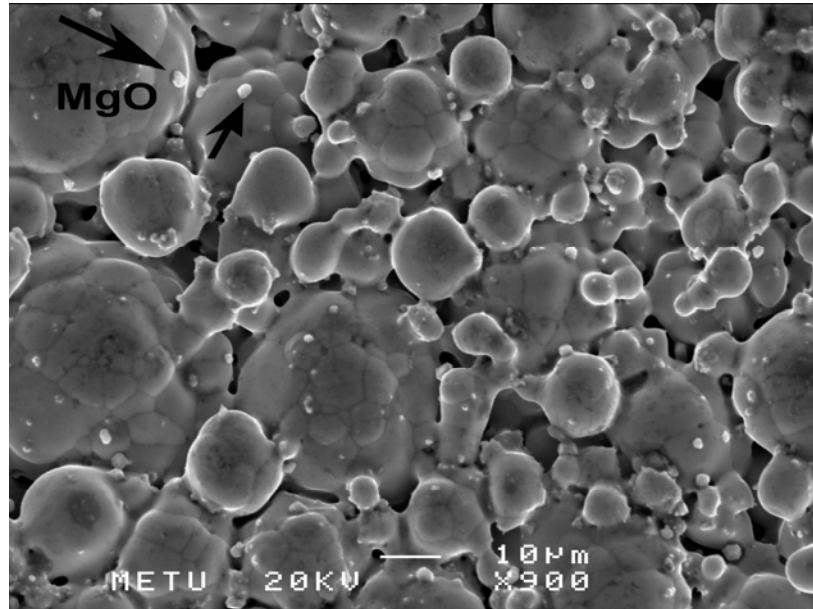
Figure 4.14 SEM image showing MgO particles condensated onto sintered (1100 °C, 1 h) TiNi powders.

Figure 4.15 Macrograph of sintered (1100 °C, 1 h) TiNi compact without residual MgO.

XRD patterns of as-sintered (1100 °C, 1 h) porous TiNi SMAs previously compacted at various pressures are shown in Figure 4.16. Neither undesired secondary Ti-Ni intermetallics nor contamination compounds such as oxides and carbides or carbonitrides of titanium and magnesium were detected. Single B2 austenite TiNi was the only phase present in all the samples.
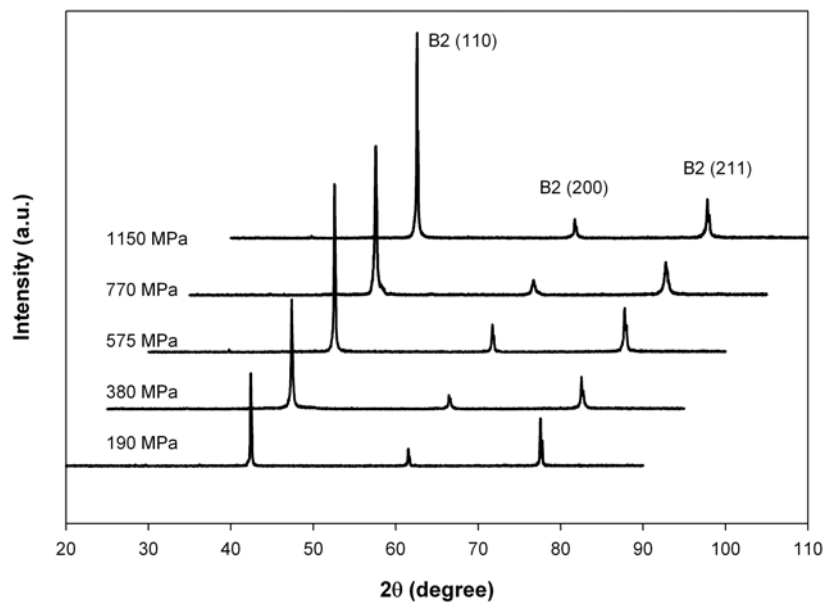
Figure 4.16 XRD spectra of sintered (1100 °C, 1 h) porous TiNi alloys. For clarity peak positions are shifted 5° to the right beyond 190 MPa.

SEM micrograph displayed in Figure 4.17 also confirms retention of single B2 austenite phase after sintering operation. Figure 4.17 also shows boundaries of grains formed in austenitic TiNi with a size around 5-15 μm. It is clear that, only initial stage of sintering is achieved during processing. Individual powders are easily distinguishable from each other and large curvatures are quite explicit. Both neck size ratio (< 0.3) and shrinkage (solely in diameter, 1.4%) were small and the grain size was found no larger than the initial particle size, 20 μm.

As a result of aging treatment at 400 °C for 1 hour, Ti_3Ni_4 precipitates formed in austenite TiNi matrix of porous TiNi alloys as could be seen from the XRD pattern given in Figure 4.18. Since this heat treatment is expected to produce coherent

precipitates, which are a few tens of nm in size [6], they have not been observed under SEM.
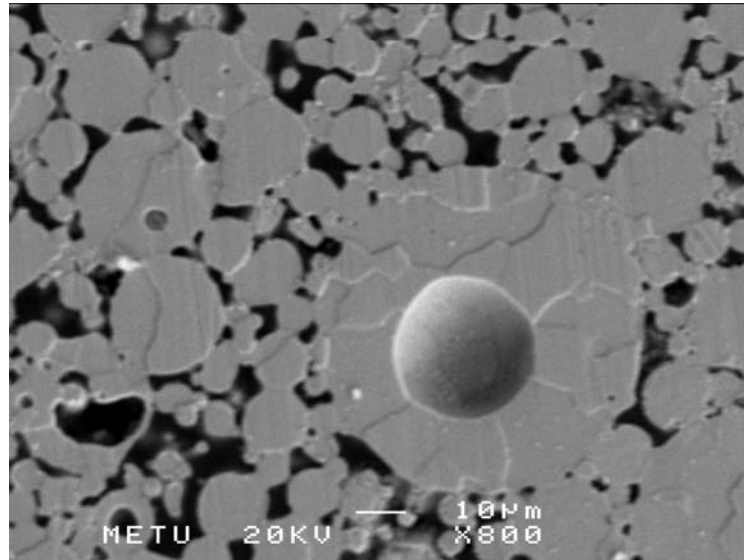
Figure 4.17 Microstructure of porous TiNi sintered at 1100 °C for 1 h and with a porosity of 23% showing austenite grain boundaries.
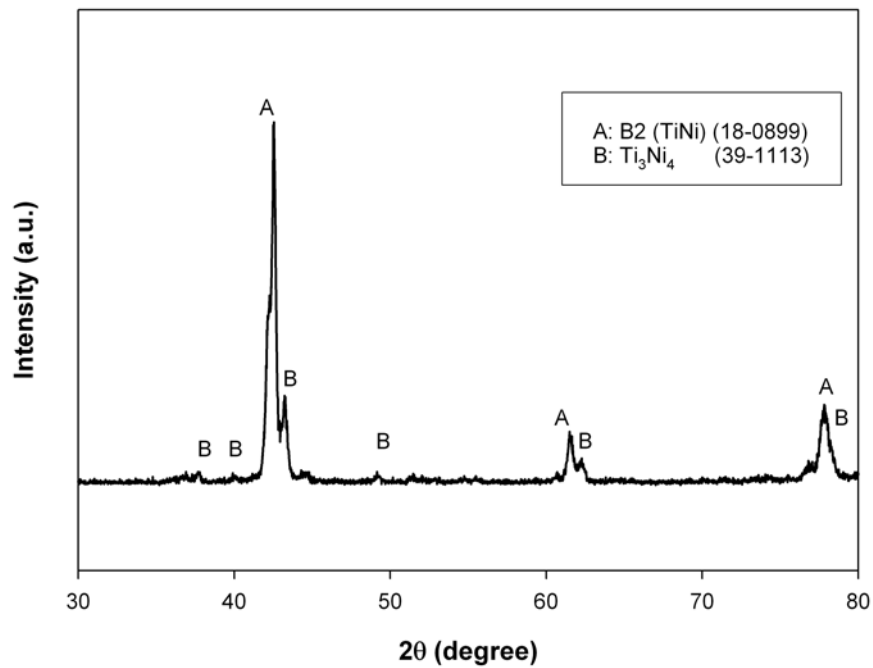
Figure 4.18 XRD pattern of aged porous TiNi at 400 °C for 1 hour. (Numbers in parentheses represent JCPDS card numbers.)

4.1.3. Phase Transformation Behavior in Porous TiNi Alloys

Figure 4.19 represents the typical DSC curves of raw powder used, porous TiNi sintered at 1100 °C for 1 hour and porous TiNi aged at 400 °C for 1 hour after sintering at the same conditions. Prealloyed TiNi powders show broad austenite and martensite peaks during heating and cooling, and as a result M_s, M_p, M_f, and A_s temperatures could not be determined precisely. This may arise from the compositional inhomogenities of the powders formed during atomization process. It is well known that Ni content plays an important role in phase transformation temperatures and local regions with varying Ni content in the powders will transform at different temperatures which will result in a broad transformation peak. The second peak observed in the cooling curve can not be attributed to R-phase since Ti_3Ni_4 precipitate phase that asist R-phase formation is not present (as confirmed by XRD). Probably, this second peak also originates from local deviations in Ni content. As-sintered porous TiNi alloy, on the other hand, exhibited single distinct peak during both heating and cooling as a result of compositional homogenization during sintering. Transformation temperatures of as-sintered porous TiNi were slightly higher than those of the raw powder as it can be seen in Table 4.3. Aging treatment caused an additional increase in phase transformation temperatures; A_s and A_f temperatures were found to be 21 and 65 °C, respectively whereas M_s and M_f were measured as 62 and 24 °C, respectively. The areas under the martensite and austenite peaks (i.e., latent heat of forward and reverse transformations) were only 4.5 and 7.1 J/g, respectively. It was reported in a previous study that a melt cast TiNi alloy of the same Ni content (50.6 at.%) had a forward transformation latent heat of around 25 J/g [233]. This suggests that non-transforming phases, e.g., Ti_3Ni_4, are present in the sample. It is peculiar that although the M_f temperature was 24 °C and XRD studies were carried out around 25 °C, XRD spectrum (Figure 4.18) of aged specimens did not display any B19' martensite phase peak which is expected be observed at room temperature beside Ti_3Ni_4 precipitates. This discrepancy has also been found in aged foams produced by space holder technique and possible reasons have been discussed in detail in related chapter.
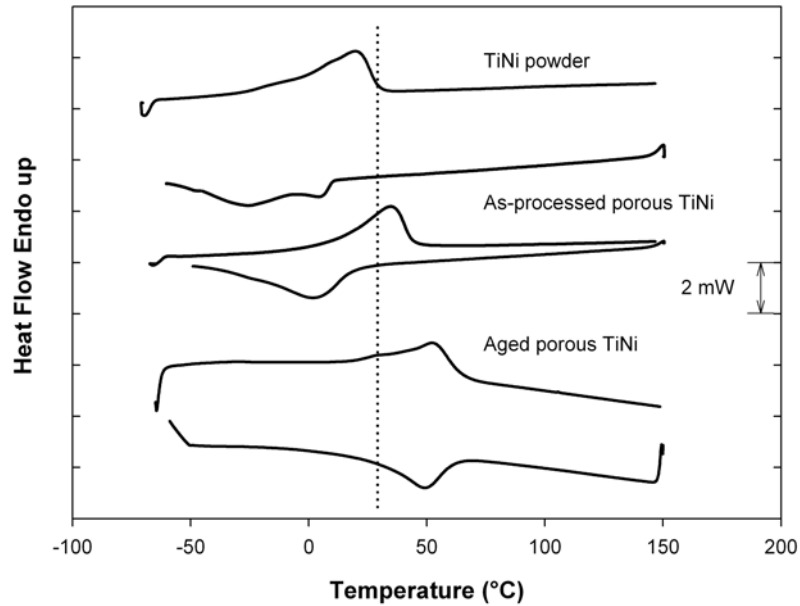
Figure 4.19 DSC curves of TiNi powder, as-sintered porous TiNi (1100 °C, 1 h) and subsequently aged porous TiNi, 400 °C, 1 h (porosity 23%).

Table 4.3 Phase transformation temperatures and related latent heats of transformations of porous TiNi samples sintered at 1100 °C for different times.

Sintering time (h)	Phase transformation temperatures (°C)						Latent heat of transformations (ΔH, J/g)	
	M_s	M_p	M_f	A_s	A_p	A_f	$-\Delta H_{forw}$	ΔH_{rev}
Powder	10	-25	-53	-11	20	30	14.4	13.8
1	16	4	-39	8	35	41	18.0	17.0
2	8	-3	-43	-4	25	37	10.1	11.8
3	2	-25	-47	-36	-4	20	8.3	7.9
5	-	-	-	81	82	85	-	0.7

It is clear from Table 4.3 that extended sintering reduces martensitic transformation temperatures and this is most probably due to oxidation. An increase of 1% in oxygen content results in a 100 °C decrease in transformation temperatures [99]. Oxidation also reduces the latent heat of transformations. The sample sintered for 3 hours exhibited the lowest transformation energy as 7.9 J/g during reverse transformation. Sample sintered for 5 hours, on the other hand, displayed quite

higher transformation temperatures during reverse transformation. For example, A_f temperature was measured to be 85 °C. However martensitic transformation has not been observed during cooling. In fact, reverse transformation was also negligible as can be understood from its considerably low latent heat, 0.7 J/g. Secondary Ti-rich phases formed as a result of oxidation cause the phase transformation temperatures reduce down because of the increased nickel content of the TiNi matrix. Ni-rich phases on the other hand, increases the phase transformation temperatures leading to a decrease in nickel content of TiNi. Intermetallics other than TiNi, such as Ti_2Ni or $TiNi_3$ do not undergo martensitic transformation. Therefore, decrease in TiNi amount appears in DSC charts as lower transformation heats. Nickel content of the TiNi matrix is the main parameter controlling the transformation temperatures. Since final Ni content of TiNi phase (measured using EDS) after 5 hours sintering (49.99 ± 0.25 at.%) was smaller than those of lower sintering times (50.73 ± 0.34 at.%), transformation temperatures were higher. Sample sintered without using magnesium getters, on the other hand, did not show any transformation. Nickel content of its matrix was 51.64±0.44 at.% meaning that transformations, if there were, would be at very low temperatures, which are out of the measurement capacity of DSC equipment used in the present study.

4.1.4. Mechanical and Superelastic Properties

Compression stress-strain curves of as-processed, as-quenched and aged porous TiNi alloys with a porosity content of 23% are presented in Figure 4.20. As-quenched one displayed the highest strength due to severe oxidation occuring during rapid cooling from 1100 °C to room temperature using water at ambient temperature as cooling medium. Oxidation might also trigger lower martensitic transformation temperatures. Since all the mechanical tests were carried out at the same temperature, room temperature, sample with the lowest transformation temperatures would be the strongest. Mechanical properties of the aged sample was in between that of the as-processed and as-quenched samples.

Table 4.4 lists the elastic moduli, critical stress required for inducing martensite and compressive strength values quantitatively obtained from the stress-strain

diagram. It is clear that, while strength improves and unrecovered strains decrease with cycling, specially after the first one, elastic moduli values stay almost at the same level. It is also noted that, unloading elastic moduli were not very different from the ones calculated from the loading curves. Another observation was linear superelasticity behaviour after cycling process. All the three samples in different conditions showed incomplete strain recovery in the first cycle. Irrecoverable strains were 1.16% for as-guenched sample and 1.46% for aged one whereas 1.7% for as-processed sample. The existence of nonrecoverable strain is owing to two reasons: one is that their A_f temperatures are higher than room temperature and the other is that the irregular shape of the pores easily causes stress concentration, which results in irrecoverable deformation. Reasons of these results and observations have been eloborated in Section 4.4 of this chapter.
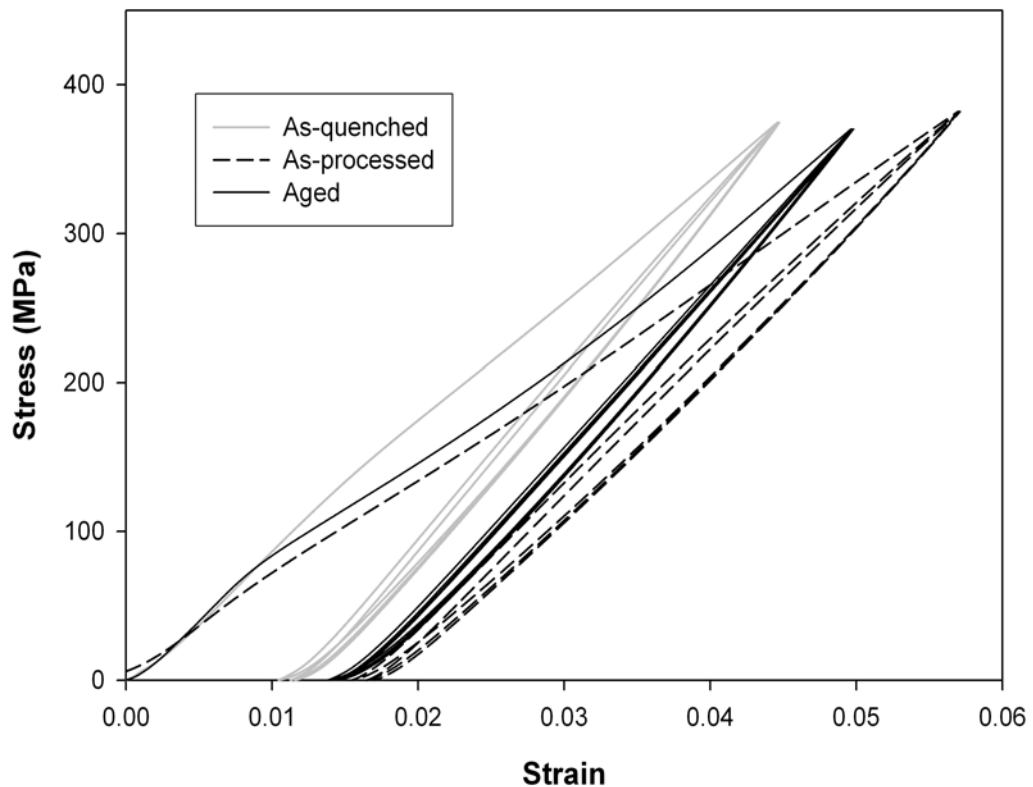
Figure 4.20 Stress-strain curves of porous TiNi in as-processed (sintered at 1100 °C for 1 h) and aged (400 °C, 1 h) condition. (porosity: 23%)

Table 4.4 Mechanical properties of porous TiNi alloys in various conditions.

Sample	Young's Modulus (E, GPa)	Critical Stress for Inducing Martensite (σ_{cr}, MPa)	Compressive strength at 2% strain (σ, MPa)		
			First cycle	Second cycle	Third cycle
As-quenched	17	161	176	216	220
As-processed	13.2	140	135	186	188
Aged	16.8	112	146	198	199

Although porous TiNi alloys produced by conventional sintering have not been found appropriate for bone replacement applications due to their unsuitable pore size and pore amount, there were not any problem detected in terms of mechanical properties. They meet the main requirements such as high strength and ductility, strain recovery ability, etc. expected from an implant material already. In this sense, they can easily be used in producing metallic materials with gradient porosity applications. For example it can be used in hard tissue replacement material as denser core of the implant. While the high porosity and large pore case at the outer surface would allow and promote tissue cell ingrowth, the dense core inside the implant material would be capable of bearing loads and strain recovery. Porous TiNi is better than bulk TiNi because of providing transportation of body fluids through its micro-pores. Moreover, it is sufficient in strength and toughness and has a lower elastic modulus value. Thus, stress shielding effect also may be minimised.

4.2. TiNi Foams by Space Holder Technique

Space holder technique seems to be best suited one among the powder metallurgical metallic foam production methods for the TiNi foams. Because porosity, pore shape and size can be controlled reasonably well in a broad range as long as a suitable space former is chosen. First of all, space holder material to be used must be chemically unreactive with TiNi. Magnesium solubility in TiNi is

expected to be negligible since magnesium is not soluble in any appreciable amount neither in Ti nor in Ni, so that superelasticity and shape memory properties would not be affected. Preliminary experiments confirmed this prediction. Magnesium did not react with TiNi when it is in solid, liquid or vapor state. Alternative space holder materials used frequently to produce TiNi foams are organic or inorganic salts such as carbamide (or urea) ($CO(NH_2)_2$), ammonium bicarbonate (NH_4HCO_3) and alkali metal salts such as sodium chloride (NaCl) or sodium fluoride (NaF) and also various polymers. Space holder agents are removed from the compact either by heating to their decomposition temperatures (270 °C for NH_4HCO_3; 250 °C for $CO(NH_2)_2$) or by dissolution in water, which is suitable for alkali metal salts. Incomplete removal of decomposition products mainly consisting of carbon, hydrogen, nitrogen or oxygen compounds will definitely react with TiNi due to extreme affinity of titanium to stated elements. In a similar manner, TiNi may also react with residual NaCl or NaF to form titanium chloride or fluoride compounds which are thermodynamically much more favored. Possible selective reactions of titanium with the elements mentioned above alters the Ni/Ti ratio of TiNi matrix. Since the shape memory and superelasticity properties as well as phase transformation temperatures are very sensitive to nickel content of TiNi matrix, they all will be effected seriously, and most of the times negatively.

Secondly, space holder material should have a sufficient strength, but not higher than that of TiNi, to enable the use of higher compaction pressures which assists sintering and minimizes the micro-porosity content. Moreover, desired pore shape and size should be ensured in the produced foam. Since prealloyed powders are much more difficult to compress and require higher compaction pressures relative to elemental powders, strength issue comes into prominence much. Lower durability of rival space holders such as polymers, organic, inorganic or metal salts can not guarantee the final desired pore shape.

Another critical issue to be noted for spacer particles is their biocompatibility, which is a prerequisite for biomedical applications. Magnesium dissolves in the body and compounds that form are non-toxic in small quantities, and can be removed by the body [234] so that its incomplete removal from the foam does not constitute a drawback for biomedical applications. On the other hand, at removal

step, decomposition of NH_4HCO_3 and $CO(NH_2)_2$ releases NH_3 which is harmful to human health [224, 226]. NaF forms fluoride ions which are highly toxic during dissolution [221]. It should not be forgotten that, to have residual compounds present in as-sintered foams is very likely.

Compared to lower decomposition temperatures of alternative spacers, higher melting point of magnesium (650 ºC) allows partial sintering of the compact before its removal and prevents the collapse of the preform. TiNi foams with up to 81% porosity (by 80% Mg addition) shown in Figure 4.21 (a) were produced successfully maintaining the initial shape. 90% Mg added mixtures (Figure 4.21 (b)) were also compacted and tried to be sintered, however resulted in partial collapse of the foam. Nevertheless, it is possible to produce TiNi foams with a porosity level higher than 81% applying two-step sintering method [168]. Holding the compacted sample at a temperature just below the melting point of magnesium for 1-2 hours will give rise to additional sintering adequate to prevent preform from collapsing during melting of magnesium.

(a)   (b)

Figure 4.21 (a) TiNi foam with a porosity of 81% (80% Mg added), (b) 90% Mg added sample after sintering (1100 °C, 1 h) (left) and after compaction (400 MPa) (right).

Magnesium is a common, easily available and relatively low cost metallic material. Also, it is possible to purchase magnesium particles almost in any shape

and in a broad size range produced by common powder production techniques such as atomization and machining. Therefore, desired porosity level, porosity distribution and pore shape that the specific application requires can be attained readily.

Finally and most importantly, magnesium provides a reducing atmosphere, which is not possible to attain using high vacuum or argon atmosphere with titanium getters used frequently in other metallic foam methods, that prevents oxidation of TiNi and secondary intermetallic formation during sintering as explained in detail in the previous section. Calcium, a better reducing material, could also be used as space filler. However, its higher boiling temperature, 1484 ºC, would not permit its complete removal since melting point of TiNi is 1310 ºC. Therefore, residual calcium oxide (CaO) amount would be excessive. Furthermore, it is more reactive than magnesium and easily oxidizes even at room temperature. Thus, it is quite difficult to handle and store.

Magnesium vapor do not only prevents secondary phase formation and contamination, but also provides higher temperature sintering opportunity. Foaming experiments carried out at 1100 °C were successful; however when the sintering temperature increased to 1200 °C, all the samples collapsed. An endothermic peak corresponding to 1120-1125 °C has been observed while conducting TG-DTA studies on the raw powders under air and nitrogen atmosphere, Figure 4.22. Air atmosphere experiments resulted in a white thick layer of oxide (probably TiO_2) while N_2 atmosphere caused formation of titanium nitride (TiN) in gold color. As can be seen from TG curves in Figure 4.23, mass gain was quite high for both powders for both of the atmospheres used.

Pure Ti used as getter can theoretically create an extremely low oxygen partial pressure of 10^{-27} and 10^{-24} atm at 1100 and 1200 °C, respectively and thus, can prevent the sample from oxidizing. However, this cannot be achieved kinetically if Ti is placed in a high vacuum, as it would take a very long time to achieve equilibrium. Utilization of titanium getters with the gas mixture can enhance the oxidation reaction and provide a better protective atmosphere but an increase in partial pressure of oxygen is unavoidable. Zhang and his co-workers [78] also detected an endothermic peak at 1124 °C in DTA experiments carried out under the
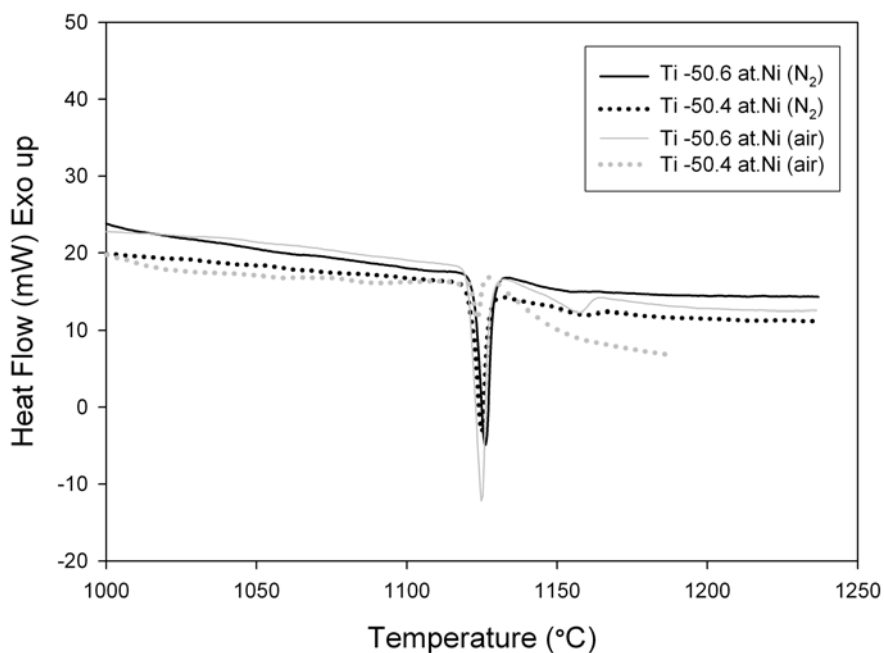
110

Figure 4.22 DTA curves for prealloyed powders used, under air and nitrogen atmosphere.
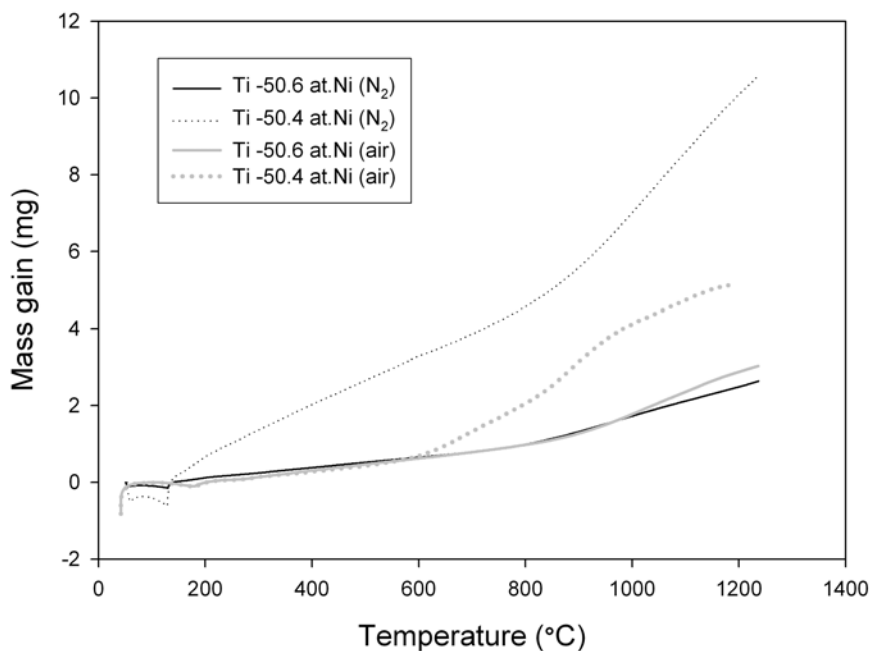

Figure 4.23 TG curves of prealloyed TiNi powders under air and nitrogen atmospheres.

Ar-1%H$_2$ gas mixture. The peak totally disappeared when they used titanium getters to clean the gas mixture. As depicted before, selective oxidation of titanium results in nickel release. Nickel amount increases with further oxidation in the regions close to surface of the powders. When the nickel content reaches to eutectic regime (57-75 at.% Ni), appearance of liquid phase is inevitable at 1118 °C and higher temperatures, as schematically shown in Figure 4.24. Ar-1%H$_2$ gas mixture failed to prevent liquid phase formation while combination of titanium getters with the same gas mixture effectively prevented liquid phase formation. At 1100 and 1200 °C, critical oxygen partial pressure for formation of MgO is 10^{-34} and 10^{-32} atm, respectively, and it can not only reduce oxides of titanium, but also prevents liquid phase formation and enables employment of higher sintering temperatures. Magnesium is much more effective in these issues than titanium. For example, Ar-1%H$_2$ gas mixture + titanium getters in Zhang and his colleagues' study avoided from liquid phase formation but could not prevented secondary phase formation. The thickness of the layer affected from oxidation was 100 μm and Ti$_4$Ni$_2$O, TiNi$_3$ as well as TiO$_2$ were the phases formed. Moreover, from the end of the oxidation layer to the interior regions TiNi$_3$ precipitates in TiNi matrix were observed meaning that actual oxidation affected layer was greater than 100 μm in fact. On the other hand, sintered TiNi foams prepared from prealloyed powders 21 and 40 μm in average sizes under magnesium vapor atmosphere in the present study did not show any secondary intermetallics or oxide compounds, as will be discussed in the following sections.

Since TiNi starts to oxidize rapidly at 200 °C [98], direct heating of compacted samples to 1200 °C resulted in their collapse due to liquid phase formation at the eutectic temperature (1118 °C). Magnesium could not reduce oxides of TiNi powders and prevent nickel enrichment of the powder surface due to lack of enough time upon rapid heating. However, holding the sample at 1100 °C for 30 minutes was sufficient to prevent the shift to eutectic composition. Subsequently, sintering done at 1200 °C resulted in chemically homogeneous TiNi foams free from secondary intermetallics and contamination products. By this two step processing, magnesium may allow sintering probably up to the melting point of TiNi. Other TiNi foam production techniques, especially HIP although allow elevated

112

temperature sintering (> 1118 °C) using titanium getters, fail in preventing secondary phase formation and contamination which results in brittleness of the foams.
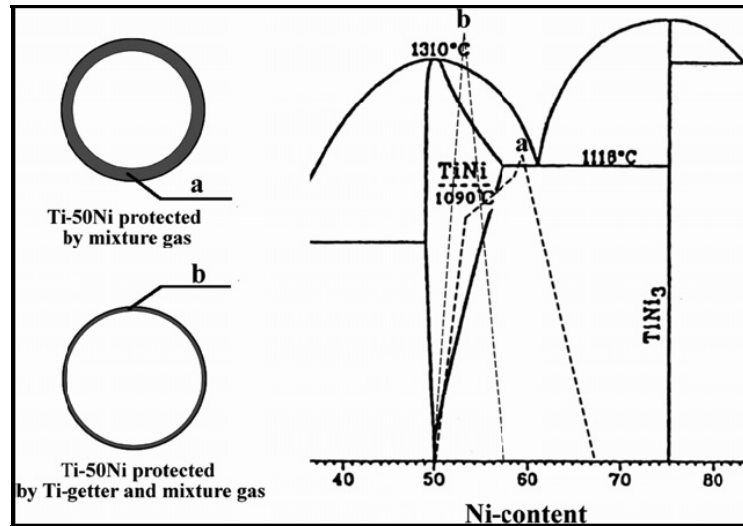
Figure 4.24 Schematical surface nickel content change during heating and cooling [78].

4.2.1. Structural Characterization

4.2.1.1. Porosity and Pore Characteristics of TiNi SMA Foams

Ti-50.4 at. %Ni and Ti-50.6 at. %Ni alloy foams with porosities in the range 37%-81% produced using space holder technique via powder metallurgy are shown in Figure 4.25. Sintering temperatures employed were 1100 and 1200 °C, while sintering time was choosen as 1 and 2 hours. Relation between the amount of Mg added to the compact, and final density and porosity after sintering is shown in Figure 4.26 for the Ti-50.6 at. %Ni samples sintered at 1100 °C for 1 hour. Porosity increases with increasing Mg addition linearly, while density decreases in the same manner.

113

<div align="center">(a)   (b)</div>

Figure 4.25 Macrograph of TiNi foams produced by space holder method with increasing porosity content from left to right, (a) Ti-50.6 at. %Ni foams sintered at 1100 °C for 1 h and with porosity content of 37-81% and (b) Ti-50.4 at.%Ni foams sintered at 1100 °C for 2 h and with porosity content of 53-73%.
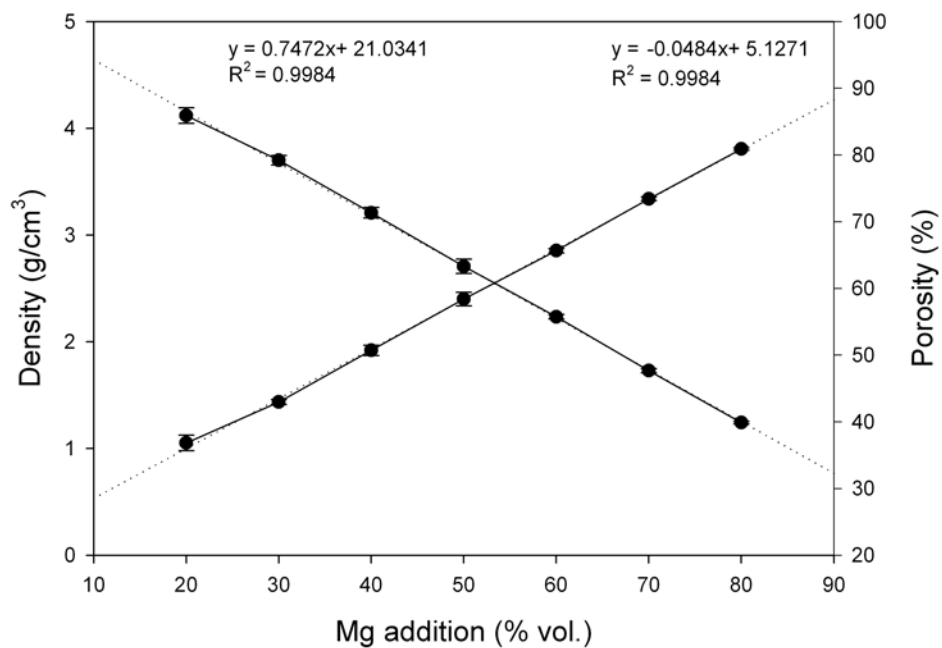
Figure 4.26 Relation between Mg addition and resulting porosity and density after sintering process (1100 °C, 1h) for the Ti-50.6 at. %Ni foam.

In all samples, but especially in the samples with lower porosity, the resultant pore volume fraction was observed to be fairly higher than the magnesium added. The reason behind this phenomenon is the micro-pores remained on the macro-pore

walls due to partial sintering of TiNi powders. It has also been observed that the amount of excess porosity (micro-pore content) is reduced with increasing magnesium addition, e.g., it decreases down to 1% in the 80% Mg added specimen, Table 4.5, due to the decrease in the wall thickness with the decreasing amount of TiNi powder in the mixture. Micro-pore content actually can be calculated easily just by subtracting initial magnesium amount added into the mixture from total porosity measured. Results obtained from image analyzer by optical microscopy were in good agreement with the ones calculated, Table 4.5. Thus, other samples were not processed in image analyzer to find out micro-porosity content.

Table 4.5 Effect of Mg addition on total, macro and micro-porosity in Ti-50.6 at. %Ni foams which were sintered at 1100 °C for 1 h.

%Mg added	% Total Porosity (by density measurements)	% Macro-porosity (by optical microscopy)	% Micro-porosity (by optical microscopy	% Micro-porosity calculated
50	59	48	10	9
60	66	60	4	6
70	73	72	2	3
80	81	80	0.5	1

There is a tendency to deviate from linearity at both ends of the two lines in Figure 4.26 possibly due to low compressibility of TiNi alloy powders and slight collapse of the preform during sintering. Increase in the number of micro-voids between TiNi powders leads to lower density values when lower Mg addition is made. On the other hand, it has been observed that higher amount of Mg addition (exceeding 70% vol.) resulted in slight collapse of the foam structure during sintering.

Figure 4.27 presents porosity content of TiNi foams produced using Ti-50.4 at. %Ni (sintered at 1100 °C for 2 hours) and Ti-50.6 at. %Ni powder (sintered at 1100 and 1200 °C for 2 hours). Ti-50.4 at. %Ni foams exhibited higher porosity than Ti-

50.6 at. %Ni foams fabricated at the same conditions probably due to the larger initial powder size of Ti-50.4 at. %Ni foams. Longer sintering times reduced the porosity content slightly (around 1%) whereas employing higher sintering temperature reduced the porosity only by around 4%. Since sintering occurs by diffusion mechanisms, while it is linearly dependent on time, there is an exponential relation with temperature. Table 4.6 summarizes effects of Mg addition, powder size, sintering time and sintering temperature on total, macro and micro-porosity.
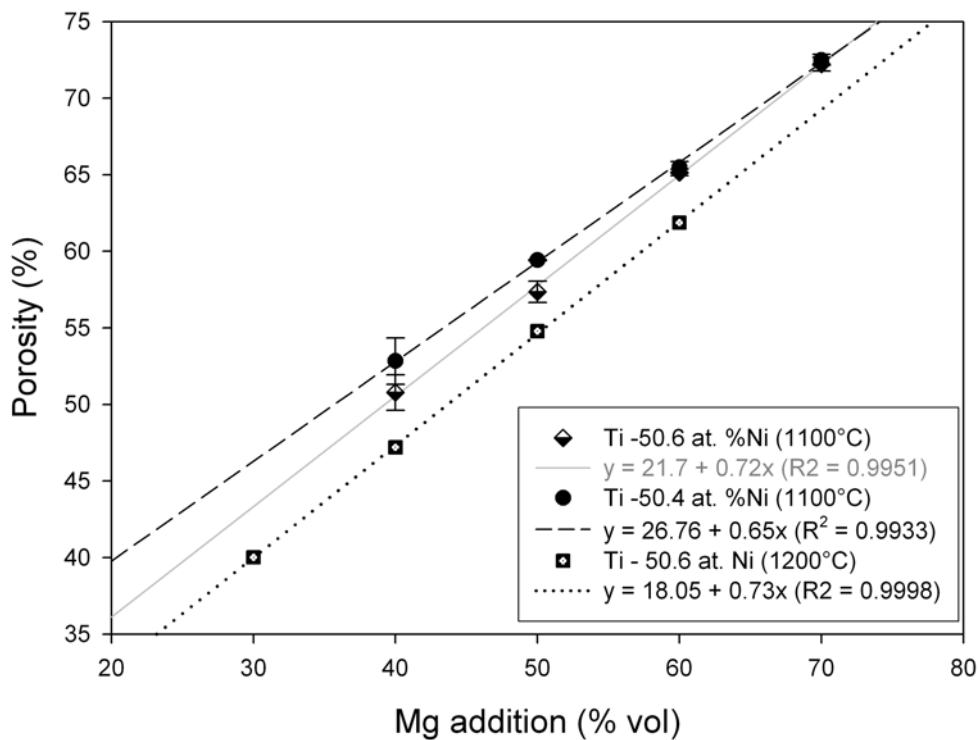
Figure 4.27 Porosity of TiNi foams prepared from two different powders sintered at 1100 or 1200 °C for 2 hours.

As-processed Ti-50.6 at. %Ni foams have exhibited some shrinkage during Mg evaporation and sintering as can be seen from Figure 4.28 (a), 4.28 (b) and 4.28 (d). Shrinkage has been observed to increase proportionally with Mg content and was < 3% in height and < 3.5% in diameter in the 80% Mg added alloy (81% porosity) sintered at 1100 °C for 1 hour. An additional sintering for 1 h at the same

116

temperature did not cause a distinct change in shrinkage amount. However, rising the sintering temperature to 1200 °C resulted in increase of shrinkage for both longitudinal and radial directions by about 2%. Shrinkages observed arise from the decrease in the micro-porosity content and they are the indication of sintering degree.

Table 4.6 Effects of Mg addition, powder size, sintering time and sintering temperature on total, macro and micro-porosity

| Powders used	%Mg added	% Total porosity (by density measurements)	% Micro-porosity calculated	Sintering temperature and time
Ti-50.6 at. %Ni (21 μm)	20	37	17	1100 °C, 1 hour
	30	43	13	
	40	51	11	
	50	59	9	
	60	66	6	
	70	73	3	
	80	81	1	
	40	51	11	1100 °C, 2 hour
	50	58	8	
	60	65	5	
	70	72	2	
	30	40	10	1200 °C, 2 hour
	40	47	7	
	50	55	5	
	60	62	2	
Ti-50.4 at. %Ni (40 μm)	40	53	13	1100 °C, 2 hour
	50	59	9	
	60	66	6	
	70	73	3	

Ti-50.4 at. %Ni foams on the other hand did not display any shrinkage, instead they showed swelling, Figure 4.28 (c). This swelling, however, is not a consequence of liquid phase formation, a phenomenon frequently occured during elemental powder sintering. In fact, enlargement of Ti-50.4 at. %Ni foams in both dimensions after sintering is a result of the shape memory effect. These powders are mainly in martensitic state at room temperature. During compaction step they are deformed by

martensite detwinning mechanism and after ejection from the die they do not recover their initial shapes. They only recover elastic strains. When the temperature reaches their A_f (58 °C) at the very beginning of the heating in the furnace for sintering, they regain their shapes before compaction. Since initial height and diameter of the compact were measured just after compaction, an increase in the dimensions has been observed after sintering. Less amount of raw TiNi powder in the mixture at the beginning reduced the swelling of foams as it is seen in Figure 4.28 (c).
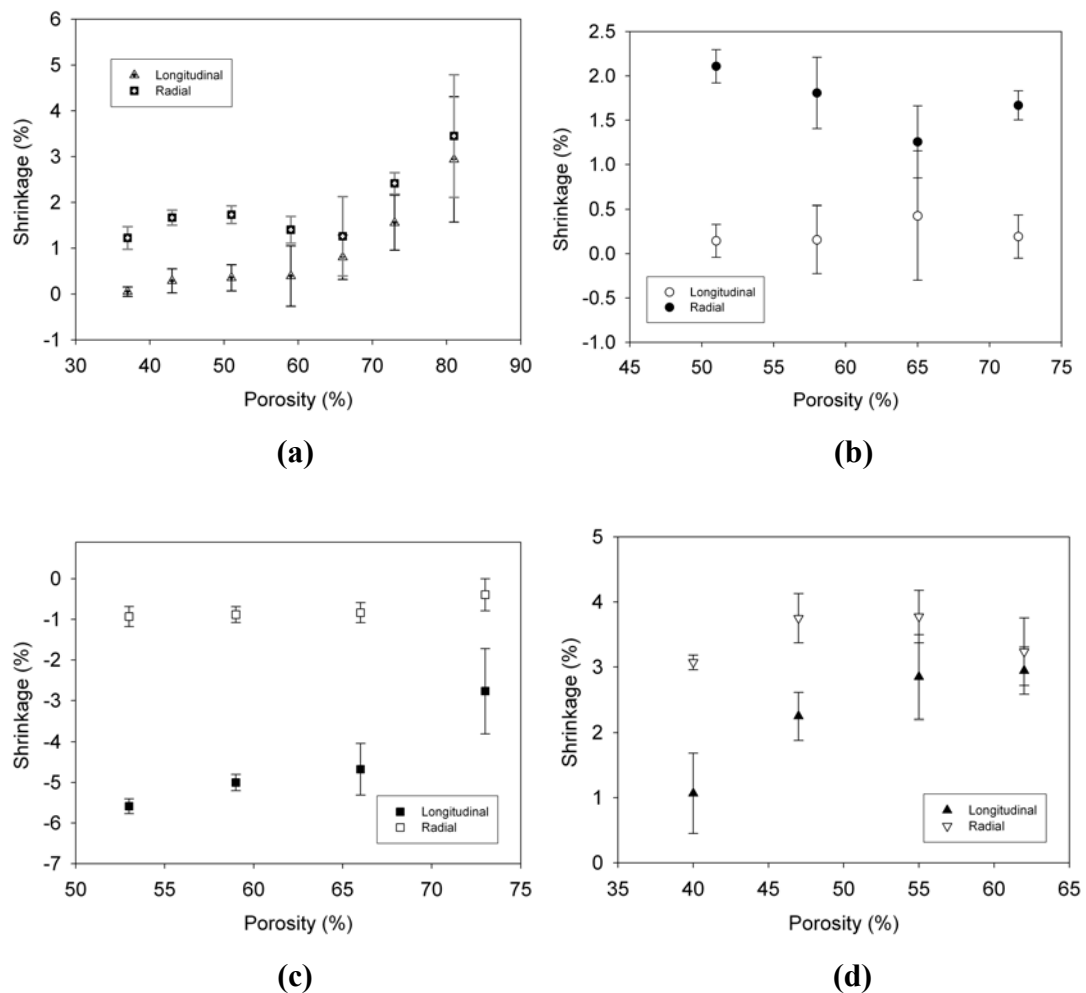

(a)

(b)

(c)

(d)

Figure 4.28 Shrinkage measured in TiNi foams produced from Ti-50.6 at. %Ni powder, (a) 1100 °C, 1 h, (b) 1100 °C, 2 h, (d) 1200 °C 2 h, and from Ti-50.4 at. %Ni powder (c) 1100 °C, 2 h.

In contrast, Ti-50.6 at. %Ni powders were completely austenitic at room temperature and they deformed by transforming into martensite during compaction. They regained the initial shape (only partly due to martensite stabilisation) by superelasticity mechanism as a result of retransforming into austenite upon unloading. Their initial dimensions were recorded at this stage. Subsequent heating for sintering did not lead to a considerable shape change and final foams did not show any dilation. Actually, Ti-50.4 at. %Ni foams maybe would exhibit some shrinkage if their initial dimensions were recorded after heating to a temperature higher than A_f.

Figure 4.29 (a) and 4.29 (b) show the morphology and distribution of pores through axial and radial directions, respectively, in a sample with 73% porosity. It is clear that pores are almost completely spherical and distributed homogeneously in the structure along both directions making the foam isotropic. A few non-spherical pores seen in the micrographs results from either non-spherical Mg powders present initially or smearing of partially sintered TiNi particles into the pores during metallographic specimen preparation routes.
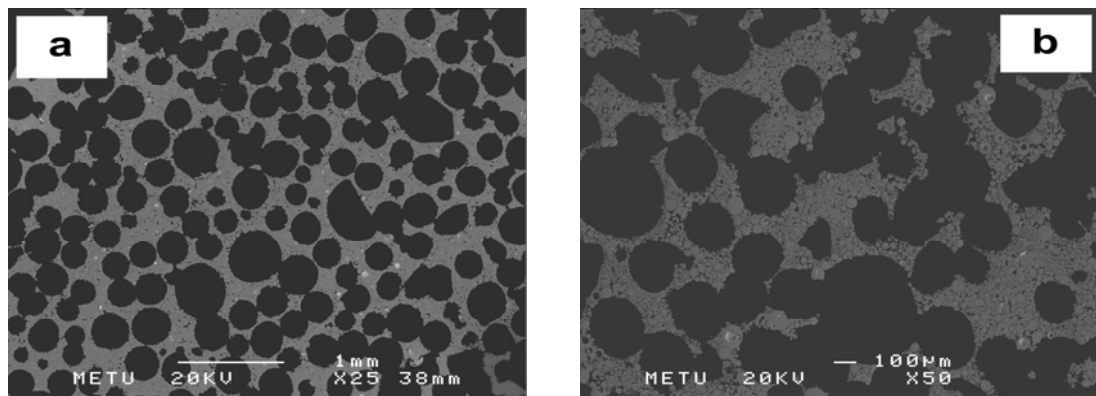
Figure 4.29 Typical SEM micrographs of polished cross sections of TiNi foam (1100 °C, 1 h) samples with 73% porosity, (a) along transverse direction, (b) along longitudinal direction.

66% porous specimens exhibited the best porosity distribution as it presented in Figure 4.30. It has been observed that samples with a porosity less than 59% have relatively poor pore distribution probably due to rearrangement of the Mg powders

during compaction step, rather than their agglomeration during mixing. In TiNi foams with 73 and 81% porosity, on the other hand, coalescence of the macro-pores was observed to adversely affect the pore distribution.
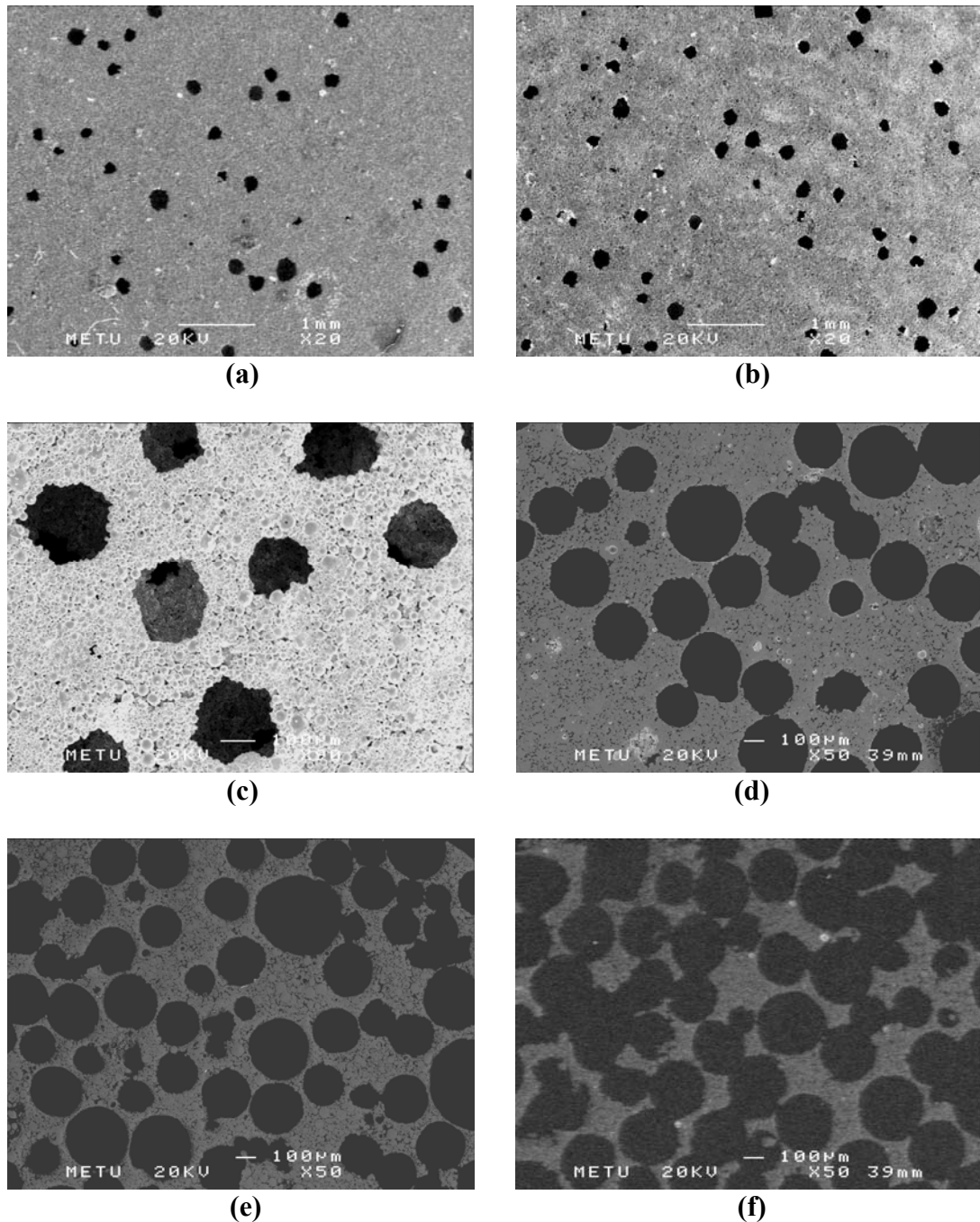
Figure 4.30 SEM micrographs of porous TiNi samples produced with Ti-50.6 at. %Ni powders (1100 °C, 1 h) with the porosity of (a) 37%, (b) 43%, (c) 51%, (d) 59%, (e) 66% and (f) 81%.

Figure 4.31 shows macro-pores connected partially in 59% porous and completely in 66% and 73% porous TiNi foam samples. Macro-pores in 51% porous samples were also partially interconnected and most of them were found to be isolated from each other. 43 and 37% porous samples on the other hand, exhibited almost completely isolated macro-pores.

(a)

(b)

(c)

(d)
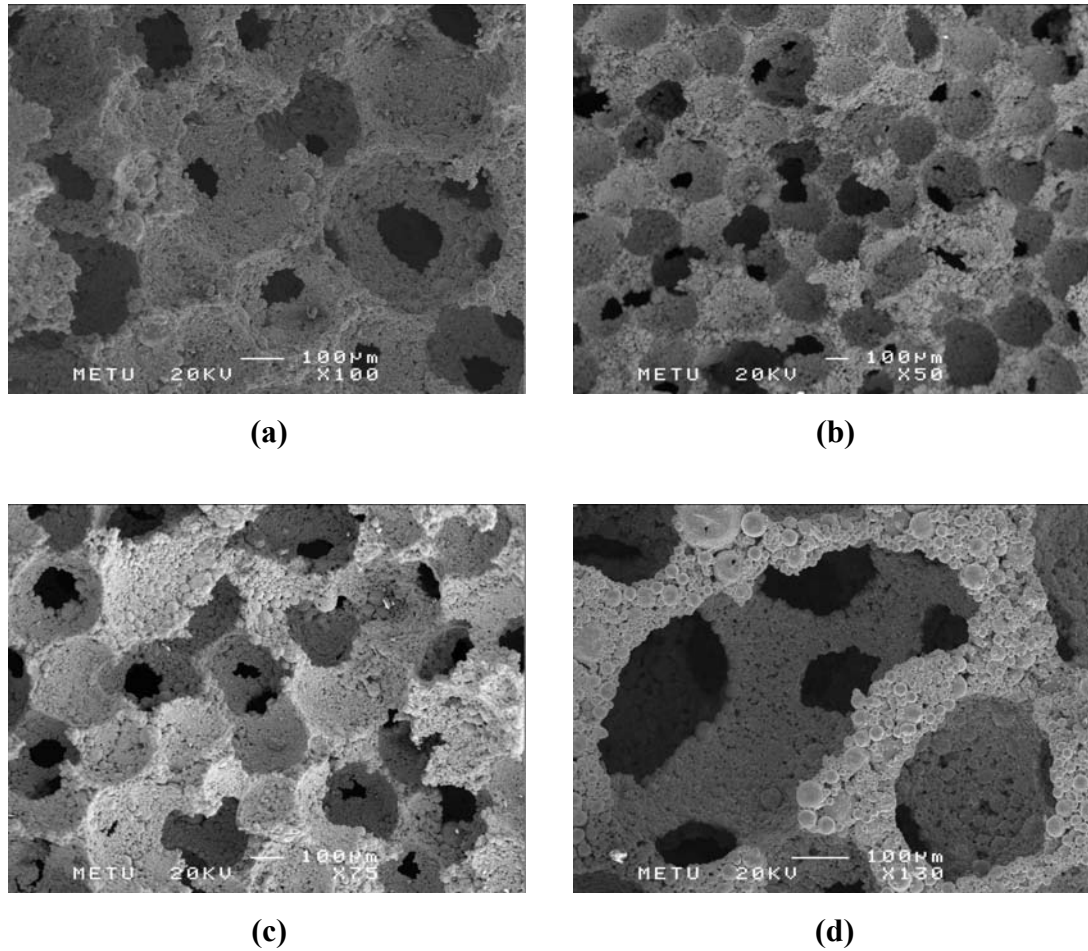
Figure 4.31 SEM images of fractured TiNi foams (1100 °C, 1 h) showing interconnected pore structure (a) 59%, (b) 66%, (c) 73% and (d) side view of interconnected pores in 73% porosity TiNi foam.

Nevertheless, all the specimens produced exhibited primarily open porosity in amounts over 90% due to existence of micro-pores interconnected to each other as well as to macro-pores. Less than 10% closed or isolated porosity measured in the samples were observed to vary non-systematically from sample to sample and

121

probably stems from the voids already present in the powder particles and formed during atomization process. Some of these pores observed commonly throughout metallographic and SEM investigations have been pointed with arrows in Figure 4.32. Another source for closed pores may be cell walls. During partial sintering some micro-pores in the cell walls may become isolated.
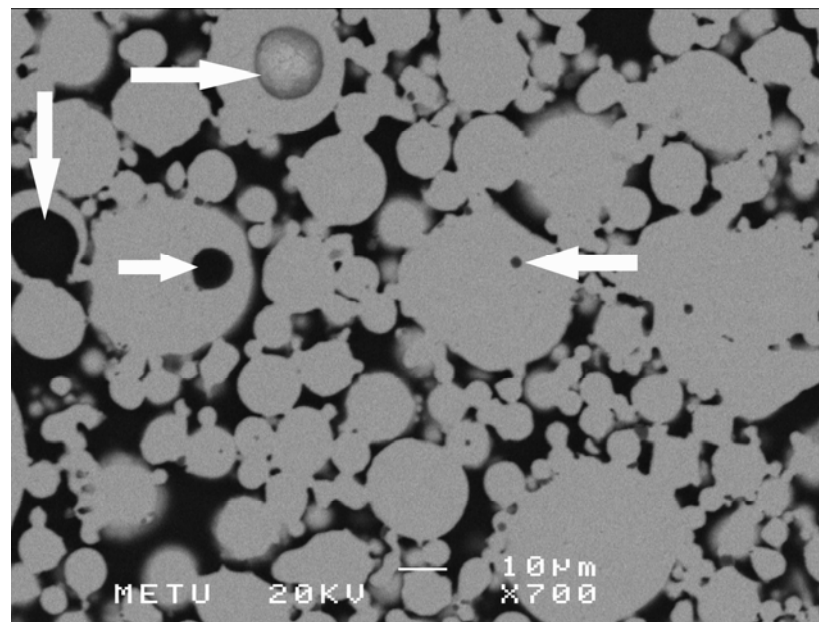
Figure 4.32 BSE image of 59% porous TiNi showing closed porosities in partially sintered (1100 °C, 1 h) TiNi powders.

Interconnected porosity is very important for biomedical applications of TiNi foams in terms of transportation of body fluids, bone ingrowth etc. However, there is an optimum pore size (100-600 μm) determined appropriate for bone ingrowth in bone replacement applications. Therefore, micro-pores, which are usually < 20 μm in size, do not count for bone growth and the macro-pores must be directly interconnected to each other, not through the micro-pores in the walls. Space holder technique can easily control the resulting macro-pore size since the macro-pores are formed by replication of the initial spacer particles used. In contrast, control of the fenestration (window or throat at cell walls connecting macro-pores) size is quite
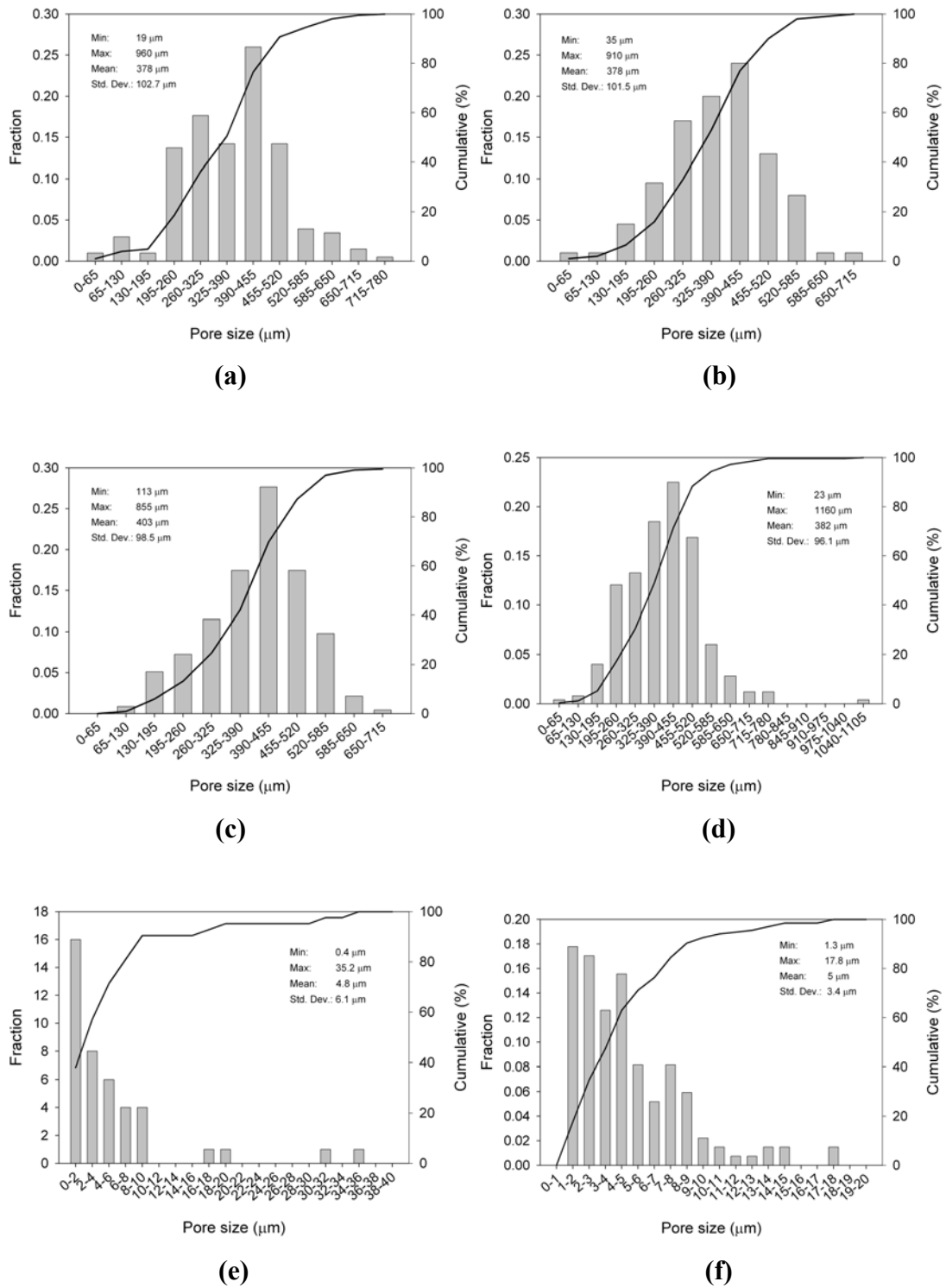
Figure 4.33 Macro-pore size distribution in TiNi foams with different porosity content, (a) 59%, (b) 55%, (c) 37%, (d) 73% and micro-pore size distribution, (e) 55%, (f) 43%.

difficult. It is attainable only by appropriate adjustment of the space holder size and packing. It is also important to choose suitable spacer shape. That is why magnesium powders with a narrow particle size range (250-600 μm) were used in the present study. Magnesium particles smaller than 250 μm in size could not produce fenestrations of sufficient size. If the fenestration size is smaller than 100 μm bone ingrowth may be inhibited. It is clear from Figure 4.31 that most of the fenestrations present in TiNi foams are larger than 100 μm. However, a decrease in fenestration size with decreasing porosity content is probable. In that case, enlargement of the fenestration size may be attempted after processing, by dissolution in a suitable acid solution without damaging the partially sintered structure of the TiNi wall.

Image analyses indicated that the mean pore size of the macro-pores (385 ± 100 μm) and micro-pores (5.6 ± 5.1 μm) were almost independent of the porosity contents in all the samples produced, Figure 4.33. However, a few larger pores with sizes reaching up to 2000 μm has also been observed due to coalescence of macro-pores as the pore volume fraction reaches to high values. Consistency of the macro-pore size distribution results can be attributed to relatively high strength of magnesium. Since magnesium did not subject to plastic deformation during compaction step, neither pore size nor pore shape changed. It should be noted that, macro-pore size distribution in TiNi foams and particle size distribution of magnesium powder used were almost the same. Therefore, to maintain the homogeneity of pore size distribution, possible separation of coarser and finer magnesium powders in the period of storage because of settling effects should be prevented by blending the powders properly, before use.

4.2.1.2. Microstructure

XRD patterns of the prealloyed Ti-50.6 at. %Ni powders in as-received condition and as foams with various porosity contents produced by compaction at 400 MPa and sintering at 1100 °C for 1 hour and 2 hours, are presented in Figure 4.34 and Figure 4.35, respectively. Prealloyed TiNi powders and the processed samples with less than 60% porosity were found to consist of only cubic B2

austenite phase, while additionally a small quantity of monoclinic B19' martensite phase was also detected in samples with porosity content exceeding 60%.
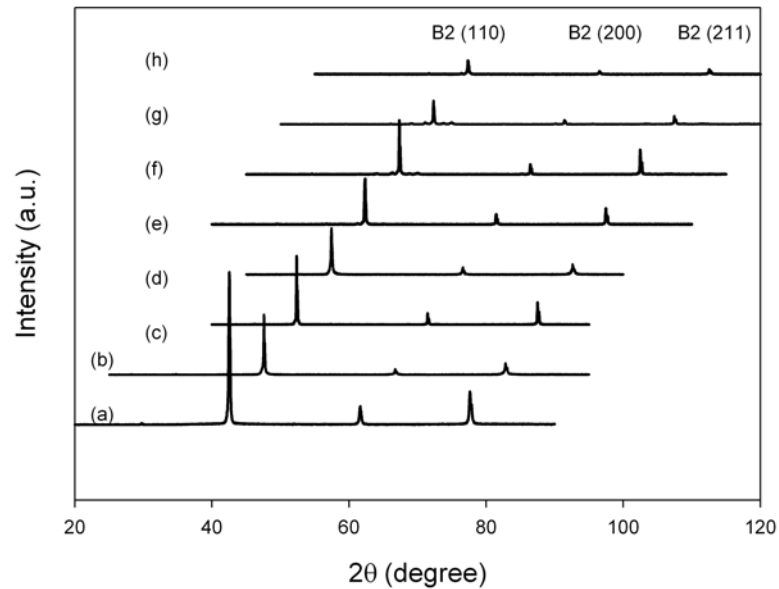
Figure 4.34 XRD patterns of (a) as received prealloyed Ti-50.6 at. %Ni powders and foams sintered at 1100 °C for 1 hour to yield porosities of (b) 37%, (c) 43%, (d) 51%, (e) 59%, (f) 66%, (g) 73% and (h) 81%.
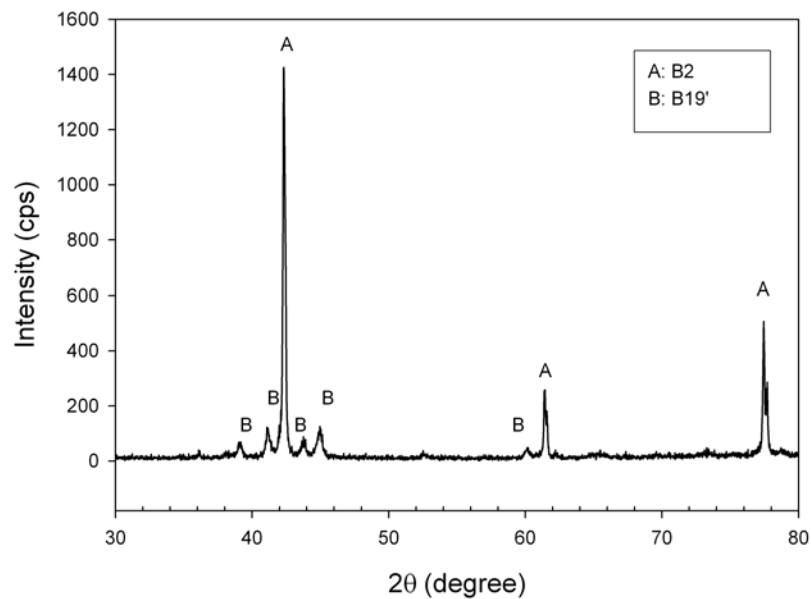
Figure 4.35 XRD pattern of Ti-50.6 at. %Ni foam with a porosity content of 72% sintered at 1100 °C for 2 hours.

Ti-50.6 at. %Ni foams compacted at the same pressure but sintered at 1200 °C for 2 hours exhibited merely austenite peaks for all the porosity levels. Figure 4.36 represents the XRD spectra of such a sample with 62% porosity. SEM investigations confirmed XRD analysis results. Figure 4.37 shows SEM micrographs of 58 and 72% porous samples.
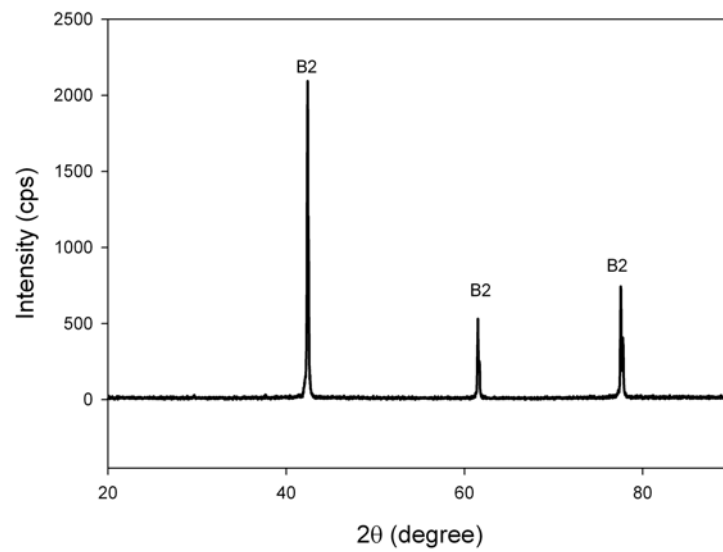
Figure 4.36 XRD pattern of 62% porous Ti-50.6 at. %Ni foam sintered at 1200 °C for 2 hours.
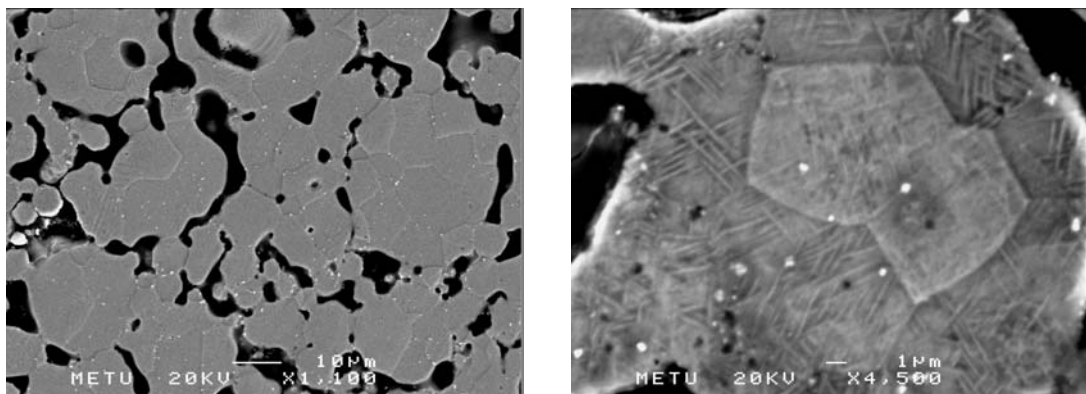
(a)   (b)

Figure 4.37 SEM micrographs of Ti-50.6 at. %Ni foams produced by sintering at 1100 °C for 2 hours. (a) 58% porous sample only displays austenite grains while (b) 72% porous sample exhibits martensite plates in austenite grains.

Room temperature microstructure of the foams produced using Ti-50.4 at. %Ni powder, on the other hand, was observed to compose of both austenite and martensite (mainly) phases together as confirmed by both XRD analysis and SEM investigations, Figure 4.38 and Figure 4.39, respectively. It has been found that TiNi foams produced from both prealloyed powders were entirely free from secondary undesired brittle intermetallics as well as oxide, nitride and carbonitride compounds of titanium.
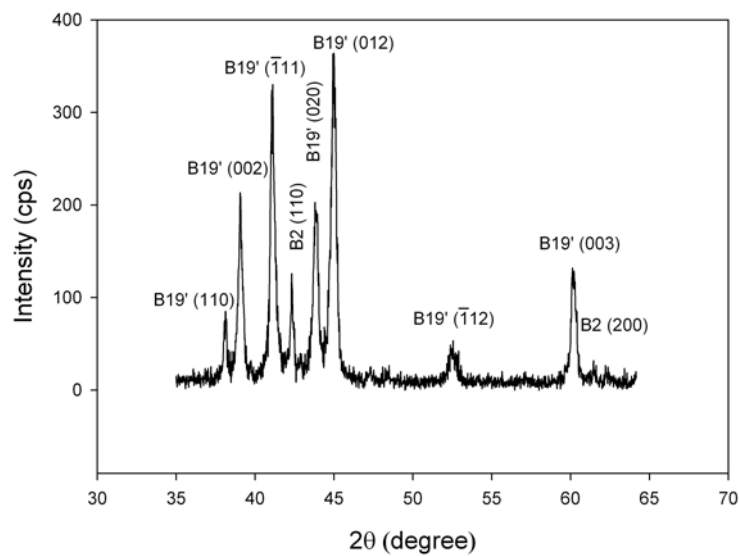
Figure 4.38 XRD pattern of Ti-50.4 at. %Ni foam sintered at 1100 °C for 2 hours resulting in a porosity content of 66%.
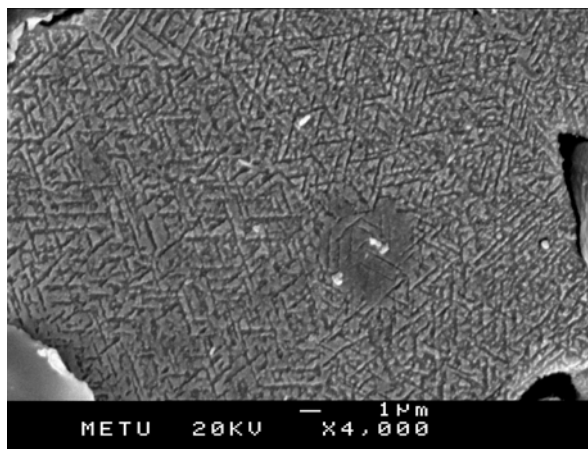
Figure 4.39 SEM micrograph of Ti-50.4 at. %Ni foam with a porosity of 53%.

127

Aging treatment applied to Ti-50.6 at. %Ni foams was carried out at 400 °C for 1 hour and ended up with precipitation of Ti_3Ni_4 particles. XRD diagram in Figure 4.40 shows the peaks of Ti_3Ni_4 precipitates beside B2 phase. Since precipitation reduces the amount of nickel in TiNi matrix, martensitic transformation temperatures increase. As a result, some of the austenite transforms into martensite and B19' martensite peaks appear in the XRD chart.
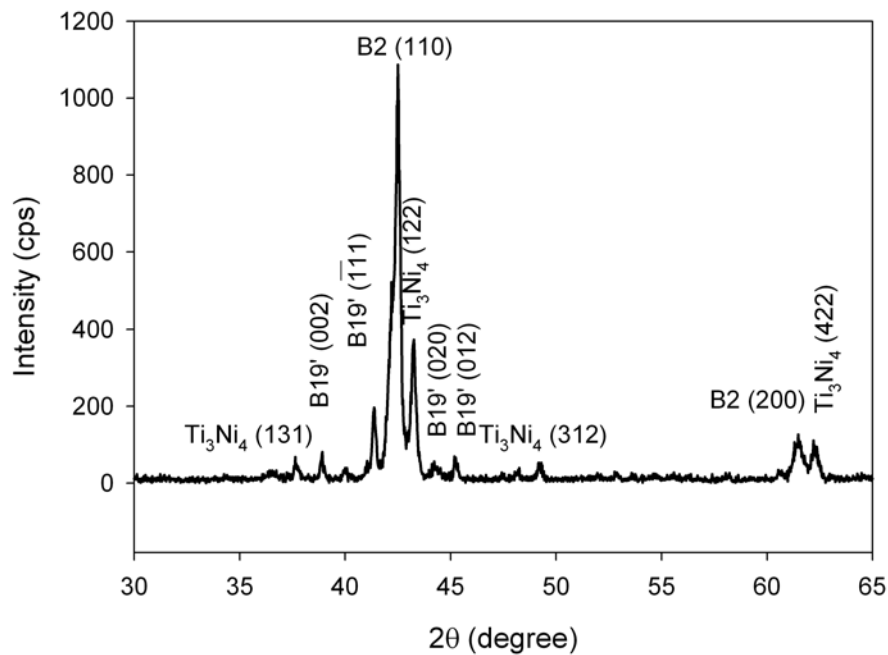
Figure 4.40 XRD pattern of aged (400 °C, 1 h) Ti-50.6 at. %Ni foam with a porosity content of 51%.

Surprisingly, XRD results did not show any residual magnesium or magnesium oxide, which may be expected as a result of condensation onto TiNi foam during processing. However, this does not completely rule out the probability of presence of trace amount of Mg and MgO in the samples that could not be detected by X-Ray diffraction. Indeed, MgO particles with a few micrometer size, possibly condensed onto specimens during cooling, especially into macro-pores and their vicinity, has been observed during SEM investigations, Figure 4.41. Since magnesium is a well known biodegredable material that is also present in bone structure, it is not

expected to constitute a problem even if it has not been removed from the structure completely by evaporation during processing. MgO particles present, on the other hand, can be easily removed by a suitable leaching procedure such as dipping into a dilute HCl solution in case their existence and motion induce problems in biomedical and other applications. Independent of powder size and process parameters, some residual MgO particles have been found in all the samples produced. Figure 4.42 presents SEM images of residual MgO located into pore walls of TiNi foams produced from powders different in size and composition employing different processing temperature and times.

(a)

(b)

(c)

(d)
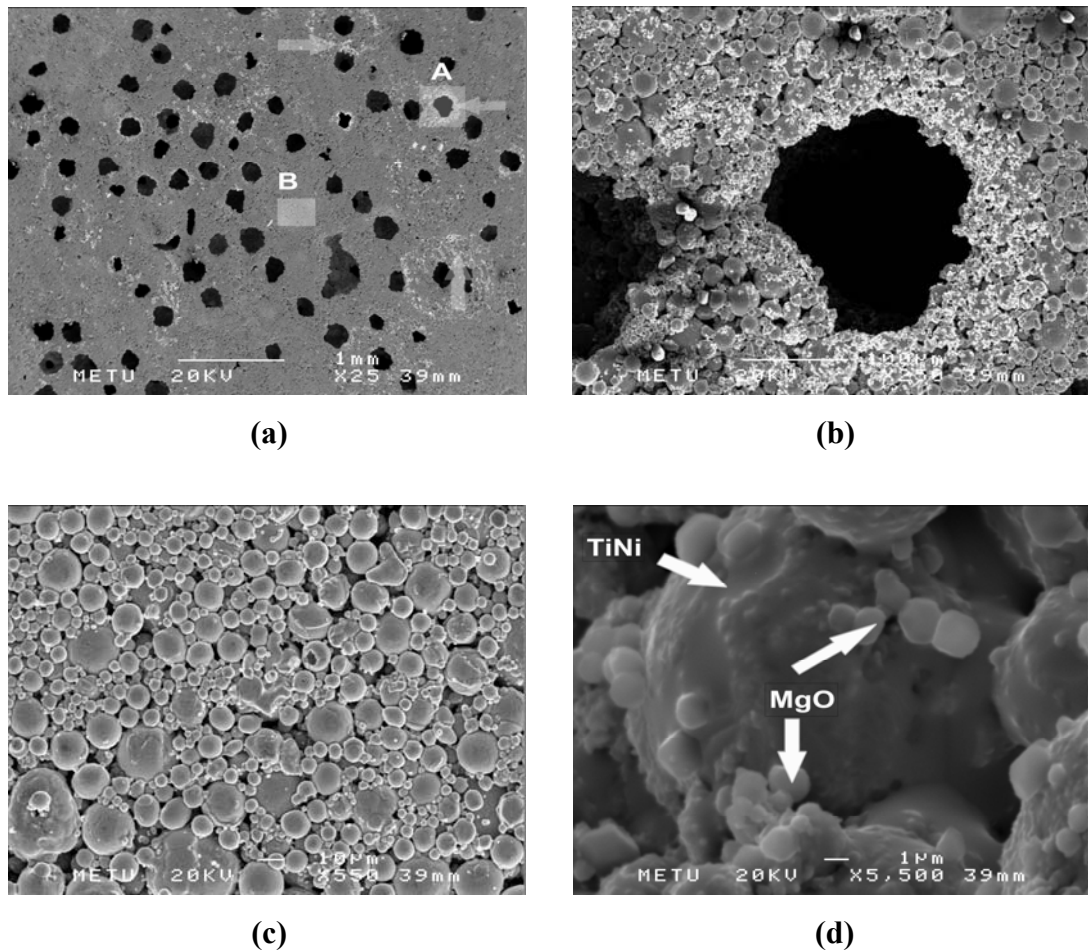
Figure 4.41 SEM micrographs showing residual MgO particles in a region where they have extraordinarily accumulated. (a) general view, (b) region A and (c) region B at higher magnifications, (d) inside the macro-pore in region A.

129

(a)   (b)

(c)
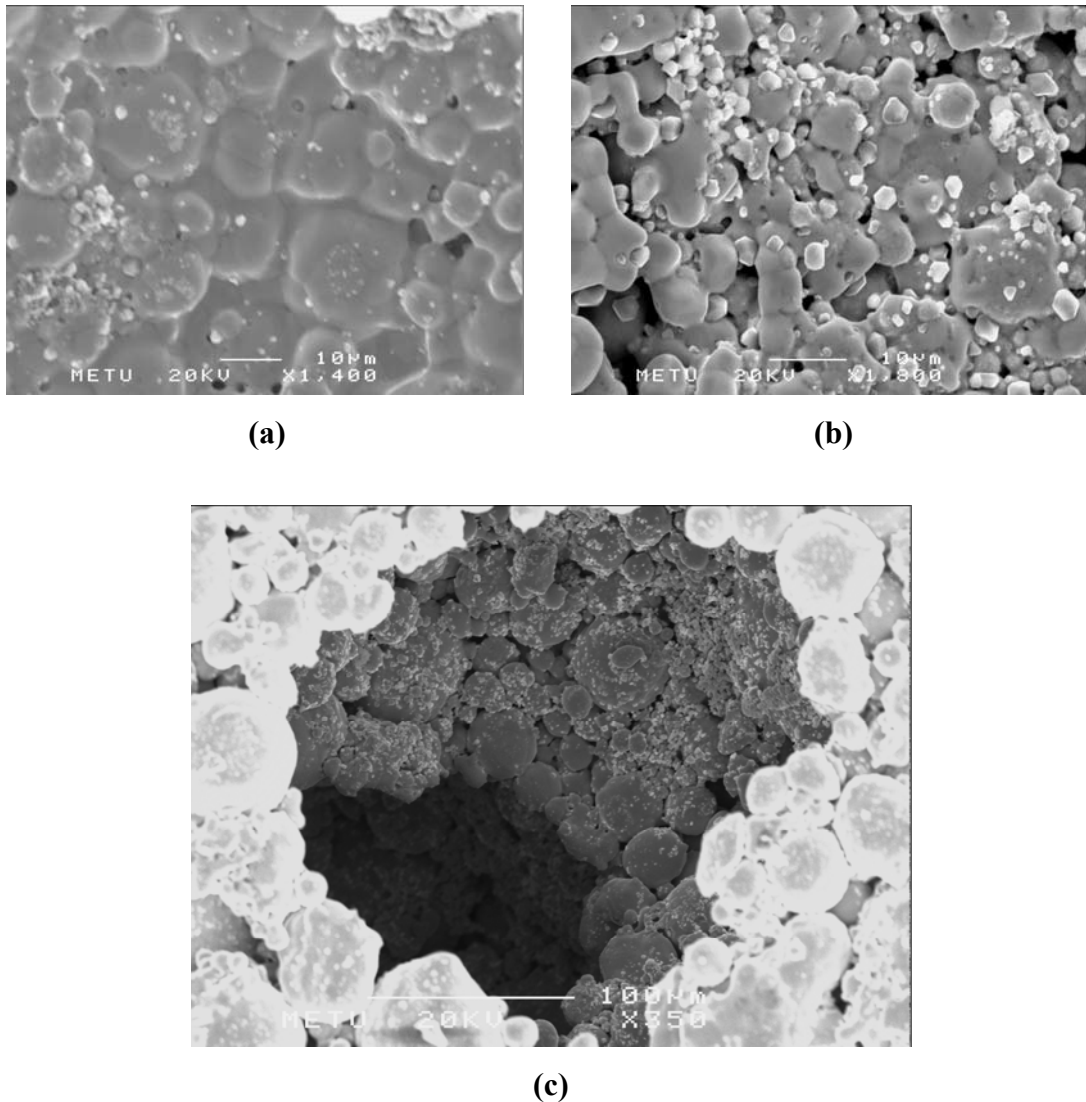
Figure 4.42 SEM micrographs displaying residual MgO particles present in Ti-50.6 at. %Ni foams: (a) 40% porous TiNi sintered at 1200 °C for 2 hours, (b) 73% porous TiNi sintered at 1100 °C for 1 hour and (c) 53% porous Ti-50.4 at. %Ni foam.

The present study has shown that using Mg as space forming agent in foam production from prealloyed TiNi by sintering enables obtaining TiNi as a single phase or with some B19' but definitely without any Ti or Ni-rich compound as well as Mg_2Ni or $MgNi_2$, and also effectively prevents oxide, nitride and carbide formation. SEM micrograph, Figure 4.43, in back scattered electron mode (BSE) also confirms that the resulting porous TiNi foams are free of secondary intermetallics. Also, in facilitating the sintering process by reducing the surface oxygen of raw powders, it has been observed that Mg is very impressive.
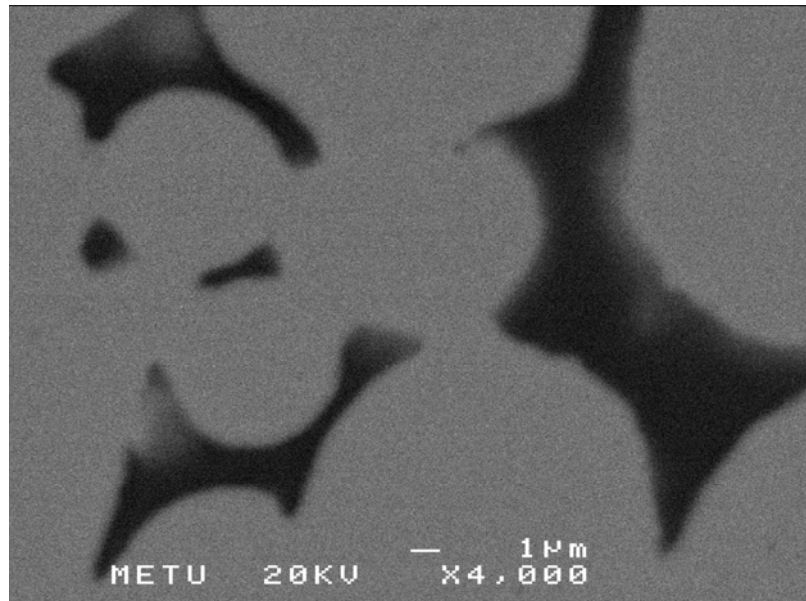
Figure 4.43 BSE micrograph of Ti-50.6 at. %Ni foam with a porosity content of 43%.

4.2.2. Phase Transformation Temperatures

TiNi foams with different porosities all exhibited single distinct peak during both heating and cooling, Figure 4.44. Transformation temperatures given in Table 4.7 and Table 4.8 show that transformation temperatures are quite variable and usually higher than those of the raw powder with a few exception. Phase transformation temperatures of TiNi alloys are very sensitive to various parameters such as composition, deformation and heat treatment details, and the oxidation state. The outcome of DSC studies are mostly confusing because these parameters are difficult to control very closely and display contradictory effects on phase transformation temperatures. For example, generally oxidation, deformation and Ti-rich precipitates lead to a decrease in transformation temperatures while Ni-rich precipitates and aging result in an increase in martensitic transformation temperatures. Also, the extent of deformation produced during cutting samples from porous TiNi alloys for DSC by a non-standard procedure may be an important parameter that leads to inaccurate results. In the present study, all these factors have been tried to be fixed. Nevertheless, it was not possible unfortunatelly to produce

samples completely under identical conditions. For example, an increase of 1000 ppm in oxygen content may results in a change of 10-15 °C [99] in phase transformation temperatures. At the beginning of the sintering process, firstly, furnace was purged with high pressure Ar flow. The pressure and time was kept constant for all the samples produced. However, residual air in the crucible may not be exactly the same for all the experiments and hence the amount of oxygen dissolved. Moreover, removal of magnesium vapour may not be at the same rate although Ti getters with similar dimensions were used. In addition, when moving the sintered sample into the cold zone of the furnace there may be some air leakage into the furnace. Quenching was not preferred after sintering due to risk of considerable oxidation. Cooling in the cold zone of the furnace also may have triggered some Ti_3Ni_4 precipitation although they were not detected by XRD. TiNi alloys with different compositions and porosity contents show different resistance to deformation during DSC sampling. Constant speed cutting has been used for DSC sampling but this does not guarantee same amount of deformation for samples with different porosities.
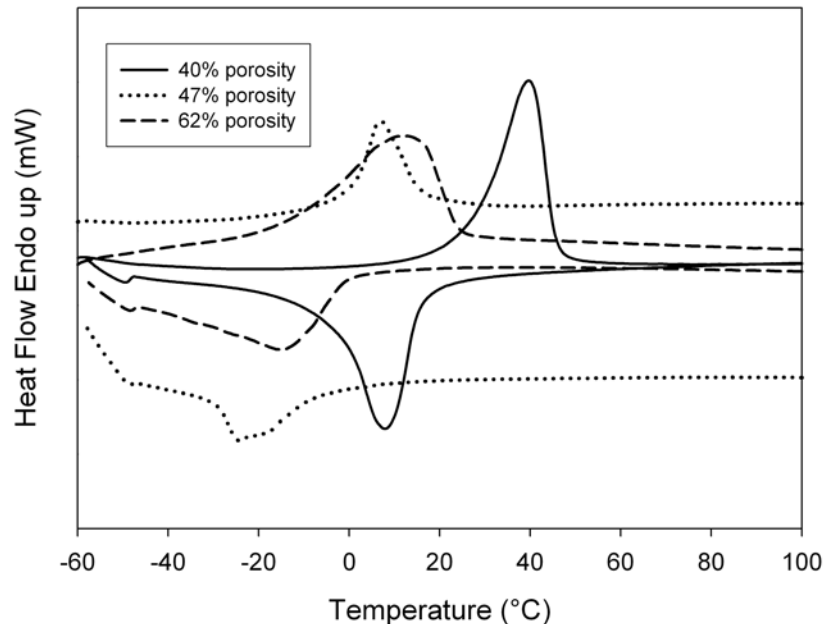
Figure 4.44 DSC curves for Ti-50.6 at. %Ni TiNi foams with different porosities sintered at 1200 °C for 2 hours.

132

Table 4.7 Transformation temperatures of prealloyed Ti-50.6 at. %Ni powder and TiNi foams with different porosities sintered at 1100 °C for 1 hour.

Porosity (%)	Phase transformation temperatures (°C)						Latent heat of transformations (ΔH, J/g)	
	M_s	M_p	M_f	A_s	A_p	A_f	$-\Delta H_{forw}$	ΔH_{rev}
Powder	10	-25	-53	-11	20	30	14.4	13.8
38	17	-5	-28	17	26	42	9.3	7.6
43	6	-8	-34	21	25	36	7.1	8.4
51	15	-21	-37	15	23	40	10.5	13.1
59	5	-17	-38	19	28	34	2	1.5
66	5	-13	-32	16	25	35	3.5	7
73	9	0	-15	18	29	43	3.8	6.4
81	14	-4	-29	17	30	40	4.9	5.5

Table 4.8 Transformation temperatures of Ti-50.6 at. %Ni TiNi foams with different porosities sintered at 1200 °C for 2 hours.

Porosity (%)	Phase transformation temperatures (°C)						Latent heat of transformations (ΔH, J/g)	
	M_s	M_p	M_f	A_s	A_p	A_f	$-\Delta H_{forw}$	ΔH_{rev}
40	18	8	-4	27	40	45	16.3	18.4
47	-4	-24	-32	2	7	20	10	13.2
55	4	-7	-34	-16	21	37	11.3	16.6
62	-2	-16	-50	-11	12	26	12.5	16.7

4.2.2.1. Effect of Oxidation and Porosity Content on Martensitic Transformations

DSC curves of TiNi foams with porosity contents varying from 51 to 73%, as well as those of the raw powders used in their production are presented in Figure 4.45. Sintering time and temperatures were the same for all the specimens prepared

from both of the powders as 2 hours and 1100 °C. It is clearly seen from both the cooling and heating curves of all the samples that, the transformation temperatures of the foams are considerably higher than those of the starting powder, and there is a tendency for the transformation temperatures to shift towards higher values with increasing porosity content.
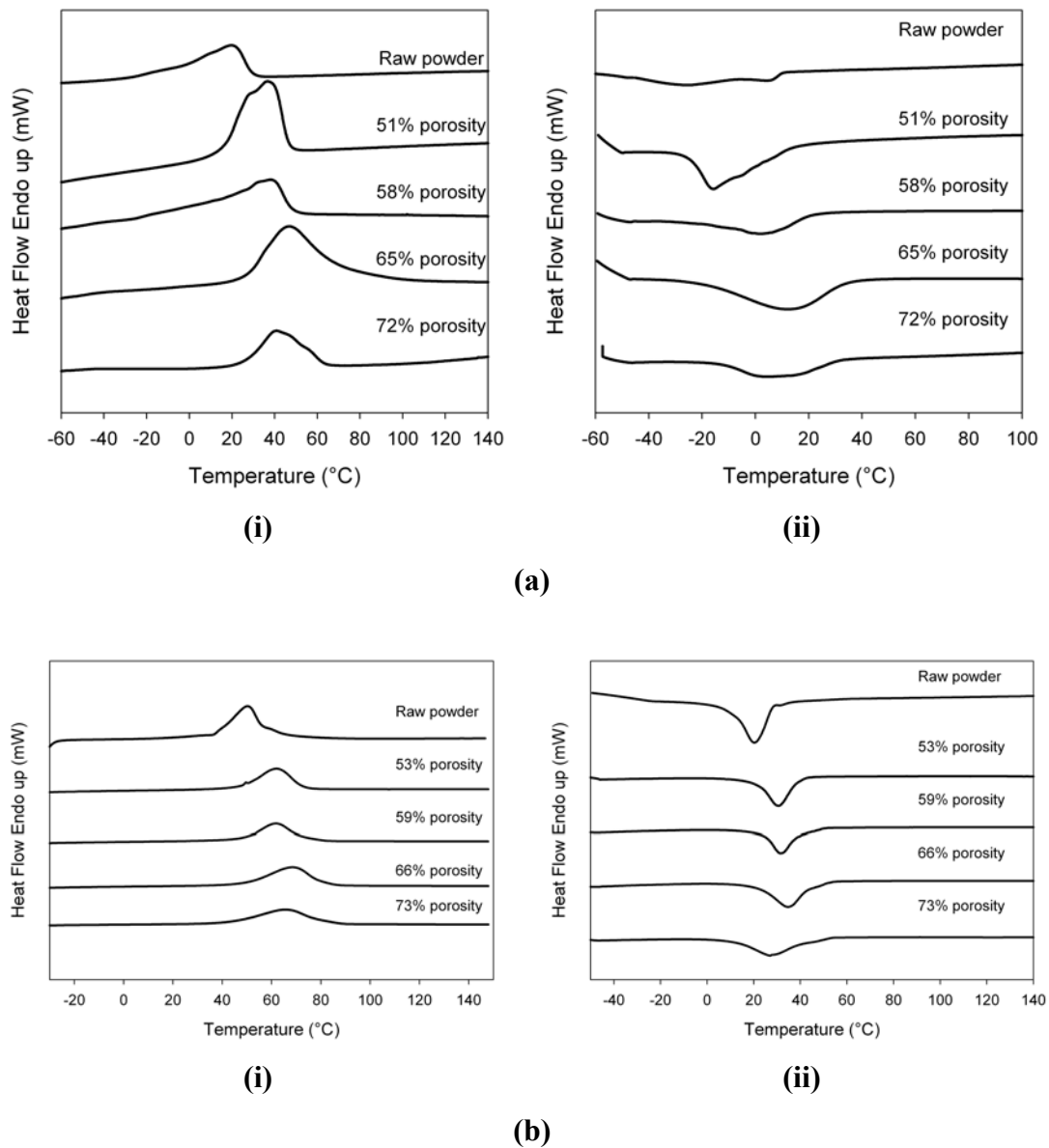
Figure 4.45 DSC curves of TiNi foams sintered at 1100 °C for 2 hours with different porosities. (a) Ti-50.6 at. %Ni powder and (b) Ti-50.4 at. %Ni powder. (i) heating, (ii) cooling.

Increase in the transformation temperatures of the foams produced, compared to the starting prealloyed powder, was in the range 8-20 °C for M_s and 17-38 °C for A_f temperatures in Ti-50.6 at. %Ni foams and 12-19 °C for M_s and 15-25 °C for A_f temperatures in Ti-50.4 at. %Ni foams. A similar tendency was observed also for the peak transformation temperatures as can be seen from Table 4.9. Latent heats of transformations, especially those for the foams produced from Ti-50.4 at. %Ni, were found to be similar to those of the bulk TiNi alloys with the same composition [233].

Table 4.9 Phase transformation temperatures and the corresponding latent heats of transformations of porous TiNi samples sintered at 1100 °C for 2 hours.

Powder used	Porosity (%)	Phase transformation temperatures (°C)						Latent heat of transformations (ΔH, J/g)	
		M_s	M_p	M_f	A_s	A_p	A_f	$-\Delta H_{forw}$	ΔH_{rev}
	powder	10	-25	-53	-11	20	30	14.4	13.8
	51	18	-16	-25	16	36	47	16.8	19.3
Ti-50.6 at. %Ni	58	20	6	-14	-1	38	49	11.4	16.5
	65	30	12	-19	26	46	68	17.1	18.8
	72	28	4	-10	24	40	60	28.4	18.9
		M_s	M_p	M_f	A_s	A_p	A_f	$-\Delta H_{forw}$	ΔH_{rev}
	powder	28	20	10	36	50	58	18.3	18.3
	53	40	31	20	47	62	73	23.6	23.1
Ti-50.4 at. %Ni	59	43	31	21	50	62	75	22.5	22.7
	66	47	34	21	52	68	80	24.2	24.8
	73	46	27	13	47	66	83	27.5	24.7

Since the porous TiNi alloys produced were chemically homogeneous, i.e. free from secondary intermetallics present in Ti-Ni binary system, increase in the transformation temperatures may be attributed to porosity, oxidation or the deformation which is unavoidable during cutting the samples despite the low cutting speeds employed. But there does not seem to be an obvious reason for the transformation temperatures to be affected directly from porosity content. Ti_3Ni_4 precipitates may be formed during cooling after processing, although they were not observed in XRD analysis. These precipitates consume more nickel atoms in the

matrix compared to titanium atoms during their formation. Then transformation temperatures of the foams increase due to nickel depletion in TiNi matrix. However, only Ti-50.6 at. %Ni foams produced in the present study are capable of precipitation. On the other hand, increments in phase transformation temperatures in Ti-50.4 at. %Ni foams are at similar levels with those of Ti-50.6 at. %Ni foams. Therefore, increase in martensitic transformation temperatures can not be attributed to Ti_3Ni_4 precipitates.

Increase in the transformation temperatures with the porosity content of the samples is believed to be more closely related with the oxidation of the samples as elaborated in the following. TiNi foams in the present study were produced using a new space holder material, magnesium, which creates a strongly reducing atmosphere during sintering of prealloyed TiNi powders. Sintered foams consisted of single B2 austenite or a mixture of B2 austenite and B19' martensite phases depending on the composition of the powders used. As explained before, sintering of TiNi alloys under protective Mg atmosphere ensures contamination free specimens, not attainable by other techniques such as SHS, HIP, argon sintering or MIM. Amount of Mg added to the compacts during sintering seems to be the major parameter effective on phase transformation temperatures. Since pores are formed by the Mg particles added as space holder, porosity of the foam is directly correlated with the amount of Mg added and hence, their effect on the transformation temperatures are equivalent. Transformation temperatures increase with porosity content due to the increase in Mg addition which reduce the oxidation tendency. This is confirmed also by comparing the phase transformation temperatures (Table 4.9) of the Ti-50.6 at. %Ni foams with 51 and 58% porosity or Ti-50.4 at. %Ni foams with 53 and 59% porosity. They have almost the same transformation temperatures because despite the difference in porosity, same amount of Mg was added (part as space holder rest as oxygen getter) into both crucibles during sintering. Figure 4.46 shows the heating DSC curves of Ti-50.6 at. %Ni TiNi foams with porosities around 43 and 51% but sintered without extra Mg addition. Decrease in A_s and A_f temperatures due to oxidation are clearly observable. Both foams did not show a clear transformation upon cooling. As it is well known, an increase of 1% in oxygen content results in a 100 °C decrease in transformation temperatures.
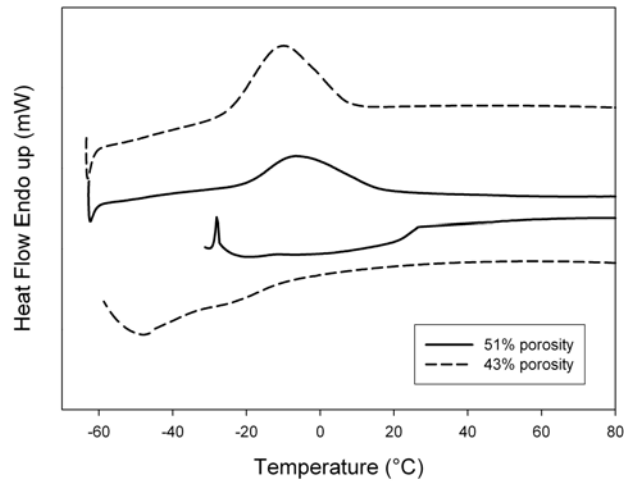
Figure 4.46 DSC charts of porous TiNi samples produced using Ti-50.6 at. %Ni powder without addition of extra magnesium as getter.

Figure 4.47 shows the effect of Mg addition or porosity content on A_s, A_p and A_f temperatures. Lower porosity foams did not show a distinct forward transformation as stated before thus, they were not shown in the figure. It is apparent that transformation temperatures are highest around 65% porosity level (obtained by addition of 60% Mg) which can be presumed to be completely free of oxidation because further Mg addition did not cause a considerable change in the transformation temperatures.

Figure 4.48 presents the transformation tempereature change with porosity in Ti-50.4 at. %Ni foams. M_f and M_p display a little drop with increasing porosity in contrast to M_s, A_p and A_f all increasing slightly. A_s temperature stays at the same level through different porosities. Actually, all the transformation temperatures of Ti-50.4 at. %Ni foams were found to be more stable than those of Ti-50.6 at. %Ni foams and did not exhibit pronounced change with porosity content. Ti-50.4 at. %Ni powders used in foam production are two times larger in size (40 µm) than Ti-50.6 at. %Ni powders (21 µm) corresponding to a considerably smaller surface area. Since diffusion of oxygen towards the surface to be reduced by magnesium require much time, the experiment period of 2 hours was not sufficient for the oxygen to be effectively removed from the coarse Ti-50.4 at. %Ni powders. That is why they have a lower increment in phase transformation temperatures.

137

Figure 4.47 Effect of porosity on transformation temperatures for porous TiNi alloys produced from Ti-50.6 at. %Ni powder. Unfilled legends (used in regressions) represent the phase transformation temperatures of 43 and 51% porous foams sintered with extra magnesium.

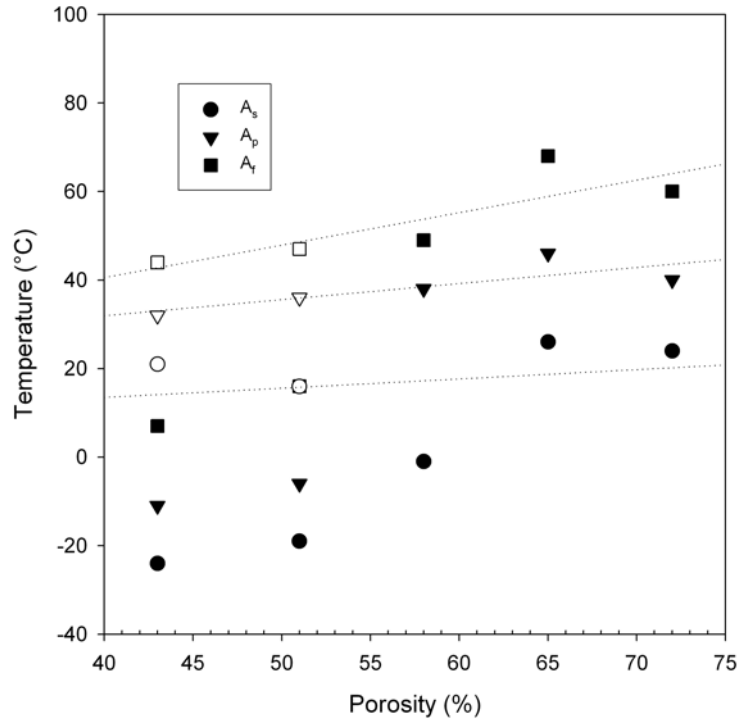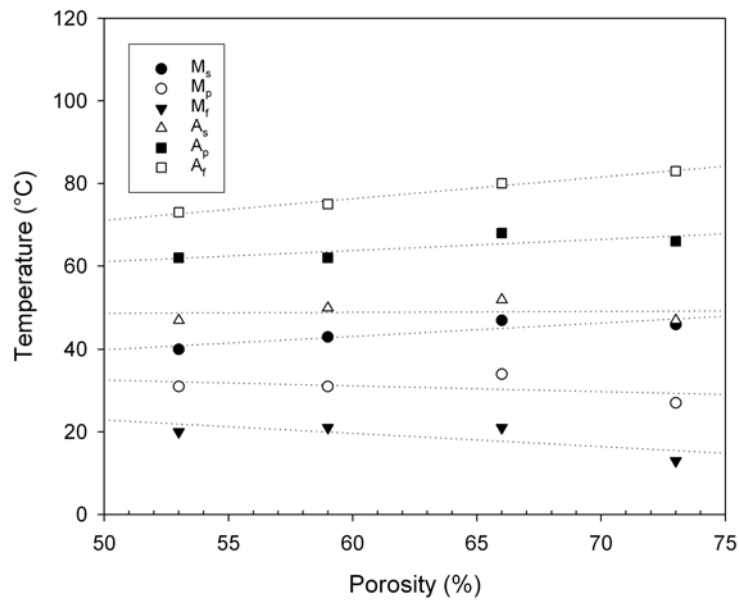**Figure 4.48** Effect of porosity on transformation temperatures for porous TiNi alloys produced from Ti-50.4 at. %Ni powder.

138

4.2.2.2. Influence of Deformation during Sampling on Phase Transformation Temperatures

Deformation during DSC sample cutting operation has been responded quite differently by samples of different composition and porosity. For example, porous samples of Ti-50.4 at. %Ni were effected less from deformation during the cutting process than the Ti-50.6 at. %Ni ones because they are softer due to the martensite phase present and display less resistance to deformation. In a similar manner, since the samples with lower porosity exhibit higher resistance to deformation, density of dislocations created in them during cutting is expected to be more in addition to the spatial variations, compared to that in samples of higher porosity. In turn, the transformation temperatures are expected to be effected from the porosity content of the samples as well as the composition through their differing contribution to the deformation microstructure during sample cutting, as will be further discussed below. However, increase in the transformation temperatures by around 20-30 °C in the present study cannot be justified by the deformation alone considering the behaviour of the samples to which lower cutting speeds applied.

Transformation temperatures were observed to increase when the cutting speed employed in sample preperation for DSC analysis increased as shown in Figure 4.49. Also, the DSC peaks became more distinct and narrow at higher cutting speeds compared to the ones obtained from the samples cut at lower speeds. This behavior proves that specimens produced, in fact, do not have compositional inhomogeneties which would be concluded incorrectly just examining the DSC curves obtained from the specimens cut at lower speeds. Broadening of the peaks as a result of slow cutting may arise from inhomogeneous deformation of the specimens, which also leads to incomplete transformations. On the contrary, fast cutting results in homogeneous deformation leading to more distinct peaks, lower hysteresis and complete transformations as may be concluded from the latent heats given in Table 4.10. Since martensitic transformations take place with shear like mechanisms deformation facilitates transformations decreasing the driving force required and resulting in an increase in transformation temperatures. However, results obtained from fast cutting are found to be inaccurate. M_s and M_f temperatures found in the

range 35-38 °C and 5-20 °C, respectively imply that there should be martensite phase in addition to austenite in the samples. However, martensitic phase did not observed neither in XRD nor SEM analysis carried out at RT, as explained in detail in chapter 4.2.1.2.
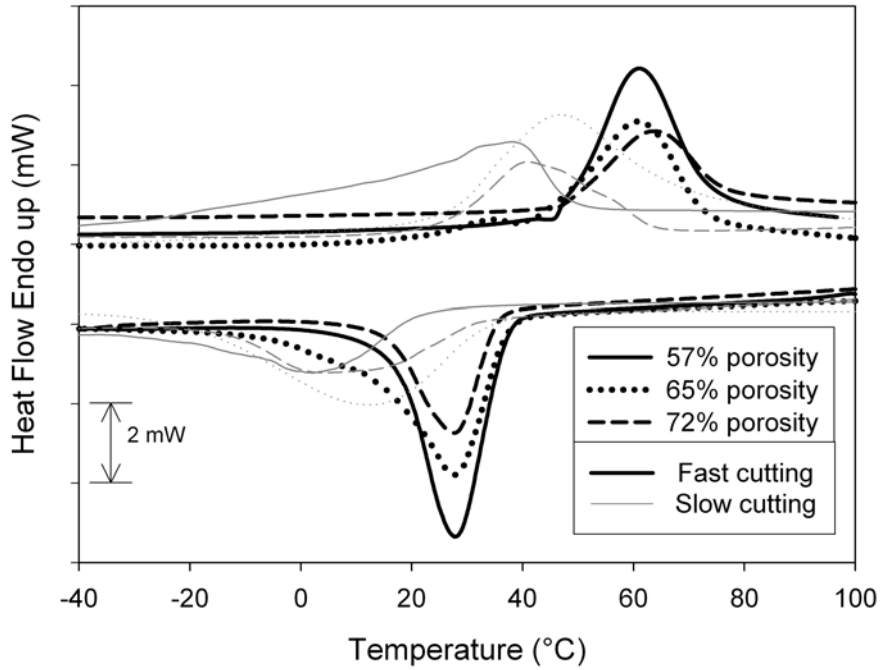
Figure 4.49 DSC charts of samples cut at low and high speeds from porous TiNi alloys fabricated from Ti-50.6 at. %Ni powder.

Table 4.10 Latent heats of transformations measured after fast and slow cutting of Ti-50.6 at. %Ni foams.

Porosity (%)	Latent heat of transformations (ΔH, J/g)			
	Fast cutting		**Slow cutting**	
	$-\Delta H_{forw}$	ΔH_{rev}	$-\Delta H_{forw}$	ΔH_{rev}
57	24.8	24.7	11.4	16.5
65	25.8	24.8	17.1	18.8
72	26.4	25.0	28.4	18.9

4.2.2.3. Aging effects on Martensitic Transformation Temperatures

DSC curves of aged specimens are given in Figure 4.50. From Figure 4.51 it is clearly seen that, the transformation temperatures, especially those for forward transformations, were increased considerably by aging treatment. Increase in M_s and M_f temperatures were found to be in the range 31-48 °C while in A_f temperatures it is found to be 20 °C in average. A_s temperatures on the other hand, did not display a considerable change interestingly and as a result hysteresis between forward and reverse transformations got narrower upon aging. DSC curves recorded during heating exhibited two superimposed endothermic peaks which appeared more distinctively for the specimens with porosities of 57 and 72%. However, only one distinct exothermic peak was observed during cooling for all the samples with different porosities.
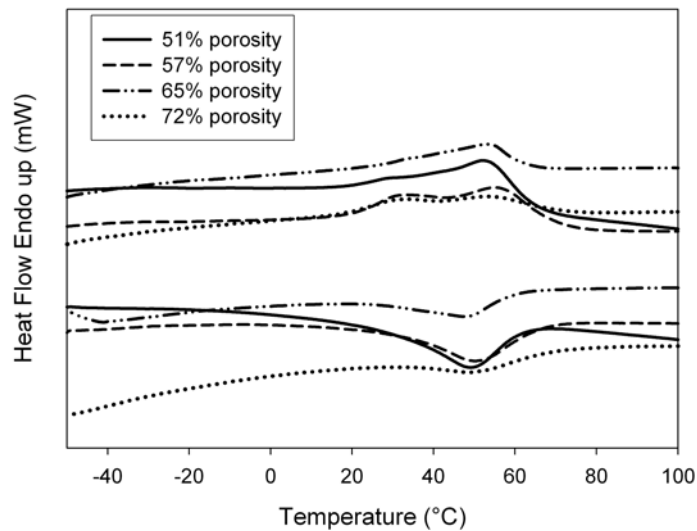
Figure 4.50 DSC curves of specimens aged at 400 °C for 1 hour.

It is thought that, formation of two superimposed peaks during heating is attributable to the chemical inhomogeneities that originate from Ti_3Ni_4 phase precipitation as a result of aging processing as confirmed by XRD results given in Figure 4.40. Precipitation of Ti_3Ni_4 phase give rise to a decrease in Ni content of parent TiNi matrix which results in an increase of the transformation temperatures.
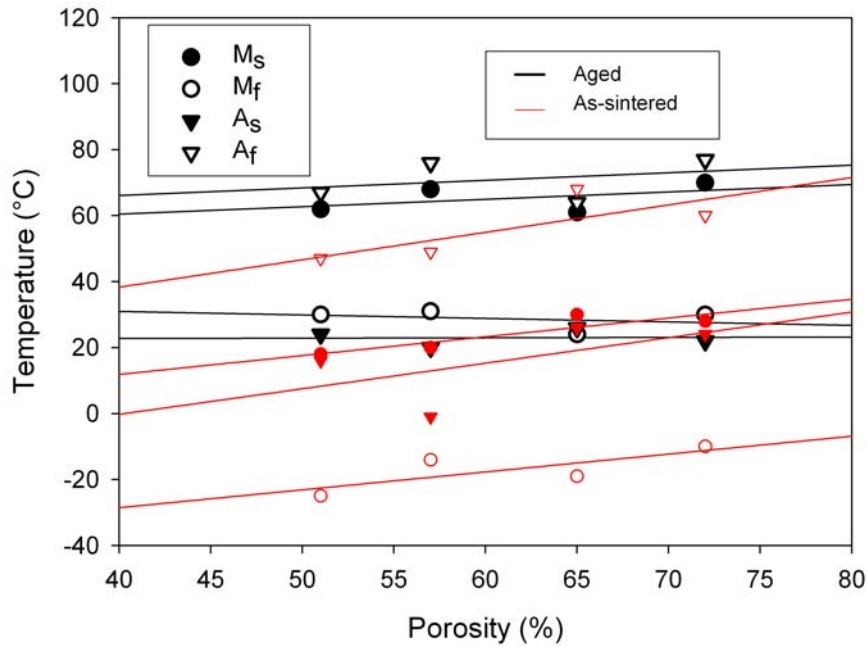
Figure 4.51 Effect of porosity on transformation temperatures in aged condition.

It has been shown [235-238] that, Ti_3Ni_4 precipitates formed during ageing are distributed inhomogeneously in Ni-rich TiNi alloys with lower Ni contents, such as the 50.6 at. %Ni alloy used in foam form for aging in the present study. Precipitates were found to prefer the grain boundaries and their vicinity. This precipitation behaviour explains why A_s temperatures did not change after aging process: the precipitate free zones (interior region of grains) start to transform much earlier than precipitate-rich regions leading to broadening of peaks during heating cycle of DSC.

Ti_3Ni_4 precipitates may favor R phase formation leading to two or more distinct peaks in DSC curves [6, 235-243], depending on whether the precipitate distribution is uniform or not in the TiNi matrix. R phase formation energetically may become favorable because transformation of austenitic B2 phase into martensitic B19' phase creates huge lattice strains while R phase formation from B2 end up with limited increase in lattice strain [6]. However, for its occurance R phase must be more stable than B19' martensite. Stress fields of coherent Ti_3Ni_4 precipitates may facilitate nucleation of martensite, but they behave also as obstacles preventing growth of martensites leading to incomplete transformations observeable from Table 4.11.

Why austenite is present as the main phase instead of martensite in the XRD pattern of aged 51% porous Ti-50.6 at. %Ni foam given in Figure 4.40 can be interpretted in terms of the DSC curves of aged porous TiNi alloys; Ms and M_f temperatures shift to around 60 and 25 °C in aged TiNi foams. Appearance of one single peak during cooling may results from B19' martensite being more stable than R phase or the individual peaks of formation of these two phases from austenite may be overlapping on DSC curves. Shorter aging periods also may cause precipitate density to be insufficient in strengthening the TiNi matrix so that transformation of B2 into B19' martensite is enhanced against R phase formation. It has been reported that Ti_3Ni_4 precipitates with a size close to 100 nm and coarser trigger R phase formation [244]. However, mechanism of this observation has not been mentioned by the authors. Aging treatment carried out in the present study is expected to form precipitates in size of only a few tens of nanometers considering the counterparts [6] done yet in bulk samples. These interpretations, which are not in the scope of present study, need further elaboration and require transmission electron microscoby (TEM) studies.

Table 4.11 Latent heat of forward and reverse transformations in aged samples.

Porosity (%)	Latent heat of transformations (ΔH, J/g)	
	$-\Delta H_{forw}$	ΔH_{rev}
51	4.1	7.5
57	4.3	8.5
65	2.9	10
72	1.5	5

4.2.3. Mechanical Behavior of TiNi Foams

4.2.3.1. Compression Behavior and Superelasticity Properties

Figure 4.52 shows the compressive stress-strain curves of the as-processed Ti-50.6 at. %Ni foams with various porosity contents and sintered at different

temperatures and times. It is clear that, compression behavior of porous TiNi produced by space holder technique in the present study differs from that of the typical elastic-plastic metallic foams which exhibit a linear elastic deformation region followed by a horizontal plateau region, and finally a densification stage as also proposed by Gibson and Ashby [245]. Open cells foams have a well-defined plateau stress because the cell edges and walls yield in bending resulting in plastic collapse or buckling of the foam. Plastic collapse occurs, when the moment exerted on the cell walls exceeds the fully plastic moment creating plastic hinges. However, closed cell foams show more complicated behavior which can cause the stress to rise with increasing strain because the cell faces are subjected to tensile stresses. In the present study, the horizontal plateau region that normally occurs in metallic foams has not been observed, as well as the last stage that corresponds to densification, except for highly porous specimens. Instead, a yielding region with linearly increasing stress is terminated by a maximum stress and followed by the collapse of the structure, as shown in Figure 4.52 (a) and 4.52 (b). This can be explained with pore-type and the distribution of neck size. Low porosity or high relative density foams have closed pores or cells. As a result, the plateau region of the stress-strain curves are not flat, and a slope increasing with decreasing porosity occurs. Every sintering neck formed randomly as a result of geometrical relations among the raw prealloyed powders actually behaves as a small compression sample of different shape, dimension and orientation experiencing the different stress even though the applied gross load is the same. Phase transformations occuring during loading, therefore, cannot take place at constant stress levels. Each of these necks transforms at roughly the same local stress which is achieved at different overall sample load and this sample load is the one used in calculating the stress used in plotting Figure 4.52. So we end up with a wide transformation region which commence by the transformation of smallest necks and terminate by transformation of the largest necks. However, higher sintering temperature (1200 °C) resulted in appearance of both horizontal plateau and densification stages at relatively lower porosity levels such as, 55 and 62% as can be seen from Figure 4.52 (c).
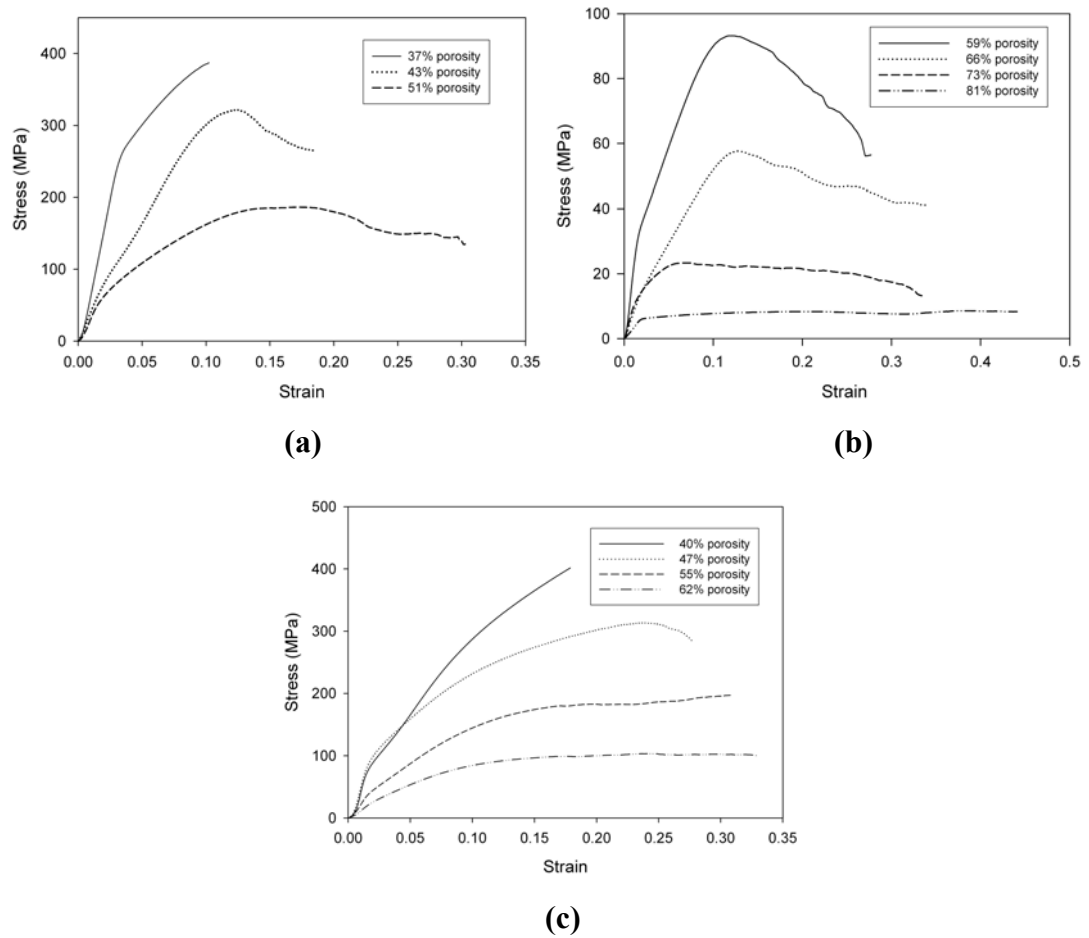
Figure 4.52 Stress-strain curves of Ti-50.6 at. %Ni foams produced by sintering at (a) and (b) 1100 °C for 1 hour, (c) 1200 °C for 2 hours.

Mechanical properties of the higher porosity foams produced by sintering at 1100 °C for 1 hour, as obtained from compression tests, are summarized in Table 4.12 together with the mechanical properties of cancellous bone [246] for comparison. TiNi alloy foams with 59% porosity appear to be appropriate for cancellous bone replacement applications despite the somewhat higher elastic moduli. TiNi foams with greater porosities, on the other hand, do not seem suitable for load bearing biomedical applications due to their insufficient strengths. TiNi foams with relatively lower porosities, 51% and less, were found to be appropriate for both cancellous and cortical bone (E= 12-17 GPa, σ_{cr}= 105-121 MPa, σ_{max}= 156-212 MPa [245, 246]) replacement applications, Figure 4.53 (a). TiNi foams

sintered at 1200 °C and with porosities in the range 40-55% were also acceptable as implant materials whereas 62% porous TiNi was insufficient in strength (125 MPa). However, sintering at higher temperatures, for example 1250 °C, may improve the strength by eliminating the micro-pores present in the cell walls. If these results are to be compared with those in literature; a porous TiNi with 57.3% porosity and having austenite and martensite phases together have been produced by SHS method to exhibit a high compressive strength (208 MPa) and a low elastic modulus (2.26 GPa) and a lower ultimate compressive strain (4.8%) [247]. In another study, a martensitic porous TiNi with 62-65% porosity produced also by SHS has been shown to display a low elastic modulus (1.21 GPa), and a similar compressive strength (122 ± 29 MPa) and ductility (22 ± 8%) [179]. But in both cases, because of the production technique, the foams suffer from inhomogeneous size, shape and spatial distribution of pores. The alloy foams produced in the present study, also meet the ductility requirement; while the strain to fracture for cancellous bone is around 7% all the samples produced exhibited fracture strains considerably higher than this value. In the light of the present results, space holder technique seems to be a promising method for production of porous TiNi alloys. Desired porosity level, pore shape and accordingly mechanical properties were found to be easily adjustable.

Table 4.12 Mechanical properties of TiNi foams sintered at 1100 °C for 1 hour and tested in compression, where E is Young's modulus, σ_{cr} is critical stress for inducing martensite (yield strength for cancellous bone), σ_{max} is compressive strength. The values given together with the standard deviations are average of four or more tests.

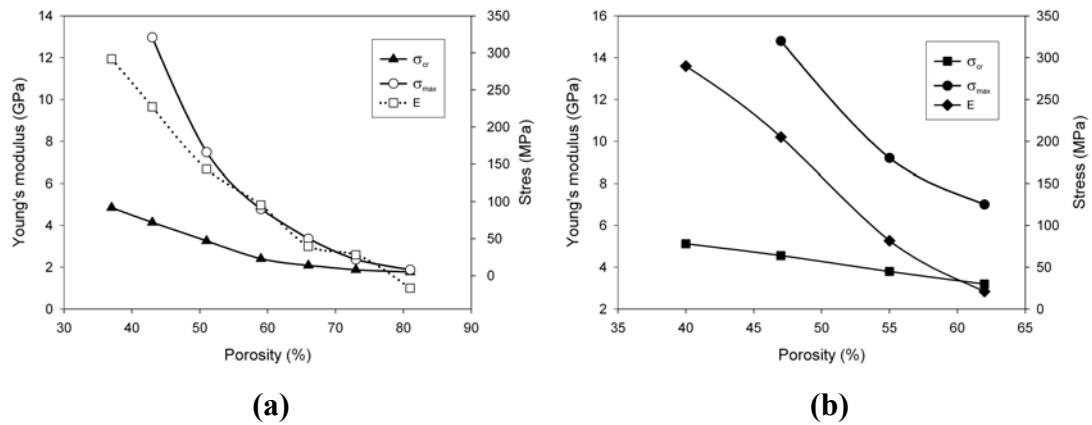| Porosity (%)	E (GPa)	σ_{cr} (MPa)	σ_{max} (MPa)
59	4.9±2.7	23±8	89±4
66	3 ±0.6	14±3	45±10
73	2.6±0.8	8±3	22±2
81	1±0.4	5±2	8±1
Cancellous bone	1±0.8	15±8	25±8

Figure 4.53 Effect of porosity on elastic moduli, compression strength and critical stress for inducing martensite in TiNi foams sintered at (a) 1100 °C for 1 hour and (b) 1200 °C for 2 hours.

Figure 4.54 shows the compressive stress-strain curves exhibiting the elastic shape recovery of porous TiNi shape memory alloys tested at room temperature in as-sintered condition. The figure reveals that both strength and Young's moduli of porous TiNi alloys and also the critical stress for inducing martensite decrease with increasing porosity, as expected. Moreover, it was concluded that the effect of porosity content on superelasticity is quite complicated. Specimens produced at 1100 °C, Figure 4.54 (a), displayed a better superelastic strain recovery with decreasing porosity. For example, specimen with 38% porosity recovers 65% of the total strain after unloading subsequent to 7.7% straining, while sample with a higher porosity (e.g. 51%) can recover only the 52% of the total strain after being deformed to a similar strain level, 7.2%. On the contrary, samples produced at 1200 °C, Figure 4.52 (b), with 40-47% porosity recovered similar amounts of strain upon unloading after they were deformed to 4% strain. Surprisingly, the sample with a higher porosity (62%) exhibited the best superelasticity. It may be attributed to its best macro-porosity distribution and accordingly more homogeneous pore/cell wall distribution. As a result, probably more homogeneous deformation of sintering necks and cell walls provided a better strain recovery. 1200 °C sintering also contributed to this behavior by strengthening the sintering necks. Since depending on the extent of oxidation of the samples transformation temperatures would vary,

147

slight oxidation of 62% porosity sample would also be the reason of the better strain recovery.
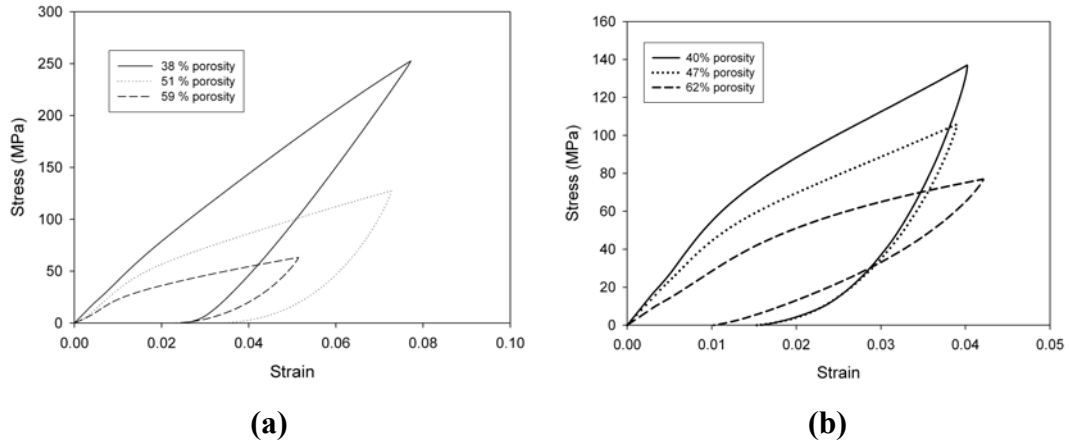
Figure 4.54 Room temperature **s**tress-strain behaviour of porous TiNi alloys with different porosity sintered at (a) 1100 °C for 1 hour and (b) 1200 °C for 2 hours.

It was also observed that, superelastic strain recovery was incomplete for all the specimens with different amounts of porosities due to both accompanying dislocation deformation and test temperatures lower than A_f temperatures of the specimens. It is well known that, there are two main requirements to be met for complete superelastic behaviour. Firstly, critical stress for slip must be higher than critical stress initiating martensite formation upon loading. Thus, it is ensured that deformation occurs by only stress-induced martensitic (SIM) transformation mechanism, which is completely recoverable up to 7% strain in compression [248]. In case of slip, which occurs by dislocation motion, deformation is fully stable and cannot be recovered. Secondly, test temperature must be higher than A_f temperature of the superelastic material. Otherwise, strain applied may not be recovered fully because all the martensite plates created during loading are not completely unstable at a temperature lower than A_f. It should also be noted that increase in transformation temperatures resulting from deformation during testing may lead to SIMs to be stable at constant testing temperatures even higher than A_f. Therefore, superelasticity tests aiming perfect strain recovery either in tension or compression

are usually conducted in a temperature range 10-20 °C greater than A_f temperature [249] in order to compensate the stated temperature increase. As it is well known that, superelasticity mechanism can operate up to M_d temperature, which is the maximum temperature for superelastic deformation. However, while critical stress for inducing martensite increases only slightly with increasing temperature, temperature increase results in an appreciable decrease in the critical stress for slip. T_c is the minimum temperature where slip starts to occur. Consequently, complete superelasticity could be attained in a narrow temperature range, between A_f and T_c.

Figure 4.55 (a) and 4.55 (b) present the stress-strain curves, obtained at different temperatures under constant stress conditions, for respectively 51% and 59% porous, TiNi alloys sintered at 1100 °C for 1 hour. Strength, Young's moduli and critical stress for SIM formation increase with increasing test temperature. Table 4.13 summarizes the % unrecovered strains of the same set of specimens. It is clear that, irrecoverable strain decreases with increasing temperature under constant stress conditions, but they are still present even at temperatures greater than A_f due to partial stabilisation of martensite formed by applied stress. A few samples that have been deformed at room or body temperatures were then heated to austenitic temperatures where additional strain recovery by shape memory mechanism has been observed. For example, residual strain decreased from 3.75% to 1.8% when the porous TiNi alloy with a porosity level of 51% was subjected to this procedure. Nevertheless, complete strain recovery could not be achieved proving that both dislocation motion and SIM transformation occured during loading. Miyazaki et. al. [50] reported that bulk TiNi with the same Ni content (50.6 at. %Ni) has a critical stress for dislocation motion (slip) around 400 MPa (in tension and corresponding to 8% strain) in solutionized and quenched condition. Exceeding this stress level results in incomplete superelasticity. Although we have not increased the stress during experiments to such high levels, we observed incomplete strain recovery. Reason might be inhomogeneous deformation during compression test. Since every individual sintering neck (load bearing walls) with a different shape, dimension and orientation will be exposed to different stresses during the test resulting in different strain levels. For example, two sintering necks with the same shape (having exactly the same load bearing areas) and orientation but with different heights, one of them

149

is just 20% of the other, will deform certainly up to different strain levels. When the longer neck experiences 6% strain, 30% strain will exist on the shorter one. Higher strain levels end up with plastic deformation of martensite plates formed previously from austenite by stress-induced martensite mechanism. These plastically deformed martensites can not retransform into austenite upon unloading due to interlocking of the mobile austenite-martensite interfaces by the dislocations created.

(a)   (b)
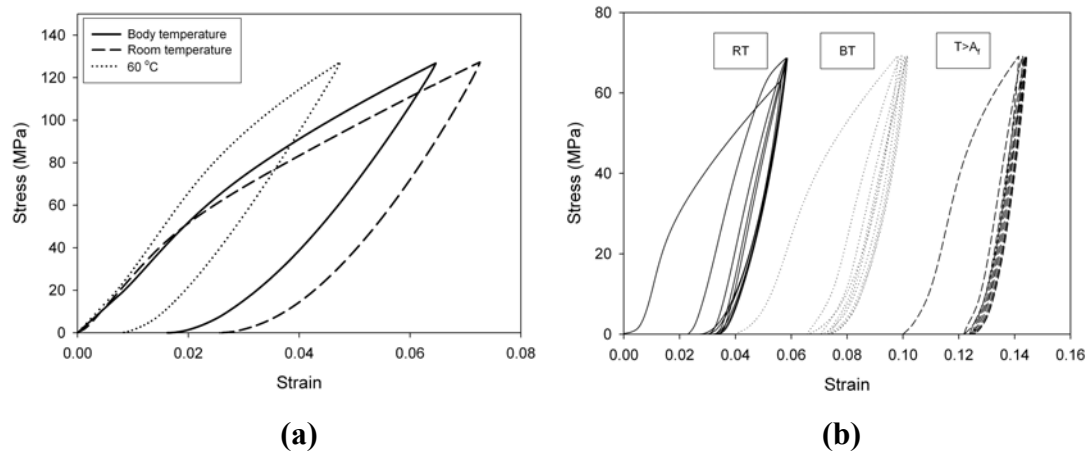
Figure 4.55 Influence of temperature on superelasticity and mechanical behaviour of porous TiNi alloys sintered at 1100 °C for 1 hour, (a) 51% porosity and (b) 59% porosity.

Table 4.13 Unrecovered strain-temperature-porosity relationship of the set of specimens given in Figure 4.55.

Porosity (%)	Unrecovered strain (%)		
	RT	BT	$T>A_f$ (60 ^{o}C)
51	42	32	22
59	51	31	26

Superelastic behaviour of porous TiNi alloys under compression differ from that of the bulk ones. Bulk TiNi alloys exhibit a complete superelasticity hysteresis loop in appropriate stress ranges, if they were subjected to suitable thermomechanical

treatments. However, almost linear stress-strain regions (plateau regions) displayed during both forward and reverse phase transformation are more steeper in compression than that observed in tension test, recoverable strain levels are smaller and also higher critical transformation stress levels are observed during compression test [250-256]. In tension testing of polycrystalline materials grains with different orientations align themselves in the loading direction. On the contrary, grains cannot orient themselves in the loading direction when they are deformed in compression mode. Moreover, applied load is less uniaxial and homogeneous in compression when compared to one which is in tension. These inherent compressive characteristics are much more effective in case of porous TiNi alloys where the load is carried by the cell walls. In fact, great amount of the load is carried by the sintering necks when sintering is not complete as in the present study. The sintering necks formed randomly as a result of geometrical placement of the raw prealloyed powders have different shapes and dimensions and also different orientations. Therefore, they inevitably deform at different stress levels that they experience even though the applied gross load is the same. Phase transformations occuring during loading and unloading steps, therefore, cannot take place at constant stress levels. Instead, transformations become possible at different stress levels. That is why almost horizontal stress-strain regions (plateau regions) are not observed in porous TiNi alloys.

Figure 4.56 shows the stress-strain curves of 59% porous specimens deformed at three different strain levels. It can be seen that unrecovered residual strains increase with increasing strain amount. Two virgin specimens deformed at lower stress levels (45 and 60 MPa in the figure) while the third one was loaded to 80 MPa and unloaded prior to deformation around 7%. However, it was the specimen having the most residual strain due to having highest dislocation density.

Figure 4.57 presents the effect of cycling under constant compressive stress on superelastic properties of porous TiNi alloys at room temperature. The magnitude of the residual strains have been found to decrease with increasing number of cycles for each specimen with a different porosity. At the end of the fifth cycle there were no apparent residual strain observable anymore as can be seen clearly from Figure 4.57 (d).
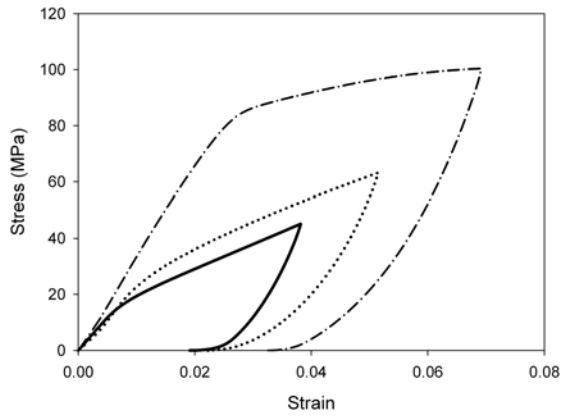
Figure 4.56 Effect of strain level on the strain recovered by superelasticity at room temperature testing of 59% porous specimen sintered at 1100 °C for 1 hour.
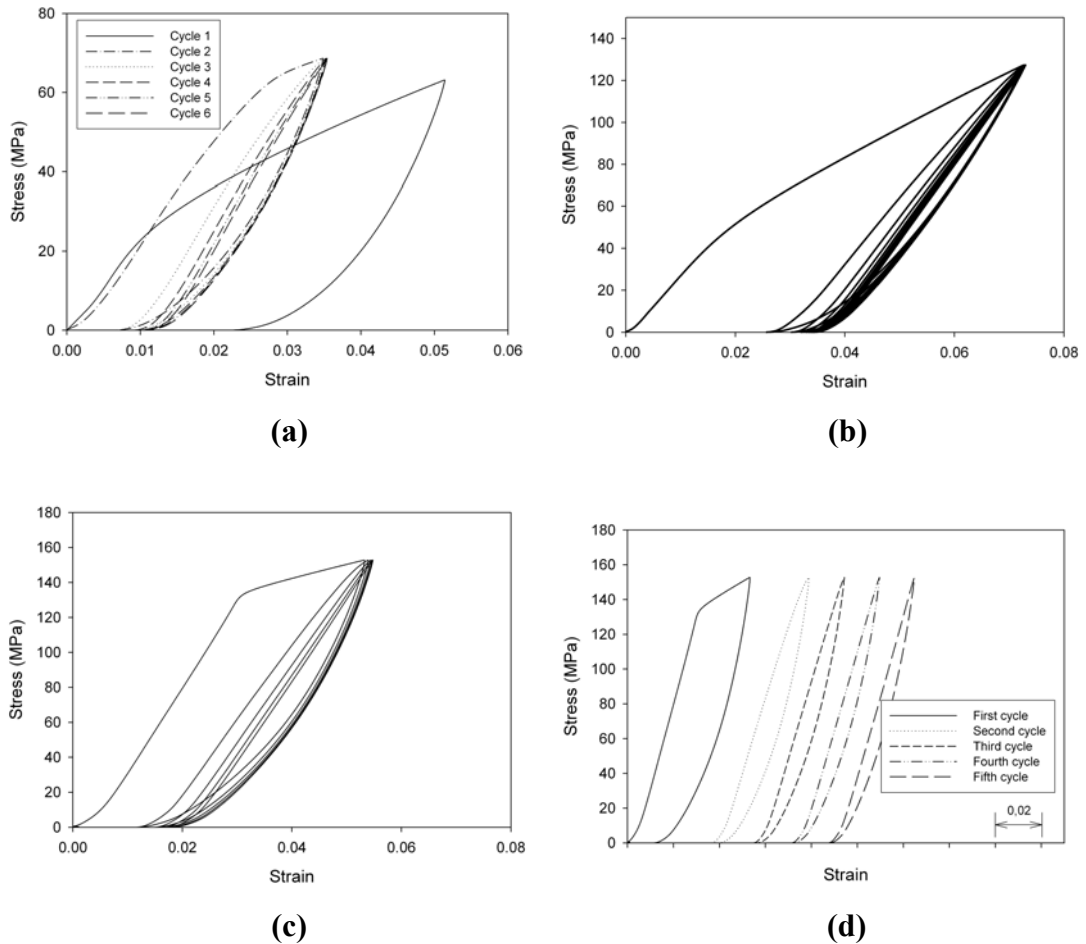

Figure 4.57 Effect of cycling on superelasticity behavior of porous TiNi alloys produced at 1100 °C for 1 hour: (a) 59% porous at 70 MPa, (b) 51% porous at 125 MPa, (c) 51% porous at 150MPa (same specimen used in b) and (d) individual cycles in c. (Test temperature: RT)

Figure 4.58 (a) exhibits typical compressive stress-strain curves of a porous TiNi sample with a porosity of 43% loaded and unloaded cyclicly five times at six different stress levels. It is obvious from the figure that, after first loading and unloading cycle, reloading the porous specimen up to the same stress level induces almost a linear deformation behaviour. When the stress applied is increased to a higher value, deformation occurs linearly until the previous stress level is reached. After that, deformation deviates from linearity and proceeds in a similar manner observed in prior cases. Critical stress for SIM is attained at different levels by sintering necks due to stress gradients forming locally leading to inhomogeneous deformation of porous TiNi alloys. Thus, forward transformation during loading may occur even in elastic region leading to lower elastic moduli. When observeable critical stress is attained, dislocation motion severely accompanies the martensitic transformation resulting in deviation from linearity. When porous TiNi is reloaded at the same stress, there will not be additional dislocation motion, hence, deformation will take place by elastic and SIM transformation mechanisms only. When conditions are suitable (e.g. test temperature is higher than A_f and no martensite stabilisation due to serious deformation) all the strain will be recovered. If the stress applied is higher than the previous one, firstly elastic deformation and SIM transformation will occur up to previous stress level, and then dislocation motion will take place together with SIM transformation. Stress-induced martensites are then going to be subjected to plastic deformation due to the different geometrical properties of sintering necks. Note that, it is not possible to obtain end of the elastic deformation accurately from the stress-strain curves after first cycle.

Practically porous TiNi shape memory alloys are aimed satisfy main prerequisites for implantation purpose in terms of mechanical properties such as high strength (min. 100 MPa at 2% strain) and more than 2% recovered strain after having been deformed to 8% strain [135]. Recovery condition has been already fulfilled in as-processed condition however sufficient strength can not be provided even by the most dense specimen (37% porous) produced in the present study except for the test conducted at a temperature greater than A_f. Having applied cyclic loading (higher than 100 MPa) and unloading, it was found that porous TiNi alloys with porosities 37%, 40%, 43% and 47% meet the strength requirement even at

room temperature, while the 51% porous TiNi satisfies the requirement only at temperatures higher than A_f. 3.8% strain has been completely recovered by 43% porous specimen after 5 cycles at 150 MPa while strain recovered completely was 3.3% for 37% porous specimen after cyclic loading and unloading at 215 MPa for 5 cycle. Cyclic loading and unloading might be a cheap and easy alternative method to aging treatment in order to improve superelasticity properties of porous TiNi alloys. By applying this basic mechanical treatment, good linear superelasticity can be attained. Also the strain amount desired to be recovered fully for a specific application is readily predictable due to linear nature of superelasticity observed in porous TiNi alloys. Another solution to increase strenght may be use of higher nickel content TiNi powders such as 50.8 and 51% at. initially. Then the transformation temperatures of the foams, especially A_f would be lower than body temperature.

(a)   **(b)**
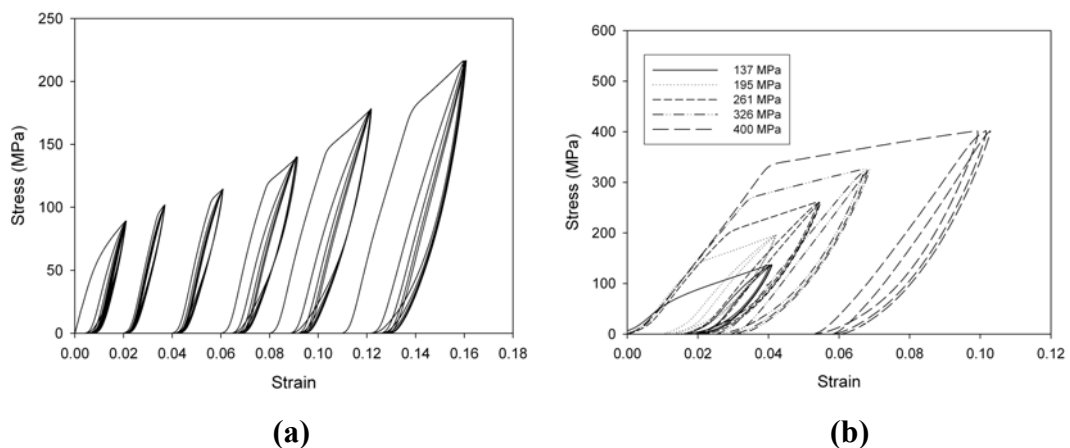
Figure 4.58 Stress-strain curves of (a) 43% porous (1100 °C, 1 hour) and (b) 40% porous (1200 °C, 2 hours) TiNi alloys exposed to subsequent loading and unloading cycles at different stress levels.

Figure 4.59 displays the effect of cyclic loading and unloading or pre-straining on strength and ductility. Ductility has been accepted as the strain corresponding to stress level at which first crack occurs in this study. Because porous metallic alloys do not fracture suddenly even at very high strains in compression. Maximum compression strength seems to be not dependent on pre-straining but decrease in

ductility is quite severe especially for the foam sintered at 1100 °C for 1 hour. It is obvious from Figure 4.59 (a) that after cyclic loading for 20 times at 150 MPa initiation of the first crack occured at half of the strain determined for a virgin porous TiNi alloy with the same porosity of 51%. Since 1200 °C, 2 hours sintering results in stronger and more homogeneous sintering necks the foam produced in this condition exhibited less decrease in ductility.

(a)   (b)
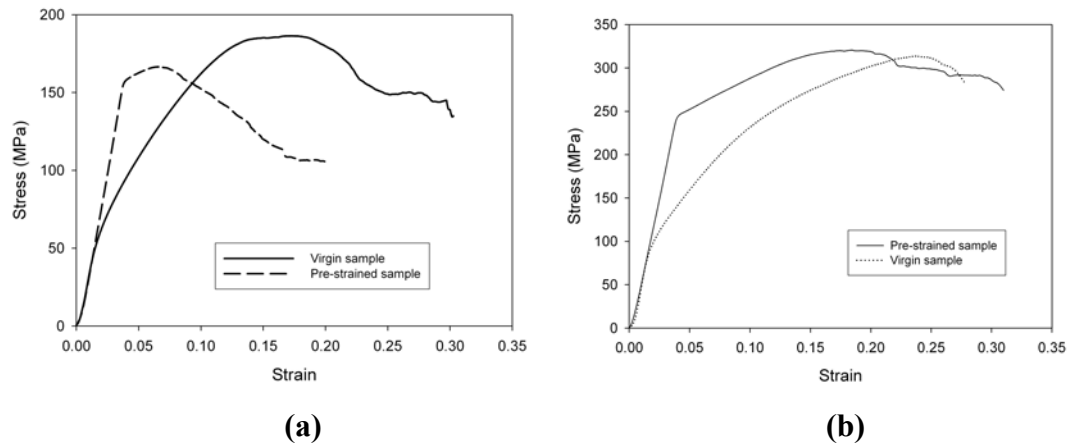
Figure 4.59 Effect of 20 cycles of pre-straining on maximum compression stress and fracture strain. (a) 51% porosity (1100 °C, 1 hour), (b) 47% porosity (1200 °C, 2 hours).

Figure 4.60 presents ambient temperature compressive stress-strain curves of 37 and 47% porous TiNi shape memory alloys in as-processed and aged at 400 °C for 1 hour conditions. Since the aged specimens exhibited insufficient superelastic behaviour at room temperature, all of the subsequent compression tests were carried out at only 80 °C, which is greater than A_f temperatures of aged porous TiNi alloys. Aged specimens composed of martensite and austenite phases at room temperature were deformed by detwinning or reorientation of martensite plates present and SIM transformation of austenite during compression tests. As a result, strain recovery decreased since detwinned martensites transform into austenite only by heating. Furthermore, higher transformation temperatures of aged samples led to irrecoverable strains stabilizing the martensites formed by SIM mechanism during testing.

155

(a)   **(b)**

Figure 4.60 Room temperature stress-strain diagrams of porous TiNi alloys with a porosity of (a) 37% (1100 °C, 1 hour), (b) 47% (1200 °C, 2 hours) in as-processed and aged conditions.
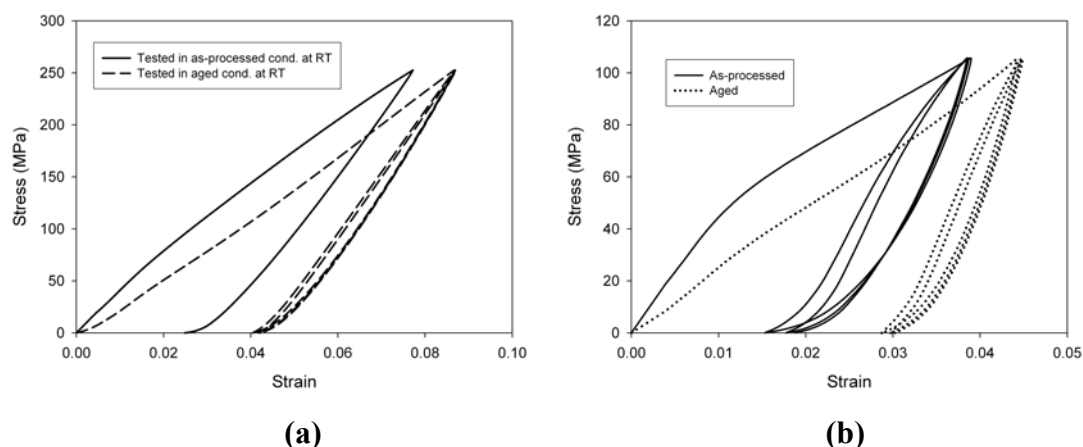
Stress-strain diagrams of aged porous TiNi alloys tested at 80 °C are given in Figure 4.61. Better superelastic strain recovery has been observed compared to specimens tested at room temperature or body temperature in as-sintered conditions. Greater strain as high as 5% have been recovered as can be seen from Figure 4.61 (a) and 4.61 (b). However, results were quite similar to the ones obtained at 60 °C from the samples with the same porosity level in the as-processed condition (Figure 4.61 (c)). Coherent Ti_3Ni_4 precipitates formed during aging process act as nucleation site for martensite during deformation. In addition, they also behave as obstacles for dislocation motion. As a result, they increase the critical stress for dislocation motion while decreasing the critical stress for inducing martensite as reported by Miyazaki et. al. [33]. They stated that, after 1 hour aging at 400 °C, bulk Ti-50.6 at. %Ni alloy has a critical stress for slip around 500 MPa. Stress fields created around Ti_3Ni_4 precipitates and decrease in Ni content of the TiNi matrix are the main mechanisms which favour stress-induced martensitic transformations. After the aging process all the strains up to 7% (in compression) should be recovered in normal conditions and this is almost achieved in bulk TiNi alloys. However, porous TiNi alloys could not manage to recover all the strain applied even when as low as %3.5 as can be seen from Figure 4.61 (d). It is clear that, incomplete superelasticity is result of martensite stabilisation as elucidated before. Figure 4.62 also confirms

156

this opinion. SEM micrographs in the figure shows martensite plates formed during compression test in as-sintered samples.

(a)

(b)

(c)

(d)

(e)
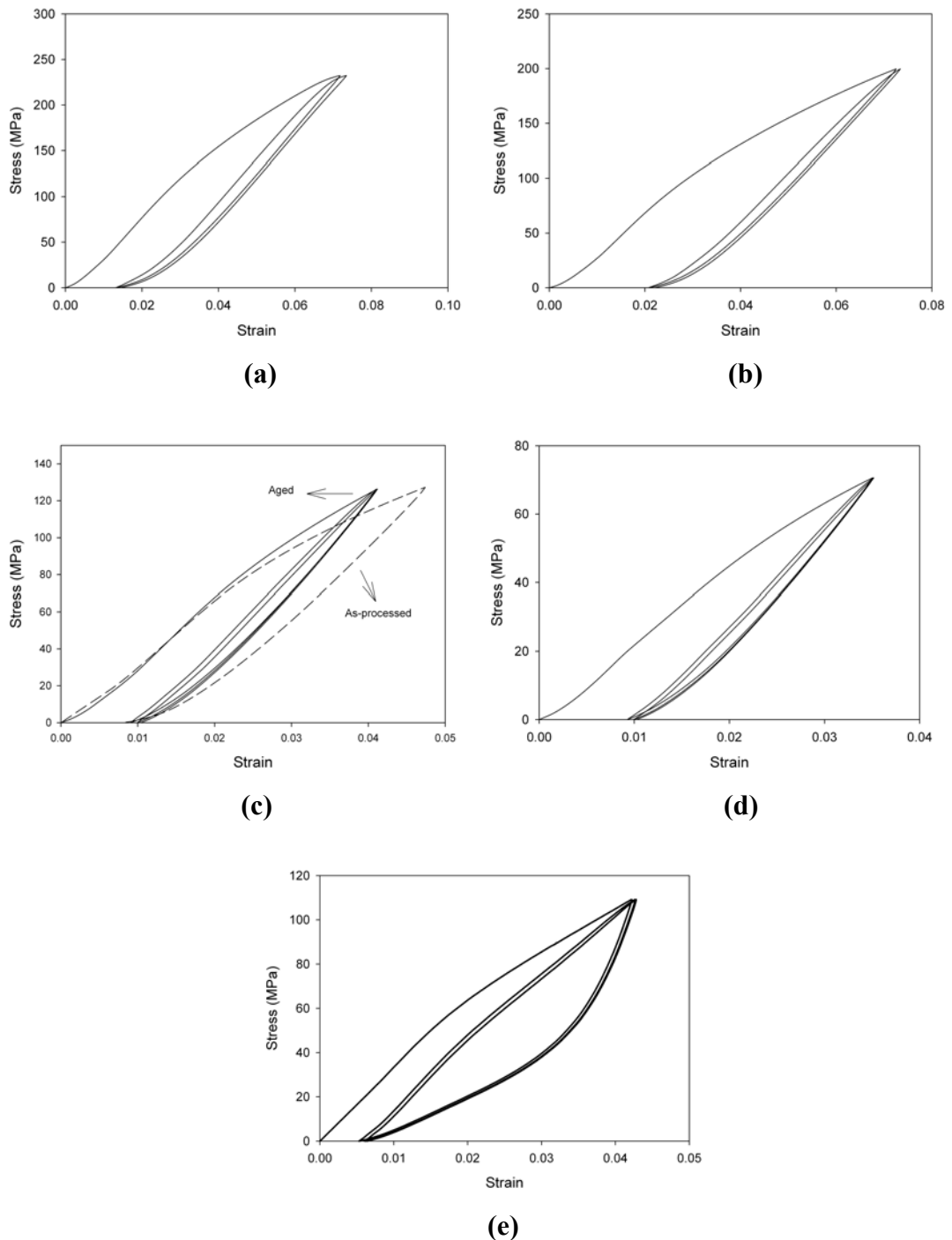
Figure 4.61 Stress-strain curves of porous TiNi alloys with different porosities aged at 400 °C for 1 hour and tested at 80 °C, (a) 37% porosity (1100 °C, 1 hour), (b) 43% porosity (1200 °C, 2 hours), (c) 51% porosity (1100 °C, 2 hours) (also shows the as-sintered condition), (d) 59% porosity (1100 °C, 1 hour), (e) 55% porosity (1200 °C, 2 hours).
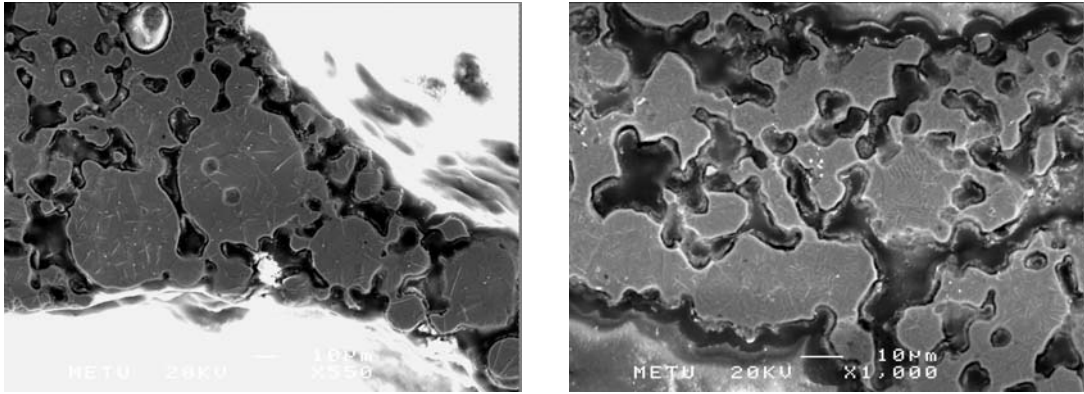
(a)   (b)

Figure 4.62 SEM micrographs of as-sintered (1200 °C, 2 hours) porous TiNi alloys after deformed to 6% strain in compression test. (a) 55% porosity, (b) 43% porosity.

Figure 4.63 represents typical stress-strain curve of aged TiNi foam with a porosity of 55%. As it is obvious from the figure, aging improved the strength of the foam at the expense of reducing the ductility to half. Aged sample (A_f: 67 °C) was tested at 70 °C whereas as-sintered one (A_f: 37 °C) at 40 °C to eliminate temperature effect.
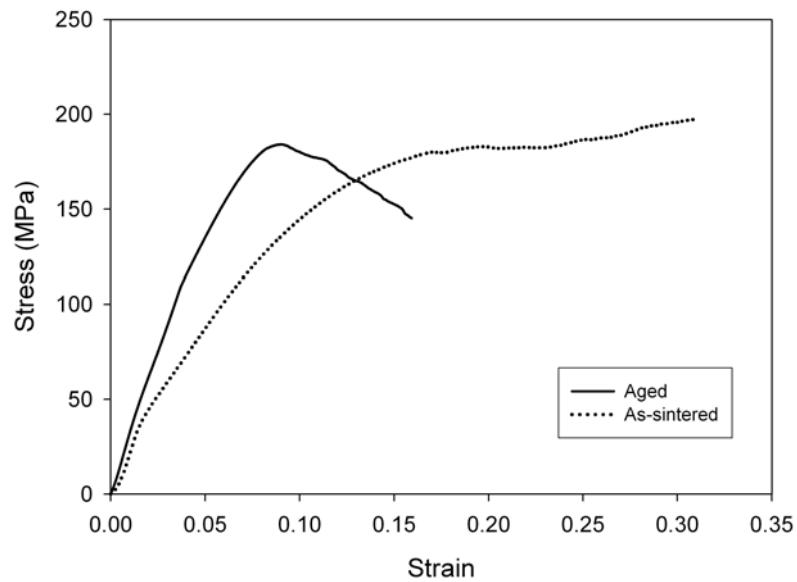
Figure 4.63 Stress-strain curve of aged TiNi foam with a porosity content of 55%. (Sintered at 1200 °C for 2 hours and subsequently aged at 400 °C for 1 hour)

158

Figure 4.64 presents elastic moduli-porosity-temperature relationship in as-processed and aged conditions. Elastic moduli decrease linearly with increasing porosity while increasing with increasing temperature. Aged porous TiNi alloys exhibit lower values compared to as-processed ones at a temperature greater than A_f. Fine precipitates formed during aging is responsible from this behaviour. They favour SIM transformation decreasing required critical stress level. All the foams produced except for 59% porous and higher, are suitable for biomedical applications in terms of elastic moduli criteria. They have similar values with the compact bone, 12-17 GPa. Lower elastic moduli results from partial sintering of TiNi powders during processing. Since temperature is much more effective than time in sintering higher temperatures must be used for better stiffness. Elimination or minimisation of micro-pores provide higher elastic moduli and mechanical features.

Figure 4.64 Change of Young's modulus with porosity at different temperatures in as-processed and aged conditions.

Table 4.14 shows the comparison of mechanical properties of TiNi foams, with similar porosity amounts, produced applying different processing routes. TiNi foams

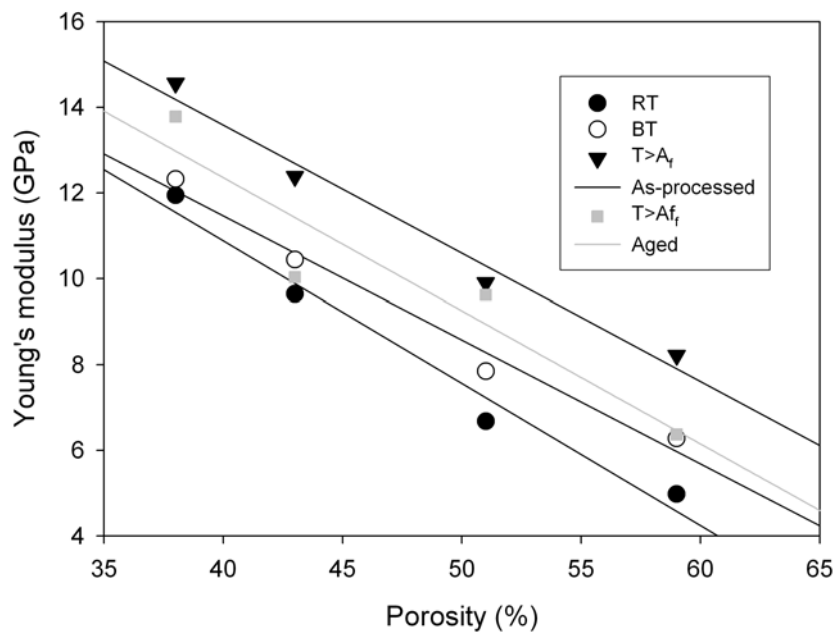produced by CS and SHS have the lowest strength because CS results in non-spherical pores and stress concentration occurs under loading, and SHS is known with its canal like pores extended through combustion propagation direction. Also, both techniques as well as HIP and SHT have undesired secondary phases leading to brittleness. HIP and SHT seem to result in better mechanical properties among all the processing routes, and the results of the present study are comparable with them. SHT combined with CS suffers from micro-pores causing a decrease in both strength and ductility. Secondary phases are also very effective in brittleness of TiNi foams. Since compression tests present in the literature are not carried out up to fracture, it is impossible to compare ductility results. Present study resulted in ductility values greater than 10% without employing pre-straining for all porosity levels. Zhang et al. [223] reported that TiNi foam produced using ammonium bicarbonate as space holder with 61.3% porosity fractured after first cycle strained to 3% and at a stress level around 15 MPa. TiNi foam produced in present study with a similar porosity level (59%) did not fracture after 20 loading-unloading cycle at 90 MPa and at a corresponding strain level of 6%. In addition to secondary TiNi phases, oxidation, carburization or nitriding also decrease ductility while increasing strength. Apart from present study all other methods are prone to oxidation inevitably since oxygen partial pressure required to prevent TiO_2 formation is around 10^{-25} atm at a classical sintering temperature, 1100 °C. Polymer based space holders cannot be removed completely from the compact leading to extra contamination ending up with decrease in ductility. In summary, results of present study in terms of strength are better than those produced using alternative space holders or any other technique. Since present study allows single TiNi phase formation and do not involve secondary Ti-Ni phases or oxide or carbo/nitride phases, all of which increase the strength, ductility results are also found to be better than those of produced by alternative methods.

It has been observed that slightly oxidised TiNi foam (deduced from lower transformation temperatures from DSC) with 43% porosity in the present study exhibited a strength of 215 MPa at 3% strain after pre-straining which is the highest value in literature (Figue 4.58 (a)). A similar behavior was also observed for TiNi foam with 55% porosity as shown in Figure 4.65. At 2 and 3% strains its strength

was 107 MPa and 130 MPa respectively, which are the highest values found in literature for the given porosity level. Intentional and controlled oxidation seems to be quite appropriate further improvement of strength without a considerable sacrifice in ductility. Fine Ti_4Ni_2O precipitates can be formed in TiNi matrix by applying slight oxidation. Ni-rich precipitates usually are not preferred from the biocompatibility point of view since they increase nickel release.

Table 4.14 Comparison of mechanical properties of TiNi foams fabricated by different techniques.

| Porosity (%)	Stress (MPa) at 3% strain	Condition	Fabricating method	Reference
32.8-61.3	250-20	Aged, 450°C 0.5 h, third cycle	CS with ammonium bicarbonate as space holder	[223]
39.2	180	Aged, 450°C 0.5 h, second cycle	Capsule free HIP	[195]
27.13	210	Aged, 450°C 0.5 h, first cycle	Capsule free HIP	[177]
42.96	90	Aged, 450°C 0.5 h, first cycle	CS	[177]
53.27	95	Aged, 450°C 0.5 h, first cycle	SHS	[177]
37.3-45.8	240-154	Aged, 450°C 0.5 h, fourth cycle after training	CS with urea as space holder	[226]
36.7-42.1	195-148	Aged, 450°C 0.5 h, fourth cycle after training	CS with ammonium bicarbonate as space holder	[226]
36-48	200-127	Aged, 450°C 0.5 h, first cycle	Capsule free HIP with ammonium bicarbonate as space holder	[224]
38-59 (1100 °C)	170-90	Aged, 400°C 1 h, second cycle	CS magnesium as space holder	Present study
40-62 (1200 °C)	245-80	As-sintered, second cycle	CS magnesium as space holder	Present study
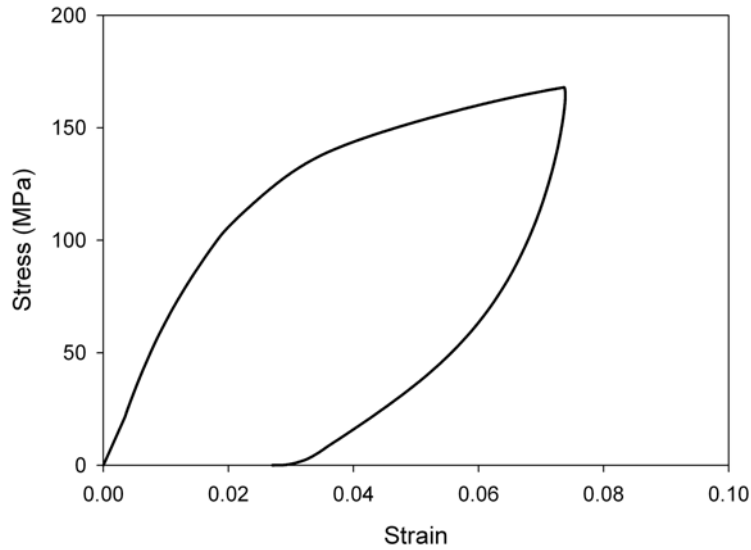
Figure 4.65 Stress-strain curve of slightly oxidised TiNi foam (1200 °C, 2hours) with 55% porosity.

4.2.3.2. Shape Memory Strain Recovery

Shape memory tests were carried out using Ti-50.4 at. %Ni foams which are martensitic at room temperature (dipped in liquid nitrogen before testing and their A_s temperatures are higher than RT) sintered at 1100 °C for 2 hours. After loading the specimens to a predetermined strain, initially 2%, and unloading at room temperature they were immersed in boiling water bath (~ 100 °C, which is above the A_f temperature) for 5 minutes for shape recovery. The sample was then dipped in liquid nitrogen to ensure it was cooled to a temperature lower than their martensite finish temperatures. And the above procedure was repeated subsequently for 4, 6 and 8% predetermined strains using the same specimen. Figure 4.66 presents the stress-strain curves from series of compressive loading and unloading tests on TiNi foams with porosity content in the range 53-73%. After fourth cycle at 8% strain, foams were subjected to final loading step resulting in fracture and collapse. It is clear from the figure that, all the foams exhibit near linear stress-strain curves and loading Young's modulus values are quite similar except for the ones of final loading. On the contrary, unloading elastic moduli were found to be 3 times higher

162

than loading modulus due to accompaniment of detwinning of martensite plates to elastic deformation during loading. The different geometrical properties of sintering necks and cell walls result in inhomogeneous deformation of the foams and thus pure elastic deformation does not occur. If detwinning did not take place during loading both elastic moduli values would be the same. Furthermore, shape memory strain recovery also would not be observed. Inelastic strain amounts seem to be same for all the foams increasing from first cycle 1.2% to fourth cycle 5-5.5% upon unloading. Final loading showed a decrease in slope of the stress-strain curves. Because at fourth cycle micro-cracks formed in all the samples resulting in a decrease in strength. Maximum compression stress observed for the foam with 53% porosity is 55 MPa and for the foam with 59% porosity it is 30 MPa. Higher porosity foams do not have a considerable strength. Young's moduli were also found to be anomalously low, around 1 GPa for the lowest porosity sample and much lower for the others. Reason for these lower results may be higher initial powder size and accordingly larger micro-pores, insufficient sintering, shape memory effect during heating in the furnace for sintering after compaction. DTA results had showed that Ti-50.4 at. %Ni powders were much more oxidized and nitrated in comparison with Ti-50.6 at. %Ni powders. However, Ti-50.4 at. %Ni powders were coarser meaning much less surface area and thus they would be affected from oxygen or nitrogen less at normal conditions. Maybe some lubricants had been added into them to decrease friction and improve packing and flow characteristics and the lubricants somewhat triggered contamination. It should also be noted that, austenite phase is stronger than martensite. A martensitic porous TiNi produced by HIP using NaCl [221] as space holder and with 36% porosity exhibited 200 MPa maximum compression stress whereas the one produced using NaF particles [220] as spacers and with 39.5% porosity showed 135 MPa at failure. However, they both failed at relatively lower strain, 6%. Although HIP was used for these foams, their strengths were also lower possibly due to contamination.

Although TiNi foams were insufficient in strength, they displayed quite well shape memory behavior as can be seen from Figure 4.67. Strain recoveries by shape memory mechanism were calculated subtracting the fraction of elastic recovery from total recovery. However, in literature total recovered strain is acepted as shape

163
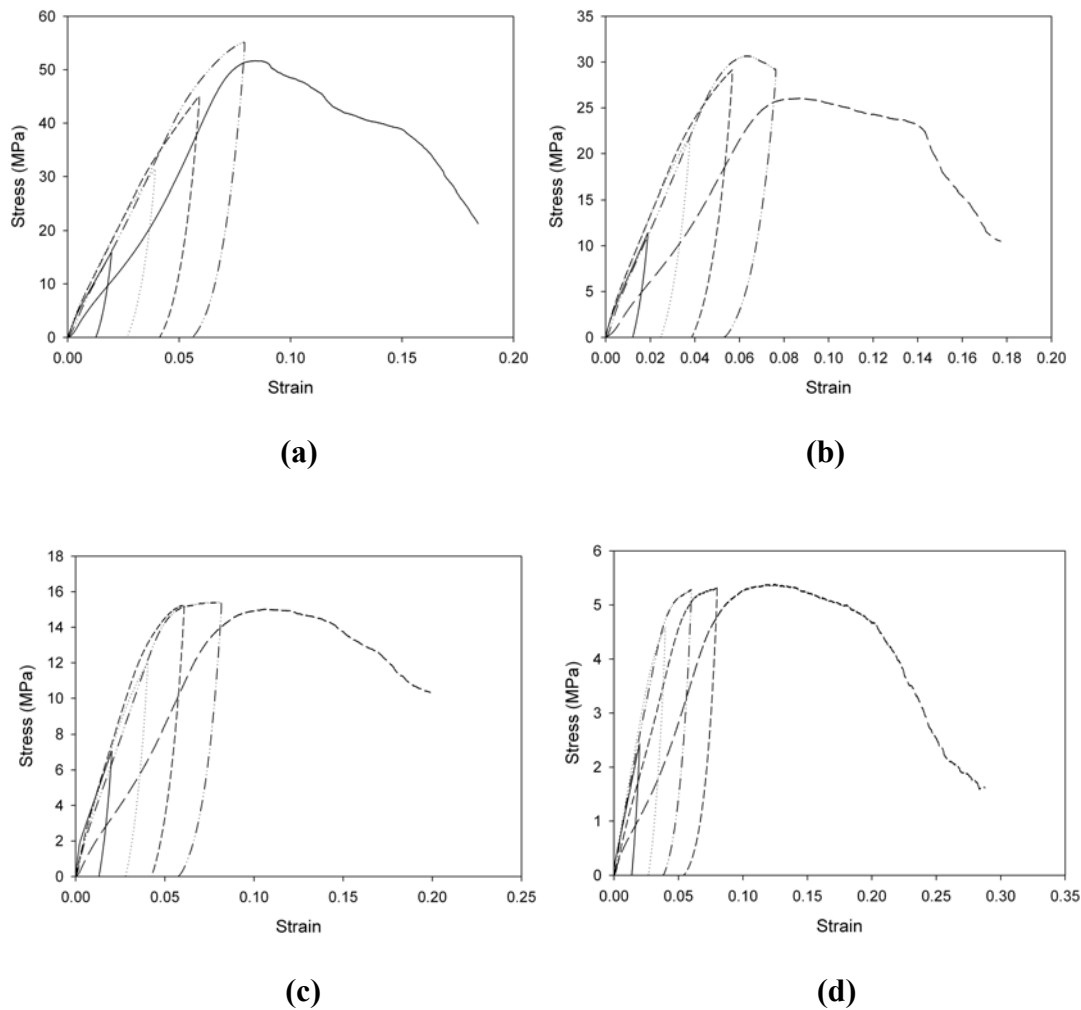
Figure 4.66 Stress-strain curves for (a) 53%, (b) 59%, (c) 66%, (d) 73% porosity foams at RT.

memory strain recovery. Therefore, total strain recovery may be used for comparison. Higher porosity resulted in less strain recovery and accumulation of more plastic strains. For 53 and 59% porosity samples total strain recovery was found to be higher than 90% of the applied strain. 66 and 73% porosity samples recovered 80 and 70% of the total strain, respectively. Lower porosity samples were not affected much from the strain amount employed wheras a distinct drop in recovered strains (total and shape memory) was observed for higher porosity samples with increasing strain amount.
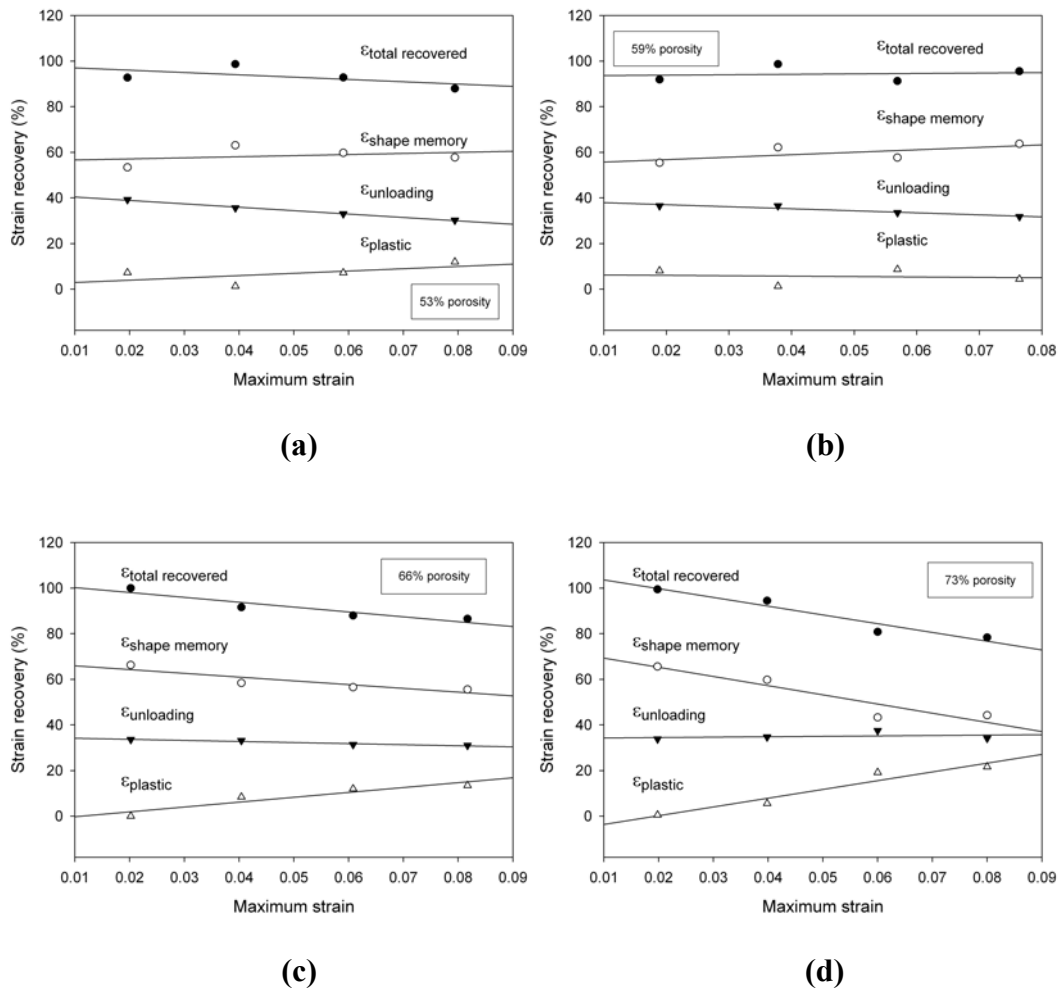
Figure 4.67 Strain recovery as a function of maximum compressive strain for (a) 53%, (b) 59%, (c) 66%, (d) 73% porosity foams.

Ductility of the foams were fairly well: 8 and 10% for lower and higher porosity samples, respectively. Total plastic strain accumulated in the samples were 2.4 and 3% for lower and higher porosity samples, respectively before final loading for fracture. In the light of the present results, lower strength seems to be resulted from insufficient sintering rather than contamination. Phase transformation temperatures measured also support this idea. SEM images presented in Figure 4.68 confirms that both Ti-50.6 at. %Ni and Ti-50.4 at. %Ni foams fractured in ductile manner. Dimples, characteristic sign of ductile deformation, in the sintering necks have been observed for both foams.
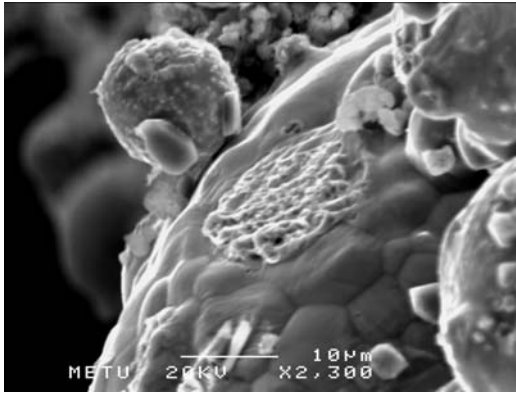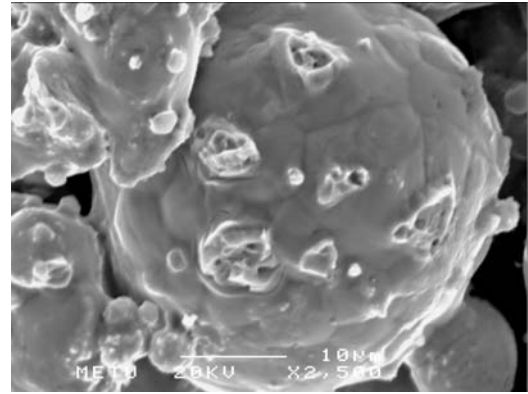
(a) **(b)**

Figure 4.68 Fracture at sintering necks. (a) Ti-50.4 at. %Ni foam, (b) Ti-50.6 at. %Ni foam.

CHAPTER 5

CONCLUSIONS

1. Secondary intermetallic free, porous TiNi shape memory alloys with porosities in the range 21-81% have been produced sucessfully by applying a new processing route, in which magnesium particles were used as space forming agent and getter. The processed alloys were observed to have isotropic and uniform distribution of spherical macro-pores of sizes ranging from 123 to 645 μm while over 90% open and throughly interconnected. It has also been found that there were micro-pores in the cell walls with sizes in the range 1-20 μm resulting from incomplete sintering.

2. Magnesium vapor do not only prevents secondary phase formation and contamination but also provides higher temperature sintering opportunity. By two step sintering processing (holding the sample at 1100 °C for 30 minutes and subsequently sintering at temperatures higher than the eutectic temperature, 1118 °C) magnesium may allow sintering probably up to the melting point of TiNi.

3. Space holder technique seems to be a promising method for production of porous TiNi alloys. Desired porosity level, pore shape and accordingly mechanical properties were found to be easily adjustable.

4. Porous TiNi alloys in as-sintered condition exhibit almost complete transformation. Porosity content of the porous TiNi shape memory alloys produced using Mg as space holder found not to play a direct role in the transformation temperatures. Increase in transformation temperatures with increasing porosity arise from the increase of Mg addition resulting in more effective deoxidation of porous TiNi alloys by liquid or vaporized

magnesium during sintering process. Aging process resulted in incomplete transformations and an additional increase of transformation temperatures.

5. Fast cutting speeds are not suitable to prepare DSC samples, on the contrary slower cutting speeds are found to be acceptable, although they are not completely ineffective on transformation temperatures.

6. Compression behaviour of porous TiNi differs from that of bulk TiNi. Superelasticity exhibited by porous TiNi is linear and have a slope decreasing with increasing porosity. Strength, critical stress for inducing martensite and elastic moduli of TiNi foams decrease with increasing porosity.

7. Partial superelasticity have been observed in as-sintered and aged conditions. Linear and complete superelasticity up to 5% has been observed after cycling. Even at temperatures higher than A_f in as-sintered condition and aged condition, strain applied could not be recovered fully due to martensite stabilisation resulting from heavy deformation of macro-pore walls and sintering necks.

8. Aging decreases critical stress for inducing martensite leading to lower elastic moduli. Another reason for lower elastic moduli is micro-pores formed due to partial sintering.

9. TiNi foams with the porosities in the range of 30-55% porosity meet the main requirements of biomaterials in terms of mechanical properties for use as bone implant. As-processed ones after pre-straining are especially suitable for bone replacement applications.

10. TiNi foams exhibited good shape memory strain recovery decreasing with increasing porosity.

REFERENCES

[1] D.A. Porter, K.E. Easterling, *Phase Transformations in Metals and Alloys,* Second Edition, Chapman & Hall, London, pp.353,1992.

[2] J.D. Verhoeven, *Fundamentals of Physical Metallurgy,* First Edition, John Wiley & Sons Inc., New York, pp.459,1975.

[3] K. Otsuka and C.M. Wayman, *Shape Memory Materials,* Cambridge University Press, Cambridge, pp.3,1998.

[4] K. Shimizu, T. Tadaki, *Shape Memory Alloys,* edited by H. Funakubo, Gordon and Breach Science Publishers S.A., Amsterdam,pp.1-60,1987.

[5] E.C. Bain, *Trans. AIME,* 1924;70:25.

[6] K. Otsuka, X. Ren, *Prog. Mater. Sci.,* 2005;50:511.

[7] T. Ohba, Unpublished work, 2004.

[8] K. Otsuka, T. Sawamura, K. Shimizu, *Phys. Status Solidi,* 1971;5:457.

[9] R.F. Hehemann, G.D. Sandrock, *Scripta Metall.,* 1971;5:801.

[10] G.M. Michal, R. Sinclair, *Acta Crystallogr.,* 1981;B37:1803.

[11] Y. Kudoh, M. Tokonami, S. Miyazaki, K. Otsuka, *Acta Metall.,* 1985;33:2049.

[12] M.S. Wechsler, D.S. Lieberman, T.A. Read, *Trans. AIME,* 1953;197:1503.

[13] J.S. Bowles, J.K. Mackenzie, *Acta Met.,* 1954;2:129,138,224.

[14] K. Otsuka and C.M. Wayman, *Shape Memory Materials,* Cambridge University Press, Cambridge, pp.11,1998.

[15] O. Matsumoto, S. Miyazaki, K. Otsuka, H. Tamura, *Acta Metall.,* 1987;35:2137.

[16] K.M. Knowles, D.A. Smith, *Acta Metall.,* 1981;29:101.

[17] O. Matsumoto, M.S. thesis, University of Tsukuba, 1986.

[18] Y. Murakami, K. Otsuka, S. Hanada, S. Watanabe, *Mater. Sci. Eng.,* 1994;A189:191.

[19] T. Saburi, S. Nenno, *Proceedings, Proc. Int. Conf. Solid-Solid Phase Transformations,* AIME, New York, pp.1455,1981.

[20] T. Saburi, C.M. Wayman, *Acta Metall.,* 1979;27:979.

[21] K. Otsuka, X. Ren, *Mater. Sci. Eng.,* 1999;A273-275:89.

[22] K. Madangopal, *Acta Mater.,* 1997;45:5347.

[23] L. Kaufman, M. Cohen, *Progress in Metal Physics,* 1958;7:165.

[24] K. Otsuka and C.M. Wayman, *Shape Memory Materials,* Cambridge University Press, Cambridge, pp.23,1998.

[25] H. Kessler, W. Pitsch, *Acta Metall.,* 1967;15:401.

[26] E. Patoor, D.C. Lagoudas, P.B. Entchev, L.C. Brinson, X. Gao, *Mechanics of Materials,* 2006;38:391.

[27] K. Otsuka, K. Shimizu, *Scr. Metall.,* 1970;4:467.

[28] J.R. Patel, M. Cohen, *Acta Metall.,* 1953;1:531.

[29] M.W. Burkart, T.A. Read, *Trans AIME*, 1953;197:1516.

[30] P. Wollants, D.M. Bonte, J.R. Roos, *Z. Metallkd,* 1979;70:113.

[31] K. Otsuka, K. Shimizu, *Int. Metals Rev.,* 1986;31:93.

[32] F. Takei, T. Miura, S. Miyazaki, S. Kimura, K. Otsuka, Y. Suzuki, *Scripta Metall.*, 1983;17:987.

[33] S. Miyazaki, Y. Ohmi, K. Otsuka, Y. Suzuki, *J. Phys.,* 1982;43:C4-255.

[34]. K. Otsuka, K. Shimizu, *Scripta Metall.,* 1970;4:469.

[35] C.M. Wayman, K. Shimizu, *Metal Sci. J.*, 1972;6:175.

[36] L. Delaey, R.V. Krishnan, H. Tas, H. Warlimont, *J. Mater. Sci.,* 1974;9:1521.

[37] J.W. Christian, *Metall. Trans.,* 1982;13A:509.

[38] T. Maki, *Shape memory materials*, edited by K. Otsuka, C.M. Wayman, Cambridge University Press, Cambridge, pp.117-133,1998.

[39] J. Ryhanen, E. Niemi, W. Serlo, E. Niemela, P. Sandvik, H. Pernu, T. Salo, *J. Biomed. Mater. Res.,* 1997;35:451.

[40] J. Ryhanen, M. Kallioinen, J. Tuukkanen, J. Junila, E. Niemela, P. Sandvik, W. Serlo, *J. Biomed. Mater. Res.,* 1998;41:481.

[41] M. Assad, L.H. Yahia, C.H. Rivard, N. Lemieux, *J. Biomed. Mater. Res.,*1998;41:154.

[42] S.D. Prokoshkin, V.G. Pushin, E.P. Ryklina, I.Y. Khmelevskaya, *Phys. Metal. Metall.,* 2004;97:S56.

[43] M. Es-Souni, M. Es-Souni, H. Fischer-Brandies, *Anal. Bioanal. Chem.,* 2005;381:557.

[44] L. Ponsonnet, D. Treheux, M. Lissac, N. Jaffrezic, B. Grosgogeat, *Int. J. Appl. Electromag. Mech.,* 2006;23:147.

[45] P. Filip, *Titanium in Medicine,* edited by D.M. Brunette, P. Tengvall, M. Textor, P. Thomsen, Springer-Verlag, Berlin Heidelberg, pp.53-86,2001.

[46] S.A Shabalovskaya, *Biomed. Mater. Eng.,* 1996;6(4):267.

[47] H.M. Wu, L.McD. Schetky, *Proceedings, SMST-2000,* Pacific Grove, California, pp.171-182, 2000.

[48] K.N. Melton, *Shape Memory Materials,* edited by K. Otsuka and C.M. Wayman, Cambridge University Press, Cambridge, pp.220-239,1998.

[49] W.J. Buehler, J.W. Gilfrich, R.C. Wiley, *J. Appl. Phys.,* 1963;34:1473.

[50] S. Miyazaki, K. Otsuka, Y. Suzuki, *Scr. Metall.,* 1981;15:287.

[51] S. Miyazaki, T. Imai, K. Otsuka, Y. Suzuki, *Scr. Metall.,* 1981;15:853.

[52] D.J. Hartl, D.C. Lagoudas, *J. Aerospace Eng.,* 2007;211:535.

[53] H.M. Wu, *Proceedings, SMST-2001*, Kunming, pp.285-292, 2001.

[54] Y. Suzuki, *Shape Memory Alloys,* edited by H. Funakubo, Gordon and Breach Science Publishers S.A., Amsterdam,pp.176-267,1987.

[55] T. Duerig, A. Pelton, D. Stöckel, *Mater. Sci. Eng. A,* 1999;273-275:149.

[56] V.I. Itin, V.E. Gjunter, S.A. Shabalovskaya, R.L.C. Sachdeva, *Mater. Charac.,* 1994;32:179.

[57] H. Fischer, B. Vogel, A. Welle, *Minim. Invasive Therapy Allied Technol.,* 2004;13:248.

[58] R. Ayers, D. Burkes, G. Gottoli, H.C. Yi, J.J. Moore, *Mater. Manufact. Proc.*, 2007;22:481.

[59] S. Miyazaki, *Shape Memory Materials*, edited by K. Otsuka and C.M. Wayman, Cambridge University Press, Cambridge, pp.267-281,1998.

[60] N.B. Morgan, *Mater. Sci. Eng. A*, 2004;378:16.

[61] A.R. Pelton, J. DiCello, S. Miyazaki, *Minim. Invasive Therapy Allied Technol.*, 2000;9:107.

[62] S.A. Thompson, *International Endodontic Journal*, 2000;33:297.

[63] D. Stoeckel, *Minim. Invasive Therapy Allied Technol.*, 2000;9:81.

[64] A.R. Pelton, D. Stoeckel, T.W. Duerig, *Mater. Sci. Forum Vols.*, 2000;327-328:63.

[65] F. Laves, H.J. Wallbaum, *Naturwissenschaften*, 1939;27:674.

[66] P. Duwez, J.L. Taylor, *Trans. AIME*, 1950;188:1173.

[67] H. Margolin, E. Ence, J.P. Nielsen, *J. Metals*, 1953(February):243.

[68] D.M. Poole, Hume-Rothery, *J. Inst. Met.*, 1954-55;83:473.

[69] M. Hansen, R.P. Elliott, F.A. Shunk, *Constitution of binary alloys*, Second edition, McGraw-Hill, New York, pp.1050,1958.

[70] G.R. Purdy, J.G. Parr, *Trans. AIME*, 1961;221:636.

[71] D. Koskimaki, M.J. Marcinkowski, A.S. Sastri, *Trans. AIME*, 1969;245:1883.

[72] R.J. Wasilewski, S.R. Butler, J.E. Hanlon, D. Worden, *Metall. Trans.*, 1971;2:229.

[73] G.F. Bastin, G.D. Rieck, *Metall. Trans.*, 1974;5:1917.

[74] M. Nishida, C.M. Wayman, T. Honma, *Metall. Trans.*, 1986;17A:1505.

[75] T.B. Massalski, H. Okamoto, P.R. Subramanian, L. Kacprzak, *Binary alloy phase diagrams*, Second edition, ASM International, Materials Park OH, pp. 2874,1990.
[76] K. Otsuka, T. Kakeshita, *MRS Bulletin*, 2002;27:91.

[77] T. Honma, M. Matsumoto, Y. Shugo, M. Nishida, *Research Report of the Laboratory of Nuclear Science*, Tohoku University, Berlin, pp.183,1979.

[78] J. Zhang, G. Fan, Y. Zhou, X. Ding, K. Otsuka, K. Nakamura, J. Sun, X. Ren, *Acta Mater.,* 2007;55:2897.

[79] W.D. Callister, Jr., *Materials Science and Engineering An Introduction,* Sixth edition, John Wiley & Sons Inc., New York, pp.389,2003.

[80] T.V. Philip, P.A. Beck, *Trans. AIME,* 1957;209:1269.

[81] M.H. Mueller, H.W. Knott, *Trans. AIME,* 1963; 227:674.

[82] A. Taylor, R.W. Floyd, *Acta Crystall.,* 1950;3:285.

[83] W. Tang, *Metall. Trans.,* 1997;28A:537.

[84] X. Ren, K. Taniwaki, K. Otsuka, T. Suzuki, K. Tanaki, Y.I. Chumlyakov, T. Ueiki, *Philos. Mag. A,* 1999;75:31.

[85] X. Ren, K. Otsuka, *Mater. Sci. Forum,* 2000;327-328:429.

[86] X. Ren, N. Miura, J. Zhang, K. Otsuka, K. Tanaka, M. Koiwa, T. Suzuki, Y.I. Chumlyakov, M. Asai, *Mater. Sci. Eng. A,* 2001;312:196.

[87] A. Planes, L. Manosa, D. Rioa-Jara, J. Ortin, *Phys. Rev. B,* 1992;45:7633.

[88] L. Manosa, J. Zarestky, T. Lograsso, D.W. Dalaney, C. Stassis, *Phys. Rev. B,* 1993;48:15708.

[89] L. Manosa, M. Jurado, A. Planes, J. Zarestky, T. Lograsso, C. Stassis *Phys. Rev. B,* 1994;48:9969.

[90] T. Honma, *Shape Memory Alloys,* edited by H. Funakubo, Gordon and Breach Science Publishers S.A., Amsterdam, pp.61-115,1987.

[91] K.H. Eckelmeyer, *Scripta Metall.,* 1976;10:667.

[92] H.C. Donkersloot, J.H.N. Van Vucht, *J. Less-Comm. Met.,* 1970;20:83.

[93] D.R. Angst, P.E. Thoma, M.Y. Kao, *J. Phys.,* 1995;C8:747.

[94] P.G. Lindquist, C.M. Wayman, *Proc. MRS Int. Mtg. Adv. Mater.,* 1989;9:123.

[95] T.H. Nam, T. Saburi, K. Shimizu, *Trans. JIM,* 1990;31:959.

[96] T.H. Nam, T. Saburi, Y. Nakata, K. Shimizu, *Mater. Trans. JIM,* 1990;31:1050.

[97] K.N. Melton, O. Mercier, *Metall. Trans.,* 1978;9A:1487.

[98] G.S. Firstov, R.G. Vitchev, H. Kumar, B. Blanpain, J. Van Humbeeck, *Biomaterials,* 2002; 23:4863.

[99] T. Saburi, *Shape Memory Materials,* edited by K. Otsuka and C.M. Wayman, Cambridge University Press, Cambridge, pp.49-96,1998.

[100] V.G. Chuprina, I.M. Shalya, *Powd. Metall. Met. Cer.,* 2002;41:85.

[101] Y. Shugo, S. Hanada, T. Honma, *Bulletin of Research Inst. Mineral Dressing and Metallurgy,* 1985;41:23.

[102] Y. Shugo, K. Yamauchi, R. Miyagawa, T. Honma, *Bulletin of Research Inst. Mineral Dressing and Metallurgy,* 1982;38:11.

[103] J. Frenzel, Z. Zhang, Ch. Somsen, K. Neuking, G. Eggeler, *Acta Mater.,* 2007;55:1331.

[104] P. Olier, Thesis, University of Paris XI, 1995.

[105] R. Burch, N.B. Mason, *J.C.S. Farady I*, 1979;75:561.

[106] R. Burch, N.B. Mason, *J.C.S. Farady I*, 1979;75:578.

[107] A. Pelton, C. Trepanier, X.Y. Gong, A. Wick, K.C. Chen, *Proceedings, SMST-2003*, Monterey, CA, pp.357-366, 2004.

[108] B.L. Pelton, T. Slater, A.R. Pelton, *Proceedings, SMST-1997,* Pacific Grove, California, pp.395-400, 1997.

[109] C. Li, K.H. Wu, *Proceedings, SMST-1994,* Pacific Grove, CA, pp.227, 1995.

[110] S. Miyazaki, Y. Igo, K. Otsuka, *Acta. Metall.,* 1986;34:2045.

[111] P.G. McCormick, Y. Liu, *Acta. Metall. Mater.,* 1994;42:2407.

[112] D. Favier, Y. Liu, *J. Alloys Compounds*, 2000;297:114.

[113] M. Piao, K. Otsuka, S. Miyazaki, H. Horikawa, *Mater. Trans.,* 1993;34:919.

[114] Y. Liu, Y. Liu, J. Van Humbeeck, *Acta Mater.,* 1999;47:199.

[115] Y. Liu, *Mater. Sci. Eng. A*, 273-275;1999:668.

[116] Y. Liu, D. Favier, *Acta Mater.,* 2000;48:3489.

[117] H.C. Lin, S.K. Wu, T.S. Chou, H.P. Kao, *Acta Metal. Mater.,* 1991;39:2069.

[118] H.C. Lin, S.K. Wu, *Metall. Trans. A,* 1993;24A:293.

[119] Y. Liu, G.S. Tan, *Intermetallics*, 1998;8:67.

[120] G.B. Olson, M. Cohen, *Scripta Metall.,* 1975;9:1247.

[121] M. Nishida, C.M. Wayman, T. Honma, *Metall. Trans.,* 1986;17A:1505.

[122] M. Nishida, C.M. Wayman, R. Kainuma, T. Honma, *Scripta Metall.,* 1986;20:899.

[123] T. Saburi, S. Nenno, T. Fukuda, *J. Less-Comm. Metals,* 1986;125:157.

[124] T. Tadaki, Y. Nakata, K. Shimizu, K. Otsuka, *Trans. JIM,* 1986;27:731.

[125] J. Zhang, PhD thesis, University of Tsukuba, 2000.

[126] J. Zhang, W. Cai, X. Ren, K. Otsuka, M. Asai, *Mater. Trans. JIM* 1999;40:1367.

[127] J.A. Shaw, S. Kyriakides, *Acta Mater.,* 1997;45:683.

[128] M. Nishida, S. Ii, K. Kitamura, T. Furukawa, A. Chiba, T. Hara, K. Hiraga, *Scripta Mater.,* 1998;39:1749.

[129] T. Saburi, T. Tatsumi, S. Nenno, *J. De Phys.,* 1982;43:C4-261.

[130] S.K. Sadrnezhaad, S.H. Mirabolghasemi, *Mater. Design,* 2007;28:1945.

[131] S. Miyazaki, K. Otsuka, *Data Handbook of Intermetallics*, edited by M. Doyama, M. Yabe, Science Forum, Tokyo pp.293-294,1989.

[132] S. Miyazaki, T. Imai, Y. Igo, K. Otsuka. *Metall. Trans.,* 1986;17A:115.

[133] J. Banhart, *Prog. Mater. Sci.*, 2001;46:559.

[134] C.A. Engh, J.D. Bobyn, A.H. Glassman, *J. Bone Joint Surg. Br.*, 1987;69-B: 45.

[135] A. Bansiddhi, T.D. Sargeant, S.I. Stupp, D.C. Dunand, *Acta Biomaterialia,* 2008; 4:773.

[136] M. Cempel, G. Nikel, *Polish J. Environ. Studies,* 2006;15:375.

[137] E. Denkhausa, K. Salnikow, *Critical Rev. Oncol/Hematol.,* 2002;42:35.

[138] H.C. Jiang, L.J. Rong, *Surf. Coat. Technol.,* 2006;201:1017.

[139] Y.H. Li, G.B. Rao, L.J. Rong, Y.Y. Li, W. Ke, *Mater. Sci. Eng. A,* 2003;363:356.

[140] S. Rhalmi, M. Odin, M. Assad, M. Tabrizian, C.H. Rivard, LH. Yahia, *Bio-Med. Mater. Eng.,* 1999;9:151.

[141] S. Kujala, J. Ryhanen, A. Danilov, J. Tuukkanen, *Biomaterials,* 2003;24:4691.

[142] S.J. Simske, R. Sachdeva, *J. Biomed. Mat. Res.,* 1995;29:527.

[143] S.B. Kang, K.S. Yoon, J.S. Kim, T.H. Nam, V.E. Gjunter, *Mater. Trans.,* 2002;43:1045.

[144] M. Assad, P. Jarzem, M.A. Leroux, C. Coillard, A.V. Chernyshov, S. Charette, C.H. Rivard, *J. Biomed. Mater. Res. Part B: Appl. Biomater.,* 2003;64B:107.

[145] M. Assad, A.V. Chernyshov, P. Jarzem, M.A. Leroux, C. Coillard, S. Charette, C.H. Rivard, *J. Biomed. Mater. Res. Part B Appl. Biomater.,* 2003;64B:121.

[146] O. Prymak, D. Bogdanski, M. Köller, S.A. Esenwein, G. Muhr, F. Beckmann, T. Donath, M. Assad, M. Epple, *Biomater.,* 2005;26:5801.

[147] R.A. Ayers, S.J. Simske, T.A. Bateman, A. Petkus, R.L.C. Sachdeva, VE. Gyunter, *J. Biomed. Mat. Res.,* 1999;45:42.

[148] S.A. Shabalovskaya, *Bio-Med. Mater. Eng.,* 2002;12:69.

[149] S. Shabalovskaya, J. Ryhanen, L.H. Yahia, *Shape Memory Mater. Its Appl.,* 2001;394-3:131.

[150] J.P.Y. Ho, S.L. Wu, R.W.Y. Poon, C.Y. Chung, S.C. Tjong, P.K. Chu, K.W.K. Yeung, W.W. Lu, K.M.C. Cheung, K.D.K. Luk, *Surf. Coat. Technol.,* 2007;201:4893.

[151] J.H. Sui*, Z.Y. Gao, W. Cai, Z.G. Zhang, *Mater. Sci. Eng. A,* 2007;452-453:518.

[152] Y.L. Chan, K.W.K. Yeung, W.W. Lu, A.H.W. Ngan, K.D.K. Luk, D. Chan, S.L. Wu, X.M. Liu, P.K. Chu, K.M.C. Cheung, *Nucl. Instr. Meth. in Phys. Res. B,* 2007; 257:687.

[153] S.L. Wu, X.M. Liu, Y.L. Chan, J.P.Y. Ho, C.Y. Chung, P.K. Chu, C.L. Chu, K.W.K. Yeung, W.W. Lu, K.M.C. Cheung, K.D.K. Luk *J. Biomed. Mat. Res. A,* 2007;81A:948.

[154] M.H. Wong, F.T. Cheng, H.C. Man, *Materials Letters,* 2007;61:3391.

[155] C.L. Chu, T. Hu, S.L. Wu, Y.S. Dong, L.H. Yin, Y.P. Pu, P.H. Lin, C.Y. Chung, K.W.K. Yeung, P.K. Chu, *Acta Biomaterialia,* 2007;3:795.

[156] Y.W. Gu, B.Y. Tay, C.S. Lim, M.S. Yong, *Applied Surface Science,* 2005; 252:2038.

[157] Y. Cheng, Y.F. Zheng, *Surf. Coat. Technol.,* 2007; 201:4909.

[158] V. Lemaire, B. Sicotte, S. Allard, *Proceedings, MetFoam 2007: Porous Metals and Metallic Foams,* Montreal, pp.291-294, 2007.

[159] H.C. Jiang, L.J. Rong, *Surf. Coat. Technol.,* 2006;201:1017.

[160] Y.W. Gu, H. Li, B.Y. Tay, C.S. Lim, M.S. Yong, K.A. Khor, *J. Biomed. Mat. Res. A,* 2006;78A:316.

[161] V.E. Gjunter, P. Sysoliatin, T. Temerkhamor, *Superelastic Shape Memory Implants in Maxillofacial Surgery, Traumatology, Orthopaedics, and Neurosurgery,* First Edition, Tomsk University Publishing House, Tomsk, pp.15,1995.

[162] Y. Zhao, M. Taya, H. Izui, *Int. J. Solid Struct.,* 2006;43:2497.

[163] J.B. Zhou, L.P. Gao, KS. Wang, *J. Rare Earth,* 2005;23:449.

[164] M.A. Qidwai, P.B. Entchev, D.C. Lagoudas, V.G. DeGiorgi, *Int. J. Solid Struct.* 2001;38:8653.

[165] Shape Change Technologies LLC, www.shapechange.com, last visited on July 2010.

[166] G. J. Davies, S. Zhen, *J. Mater. Sci.,* 1983;18:1899.

[167] L.J. Gibson, M.F. Ashby, *Cellular solids,* Cambridge University Press, Cambridge, 1997.

[168] Z. Esen, Ph. D. Thesis, Middle East Technical University, 2008.

[169] G. Ryan, A. Pandit, D. P. Apatsidis, *Biomaterials*, 2006;27:2651.

[170] M. Sugiyama, S-K. Hyun, M. Tane, H. Nakajima, *Proceedings, MetFoam 2005.* The Japan Institute of Metals, Sendai, pp.233, 2006.

[171] B.Y. Li, L.J. Rong, Y.Y. Li, V.E. Gjunter, *Acta Mater.,* 2000;48:3895.

[172] C.L. Chu, C.Y. Chung, P.H. Lin, S.D. Wang, *J. Mater. Process. Technol.*, 2005;169:103.

[173] C.Y. Chung, C.L. Chu, S.D. Wang, *Mater. Lett.*, 2004;58:1683.

[174] C.W. Goh, Y.W. Gu, C.S. Lim, B.Y. Tay, *Intermetallics*, 2007;15:461.

[175] Y.H. Li, L.J. Rong, Y.Y. Li, *J. Alloys Compd.*, 2001;325:259.

[176] J.S. Kim, J.H. Kang, S.B. Kang, K.S. Yoon, Y.S. Kwon, *Adv. Eng. Mater.*, 2004;6:403.

[177] B. Yuan, X.P. Zhang, C.Y. Chung, M.Q. Zeng, M. Zhu, *Metall. Mater. Trans.*, 2006;37A:755.

[178] B.Y. Li, L.J. Rong, Y.Y. Li, V.E. Gjunter, *Intermetallics*, 2000;8:881.

[179] C.L. Chu, C.Y. Chung, P.H. Lin, S.D. Wang, *Mater. Sci. Eng. A*, 2004;366:114.

[180] B.Y. Li, L.J. Rong, V.E. Gjunter, Y.Y. Li, *Z. Metallkd.*, 2000;91:291.

[181] A. Biswas, *Acta Mater.*, 2005;53:1415.

[182] B. Bertheville, *Biomater.*, 2006;27:1246.

[183] C.W. Goh, Y.W. Gu, C.S. Lim, B.Y. Tay, *Intermetallics*, 2007;15:461.

[184] C.L. Chu, J.C.Y. Chung, P.K. Chu, *Trans. Nonferrous Met. Soc. China*, 2006; 16:49.

[185] M. Kaya, N. Orhan, B. Kurt, T.I. Khan, *J. Alloys Compd.*, 2009;475:378.

[186] G. Tosun, L. Ozler, M. Kayac, N. Orhan, *J. Alloys Compd.*, 2009;487:605.

[187] C.L. Chu, B. Li, S.D. Wang, S.G. Zhang, X.X. Yang, Z.D. Yin, *Trans. Nonferr. Met. Soc. China*, 1997;7:84.

[188] H. Li, B. Yuan, Y. Gao, C. Y. Chung, M. Zhu, *J. Mater. Sci.*, 2009;44:875.

[189] K.I. Hirano, K.I. Ouchi, *J. Jpn. Inst. Metals*, 1968;32:613.

[190] B.Y. Li, L.J. Rong, Y.Y. Li, *Scr. Mater.*, 2001;44:823.

[191] C.L. Chu, P.H. Lin, C.Y. Chung, *J. Mater. Sci.*, 2005;40:773.

[192] C.L. Chu, C.Y. Chung, P.H. Lin, *Mater. Sci. Eng. A*, 2005;392:106.

[193] C. Greiner, S.M. Oppenheimer, D.C. Dunand, *Acta Biomater.*, 2005;1:705.

[194] D.C. Lagoudas, E.L. Vandygriff, *J. Intel. Mater. Syst. Struct.*, 2002;13:837.

[195] B. Yuan, C.Y. Chung, X.P. Zhang, M.Q. Zeng, M. Zhu, *Smart Mater. Struct.*, 2005;14:201.

[196] L. Krone, E. Schuller, M. Bram, O. Hamed, H.P. Buchkremer, D. Stover, *Mater. Sci. Eng. A,* 2004;378:185.

[197] E. Schuller, L. Krone, M. Bram, H.P. Buchkremer, D. Stover, *J. Mater. Sci.*, 2005;40:4231.

[198] L. Krone, J. Mentz, M. Bram, H.P. Buchkremer, D. Stover, M. Wagner, G. Eggeler, D. Christ, S. Reese, D. Bogdanski, M. Koller, S. A. Esenwein, G. Muhr, O. Prymak, M. Epple, *Advanced Engineering Materials,* 2005;7:613.

[199] J. Mentz, M. Bram, H.P. Buchkremer, D. Stover, *Advanced Engineering Materials,* 2006;8:247.

[200] B. Yuan, C.Y. Chung, P. Huang, M. Zhu, *Mater. Sci. Eng. A,* 2006;438-440:657.

[201] B. Yuan, C.Y. Chung, M. Zhu, *Mater. Sci. Eng. A,* 2004;382:181.

[202] B. Yuan, X.P. Zhang, C.Y. Chung, M. Zhu, *Mater. Sci. Eng. A,* 2006;438-440:585.

[203] D.S. Grummon, J.A. Shaw, A. Gremillet, *Appl. Phys. Lett.,* 2003;82:2727.

[204] H. Guoxin, Z. Lixiang, F. Yunliang, L. Yanhong, *J. Mater. Process. Technol.*, 2008;206:395.

[205] S.L. Zhu, X.J. Yang, D.H. Fu, L.Y. Zhang, C.Y Li, Z.D. Cui, *Mater. Sci. Eng. A,* 2005;408:264.

[206] S.L. Zhu, X.J. Yang, F. Hu, S.H. Deng, Z.D. Cui, *Mater. Lett.,* 2004;58:2369.

[207] S.K. Sadrnezhaad, H. Arami, H. Keivan, R. Khalifezadeh, *Mater. Manuf. Processes,* 2006;21:727.

[208] B.Y. Li, L.J. Rong, Y.Y. Li, *J. Mater. Res.,* 1998;13:2847.

[209] B.Y. Li, L.J. Rong, Y.Y. Li, *Intermetallics,* 2000;8:643.

[210] B.Y. Li, L.J. Rong, X.H. Luo, Y.Y. Li, *Metall. Mater. Trans.,* 1999;30A:2753.

[211] Y. Zhao, M. Taya, Y. Kang, A. Kawasaki, *Acta Mater.,* 2005;53:337.

[212] M. Hakamada, T. Kuromura, Y.Q. Chen, H. Kusuda, M. Mabuchi, *J. Appl. Phys.,* 2006;100:114908.

[213] B. Jiang, N.Q. Zhao, C.S. Shi, X.W. Du, J.J. Li, H.C. Man, *Mater. Lett.,* 2005;59:3333.

[214] M. Bram, C. Stiller, H.P. Buchkremer, D. Stover, H. Baur, *Adv. Eng. Mater.,* 2000;2:196.

[215] E.L. Zhang, B. Wang, *Int. J. Mech. Sci.,* 2005;47:744.

[216] Y.Y. Zhao, T. Fung, L.P. Zhang, F.L. Zhang, *Scripta Mater.,* 2005;52:295.

[217] M. Li, Y. Liu, J.W. Ye, L.F. Zhang, J. Li, M.J. Tu, *Powder Metall.,* 2006;49:114.

[218] A. Laptev, M. Bram, H.P. Buchkremer, D. Stover, *Powder. Metall.,* 2004;47:85.

[219] Z. Esen, S. Bor, *Scripta Mater.,* 2007;56:341.

[220] A. Bansiddhi, D.C. Dunand, *Intermetallics,* 2007;15:1612.

[221] A. Bansiddhi, D.C. Dunand, *Acta Biomater.,* 2008;4:1996.

[222] Y.P. Zhang, B. Yuan, M.Q. Zeng, C.Y. Chung, X.P. Zhang, *J. Mater. Process. Technol.,* 2007;192-193:439.

[223] Y.P. Zhang, D.S. Li, X.P. Zhang, *Scr. Mater.,* 2007;57:1020.

[224] S. Wu, C.Y. Chung, X. Liu, P.K. Chu, J.P.Y. Ho, C.L. Chu, Y.L. Chan, K.W.K. Yeung, W.W. Lu, K.M.C. Cheung, K.D.K. Luk, *Acta Mater.,* 2007;55:3437.

[225] D.S. Li, Y.P. Zhang, X. Ma, X.P. Zhang, *J. Alloys Compd.,* 2009;474:L1.

[226] D.S. Li, Y.P. Zhang, G. Eggeler, X.P. Zhang, *J. Alloys Compd.,* 2009;470:L1.

[227] T. Aydoğmuş, Ş. Bor, *J. Alloys Compd.,* 2009;478:705.

[228] C.H.P. Lupis, *Chemical Thermodynamics of Materials,* First Edition, Elsevier Science Publishing Co., New York, pp.133,1983.

[229] ASTM F2004-05, Standard Test Method for Transformation Temperature of Nickel-Titanium Alloys by Thermal Analysis.

[230] S. Schirmer, J.K.N. Lindner, S. Mandl, *Nuclear Instruments and Methods in Physics Research B.,* 2007;257:714.

[231] I. Barin, *Thermochemical Data of Pure Substances*, First Edition, Verlagsgeselischaft, Weinheim, 1989.

[232] R.M. German, *Powder Metallurgy. Science*, Second Edition, Metal Powder Industries Federation, Princeton, New Jersey, pp.210, 1994.

[233] J. Otubo, O.D. Rigo, C.M. Neto, P.R. Mei, *Mater. Sci. Eng. A,* 2006;438-440:679.

[234] M.P. Staiger, A.M. Pietak, J. Huadmai, G. Dias, *Biomater.,* 2006;27:1728.

[235] G. Fan, W. Chen, S. Yang, J. Zhu, X. Ren, K. Otsuka, *Acta Mater.,* 2004;52:4351.

[236] J. Khalil-Allafi, X. Ren, G. Eggeler, *Acta Mater.,* 2002;50:793.

[237] J. Khalil-Allafi, A. Dlouhy, G. Eggeler, *Acta Mater.,* 2002;50:4225.

[238] A. Dlouhy, J. Khalil-Allafi, G. Eggeler *Philos. Mag.,* 2003;83:339.

[239] H. Morawiec, J. Ilczuk, D. Stroz, T. Goryczka, D. Chrobak, *J. Phys. IV*, 1997;C5:155.

[240] L. Bataillard, J.E. Bidaux, R. Gotthardt, *Philos. Mag.,* 1998;78:327.

[241] D. Favier, Y. Liu, P.G. McCormick, *Scripta Metall. Mater.,* 1992;28:669.

[242] L. Bataillard, R. Gotthardt, *J. Phys. IV,* 1995;C8:647.

[243] H. Morawiec, D. Stroz, T. Goryczka, D. Chrobak, *Scripta Mater.,* 1996;35:485.

[244] K. Gall, K. Juntunen, H.J. Maier, H. Sehitoglu, Y.I. Chumlyakov, *Acta Mater.,* 2001;49:3205.

[245] L.J. Gibson, M.F. Ashby, *Cellular Solids; Structure and Properties*, Second Edition, Cambridge University Press, 1999.

[246] M. Ontanon, C. Aparicio, M.P. Ginebra, J. Planell, *Structural Biological Materials Design and Structure-Property Relationships,* edited by M. Elices, Pergamon Press, Oxford, pp.31-72, 2000.

[247] M. Barrabes, A. Michiardi, C. Aparicio, P. Sevilla, J.A. Planell, F.J. Gil, *J. Mater. Sci.: Mater. Med.*, 2007;18:2123.

[248] X.P. Zhang, H.Y. Liu, B. Yuan, Y.P. Zhang, *Mater. Sci. Eng. A,* 2008;481-482:170.

[249] D.Y. Liu, S.P. Galvin, *Acta Mater.,* 1997;45:4431.

[250] K. Gall, H. Sehitoglu, *Int. J. Plasticity,* 1999;15:69.

[251] R.J. Wasilewski, *Metall. Mater. Trans.,* 1971;2A:2973.

[252] L. Orgeas, D. Favier, *J. Physique,* 1995;5:605.

[253] K. Jacobus, H. Sehitoglu, M. Balzer, *Metall. Mater. Trans.,* 1996;27A:3066.

[254] R. Plietsch, K. Ehrlich, *Acta Mater.,* 1997;45:2417.

[255] Z. Xie, Y. Liu, J. Van Humbeeck, *Acta Mater.,* 1998;46:1989.

[256] K. Gall, H. Sehitoglu, Y.I. Chumlyakov, I.V. Kireeva, *Acta Mater.,* 1999;47:1203.

APPENDIX A

Schematic Drawing of Vertical Furnace and Its Equipment
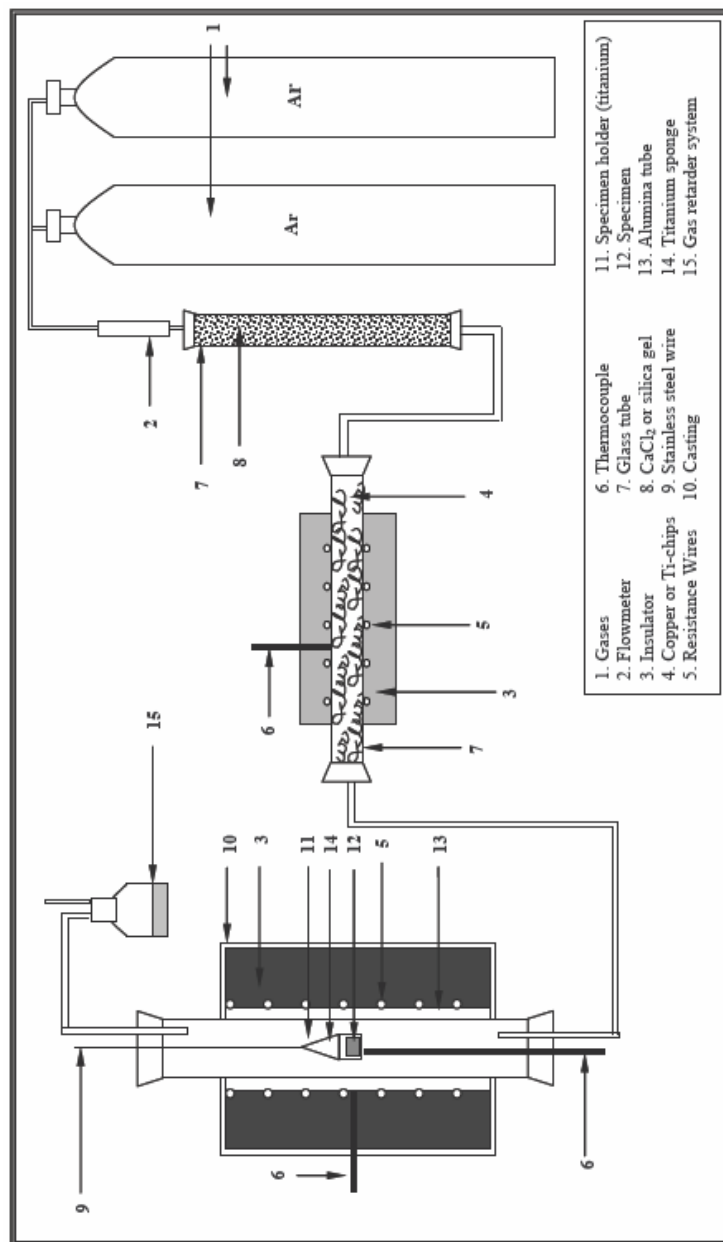
CURRICULUM VITAE

PERSONAL INFORMATION

Surname, Name: Aydoğmuş, Tarık
Nationality: Turkish (TC)
Date and Place of Birth: 24 June 1977, Eskişehir
Marital Status: Married
Phone: +90 312 210 5849
Fax: +90 312 210 2518
e-mail: aydogmus@metu.edu.tr

EDUCATION

Degree	Institution	Year of Graduation
BS	ITU Metallurgical Engineering	2000
High School	Eskişehir Yunusemre Anatolian Teacher Training High School	1995

WORK EXPERIENCE

Year	Place	Enrollment
2002-present	METU, Department of Metallurgical and Materials Engineering	Research Assistant
2001-2002	Turkish Armed Forces, Commandership of 500th Main Depot and Plant	Second Lieutenant, R&D Engineer
2000 July	ERDEMİR	Intern Engineering Student
1999 July-August	Diler Iron and Steel Corp.	Intern Engineering Student

FOREIGN LANGUAGE

Advanced English

PUBLICATION

T. Aydoğmuş, Ş. Bor, Processing of porous TiNi alloys using magnesium as space holder, J. Alloys Compd. 478 (2009) 705-710.